EPFL

Thèse n° 9826

Ultrafast carrier and quasiparticle dynamics in strongly confined perovskite nanoplatelets

Présentée le 11 novembre 2022

Faculté des sciences de base
Groupe Moser
Programme doctoral en chimie et génie chimique

pour l'obtention du grade de Docteur ès Sciences

par

Etienne Christophe SOCIE

Acceptée sur proposition du jury

Prof. K. Sivula, président du jury
Prof. J.-E. Moser, directeur de thèse
Prof. N. Banerji, rapporteuse
Dr A. R. S. Kandada, rapporteur
Prof. M. Chergui, rapporteur

École polytechnique fédérale de Lausanne

2022

Résumé

Au cours de la dernière décennie les pérovskites d'halogénures de plomb ont reçu un intérêt considérable grâce à leurs propriétés optoélectroniques. Aujourd'hui, les cellules photovoltaïques à jonction simple en pérovskite font partie des plus efficaces, avec un rendement de conversion atteignant les 25.7%. De la même manière, les nanostructures de ce même matériau ont émergé avec un potentiel exceptionnel pour des applications telles que les diodes électroluminescentes ou diodes laser. De plus, les pérovskites possèdent une structure dynamique et complexe qui les rendent fascinantes pour des études photophysiques fondamentales, non seulement pour améliorer ces dispositifs mais aussi pour transférer les connaissances vers d'autres types de semiconducteurs.
Généralement, les dynamiques ultra-rapides, de la dizaine de femtosecondes à plusieurs nanosecondes des porteurs de charges sont analysées par des techniques spectroscopiques résolues en temps utilisant des impulsions laser ultracourtes. Le but de cette thèse est d'associer les spectroscopies d'absorption transitoire (AT) et de photoluminescence résolue en temps (PLRT) pour étudier les mécanismes photophysiques dans les nanocristaux de pérovskite (NP) à faibles dimensionalité. Alors que la plupart des techniques expérimentales pour la PLRT sont limitées à des résolutions temporelles de plusieurs picosecondes, la spectroscopie de fluorescence par conversion ascendante de photons (FLUPS, en anglais) est utilisée ici pour obtenir des données spéctro-temporelles bidimensionnelles avec une résolution temporelle inférieure à la picoseconde.

Les chapitres 1 et 2 instaurent un contexte théorique et expérimental qui sera utile au reste de la thèse. Le chapitre 1 revoit les concepts photophysiques fondamentaux pour les semiconducteurs massifs et confinés et fourni un aperçu général sur les propriétés optoélectroniques des NP en examinant la littérature. Le second chapitre est axé sur la spéctroscopie PLRT et détaille l'approche théorique et expérimentale pour utiliser la FLUPS, qui est la principale méthode expérimentale utilisée au cours de cette thèse.

Le chapitre 3 détaille la procédure de la synthèse des nanobatonnets (NBs) de $CsPbBr_3$ colloïdaux émettant dans le bleu. Le produit est caractérisé par des méthodes standards tel que la microscopie électronique en transmisssion, la voltampérométre cyclique et la spectroscopie linéaire d'absorption et d'émission dans l'UV-Vis. Les conséquences du fort confinement quantique et diélectrique sont soulignées et provoquent des propriétés optoélectroniques particulières. Ensuite, l'accent est mis sur l'importance

des ligands de coiffage pour la passivation des états de surface des perovskites. Ces ligands de coiffage peuvent aussi augmenter l'efficacité du rendement quantique de fluorescence et la stabilité au long terme des NBs.

Les chapitres 4 et 5 abordent les dynamiques des porteurs de charges pour différentes intensités d'excitation. En recoupant les données obtenues par FLUPS et AT, des comportements photophysiques complexes sont révélés au cours des dix premières picosecondes. A faible intensité d'excitation, les dynamiques des NBs sont dominées par un ensemble d'excitons indépendants. De plus, à plus haute intensité d'excitation, les interactions accrues entre les porteurs de charges créent des paires excitons-excitons, aussi appelé biexcitons, qui sont stables et émissives. Les propriétés et mécanismes de recombinaison des biexcitons suivent les tendances observées dans les puits quantiques bidimensionnels.

Finalement, le chapitre 6 examine les mécanismes de séparation des porteurs de charges et de leur recombinaison ultérieure dans les NBs de $CsPbBr_3$ en combinant la FLUPS, AT à l'échelle de la picoseconde et nanoseconde. Les complexes NB-accepteurs sont synthétisés en attachant à la surface des NBs des molécules de phénothiazine et p-benzoquinone, qui jouent le rôle d'accepteur de trous et d'électrons, respectivement. Des mesures de FLUPS dépendantes de l'énergie d'excitation sont effectuées pour révéler le rapide transfert de charges depuis l'extrémité de la bande de la pérovskite et le transfert ultrarapide depuis les niveaux d'énergies plus élevés.

Mots clés: nanobatonnets de pérovskite - solutions colloïdales - photophysique - dynamique des porteurs de charges - excitons - spectroscopie à large bande de fluorescence par conversion ascendante de photons

Abstract

Over the past decade, lead halide perovskites (LHPs) have received considerable attention thanks to their impressive optoelectronic properties. Today, LHP-based devices are one of the most efficient single-junction solar cells, with power-conversion efficiencies reaching 25.7%. Likewise, nanostructures of the same material have emerged with tremendous potential for light-emitting and lasing applications. The perovskite complex and dynamic structures also makes them fascinating for fundamental photophysical studies, not only to apply in the context of the device improvements but also for a much broader class of semiconductors.
Typically, charge carrier dynamics on the ultrafast timescale, from a few nanoseconds down to tens of femtoseconds, are monitored by time-resolved spectroscopic techniques using ultrashort laser pulses. The aim of this work is to associate transient absorption (TA) and time-resolved photoluminescence (TRPL) spectroscopy for investigating early photophysical mechanisms in low-dimensional perovskite nanocrystals (PNCs). While most available TRPL experimental techniques are limited by a temporal resolution of a few picoseconds, broadband fluorescence upconversion spectroscopy (FLUPS) is employed to obtain two-dimensional spectro-temporal data with a sub-picosecond temporal resolution.

Chapters 1 and 2 provide the scientific background relevant to the thesis. Chapter 1 establishes the fundamental photophysical concepts for bulk and confined semiconductors and provides a general overview of the PNC optoelectronic properties, reviewing the relevant literature. The second chapter focuses on TRPL spectroscopy and details the theoretical and experimental approaches for FLUPS, the primary technique employed in this work.

Chapter 3 describes the synthetic procedure to obtain colloidal blue-emitting $CsPbBr_3$ nanoplatelets (NPls). The product is then characterized by standard methods, including transmission electron microscopy, cyclic voltammetry and linear UV-Vis absorption and emission spectroscopy. The consequences of strong quantum and dielectric confinements are highlighted and induce unique optoelectronic properties. The importance of capping ligands engineering for passivating the perovskite surface states is also stressed. Capping ligands can also increase the NPl emission efficiency and long-term stability.

Chapters 4 and 5 discuss the charge carrier dynamics under weak and strong excitation regimes. By

combining FLUPS and TA data, complex photophysical behaviors within the first ten picoseconds are revealed. Under low excitation intensities, the NPl dynamics are dominated by an ensemble of independent excitons. Besides, at high pump fluences, enhanced carrier-carrier interactions induce surprisingly stable and emissive exciton-exciton pairs, also called biexcitons. The properties and recombination mechanisms of the biexcitons display typical quantum well signatures.

Finally, chapter 6 investigates the charge separation and subsequent charge recombination mechanisms in $CsPbBr_3$ NPls combining FLUPS, TA and nanosecond flash photolysis measurements. NPl-acceptor complexes are synthesized by attaching phenothiazine and p-benzoquinone to the NPl surface, acting as hole and electron acceptors, respectively. Excitation energy-dependent FLUPS measurements are carried out to unveil fast interfacial charge transfer from the perovskite band edge and ultrafast hot carrier transfer from higher energy levels.

Keywords: perovskite nanoplatelets - colloidal solutions - photophysics - charge carrier dynamics - excitons - broadband fluorescence upconversion spectroscopy

Contents

Chapter 1

Introduction

This introductory chapter gives the basic principles of semiconductor photophysics, highlighting the differences between bulk and quantum-confined semiconductors. These concepts are then applied to understand the fascinating optoelectronic properties of lead halide perovskite nanocrystals of multiple dimensionalities.

The first part of this chapter is inspired by the books "Physical Chemistry" by Atkins and de Paula,[1] "Semiconductor Optics" by Klingshirn,[2] and "Optical properties of solids" by Fox,[3] while the second part is partially based on "Halide Perovskites: photovoltaics, light emitting devices and beyond" by Sum and Mathews,[4] and the perspective article "Exciton and Multiexciton Dynamics in Lead Halide Perovskite Nanocrystal" written equally by Dr. Vale and myself and which has just been submitted.

1.0 Global context

The Doomsday Clock, a symbol of how close human actions are to resulting in a global catastrophe, has been moved to 100 s before midnight in 2020, which is the closest approach since its creation. From the 1990s, climate change has become the predominant source of concern for the scientific community, but remains poorly addressed by world leaders. Earth's global warming is mostly attributed to the emission of greenhouse gases, via fossil fuel combustion, to answer the growth of the global energy consumption (from $43 \cdot 10^3$ TWh in 1965 up to $1.6 \cdot 10^4$ TWh in 2019).[5] Therefore, one of the greatest challenges is to achieve carbon neutrality before 2050 by using renewable energy as the dominant form of electricity generation. The most abundant renewable energy source available on Earth remains solar energy, which could easily cover the whole human consumption with a potential of up to $14 \cdot 10^6$ TWh (taking into account insolation, cloud cover and the lands used by humans).[6] One could meet the world energy demand only by covering 0.3% of the Earth's land area with solar panels (less than the territory of Metropolitan France). While constantly expanding, the photovoltaic (PV) market is still dominated by silicon-based solar cells but shifts towards the use of emerging technologies, including perovskites. The focus is now set on efficiency, long-term stability and production cost/scalability to boost the material's performance. In this way, a fundamental understanding of the physical processes behind energy generation becomes crucial for our future. Light energy conversion into electric current is achieved through a physical and chemical phenomenon called the PV effect. First evidenced by Becquerel in 1839, the PV effect is the basic principle behind solar cell devices.[7] Basically, when a material is struck by light, the absorbed photons may provide enough energy to promote electrons to the conduction band and generate electronic conductivity. The following sections aim to describe the fundamental photophysical properties of semiconductors (SCs) to better understand light energy conversion.

1.1 Photophysics of semiconductors

1.1.1 Bulk semiconductor fundamental properties

The unique conductive properties of bulk SCs, in between that of metals and isolators, arise from their electronic band structure. Macroscopic solids are composed of a considerable number of atoms interacting with each other to form molecules. As a result, atomic orbitals spatially overlap and hybridize, creating a multitude of adjacent energy levels, which are regarded as continuous energy bands. The band structure, unique for each solid, contains bands of energy states separated by ranges where no electronic state exists, called band gaps. As electrons are fermions, the Fermi-Dirac distribution gives the probability, $f(\xi)$, for

a state with energy ξ [eV] to be occupied by an electron under thermal equilibrium.[8,9]

$$f(\xi) = \frac{1}{\exp\left[\left(\xi - E_F\right)/k_b \cdot \mathrm{T}\right] + 1} \tag{1.1}$$

where E_F is the SC Fermi level [eV], T is the temperature [K], and k_b is the Boltzmann constant [eV/K]. E_F is defined as the highest energy level possibly occupied by an electron at absolute zero temperature, and its position is crucial for determining a materials electronic properties.

For T > 0 K, if the Fermi level is located within an allowed energy band, there are multiple partially filled states near E_F in which electrons flow through (i.e., are delocalized), generating electric current. These particular types of solids are called metals. Conversely, for isolators, the Fermi level lies inside the band gap, far away from the energy band edges. The bands are either totally filled or empty of electrons, preventing their delocalization and the generation of current. Intrinsic SCs are similar to isolators but with a smaller band gap, allowing the thermal excitation of electrons from a filled to an empty band at room temperature (RT) (**Figure 1.1**). Usually, the terms "valence band" (VB) and "conduction band" (CB) are used to define the highest filled band and the lowest unfilled (or partially filled) band at 0 K, respectively. Therefore, the VB is located below E_F while the CB is just above.

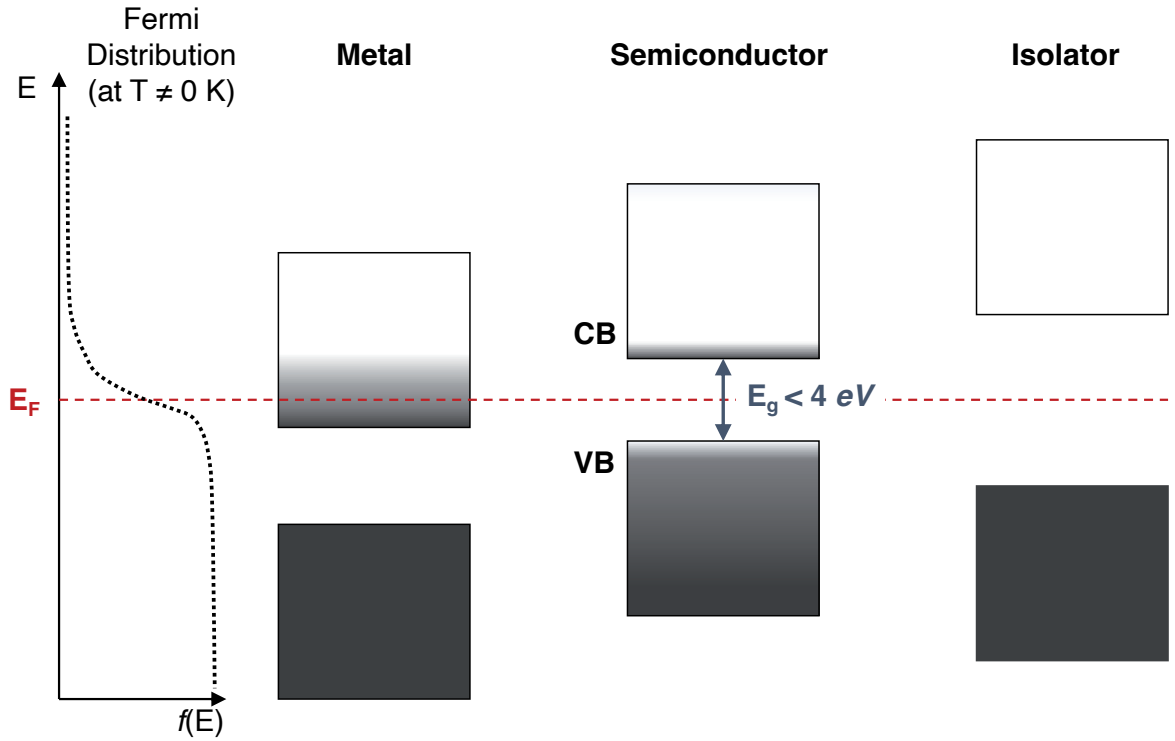

Figure 1.1: Fermi distribution with the associated Fermi level for $f(\xi) = 0.5$ and schematic representation of the band energy diagram of a metal, a semiconductor and an isolator.

By increasing the material temperature, its band gap energy, E_g (T) [eV], diminishes following the Varshini equation:[10]

$$E_g(\mathrm{T}) = E_g(\mathrm{T} = 0\ \mathrm{K}) - \frac{\alpha \cdot \mathrm{T}^2}{\mathrm{T} + \beta} \tag{1.2}$$

where α [eV/K] and β [K] are material constants. In addition, more electrons may acquire the required energy to cross the band gap resulting in an increased conductivity. Yet, the number of electrons promoted to the CB does not only depend on the occupancy probability but also scales with the number of available states at each energy, which is defined as the electron density of states (DOS). The probability of a transition from a state initial to a final state, $i \rightarrow f$, is proportional to the density of final states, ρ_f, and is given by Fermi's golden rule:

$$\Gamma_{i \rightarrow f} = \frac{2\pi}{\hbar} \langle f | H' | i \rangle \rho_f \tag{1.3}$$

where $\langle f | H' | i \rangle$ is the matrix element of the perturbation from the final and initial states. For simple 3D SC materials, the DOS rises from the bottom of the CB with the square root of the energy:

$$\rho_f = \frac{1}{2\pi^2} \left(\frac{2m_e^*}{\hbar^2} \right)^{\frac{3}{2}} \sqrt{E - E_g} \tag{1.4}$$

where $\hbar$ is the reduced Planck constant [J·s], m_e^* is the electron effective mass [kg], and E_g is the band gap [J].

Conventional routes to boost the concentration of free charges (and the conductivity of SCs) imply chemical doping. Doping an intrinsic SC changes its optical and structural properties by adding a small fraction of external atoms, from one per 10^4 to 10^8. For example, silicon (group IV) doped with boron (group III) or phosphorus (group V) atoms can increase the conductivity by a factor of 10^6.[11] Doping agents are classified into two categories depending on their nature. In the previous example, if a silicon atom is substituted with a phosphorus atom in the lattice structure, it adds an element with an additional valence electron to the system. Therefore, phosphorus acts as an electron donor, resulting in an n-type SC. Here, "n" stands for negatively charged SC since electrons are the majority carriers. In addition, the VB and CB are shifted down compared to intrinsic silicon so that the Fermi level becomes closer to the conduction band minimum (CBM). Conversely, if one boron substitutes one silicon, a valence electron is removed, which creates a p-type SC with boron acting as an electron acceptor. The bands are also shifted up so that the valence band maximum (VBM) approaches E_F. Hence, donors and acceptors bring "free" charge carriers that can move in the bands with low input energy. In terms of electronic band structure, the energy levels of the donor are located slightly below the CB, while those of the acceptor are slightly above the VB.

1.1.2 Light absorption by SCs

It has previously been mentioned that, in SCs, electrons may acquire enough energy and be promoted from the VB to the CB. This energy can be provided in the form of heat, external electric fields or light. The latter process is called photoexcitation and is the principal subject of the thesis. The number of photoexcited species is related to the ability of the SC to absorb light. As a beam of light crosses the SC, its intensity decays exponentially via:

$$I(l) = I_0 \cdot \exp(-\alpha l) \tag{1.5}$$

where I_0 and $I(l)$ are the initial light intensity and light intensity at point l [-], l the thickness of the material [cm], and α is the absorption constant [cm^{-1}] which is specific to each SC.

Once an electron leaves the VB to reach the CB, it leaves behind a positively-charged space called an electron hole, and often simplified as a "hole". The hole has the same charge magnitude as the electron but with an opposite sign. Since holes move freely within the VB, both electron and hole delocalization contribute to the material conductivity. These quasi-particles are called charge carriers. Two simple rules must be fulfilled to obtain the photogeneration of charge carriers: energy and momentum conservation.

- Energy conservation: the energy of the incoming photon should match or be greater than the band gap energy. If the absorbed photons are more energetic, electrons will be excited at higher electronic levels and will leave holes below the VB edge.
- Momentum conservation: by considering free electron and hole motions, the band structure can be represented in the reciprocal space as a combination of de Broglie's parabolas, themselves as a function of the charge carrier angular wavenumber, k [m^{-1}] (the magnitude of the wave vector **k**):

$$E = \frac{p^2}{2m_c^*} = \frac{\hbar^2 \cdot k^2}{2m_c^*} \tag{1.6}$$

  where E is the energy [J], p is the momentum [kg·m/s], $\hbar$ is the reduced Planck constant [J·s], and m_c^* the charge carrier effective mass [kg].

As shown in **Figure 1.2-left**, there are two types of transitions: vertical (direct), with no change in the momentum or non-vertical (indirect), with a **k** mismatch. Because photons do not carry enough momentum, indirect transitions require an additional absorption (or emission) of a phonon equalizing the mismatch in **k**. Similarly to how photons can be seen as quantized electromagnetic waves, phonons are quantized sound waves corresponding to lattice vibrations. Since indirect transitions are two-step

processes, they are less probable and strongly depend on the number of available phonons and the temperature. Applied to SC photophysics, materials having a vertical transition between their VBM and CBM are called "direct band gap". Conversely, if there is a change in **k**, the material is known as an indirect band gap SC. Material optoelectronic properties depend strongly on the type of band gap: for example, indirect band gap SCs have much lower absorption constants, α, than their direct band gap counterparts and require thicker films to absorb the same amount of light.

In the context of power conversion, the aim is to extract the carrier energy to produce electricity (solar cells), light (light-emitting diodes, LEDs) or promote chemical reactions (photocatalysis). However, electrons and holes do not stay indefinitely in the excited state induced by photoexcitation but rather return to their original position, i.e., to the ground state, preventing energy collection.

1.1.3 Charge carrier dynamics in bulk SCs

Directly after photoexcitation, the energy of the charge carriers matches that of the absorbed photons. Therefore, electrons and holes have a narrow and non-thermal energy distribution. **Figure 1.2** summarizes how carriers with excess energy relax to the band edge (or lowest excited state).[12]

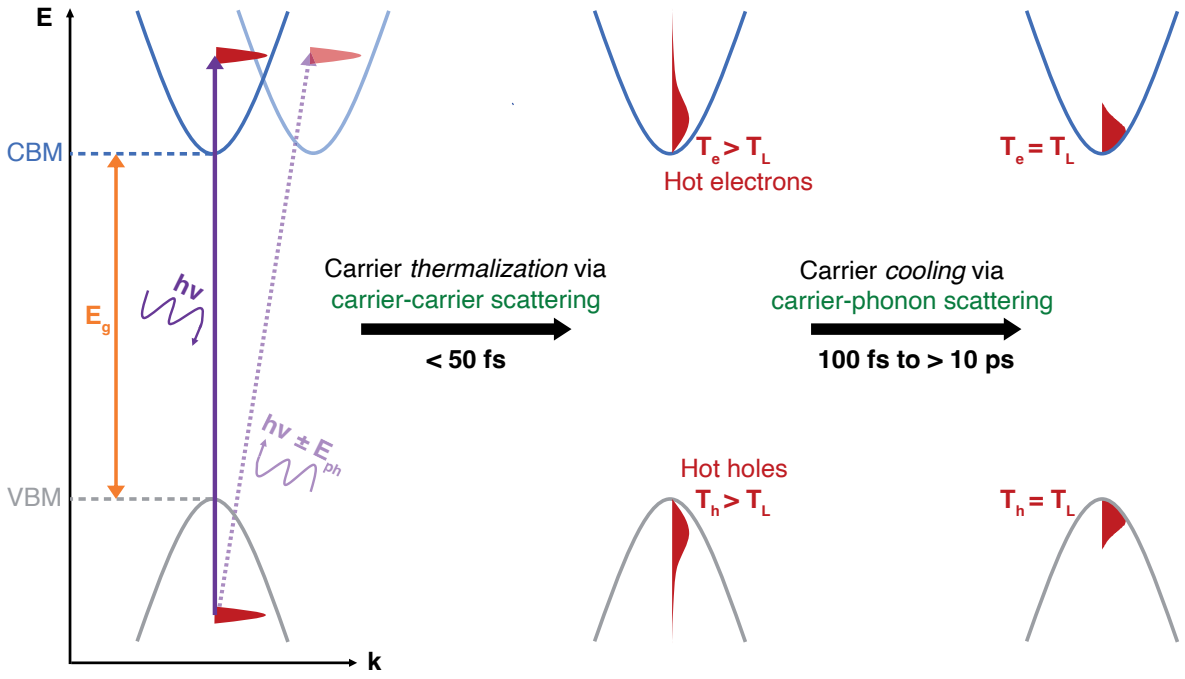

Figure 1.2: Graphic representation of light absorption in SCs and subsequent ultrafast carrier relaxation processes.

- Carrier thermalization: usually, thermal equilibrium is reached in sub-50 fs through carrier-carrier scattering. After thermalization, the energy distribution of the charge carriers follows Fermi-Dirac

statistics (**Equation 1.1**). Here, the carrier temperature, T_c, is higher than the lattice temperature, T_L, and these carriers are considered as "hot".

- Carrier cooling: hot charge carriers release heat to return to the lattice temperature, predominantly by emitting phonons. In SCs, this step is conventionally pictured as a relaxation from charge carriers in the deep VB or CB states to the band edge and takes a few hundreds of femtoseconds to tens of picoseconds depending on the band structure and the excited charge carrier properties. The carrier cooling process is decomposed into three steps:[13] 1) carrier-phonon scattering, or Fröhlich interaction, 2) optical phonons decay to acoustic phonons and 3) delocalization of acoustic phonons, increasing the lattice temperature. Multiple factors, including screening between the hot carriers and phonons, reduced photonic DOS or up-transition of acoustic phonons to re-form optical phonons, can slow down the overall cooling resulting in a "hot-phonon" bottleneck effect. Since hot carriers carry more energy, increasing their lifetime becomes crucial to improve device performances.

Charge carriers at the band edge may then return to the ground state in a few picoseconds to several hundreds of milliseconds either through radiative or non-radiative processes (**Figure 1.3**). In bulk SCs, Shockley-Read-Hall (SRH), band-to-band and Auger recombination are the most common processes.

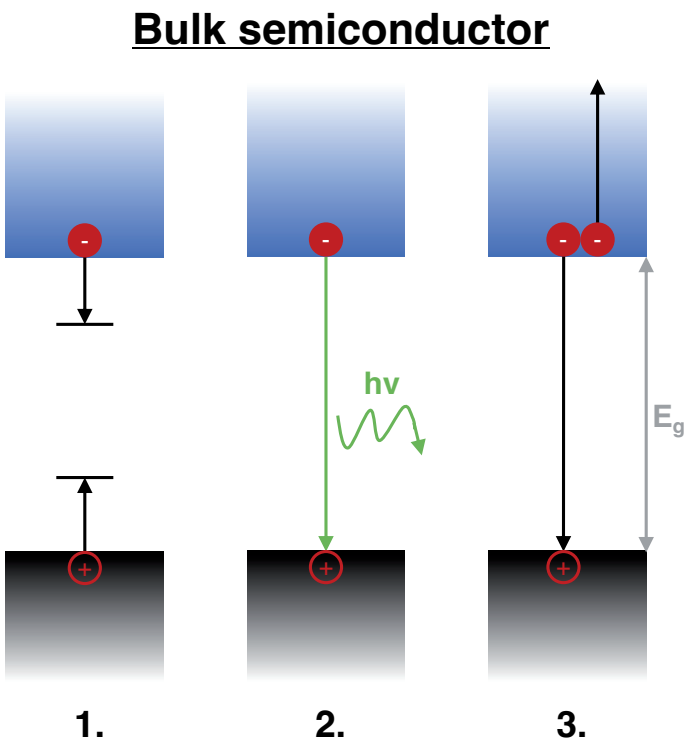

Figure 1.3: Schematic representation of the most common carrier recombination mechanisms in SCs: 1. SRH recombination. 2. Band-to-band radiative recombination. 3. Auger recombination.

- SRH recombination, also called trap-assisted recombination, emerges with the presence of mid-gap states (localized energy states within the band gap).[14,15] These states are created by intrinsic defects in the crystal structure (atom vacancies or interstitial atoms) or through the addition of doping agents. The electron (or hole) may decay in these mid-gap states by exchanging phonons with the lattice and is, therefore, "trapped" within the band gap. The trapping rate scales linearly with the carrier density. The subsequent recombination from the trap states is mainly non-radiative but can, sometimes, emit a photon of low energy. As the formulation "mid-gap states" is generic, further clarification is required to characterize their nature. Firstly, "electron traps" are employed if the state levels are close to the CB and "hole traps" if they lie near the VB. The former most likely captures electrons, while holes occupy the latter. Secondly, if the difference between the trap states and the CBM (or VBM) is lower than the thermal energy, the term "shallow traps" is assigned. In this case, carriers can be thermally de-trapped and return to their original states. If the energy difference is greater, they are labeled deep trap states.

- Band-to-band recombination is the spontaneous emission from the recombination of an electron at the CBM and a hole at the VBM. Because the photon emission requires two charge carriers at the band edge, band-to-band recombination is a bimolecular radiative process and has a quadratic dependence on the carrier density. As expressed earlier on, since photons do not carry enough momentum, radiative recombination is disfavored for indirect band gap SCs.

- Auger recombination is a non-radiative process which takes its name from the Auger effect. An electron and a hole at the band edge can relax to the ground state by transmitting their energy to a third excited carrier. The last species is promoted to higher energy levels, still within the same band, and relaxes back to the band edge by cooling. Since Auger recombination is a three particle process, it has a cubic dependence on the carrier density.

From the three main recombination pathways, the evolution of the charge carrier density, N_c [m^{-3}], is expressed as:

$$\frac{dN_c(t)}{dt} = -k_1 \cdot N_c - k_2 \cdot N_c^2 - k_3 \cdot N_c^3 \tag{1.7}$$

where k_1, k_2 and k_3 are the rate constants [s^{-1}] describing the SRH, band-to-band recombination and Auger processes, respectively.

Understanding how these rates are affected by the SC chemical composition (or by external parameters) is crucial for obtaining efficient devices. For example, LEDs require high radiative recombination rates with low SRH and Auger recombination, while low radiative and non-radiative rates are more appropriate for light-harvesting devices.[16]

Another crucial parameter is the ability of the SC to sustain charge separation. In typical PV devices, after separation the charges diffuse to the metallic electrodes and are collected to generate current. Henceforth, four methods are highlighted to obtain a built-in driving force leading to charge separation.
For crystalline Si, the 1st PV generation, the separation is achieved with a p-n homojunction by doping the silicon with A) a donor (usually phosphorus) and B) an acceptor (boron). The connection between the two materials with different doping atoms generates an electric field at the interface, which can separate the photogenerated carriers. The charge separation for 2nd and 3rd PV generations, such as CdTe/CdS, CIGS and organic PV (OPV) materials, is based on donor-acceptor bilayers, also called heterojunctions. Here, the driving force for charge separation is brought by the band offset between an electron donor and an electron acceptor material. Then, the free charges are transported to the electron transporting material (ETM) or the hole transporting material (HTM).[17] In dye-sensitized solar cells, the charges are not separated spatially, but the current generation is established by the fast kinetics of the electron transfer between the active layer (usually an inorganic dye) and the SC (usually TiO_2). To minimize charge recombination, an aqueous electrolyte also rapidly quenches the oxidized dye.[18] Finally, perovskite devices, which are the systems of interest in this work, may be pictured as double donor-acceptor heterojunctions where the active layer is sandwiched between an ETM (TiO_2 or ZnO) and a HTM (spiro-OMeTAD).[19]

One subject that has not been discussed yet is the interaction between charge carriers and atomic positions for polarizable lattices. In molecular crystals or polar SCs, atoms might displace from their equilibrium positions to screen the negative charge carried by the electrons, resulting in quasi-particles called polarons. This coupling often reduces the charge carrier mobility by increasing their effective masses.[20] Polarons are classified into categories: large polarons where the induced polarization extends over more than one unit cell (Fröhlich polarons),[21] or "small polarons" if the polaron radius is smaller than a unit cell. In that case, charge carriers are trapped in a self-induced potential well: we say that carriers are self-trapped and hop from one site to another.

1.2 Quantum-confined semiconductors

1.2.1 The effects of confinement

SC nanomaterials, i.e., SCs having at least one dimension shorter than 100 nm, are a central topic in nanotechnology as they have a vast range of potential applications from light-harvesting and light-emitting devices to medical imaging and microscopy.[22–24] By reducing the size of the SCs, the electronic and optical properties could be affected by quantum confinement. Indeed, the charge carrier motion

becomes restricted to a finite region of space if at least one of the SC dimensions, L [m], becomes smaller than the de Broglie wavelength for the electron (or hole) motion:

$$L \leqslant \frac{\hbar}{\sqrt{m_c^* \cdot k_b \cdot T}} \tag{1.8}$$

where $\hbar$ is the reduced Planck constant [J·s], m_c^* is the charge carrier effective mass [kg], k_b is the Boltzmann constant [J/K] and T the temperature [K]. At RT, this number varies from a couple of nanometers to a few tens of nanometers, depending on the carrier effective masses and, therefore, the SC band structure. Usually, SCs are classified according to the number of "free" dimensions, i.e., dimensions larger than the de Broglie wavelength: they range from bulk nanomaterials (3D), nanosheets or quantum wells (2D), nanorods or quantum wires (1D) and quantum dots (QDs, 0D). Yet, another relevant parameter to define quantum confinement is the spatial separation of the electron-hole pair which is simplified as the exciton Bohr radius, r_0 [m]:

$$r_0 = \frac{4\pi \cdot \varepsilon_r \cdot \epsilon_0 \cdot h^2}{m_{\text{ex}} \cdot e^2} \tag{1.9}$$

where ε_r (ε_0) is the material (vacuum) permittivity [F/m], h the Planck constant [J·s], m_{ex} is the reduced mass of the exciton [kg] and e is the elementary charge [C]. SCs having a dimension smaller than the exciton Bohr radius fall into strongly confined regimes, while others are named "weakly confined SCs".

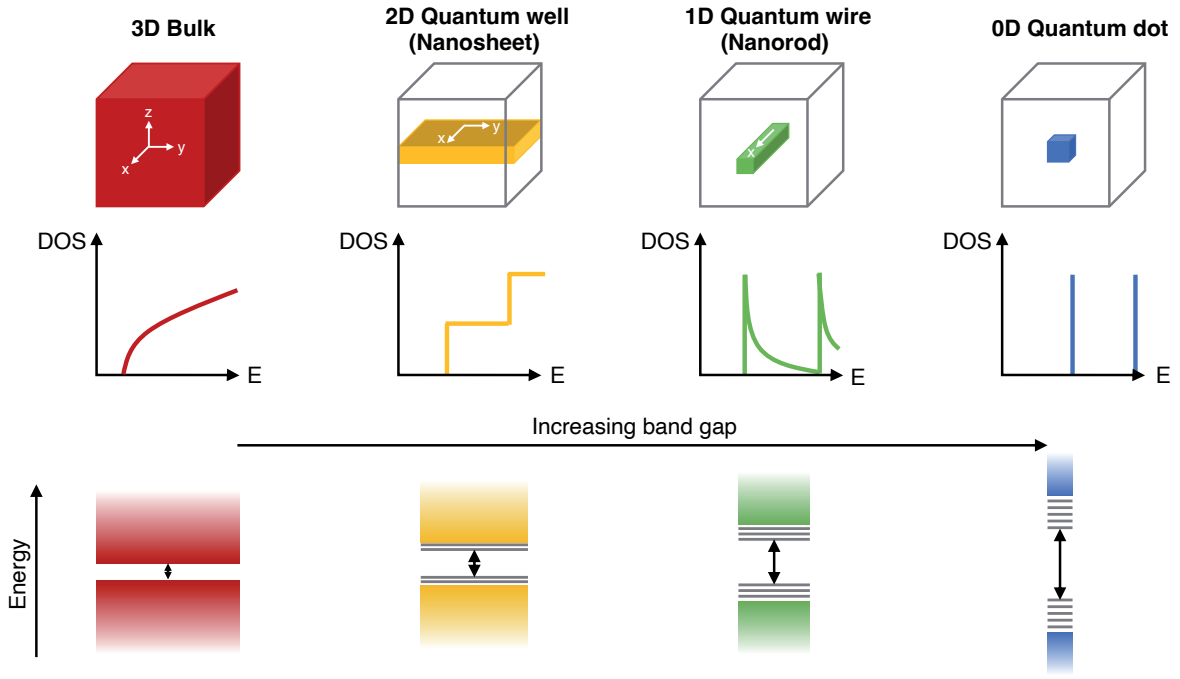

Figure 1.4: Effect of the quantum confinement on the SC structure, density of states and energy levels.

As pictured in **Figure 1.4**, the reduction of the SC dimensionality has three principal effects: 1) the formation of discrete energy levels, 2) a band gap expansion and 3) an enhanced exciton binding energy. Because of quantum confinement, electron and hole motions are reduced in one or more dimensions leading to a reduced number of available states. While for 3D SCs, the DOS is proportional to the square root of the energy, it becomes independent of the energy for 2D materials, inversely proportional to the square root of the energy for 1D structures and described as a Dirac function for 0D QDs. Besides, the deviation of the band gap for confined SCs compared to their bulk counterparts follows:[25]

$$\Delta E_g = \frac{h^2}{8 \cdot c \cdot L^2} \left(\frac{1}{m_e^*} + \frac{1}{m_h^*} \right) \tag{1.10}$$

where E_g is the band gap [eV], h is the Planck constant [J·s], c a coefficient depending on the dimensionality of the model, L is the size of the SC in the confined dimension [m], and m_e^* and m_h^* are the electron and hole effective masses [kg]. Therefore, one can easily tune the optical band gap of SC nanomaterials by controlling their size, which is of great interest for device development.[26] Additionally, SC nanostructures are often surrounded by organic capping ligands bound to the surface for stabilizing their size and shape. This structure becomes the source of another type of confinement for small SCs, called dielectric confinement.[27] Since organic capping ligands exhibit a lower optical permittivity than the inorganic core the electric field screening between electrons and holes is reduced. Hence, if the SC material is thin enough, it can further enhance the photogenerated charge interactions.

1.2.2 Excitons and biexcitons in quantum-confined SCs

The combination of quantum and dielectric confinement results in strongly bound electron-hole pairs. The Coulomb attraction between a negatively charged electron in the CB and a positively charged hole in the VB gives rise to the formation of a so-called exciton. Excitons are, by nature, electrically neutral quasi-particles and are usually divided into two categories: Wannier-Mott (WM) nd Frenkel excitons.

- WM type excitons are weakly bound quasi-particles with a radius encompassing the unit-cell and are mainly found in inorganic SCs with a high permittivity.[28] WM excitons can move freely in the system and the electron is viewed as orbiting around the hole, which is analogous to the Schrödinger equation of the hydrogen atom. For 3D materials, its kinetic energy is given by:[29]

$$E(n) = \frac{-\Delta_x}{n^2} \tag{1.11}$$

where n is a positive integer designating the principal quantum number and Δ_x is the exciton

binding energy [eV], which is equals to:

$$\Delta_{\mathrm{x}} = \frac{m_e^* \cdot m_h^*}{m_0 \cdot \varepsilon^2 \cdot (m_e^* + m_h^*)} \cdot R_H \tag{1.12}$$

where m_e^* and m_e^* are the electron and hole effective masses [kg], ε is the material permittivity [F/m] and R_H is the Rydberg energy of the hydrogen atom (13.6 eV). The exciton binding energy is inversely proportional to the medium relative permittivity but also depends on the electron and hole effective masses, which are affected by the material band structure. Typical inorganic SCs display Δ_{x} increasing with the band gap, but below the thermal energy at RT (usually 2-25 meV). Therefore, excitons split easily upon collisions with phonons, providing a balance between free carriers and WM excitons. In quantum-confined SCs, the exciton motion is constrained in space and Bohr's relationship does not hold anymore. In fact, exciton binding energies in quantum wells largely overcome the values predicted by the model.[30]

- Frenkel excitons arise from localization of electrons and holes within the unit cell breaking the prerequisites for being described by Bohr planetary model. Localization of the charge carriers results in small and strongly bound excitons. Frenkel excitons are found in organic or molecular crystals with small dielectric constants and large charge carrier effective masses. In opposition to the free WM excitons, they propagate in the material by hopping from site to site. They also exhibit high exciton binding energies, up to one eV, making them stable at RT. Finally, Frenkel excitons are prone to couple with the lattice (comparable to the formation of small polarons) and can be further localized by self-trapping.

Additionally, a particular class of excitons arises in organic crystals or bilayer SCs: charge-transfer (CT) excitons. A CT exciton is a bound electron-hole pair occupying two adjacent molecules separated by an interface, a junction or any boundary.[31] Due to their spatial separation, CT excitons possess an electric dipole moment, unlike WM or Frenkel excitons. The breaking of a CT exciton into separated free carriers is a crucial step for OPV systems.

Because of the strong overlap between the electron and the hole wavefunctions, excitons display large absorption coefficients. The absorption intensity is proportional to the exciton binding energy and is even enhanced for quantum-confined structures. As displayed in **Figure 1.5**, the excitonic absorption peak appears below the band edge, with a difference corresponding to Δ_{x}. While this peak may be convoluted with the rise of the continuum band absorption in 3D inorganic SCs, the two features become easily distinguishable for organic or quantum-confined materials with large Δ_{x}. Optical transitions to higher

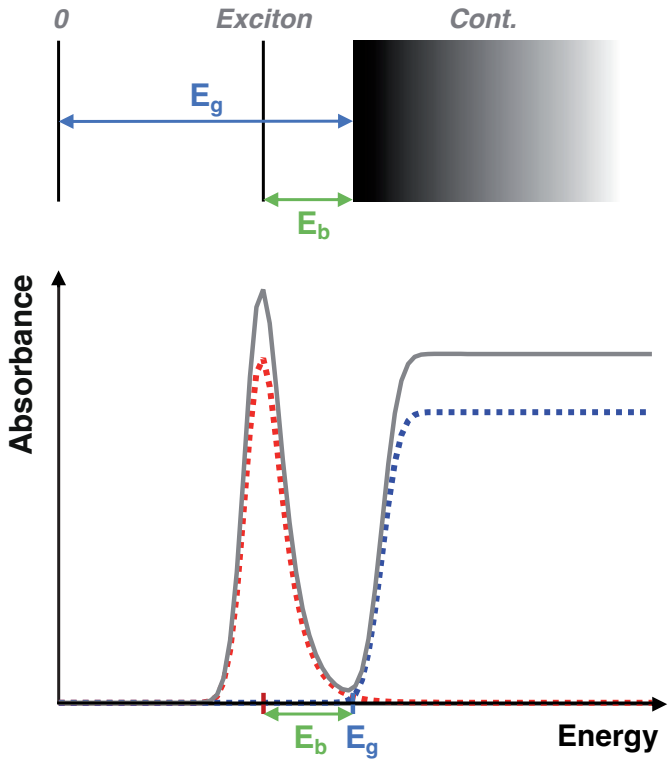

Figure 1.5: Contribution from the exciton state (red dashed line) and the continuum band (blue dashed line) to the absorbance spectrum of a SC. Highlighted in green is the exciton binding energy.

exciton energy levels (n > 1) are usually more complex to track due to their lower intensities and the overlap with the free carrier absorption.

Finally, interesting physical phenomena are observed at high photoexcitation densities for SCs having stable excitons. At high carrier densities, the distance between two neighboring excitons becomes close to the exciton diameter, leading to exciton-exciton interactions. These interactions could create electron-hole plasma,[32] Bose-Einstein condensates at low temperature,[33] or, more widely, give rise to biexcitons.[34] Biexcitons are quasi-particles resulting from the attractive interaction between two excitons and are the subject of extensive studies in quantum-confined SCs.[35–37] The biexciton binding energy, Δ_{xx} [eV], corresponds to:

$$\Delta_{xx} = 2E_x - E_{xx} \tag{1.13}$$

where E_x and E_{xx} are the energy states for the single and the biexciton [eV], respectively. In 2D quantum well structures, theoretical studies predict a ratio of 0.228 between Δ_{xx} and Δ_x.[38]

1.2.3 Photoexcited states dynamics in quantum-confined SCs

This section discusses the recombination pathways of organic or quantum-confined SCs governed by exciton dynamics. Since excitons are regarded as single entities, they generally recombine through monomolecular or bimolecular processes (**Figure 1.6**).

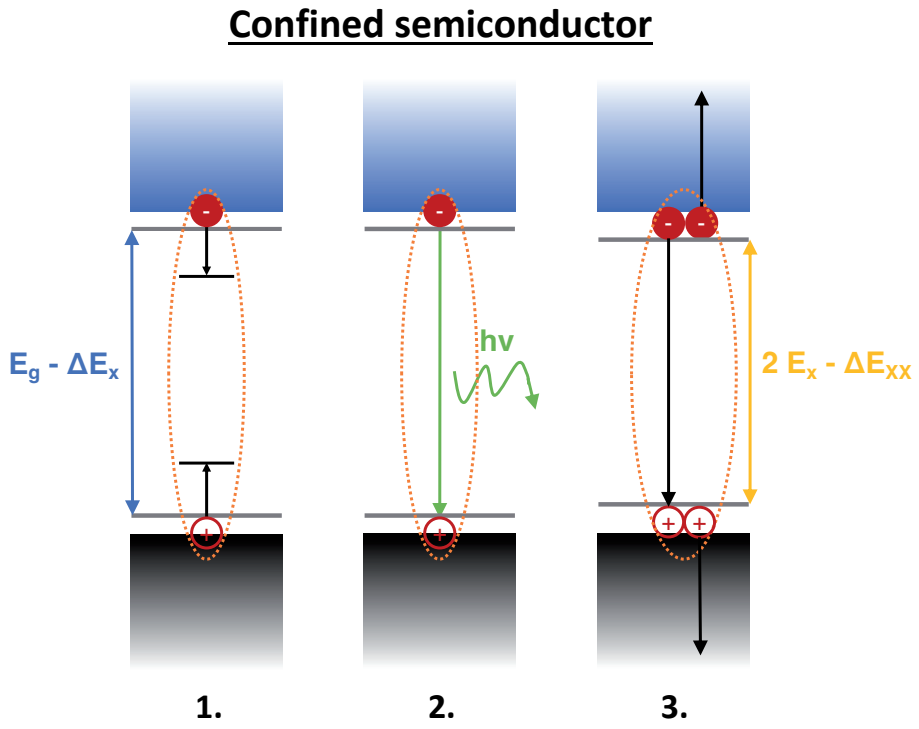

Figure 1.6: Schematic illustration of the most common carrier recombination processes in confined SCs: 1. Trap-assisted recombination. 2. Exciton radiative recombination. 3. Exciton-exciton annihilation.

- The exciton trapping process is akin to the SRH recombination described earlier. Either the electron or the hole is trapped in a mid-gap state while the energy serves to promote the other carrier to the continuum band.[39] Once localized, the charge carrier likely goes back to the ground state by heating the lattice. Importantly, surface states, such as under-coordinated atoms, are prone to act as trap centers. This process is favored in SC nanomaterials because of their high surface-to-volume ratio. Therefore, most of the quantum-confined structures exhibit a core-shell configuration, or are synthesized with capping ligands, to passivate the surface and reduce the number of defects.[40,41]

- Similarly to the band-to-band recombination for free carriers, excitons can return to the steady-state by emitting a photon. The photon energy is slightly smaller than the band gap, with a shift corresponding to the exciton binding energy. As argued before, excitonic emission intensities are enhanced due to the spatial overlap between the charge carrier wavefunctions. In addition, the recombination rates become faster as the exciton binding energy increases.

- The most common bimolecular recombination process is exciton-exciton annihilation. As Auger recombination, a first exciton recombines non-radiatively by transferring its energy to a second, neighboring, exciton that is promoted to a higher energy level or split into free carriers.[42] Exciton-exciton annihilation becomes the dominant recombination pathway for biexcitons because of the vicinity of the two quasi-particles.

Tuning the ratio between exciton and free charges is of great interest for optoelectronic devices. This ratio depends on the exciton binding energy but also on the excitation density.[43] On the one hand, enhanced exciton binding energy increases the probability of radiative recombination, which is advantageous for LEDs. On the other hand, due to the Coulomb attraction between the electron and the hole, the charge separation is more challenging, preventing the subsequent charge collection for light-harvesting applications. Therefore, finding a way to control the size, and therefore the degree of quantum confinement, of the SC becomes crucial.

1.3 Lead halide perovskite nanocrystals

Over the past 15 years, lead halide perovskites (LHPs) have received considerable attention from the scientific community for photovoltaic applications. First exploited in dye-sensitized solar cell structures,[44,45] LHP solar cells are now manufactured as thin-film solid-state devices with the perovskite acting as the light absorber and the charge transporting material.[46] Today, LHP-based devices are one of the most efficient single-junction solar cells, with a power-conversion efficiency reaching 25.7%.[47] Besides, in 2015 Kovalenko and his group reported an easy colloidal synthesis of all-inorganic LHP nanomaterials displaying tremendous potential for light-emitting applications.[48] Seven years later, the external quantum efficiency of perovskite LEDs has been pushed to 23% for red-,[49] and green-emitting devices.[50] This chapter aims to provide an overview on the optoelectronic properties of bulk and confined perovskite systems and highlight the peculiarities of LHPs.

1.3.1 Bulk perovskite structure and properties

The term "perovskite" originates from the mineral calcium titanate $CaTiO_3$, discovered in 1839. Its crystal structure consists of corner-sharing TiO_6 octahedra with Ca^+ occupying the voids. However, the referenced cubic structure obtained at high temperature is often distorted into tetragonal or orthorhombic phases, causing a rearrangement of the unit cell at RT. Nowadays, all ABX_3 compounds (**Figure 1.7**) are labelled "perovskites", making them one of the most abundant structural families. In the context of optoelectronic technologies, the central atom B is a divalent cation (usually Pb^{2+}), the coordinating anions X are halides (Cl^-, Br^- or I^-), and A is either an inorganic (Cs^+) or an organic cation ($CH_3NH_3^+$,

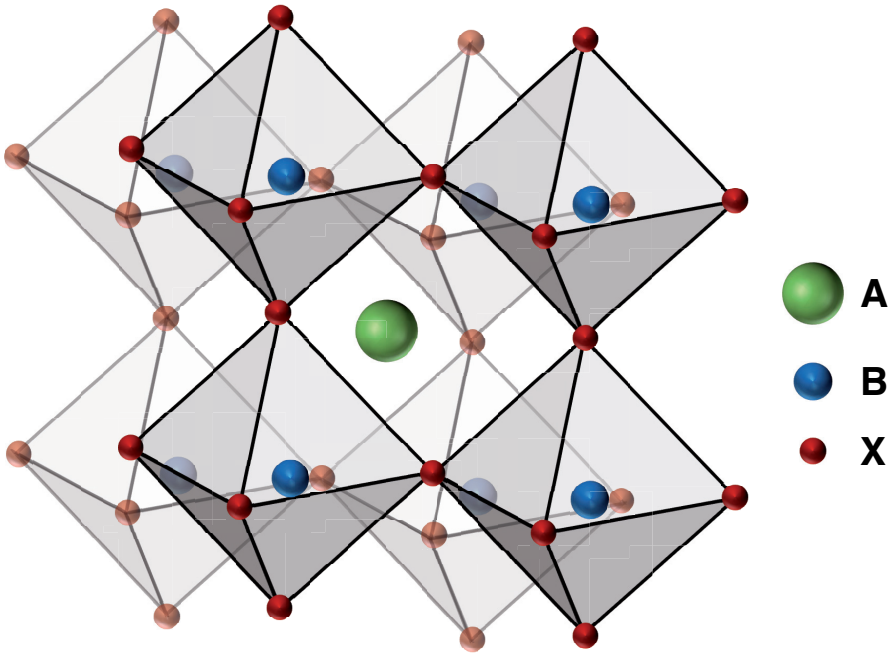

Figure 1.7: Perovskite ABX_3 structure with a cubic symmetry.

MA or $CH(NH_2)_2^+$, FA), which gives rise to a category of SCs called LHPs. The soft and dynamic perovskite crystal structure results in facile post-synthetic ion exchange for tuning the optical and physical properties.[51] For example, the size of the A cation not only influences the optical band gap but the stability of the perovskite phase. For small cations, such as Cs^+, the octahedra are tilted, giving rise to an orthorhombic phase at RT, while $MAPbI_3$ retains its cubic symmetry.[52,53] Predicting and controlling the perovskite phase is crucial since it directly impacts their optoelectronic properties.

A simplified illustration of the LHP electronic structure is displayed in **Figure 1.8**, taking CsPbBr3 as an example. Since the VBM and CBM lie at the same point in the k-space, LHPs are direct band gap SCs exhibiting high absorption coefficients, $\alpha > 10^4$ cm^{-1} for $MAPbI_3$,[55] and sharp optical absorption edges, < 15 meV.[56] Therefore, only a thin LHP layer is required to absorb most of the incident photons, reducing the energetic losses due to carrier recombination during transport. The VBM is dominated by the halide p (70%) and the Pb 6s (25%) antibonding orbitals, while the CBM mainly consists of a mixture of antibonding Pb 6p and other orbitals.[57] As pictured in **Figure 1.8**, the original atomic orbitals are close to the band edge rather than inside the band gap as for Si.[54] Hence, the majority of the trap states, caused by atom vacancies or interstitial defects, are located within the bands or close to the band edges.[58,59] These shallow traps are less detrimental to the SC optoelectronic properties,[60] explaining why LHPs are promising for light-harvesting applications, even with higher defect densities than conventional Si.[61] Computational studies have also shown that the band curvatures around the band edges are similar

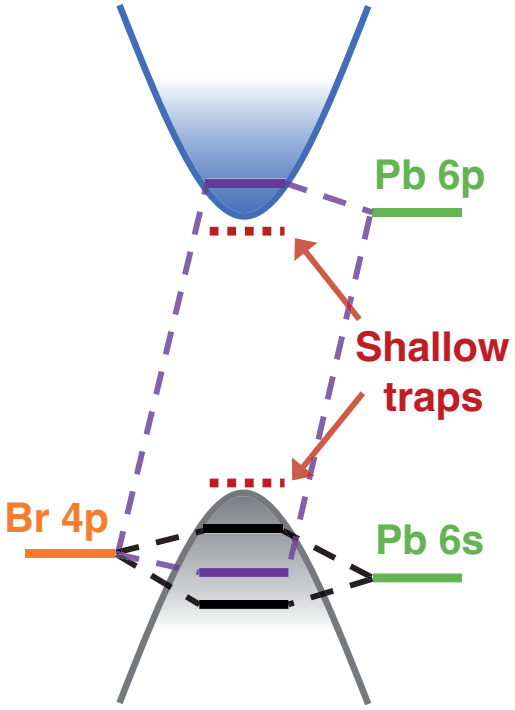

Figure 1.8: Schematic illustration of the band structure in LHPs and the origin of shallow trap states. *Inspired by Ye et al.*[54]

for VB and CB, resulting in equivalent and small electron and hole effective masses.[62] It is worth noting that the CB is degenerated (i.e., split in two bands) around the CBM because of a large spin-orbit coupling (SOC) from the presence of heavy lead and halides.[57,63] Finally, the VB position, and therefore the band gap, is easily modulated through halide exchange. The absorption onset increases from $\approx$ 1.6 eV to $\approx$ 3.0 eV when the size of the halide decreases (I $\rightarrow$ Br $\rightarrow$ Cl).[64] One can span the entire visible region by precisely adjusting the band gap energy with LHPs of mixed halide composition, which helps in obtaining high power-conversion efficiencies.[65]

3D LHPs display excellent PV performances, notably through their unique ability to produce and transport photogenerated charge carriers. They feature long diffusion length due to 1) higher carrier mobility than organic SCs and 2) extended charge carrier lifetimes. One of the key parameters accounting for high carrier mobility is the generation of free electrons and holes after photoexcitation. Because of their large optical permittivity ($\varepsilon \approx 6$), LHPs, especially $MAPbI_3$ used for PV technologies, display relatively weakly bound excitons with a binding energy ($\Delta_x \approx$ 10-30 meV) smaller than or similar to the thermal energy at RT.[66,67] Under solar irradiation, WM-type excitons are likely to split and form free carriers, increasing the overall carrier mobility. As already stipulated, the exciton binding energy increases with the material band gap, and lead chloride perovskites exhibit thermally stable excitons at RT (around 60 meV).[68] Nonetheless, these values remain almost two orders of magnitude lower than the ones observed

in OPVs.[69] Besides, the photogenerated charge carriers in LHPs have intrinsic small effective masses: $m^* \approx m_e^* \approx 0.1\ m_0$,[67] where m_0 is the free electron mass. The carrier effective mass is directly related to the mobility, μ [$cm^2 \cdot V^{-1} \cdot s^{-1}$], under the Drude model:

$$\mu = \frac{e \cdot c}{m^*} \tag{1.14}$$

where e is the elementary charge [C], and c is a scattering constant [s^{-1}]. The reported mobility values range from 1.5 to 60 $cm^2 \cdot V^{-1} \cdot s^{-1}$ for $MAPbBr_3$ and $MAPbI_3$, respectively,[70–72] and are five to six orders of magnitude higher as the ones found in OPVs.[69]

However, the calculated mobility is insufficient to explain diffusion lengths up to several micrometers.[72,73] In addition, LHPs exhibit surprisingly long charge carrier lifetimes for direct band gap SCs. The origin of the reduced recombination rates is highly debated in the literature, and four main reasons are usually cited: 1) defect tolerance, 2) formation of large polarons, 3) photon recycling, and 4) Rashba effect.

- As already mentioned, trap states in bulk LHPs only have a minimal effect on the recombination process. Indeed, the original atomic orbitals forming the CBM and the VBM lie within the bands, and most defects are shallow by nature.[58,59] As a consequence, trapped carriers can be thermally re-excited to the energy bands without loss. LHP trap states also exhibit reduced capture cross-section due to the low energy of optical phonons (16.5 meV in $MAPbI_3$).[74] Hence, carrier trapping often requires the emission of multiple phonons, which considerably decreases its rate.[75,76]

- In bulk LHPs, large polarons, i.e., polarons with strong binding energy compared to the phonon frequency, are formed because of the ability of the perovskite lattice to screen charges.[77] More evidence for the polaron formation are brought by the hot phonon bottleneck observed for charge carrier cooling.[78,79] Ultimately, charge carrier screening by polaron protects them against fast recombination.[80]

- Band-to-band radiative recombination is the spontaneous emission of a photon in any direction. In some cases, the emitted photon can be re-absorbed by the same material, extending the observed radiative lifetime and leading to so-called photon recycling or self-absorption. Photon recycling in thin films is not uncommon,[81] but requires high absorption coefficients, efficient PL, and a small or no Stokes shift between the absorption edge and the emission peak. LHPs meet all the prerequisites and some studies have shown multiple radiative emission-absorption events can occur without energy loss.[82] However, photon recycling only becomes dominant if the trapping rate is very low (for well-passivated compounds) and/or at high carrier density.[83]

- The Rashba effect describes a momentum-dependent splitting of the spins occurring under large SOC and asymmetry of the crystal potential. Large spin-splittings have been reported in 3D LHPs, leading to a displacement of the CBM in the k-space.[84,85] While the light absorption process remains governed by a direct band gap, charge carrier recombination requires the absorption or emission of a phonon and is slowed down. However, recent studies have claimed that the Rashba effect does not impact the charge carrier recombination in 3D LHPs as much as the other factors.[76,86]

One point that has not been discussed until now is the ability of light-harvesting devices to extract the energy of hot charge carriers. The relaxation of hot carriers via phonon emission induces heat, interpreted as a loss of energy. Solar-cell devices exploiting the excess photon energy can greatly overcome the Shockley-Queisser limit of 33% and reach up to 66% efficiency.[87] For bulk LHP films, hot carrier cooling strongly depends on the carrier density and for 1.5 eV excess energy varies from 0.4 ps for low carrier concentration to 30 ps for high carrier densities.[79,88] Carrier cooling rates are considerably slower than ones observed for other metal chalcogenides films and have been assigned to a hot phonon bottleneck effect.[89,90] The reasons accounting for the slower relaxation include large polaron screening, acoustical phonon upconversion and large energy separation between optical and acoustic phonons suppressing the relaxation pathways.[13,89,91] It has also been shown that the charge carrier diffusion length reaches 600 nm within ten picoseconds,[92] allowing efficient charge carrier extraction for higher carrier densities.[93,94]

1.3.2 Moving towards perovskite nanocrystals

Traditional SC nanocrystals are binary compounds, mixing metals (Pb, Cd, In, Ga) and chalcogenides (S, Se, Te) or pnictides (P, As), and are widely exploited to build electronic devices.[95,96] As discussed previously, NC optical properties are controlled via the degree of quantum confinement by varying the material size and shape. Similarly, perovskite nanocrystals (PNCs) can be obtained with sizes ranging from a few to several tens of nanometers and exhibit exciting properties.

Schmidt et al.[97] reported the first synthesis of colloidal PNCs in 2014 with the formation of an ensemble of $MAPbBr_3$ NCs capped with ammonium bromide. The colloidal solution was stable for weeks in organic solvents and displayed a photoluminescence quantum yield (PLQY) close to 20%. After careful ligand tuning to passivate the NC surface, the PLQY of the same colloids has been pushed to 83% in less than two years.[98] Yet, the major breakthrough came in 2015 with the publication of a hot-injection procedure resulting in monodisperse and cubic $CsPbX_3$ (X = I, Br, Cl) NCs (**Figure 1.9**).[48] All-inorganic PNCs were less sensitive towards oxygen and moisture than their organic-inorganic counterparts and exhibit

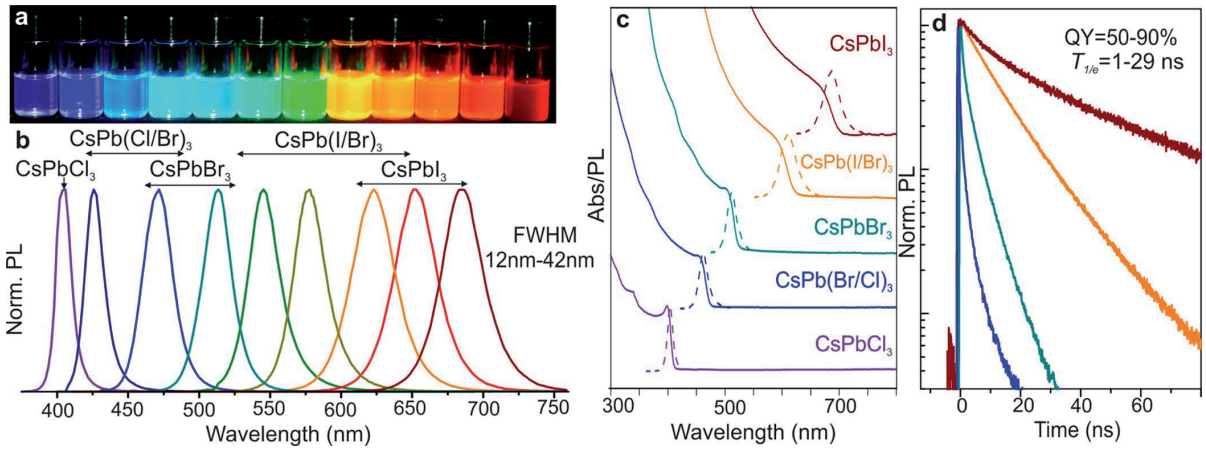

Figure 1.9: A) $CsPbX_3$ NC colloidal solutions under UV lamp. NCs B) emission and C) absorption spectra for various sizes and compositions. D) Time-resolved PL decays for the samples displayed in C. *Taken from Protesescu et al.*[48]

PLQYs of up to 90% without specific post-synthesis treatment. Nowadays, typical $CsPbX_3$ NCs are surrounded by oleylamine (OAm) and oleic acid (OA) ligands and are dispersed in an apolar (hexane, dodecane, toluene) solvent. The NC narrow size distribution is controlled by the temperature at which the precursor is injected and by the subsequent purification step to discard bigger particles. The PL is tunable across the entire visible spectral range through halide exchange and temperature control (higher injection temperatures result in larger NCs with smaller band gaps).[99] To date, green-emitting $CsPbBr_3$ and red-emitting $CsPbI_3$ NCs with near-unity PLQY are reported with an optimization of the capping ligands and surface passivation strategies.[100] These improvements allow utilization of PNCs for light-emitting devices,[101] photodetectors,[102] lasers,[103] catalysis,[104] computing,[105] and also solar cells (even if the efficiency is limited by the large PNC band gap).[106,107]

Several factors may explain why PNCs show outstanding promises for optoelectronic applications. Firstly, the perovskite band structure is defect tolerant and mostly shallow trap states are created. Therefore, unlike metal chalcogenide QDs, PNCs do not require core-shell structures to passivate the surface. Secondly, because of the combination of quantum and dielectric confinements, perovskite NCs usually display thermally stable excitons. For $CsPbX_3$, the exciton Bohr radius increases from 5 nm (X = Cl) to 12 nm (X = I).[48] Even if most PNCs synthesized with the hot-injection method have a size similar to or slightly bigger than these values, they experience weak quantum confinement. Besides, the usual organic capping ligands have a lower optical permittivity ($\varepsilon \approx 2$ vs 5-6 for the perovskite core), increasing the charge carrier interaction through dielectric confinement.[108,109] The exciton binding energy varies from a few tens to several hundreds of meV, depending on the NC size or composition, and leading to an intense and short PL accompanied by high absorption coefficients. Thirdly, narrow PL linewidths are observed

(< 100 meV) because of the NC size homogeneity and the small phonon energy, which enhances the color purity.[99] Finally, similarly to bulk LHPs, the cooling rate is reduced at high carrier density for weakly confined PNCs. Indeed, far fewer phonon modes are available to match the interlevel spacings, increasing the hot phonon bottleneck effect.[110] The formation of polarons may become faster than charge carrier relaxation, which further reduces the cooling rates.[111] In this way, multiple studies have reported efficient hot carrier transfer from PNCs to molecular acceptors adsorbed on their surface.[94,112,113]

Traditional cubic PNC colloids have yet to face two significant challenges for subsequent optoelectronic applications. Firstly, organic ligands only bind weakly to the inorganic core and become labile even in apolar solvents.[114] This dynamic equilibrium between free and bound ligands eventually creates surface trap states or NC aggregation. It is believed that OAm^+, substituting Cs-sites at the surface, and OA^-, occupying surface halide vacancies to bind under-coordinated Pb atoms, have a chance to become neutralized via a Bronsted acid-base equilibrium.[115] **Figure 1.10** highlights the surface chemistry of $CsPbBr_3$ NCs and the formation of surface defects via capping ligand desorption. Different strategies have been established to passivate the surface: quaternary ammoniums to sustain the positively charged ligands,[116] tightly bound alkylphosphonic acids,[117] or zwitterions to suppress acid-base equilibria and induce a chelate effect.[118] However, a balance between small labile and bulky static ligands must be struck since the latter isolates the PNCs and impede charge injection, resulting in less efficient devices. Yet, the main drawback of PNCs remains the instability and low PLQY ($< 20\%$) of $CsPbCl_3$ particles. The small size of the chloride anions destabilizes the perovskite structure and may induce deep trap states, which restricts the development of blue LEDs.

1.3.3 Strongly confined perovskite nanostructures

One way to face the challenge of blue-emitting PNCs is by moving towards strongly confined $CsPbBr_3$ systems. The PNC dimensions can be tuned by changing the experimental conditions (injection temperature, solvent) and the length of the capping ligands.[119] For example, some groups have reported the synthesis of strongly confined $CsPbBr_3$ NPls (2D),[120] NWs (1D),[121] or QDs (0D),[122] where at least one dimension is smaller than the exciton Bohr diameter. Perovskite NPls turn out to be the most appealing confined structure because their properties are quantized according to the number of inorganic monolayers, similar to 2D perovskite materials. There are already synthesic approaches to precisely control the plate thickness by regulating the precursor ratio.[123,124] Reducing the NPl thickness enhances the quantum confinement of the charge carriers, which substantially affects the NC photophysical and optical properties.

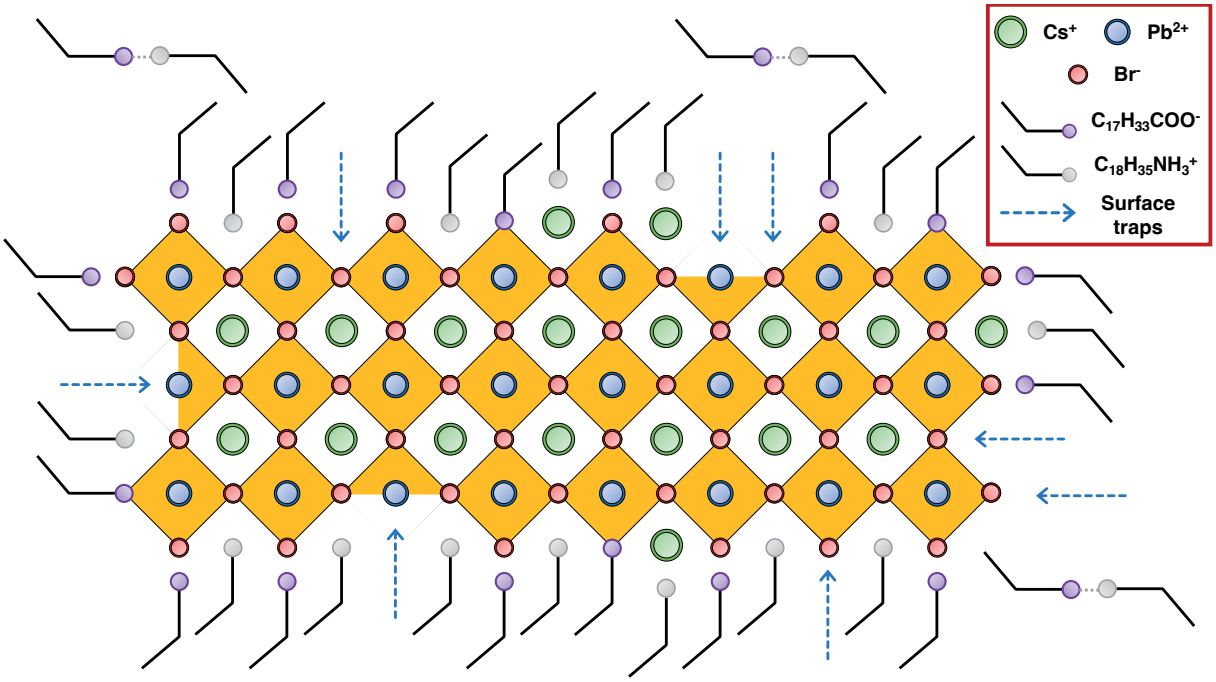

Figure 1.10: Schematic illustration of the $CsPbBr_3$ NCs structure focusing on the surface defects induced by ligand desorption and halide vacancies.

Firstly, $CsPbBr_3$ NPls display extended band gaps, up to 3.0 eV, which are blue-shifted by 0.6 eV compared to bulk systems. Their PL varies from violet-blue to blue-cyan (430-480 nm), depending on the degree of confinement. Secondly, the spatial overlap of the electron and hole wavefunctions generates tightly bound excitons, with exciton binding energies of up to 350 meV.[125] Hence, their absorption spectra are dominated by intense excitonic feature below the band edge and perovskite NPls exhibit enhanced radiative recombination rates with recombination lifetimes of around 2-8 ns. Finally, the combination of quantum and dielectric confinement induces stable biexcitons with binding energies of up to 100 meV for the smaller systems.[126] These thermally stable biexcitons considerably lower the energy threshold for amplified spontaneous emission,[127] making strongly-confined PNCs attractive for lasing.

The charge carrier dynamics of $CsPbBr_3$ NPls are also substantially different from their bulk counterparts because of their larger surface-to-volume ratio. Since more surface states act as deep traps, the PLQY is limited to 50% and small NPls are more prone to aggregation.[120] It has been demonstrated that halide vacancies are the most common defects and their resulting under-coordinated Pb_2^+ atoms are susceptible to inducing deep trap states.[100] Hence, some synthetic procedures include an excess of halide to enhance the overall PLQY.[124] In addition, the PLQY could be pushed to 80% by coating the surface with a polymer,[128] but it hinders charge injection or transfer for multi-layered devices. Finally, the broad surface coated with organic ligands provides an additional pathway for charge carrier cooling. Hintermayr et al.

have shown that perovskite NPls display sub-300 fs cooling lifetimes, even for high carrier densities.[129] They have argued that the phonon bottleneck, observed for weakly confined PNCs, is overcome by a fast nonadiabatic energy transfer to the surface ligands. Hot charge carriers do not have to travel over a long distance to find a surface state, and their excess energy is released as vibrations of the organic ligands. To summarize, **Table 1.1** provides an overview of the principal differences between bulk, weakly-confined and strongly confined $CsPbBr_3$ discussed throughout this chapter.

Table 1.1: Comparison of the optical properties of bulk, large NCs and small NCs of $CsPbBr_3$.
NB: Since the perovskite optical properties depend on their size and shape, the values displayed here are an average of what is found in the literature.

Structure	E_g **[eV]**	Δ_x **[meV]**	Δ_{xx} **[meV]**	τ_{PL} **[ns]**	**PLQY [-]**	τ_{cool}
Bulk $CsPbBr_3$	2.4	40	-	1000	8%	slow
Weakly confined NCs	2.55	60	< 20	10	$> 95\%$	slow
Strongly confined NCs	2.8	150	50	5	50%	fast

Bibliography

[1] Atkins, P. W.; De Paula, J. *Physical chemistry*; W.H. Freeman: New York, 2006.

[2] Klingshirn, C. F. *Semiconductor optics.*, 2nd ed.; Springer Sciences; 2005.

[3] Fox, M. *Optical Properties of Solids*, 2nd ed.; Oxford Master Series in Physics Ser.; Oxford University Press, Incorporated, 2010; Vol. 3.

[4] Sum, T.-C., Mathews, N., Eds. *Halide Perovskites: photovoltaics, light emitting devices and beyond*; Wiley-VCH: Weinheim, 2019.

[5] Ritchie, H.; Roser, M.; Rosado, P. Energy. *Our World in Data* **2020**,

[6] Programme, U. N. D., Council, W. E., Eds. *World energy assessment: energy and the challenge of sustainability*; United Nations Development Programme: New York, NY, 2000.

[7] Becquerel, E. M. Memoire sur les Effets Electriques Produits sous l'Influence des Rayons Solaires. *CR. Acad. Sci.* **1839**, *9*, 561–567.

[8] Fermi, E. Eine statistische Methode zur Bestimmung einiger Eigenschaften des Atoms und ihre Anwendung auf die Theorie des periodischen Systems der Elemente. *Z. Physik* **1928**, *48*, 73–79.

[9] Dirac, P. A. M. On the theory of quantum mechanics. *Prob. R. Soc. Lond. A* **1926**, *112*, 661–677.

[10] Varshni, Y. P. Temperature dependence of the energy gap in semiconductors. *Physica* **1967**, *34*, 149–154.

[11] Spear, W. E.; Le Comber, P. G. Substitutional doping of amorphous silicon. *Solid State Commun.* **1975**, *17*, 1193–1196.

[12] Richter, J. M.; Branchi, F.; Valduga de Almeida Camargo, F.; Zhao, B.; Friend, R. H.; Cerullo, G.; Deschler, F. Ultrafast carrier thermalization in lead iodide perovskite probed with two-dimensional electronic spectroscopy. *Nat. Commun.* **2017**, *8*, 376.

[13] Yang, J. et al. Acoustic-optical phonon up-conversion and hot-phonon bottleneck in lead-halide perovskites. *Nat. Commun.* **2017**, *8*, 14120.

[14] Hall, R. N. Electron-Hole Recombination in Germanium. *Phys. Rev.* **1952**, *87*, 387.

[15] Shockley, W.; Read, W. T. Statistics of the Recombinations of Holes and Electrons. *Phys. Rev.* **1952**, *87*, 835–842.

[16] Stranks, S. D.; Burlakov, V. M.; Leijtens, T.; Ball, J. M.; Goriely, A.; Snaith, H. J. Recombination Kinetics in Organic-Inorganic Perovskites: Excitons, Free Charge, and Subgap States. *Phys. Rev. Appl.* **2014**, *2*, 034007.

[17] Su, Y.-W.; Lan, S.-C.; Wei, K.-H. Organic photovoltaics. *Mater. Today* **2012**, *15*, 554–562.

[18] Grätzel, M. Dye-sensitized solar cells. *J. Photoch. Photobio. C* **2003**, *4*, 145–153.

[19] Grätzel, M. The light and shade of perovskite solar cells. *Nat. Mater.* **2014**, *13*, 838–842.

[20] Emin, D. On the existence of free and self-trapped carriers in insulators: an abrupt temperature-dependent conductivity transition. *Adv. Phy* **1973**, *22*, 57–116.

[21] Fröhlich, H. Electrons in lattice fields. *Adv. Phy.* **1954**, *3*, 325–361.

[22] Huffaker, D. L.; Park, G.; Zou, Z.; Shchekin, O. B.; Deppe, D. G. 1.3 μm room-temperature GaAs-based quantum-dot laser. *Appl. Phys. Lett.* **1998**, *73*, 2564–2566.

[23] Wood, V.; Bulović, V. Colloidal quantum dot light-emitting devices. *Nano Rev.* **2010**, *1*, 5202.

[24] Wagner, C.; Green, M. F.; Leinen, P.; Deilmann, T.; Krüger, P.; Rohlfing, M.; Temirov, R.; Tautz, F. S. Scanning Quantum Dot Microscopy. *Phys. Rev. Lett.* **2015**, *115*, 026101.

[25] Cipriano, L. A.; Di Liberto, G.; Tosoni, S.; Pacchioni, G. Quantum confinement in group III–V semiconductor 2D nanostructures. *Nanoscale* **2020**, *12*, 17494–17501.

[26] Yuan, Z.; Shu, Y.; Xin, Y.; Ma, B. Highly luminescent nanoscale quasi-2D layered lead bromide perovskites with tunable emissions. *Chem. Commun.* **2016**, *52*, 3887–3890.

[27] Hong, X.; Ishihara, T.; Nurmikko, A. V. Dielectric confinement effect on excitons in PbI_4-based layered semiconductors. *Phys. Rev. B* **1992**, *45*, 6961–6964.

[28] Wannier, G. H. The Structure of Electronic Excitation Levels in Insulating Crystals. *Phys. Rev.* **1937**, *52*, 191–197.

[29] Kayanuma, Y. Quantum-size effects of interacting electrons and holes in semiconductor microcrystals with spherical shape. *Phys. Rev. B* **1988**, *38*, 9797–9805.

[30] Chernikov, A.; Berkelbach, T. C.; Hill, H. M.; Rigosi, A.; Li, Y.; Aslan, O. B.; Reichman, D. R.; Hybertsen, M. S.; Heinz, T. F. Exciton Binding Energy and Nonhydrogenic Rydberg Series in Monolayer WS_2. *Phys. Rev. Lett.* **2014**, *113*, 076802.

[31] Zhu, X.-Y.; Yang, Q.; Muntwiler, M. Charge-Transfer Excitons at Organic Semiconductor Surfaces and Interfaces. *Acc. Chem. Res.* **2009**, *42*, 1779–1787.

[32] Schmitt-Rink, S.; Ell, C. Excitons and electron-hole plasma in quasi-two-dimensional systems. *J. Lumin.* **1985**, *30*, 585–596.

[33] Kasprzak, J.; Richard, M.; Kundermann, S.; Baas, A.; Jeambrun, P.; Keeling, J. M. J.; Marchetti, F. M.; Szymańska, M. H.; André, R.; Staehli, J. L.; Savona, V.; Littlewood, P. B.; Deveaud, B.; Dang, L. S. Bose–Einstein condensation of exciton polaritons. *Nature* **2006**, *443*, 409–414.

[34] Klimov, V.; Hunsche, S.; Kurz, H. Biexciton effects in femtosecond nonlinear transmission of semiconductor quantum dots. *Phys. Rev. B* **1994**, *50*, 8110–8113.

[35] Kato, Y.; Ichii, D.; Ohashi, K.; Kunugita, H.; Ema, K.; Tanaka, K.; Takahashi, T.; Kondo, T. Extremely large binding energy of biexcitons in an organic–inorganic quantum-well material $(C_4H_9NH_3)_2PbBr_4$. *Solid State Commun.* **2003**, *128*, 15–18.

[36] You, Y.; Zhang, X.-X.; Berkelbach, T. C.; Hybertsen, M. S.; Reichman, D. R.; Heinz, T. F. Observation of biexcitons in monolayer WSe_2. *Nat. Phys.* **2015**, *11*, 477–481.

[37] Thouin, F.; Neutzner, S.; Cortecchia, D.; Dragomir, V. A.; Soci, C.; Salim, T.; Lam, Y. M.; Leonelli, R.; Petrozza, A.; Kandada, A. R. S.; Silva, C. Stable biexcitons in two-dimensional metal-halide perovskites with strong dynamic lattice disorder. *Phys. Rev. Mater.* **2018**, *2*.

[38] Birkedal, D.; Singh, J.; Lyssenko, V. G.; Erland, J.; Hvam, J. M. Binding of Quasi-Two-Dimensional Biexcitons. *Phys. Rev. Lett.* **1996**, *76*, 672–675.

[39] Hangleiter, A. Nonradiative recombination via deep impurity levels in semiconductors: The excitonic Auger mechanism. *Phys. Rev. B* **1988**, *37*, 2594–2604.

[40] Vasudevan, D.; Gaddam, R. R.; Trinchi, A.; Cole, I. Core–shell quantum dots: Properties and applications. *J. Alloys Compd.* **2015**, *636*, 395–404.

[41] Yang, D.; Li, X.; Zeng, H. Surface Chemistry of All Inorganic Halide Perovskite Nanocrystals: Passivation Mechanism and Stability. *Adv. Mater. Interfaces* **2018**, *5*, 1701662.

[42] Delport, G.; Chehade, G.; Lédée, F.; Diab, H.; Milesi-Brault, C.; Trippé-Allard, G.; Even, J.; Lauret, J.-S.; Deleporte, E.; Garrot, D. Exciton–Exciton Annihilation in Two-Dimensional Halide Perovskites at Room Temperature. *J. Phys. Chem. Lett.* **2019**, *10*, 5153–5159.

[43] D'Innocenzo, V.; Grancini, G.; Alcocer, M. J. P.; Kandada, A. R. S.; Stranks, S. D.; Lee, M. M.; Lanzani, G.; Snaith, H. J.; Petrozza, A. Excitons versus free charges in organo-lead tri-halide perovskites. *Nat. Commun.* **2014**, *5*, 3586.

[44] Kojima, A.; Teshima, K.; Shirai, Y.; Miyasaka, T. Organometal Halide Perovskites as Visible-Light Sensitizers for Photovoltaic Cells. *J. Am. Chem. Soc.* **2009**, *131*, 6050–6051.

[45] Im, J.-H.; Lee, C.-R.; Lee, J.-W.; Park, S.-W.; Park, N.-G. 6.5% efficient perovskite quantum-dot-sensitized solar cell. *Nanoscale* **2011**, *3*, 4088.

[46] Grätzel, M. The Rise of Highly Efficient and Stable Perovskite Solar Cells. *Acc. Chem. Res.* **2017**, *50*, 487–491.

[47] NREL, Best Research-Cell Efficiency Chart | Photovoltaic Research. 2022; https://www.nrel.gov/pv/cell-efficiency.html (accessed on 03/03/2022).

[48] Protesescu, L.; Yakunin, S.; Bodnarchuk, M. I.; Krieg, F.; Caputo, R.; Hendon, C. H.; Yang, R. X.; Walsh, A.; Kovalenko, M. V. Nanocrystals of Cesium Lead Halide Perovskites ($CsPbX_3$, X = Cl, Br, and I): Novel Optoelectronic Materials Showing Bright Emission with Wide Color Gamut. *Nano Lett.* **2015**, *15*, 3692–3696.

[49] Wang, Y.-K. et al. All-Inorganic Quantum-Dot LEDs Based on a Phase-Stabilized α-$CsPbI_3$ Perovskite. *Angew. Chem. Int. Ed.* **2021**, *60*, 16164–16170.

[50] Kim, Y.-H. et al. Comprehensive defect suppression in perovskite nanocrystals for high-efficiency light-emitting diodes. *Nat. Photonics* **2021**, *15*, 148–155.

[51] Jiang, H.; Cui, S.; Chen, Y.; Zhong, H. Ion exchange for halide perovskite: From nanocrystal to bulk materials. *Nano Select* **2021**, *2*, 2040–2060.

[52] Manser, J. S.; Christians, J. A.; Kamat, P. V. Intriguing Optoelectronic Properties of Metal Halide Perovskites. *Chem. Rev.* **2016**, *116*, 12956–13008.

[53] Brivio, F.; Frost, J. M.; Skelton, J. M.; Jackson, A. J.; Weber, O. J.; Weller, M. T.; Goñi, A. R.; Leguy, A. M. A.; Barnes, P. R. F.; Walsh, A. Lattice dynamics and vibrational spectra of the orthorhombic, tetragonal, and cubic phases of methylammonium lead iodide. *Phys. Rev. B* **2015**, *92*, 144308.

[54] Ye, J.; Byranvand, M. M.; Martínez, C. O.; Hoye, R. L. Z.; Saliba, M.; Polavarapu, L. Defect Passivation in Lead-Halide Perovskite Nanocrystals and Thin Films: Toward Efficient LEDs and Solar Cells. *Angew. Chem. Int. Ed.* **2021**, *60*, 21636–21660.

[55] Yin, W.-J.; Shi, T.; Yan, Y. Unique Properties of Halide Perovskites as Possible Origins of the Superior Solar Cell Performance. *Adv. Mater.* **2014**, *26*, 4653–4658.

[56] De Wolf, S.; Holovsky, J.; Moon, S.-J.; Löper, P.; Niesen, B.; Ledinsky, M.; Haug, F.-J.; Yum, J.-H.; Ballif, C. Organometallic Halide Perovskites: Sharp Optical Absorption Edge and Its Relation to Photovoltaic Performance. *J. Phys. Chem. Lett.* **2014**, *5*, 1035–1039.

[57] Brivio, F.; Butler, K. T.; Walsh, A.; van Schilfgaarde, M. Relativistic quasiparticle self-consistent electronic structure of hybrid halide perovskite photovoltaic absorbers. *Phys. Rev. B* **2014**, *89*, 155204.

[58] Yin, W.-J.; Shi, T.; Yan, Y. Unusual defect physics in $CH_3NH_3PbI_3$ perovskite solar cell absorber. *Appl. Phys. Lett.* **2014**, *104*, 063903.

[59] Huang, H.; Bodnarchuk, M. I.; Kershaw, S. V.; Kovalenko, M. V.; Rogach, A. L. Lead Halide Perovskite Nanocrystals in the Research Spotlight: Stability and Defect Tolerance. *ACS Energy Lett.* **2017**, *2*, 2071–2083.

[60] Kang, J.; Wang, L.-W. High Defect Tolerance in Lead Halide Perovskite $CsPbBr_3$. *J. Phys. Chem. Lett.* **2017**, *8*, 489–493.

[61] Jin, H.; Debroye, E.; Keshavarz, M.; Scheblykin, I. G.; Roeffaers, M. B. J.; Hofkens, J.; Steele, J. A. It's a trap! On the nature of localised states and charge trapping in lead halide perovskites. *Mater. Horiz.* **2020**, *7*, 397–410.

[62] Shamsi, J.; Urban, A. S.; Imran, M.; De Trizio, L.; Manna, L. Metal Halide Perovskite Nanocrystals: Synthesis, Post-Synthesis Modifications, and Their Optical Properties. *Chem. Rev.* **2019**, *119*, 3296–3348.

[63] Leguy, A. M. A.; Azarhoosh, P.; Alonso, M. I.; Campoy-Quiles, M.; Weber, O. J.; Yao, J.; Bryant, D.; Weller, M. T.; Nelson, J.; Walsh, A.; van Schilfgaarde, M.; Barnes, P. R. F. Experimental and theoretical optical properties of methylammonium lead halide perovskites. *Nanoscale* **2016**, *8*, 6317–6327.

[64] Saliba, M.; Correa-Baena, J.-P.; Grätzel, M.; Hagfeldt, A.; Abate, A. Perovskite Solar Cells: From the Atomic Level to Film Quality and Device Performance. *Angew. Chem. Int. Ed.* **2018**, *57*, 2554–2569.

[65] Bi, D.; Tress, W.; Dar, M. I.; Gao, P.; Luo, J.; Renevier, C.; Schenk, K.; Abate, A.; Giordano, F.; Correa Baena, J.-P.; Decoppet, J.-D.; Zakeeruddin, S. M.; Nazeeruddin, M. K.; Grätzel, M.; Hagfeldt, A. Efficient luminescent solar cells based on tailored mixed-cation perovskites. *Sci. Adv.* **2016**, *2*, e1501170.

[66] Galkowski, K.; Mitioglu, A.; Miyata, A.; Plochocka, P.; Portugall, O.; E. Eperon, G.; Tse-Wei Wang, J.; Stergiopoulos, T.; D. Stranks, S.; J. Snaith, H.; J. Nicholas, R. Determination of the exciton binding energy and effective masses for methylammonium and formamidinium lead tri-halide perovskite semiconductors. *Energy Environ. Sci.* **2016**, *9*, 962–970.

[67] Miyata, A.; Mitioglu, A.; Plochocka, P.; Portugall, O.; Wang, J. T.-W.; Stranks, S. D.; Snaith, H. J.; Nicholas, R. J. Direct measurement of the exciton binding energy and effective masses for charge carriers in organic–inorganic tri-halide perovskites. *Nature Phys.* **2015**, *11*, 582–587.

[68] Saba, M.; Quochi, F.; Mura, A.; Bongiovanni, G. Excited State Properties of Hybrid Perovskites. *Acc. Chem. Res.* **2016**, *49*, 166–173.

[69] Wu, J.; Cha, H.; Du, T.; Dong, Y.; Xu, W.; Lin, C.-T.; Durrant, J. R. A Comparison of Charge Carrier Dynamics in Organic and Perovskite Solar Cells. *Adv. Mater.* **2022**, *34*, 2101833.

[70] Chen, Y.; Yi, H. T.; Wu, X.; Haroldson, R.; Gartstein, Y. N.; Rodionov, Y. I.; Tikhonov, K. S.; Zakhidov, A.; Zhu, X. Y.; Podzorov, V. Extended carrier lifetimes and diffusion in hybrid perovskites revealed by Hall effect and photoconductivity measurements. *Nat. Commun.* **2016**, *7*, 12253.

[71] Wehrenfennig, C.; Eperon, G. E.; Johnston, M. B.; Snaith, H. J.; Herz, L. M. High Charge Carrier Mobilities and Lifetimes in Organolead Trihalide Perovskites. *Adv. Mater.* **2014**, *26*, 1584–1589.

[72] Shi, D. et al. Low trap-state density and long carrier diffusion in organolead trihalide perovskite single crystals. *Science* **2015**, *347*, 519–522.

[73] Nie, W.; Tsai, H.; Asadpour, R.; Blancon, J.-C.; Neukirch, A. J.; Gupta, G.; Crochet, J. J.; Chhowalla, M.; Tretiak, S.; Alam, M. A.; Wang, H.-L.; Mohite, A. D. High-efficiency solution-processed perovskite solar cells with millimeter-scale grains. *Science* **2015**, *347*, 522–525.

[74] Sendner, M.; Nayak, P. K.; Egger, D. A.; Beck, S.; Müller, C.; Epding, B.; Kowalsky, W.; Kronik, L.; Snaith, H. J.; Pucci, A.; Lovrinčić, R. Optical phonons in methylammonium lead halide perovskites and implications for charge transport. *Mater. Horiz.* **2016**, *3*, 613–620.

[75] Kirchartz, T.; Markvart, T.; Rau, U.; Egger, D. A. Impact of Small Phonon Energies on the Charge-Carrier Lifetimes in Metal-Halide Perovskites. *J. Phys. Chem. Lett.* **2018**, *9*, 939–946.

[76] deQuilettes, D. W.; Frohna, K.; Emin, D.; Kirchartz, T.; Bulovic, V.; Ginger, D. S.; Stranks, S. D. Charge-Carrier Recombination in Halide Perovskites: Focus Review. *Chem. Rev.* **2019**, *119*, 11007–11019.

[77] Zhu, X.-Y.; Podzorov, V. Charge Carriers in Hybrid Organic–Inorganic Lead Halide Perovskites Might Be Protected as Large Polarons. *J. Phys. Chem. Lett.* **2015**, *6*, 4758–4761.

[78] Joshi, P. P.; Maehrlein, S. F.; Zhu, X. Dynamic Screening and Slow Cooling of Hot Carriers in Lead Halide Perovskites. *Advanced Materials* **2019**, *31*, 1803054.

[79] Frost, J. M.; Whalley, L. D.; Walsh, A. Slow Cooling of Hot Polarons in Halide Perovskite Solar Cells. *ACS Energy Letters* **2017**, *2*, 2647–2652.

[80] Miyata, K.; Meggiolaro, D.; Trinh, M. T.; Joshi, P. P.; Mosconi, E.; Jones, S. C.; De Angelis, F.; Zhu, X.-Y. Large polarons in lead halide perovskites. *Sci. Adv.* **2017**, *3*, e1701217.

[81] Asbeck, P. Self-absorption effects on the radiative lifetime in GaAs-GaAlAs double heterostructures. *J. Appl. Phys.* **1977**, *48*, 4.

[82] Pazos-Outón, L. M.; Szumilo, M.; Lamboll, R.; Richter, J. M.; Crespo-Quesada, M.; Abdi-Jalebi, M.; Beeson, H. J.; Vrućinić, M.; Alsari, M.; Snaith, H. J.; Ehrler, B.; Friend, R. H.; Deschler, F. Photon recycling in lead iodide perovskite solar cells. *Science* **2016**, *351*, 1430–1433.

[83] Brenes, R.; Laitz, M.; Jean, J.; deQuilettes, D. W.; Bulović, V. Benefit from Photon Recycling at the Maximum-Power Point of State-of-the-Art Perovskite Solar Cells. *Phys. Rev. Appl.* **2019**, *12*, 014017.

[84] Kepenekian, M.; Robles, R.; Katan, C.; Sapori, D.; Pedesseau, L.; Even, J. Rashba and Dresselhaus Effects in Hybrid Organic–Inorganic Perovskites: From Basics to Devices. *ACS Nano* **2015**, *9*, 11557–11567.

[85] Stranks, S. D.; Plochocka, P. The influence of the Rashba effect. *Nat. Mater.* **2018**, *17*, 381.

[86] Richter, J. M.; Chen, K.; Sadhanala, A.; Butkus, J.; Rivett, J. P. H.; Friend, R. H.; Monserrat, B.; Hodgkiss, J. M.; Deschler, F. Direct Bandgap Behavior in Rashba-Type Metal Halide Perovskites. *Adv. Mater.* **2018**, *30*, 1803379.

[87] Ross, R. T.; Nozik, A. J. Efficiency of hot-carrier solar energy converters. *J. Appl. Phys.* **1982**, *53*, 3813–3818.

[88] Xing, G.; Mathews, N.; Sun, S.; Lim, S. S.; Lam, Y. M.; Grätzel, M.; Mhaisalkar, S.; Sum, T. C. Long-Range Balanced Electron- and Hole-Transport Lengths in Organic-Inorganic $CH_3NH_3PbI_3$. *Science* **2013**, *342*, 344–347.

[89] Yang, Y.; Ostrowski, D. P.; France, R. M.; Zhu, K.; van de Lagemaat, J.; Luther, J. M.; Beard, M. C. Observation of a hot-phonon bottleneck in lead-iodide perovskites. *Nat. Photonics* **2016**, *10*, 53–59.

[90] Wen, Y.-C.; Chen, C.-Y.; Shen, C.-H.; Gwo, S.; Sun, C.-K. Ultrafast carrier thermalization in InN. *Appl. Phys. Lett.* **2006**, *89*, 232114.

[91] Zhu, H.; Miyata, K.; Fu, Y.; Wang, J.; Joshi, P. P.; Niesner, D.; Williams, K. W.; Jin, S.; Zhu, X.-Y. Screening in crystalline liquids protects energetic carriers in hybrid perovskites. *Science* **2016**, *353*, 1409–1413.

[92] Guo, Z.; Wan, Y.; Yang, M.; Snaider, J.; Zhu, K.; Huang, L. Long-range hot-carrier transport in hybrid perovskites visualized by ultrafast microscopy. *Science* **2017**, *356*, 59–62.

[93] Lim, S. S.; Giovanni, D.; Zhang, Q.; Solanki, A.; Jamaludin, N. F.; Lim, J. W. M.; Mathews, N.; Mhaisalkar, S.; Pshenichnikov, M. S.; Sum, T. C. Hot carrier extraction in $CH_3NH_3PbI_3$ unveiled by pump-push-probe spectroscopy. *Sci. Adv.* **2019**, *5*, eaax3620.

[94] Li, M.; Bhaumik, S.; Goh, T. W.; Kumar, M. S.; Yantara, N.; Grätzel, M.; Mhaisalkar, S.; Mathews, N.; Sum, T. C. Slow cooling and highly efficient extraction of hot carriers in colloidal perovskite nanocrystals. *Nat. Commun.* **2017**, *8*.

[95] Choi, J.-H.; Wang, H.; Oh, S. J.; Paik, T.; Sung, P.; Sung, J.; Ye, X.; Zhao, T.; Diroll, B. T.; Murray, C. B.; Kagan, C. R. Exploiting the colloidal nanocrystal library to construct electronic devices. *Science* **2016**, *352*, 205–208.

[96] Kagan, C. R.; Lifshitz, E.; Sargent, E. H.; Talapin, D. V. Building devices from colloidal quantum dots. *Science* **2016**, *353*, aac5523.

[97] Schmidt, L. C.; Pertegás, A.; González-Carrero, S.; Malinkiewicz, O.; Agouram, S.; Mínguez Espallargas, G.; Bolink, H. J.; Galian, R. E.; Pérez-Prieto, J. Nontemplate Synthesis of $CH_3NH_3PbBr_3$ Perovskite Nanoparticles. *J. Am. Chem. Soc.* **2014**, *136*, 850–853.

[98] Gonzalez-Carrero, S.; Francés-Soriano, L.; González-Béjar, M.; Agouram, S.; Galian, R. E.; Pérez-Prieto, J. The Luminescence of $CH_3NH_3PbBr_3$ Perovskite Nanoparticles Crests the Summit and Their Photostability under Wet Conditions is Enhanced. *Small* **2016**, *12*, 5245–5250.

[99] Kovalenko, M. V.; Protesescu, L.; Bodnarchuk, M. I. Properties and potential optoelectronic applications of lead halide perovskite nanocrystals. *Science* **2017**, *358*, 745–750.

[100] Di Stasio, F.; Christodoulou, S.; Huo, N.; Konstantatos, G. Near-Unity Photoluminescence Quantum Yield in $CsPbBr_3$ Nanocrystal Solid-State Films via Postsynthesis Treatment with Lead Bromide. *Chem. Mater.* **2017**, *29*, 7663–7667.

[101] Dai, X.; Zhang, Z.; Jin, Y.; Niu, Y.; Cao, H.; Liang, X.; Chen, L.; Wang, J.; Peng, X. Solution-processed, high-performance light-emitting diodes based on quantum dots. *Nature* **2014**, *515*, 96–99.

[102] Wang, Y.; Song, L.; Chen, Y.; Huang, W. Emerging New-Generation Photodetectors Based on Low-Dimensional Halide Perovskites. *ACS Photonics* **2020**, *7*, 10–28.

[103] Wang, Y.; Li, X.; Song, J.; Xiao, L.; Zeng, H.; Sun, H. All-Inorganic Colloidal Perovskite Quantum Dots: A New Class of Lasing Materials with Favorable Characteristics. *Adv. Mater.* **2015**, *27*, 7101–7108.

[104] Xu, Y.-F.; Yang, M.-Z.; Chen, B.-X.; Wang, X.-D.; Chen, H.-Y.; Kuang, D.-B.; Su, C.-Y. A $CsPbBr_3$ Perovskite Quantum Dot/Graphene Oxide Composite for Photocatalytic CO_2 Reduction. *J. Am. Chem. Soc.* **2017**, *139*, 5660–5663.

[105] Wang, Y.; Lv, Z.; Chen, J.; Wang, Z.; Zhou, Y.; Zhou, L.; Chen, X.; Han, S.-T. Photonic Synapses Based on Inorganic Perovskite Quantum Dots for Neuromorphic Computing. *Adv. Mater.* **2018**, *30*, 1802883.

[106] Li, F.; Zhou, S.; Yuan, J.; Qin, C.; Yang, Y.; Shi, J.; Ling, X.; Li, Y.; Ma, W. Perovskite Quantum Dot Solar Cells with 15.6% Efficiency and Improved Stability Enabled by an α-$CsPbI_3$/$FAPbI_3$ Bilayer Structure. *ACS Energy Lett.* **2019**, *4*, 2571–2578.

[107] Zhao, Q.; Hazarika, A.; Chen, X.; Harvey, S. P.; Larson, B. W.; Teeter, G. R.; Liu, J.; Song, T.; Xiao, C.; Shaw, L.; Zhang, M.; Li, G.; Beard, M. C.; Luther, J. M. High efficiency perovskite quantum dot solar cells with charge separating heterostructure. *Nat. Commun.* **2019**, *10*, 2842.

[108] Ha, S. K.; Mauck, C. M.; Tisdale, W. A. Toward Stable Deep-Blue Luminescent Colloidal Lead Halide Perovskite Nanoplatelets: Systematic Photostability Investigation. *Chem. Mater.* **2019**, *31*, 2486–2496.

[109] Shukla, A.; Kaur, G.; Babu, K. J.; Ghorai, N.; Goswami, T.; Kaur, A.; Ghosh, H. N. Effect of Confinement on the Exciton and Biexciton Dynamics in Perovskite 2D-Nanosheets and 3D-Nanocrystals. *J. Phys. Chem. Lett.* **2020**, *11*, 6344–6352.

[110] Hopper, T. R.; Gorodetsky, A.; Jeong, A.; Krieg, F.; Bodnarchuk, M. I.; Maimaris, M.; Chaplain, M.; Macdonald, T. J.; Huang, X.; Lovrincic, R.; Kovalenko, M. V.; Bakulin, A. A. Hot Carrier

Dynamics in Perovskite Nanocrystal Solids: Role of the Cold Carriers, Nanoconfinement, and the Surface. *Nano Lett.* **2020**,

[111] Kaur, G.; Babu, K. J.; Ghosh, H. N. Temperature-Dependent Interplay of Polaron Formation and Hot Carrier Cooling Dynamics in $CsPbBr_3$ Nanocrystals: Role of Carrier–Phonon Coupling Strength. *J. Phys. Chem. Lett.* **2020**, *11*, 6206–6213.

[112] Sarkar, S.; Ravi, V. K.; Banerjee, S.; Yettapu, G. R.; Markad, G. B.; Nag, A.; Mandal, P. Terahertz Spectroscopic Probe of Hot Electron and Hole Transfer from Colloidal $CsPbBr_3$ Perovskite Nanocrystals. *Nano Lett.* **2017**, *17*, 5402–5407.

[113] De, A.; Das, S.; Samanta, A. Hot Hole Transfer Dynamics from $CsPbBr_3$ Perovskite Nanocrystals. *ACS Energy Lett.* **2020**, *5*, 2246–2252.

[114] De Roo, J.; Ibáñez, M.; Geiregat, P.; Nedelcu, G.; Walravens, W.; Maes, J.; Martins, J. C.; Van Driessche, I.; Kovalenko, M. V.; Hens, Z. Highly Dynamic Ligand Binding and Light Absorption Coefficient of Cesium Lead Bromide Perovskite Nanocrystals. *ACS Nano* **2016**, *10*, 2071–2081.

[115] Smock, S. R.; Chen, Y.; Rossini, A. J.; Brutchey, R. L. The Surface Chemistry and Structure of Colloidal Lead Halide Perovskite Nanocrystals. *Acc. Chem. Res.* **2021**, *54*, 707–718.

[116] Imran, M.; Ijaz, P.; Goldoni, L.; Maggioni, D.; Petralanda, U.; Prato, M.; Almeida, G.; Infante, I.; Manna, L. Simultaneous Cationic and Anionic Ligand Exchange For Colloidally Stable $CsPbBr_3$ Nanocrystals. *ACS Energy Lett.* **2019**, *4*, 819–824.

[117] Tan, Y.; Zou, Y.; Wu, L.; Huang, Q.; Yang, D.; Chen, M.; Ban, M.; Wu, C.; Wu, T.; Bai, S.; Song, T.; Zhang, Q.; Sun, B. Highly Luminescent and Stable Perovskite Nanocrystals with Octylphosphonic Acid as a Ligand for Efficient Light-Emitting Diodes. *ACS Appl. Mater. Interfaces* **2018**, *10*, 3784–3792.

[118] Krieg, F.; Ochsenbein, S. T.; Yakunin, S.; ten Brinck, S.; Aellen, P.; Süess, A.; Clerc, B.; Guggisberg, D.; Nazarenko, O.; Shynkarenko, Y.; Kumar, S.; Shih, C.-J.; Infante, I.; Kovalenko, M. V. Colloidal $CsPbX_3$ (X = Cl, Br, I) Nanocrystals 2.0: Zwitterionic Capping Ligands for Improved Durability and Stability. *ACS Energy Lett.* **2018**, *3*, 641–646.

[119] Dutta, A.; Dutta, S. K.; Das Adhikari, S.; Pradhan, N. Tuning the Size of $CsPbBr_3$ Nanocrystals: All at One Constant Temperature. *ACS Energy Lett.* **2018**, *3*, 329–334.

[120] Weidman, M. C.; Goodman, A. J.; Tisdale, W. A. Colloidal Halide Perovskite Nanoplatelets: An Exciting New Class of Semiconductor Nanomaterials. *Chem. Mater.* **2017**, *29*, 5019–5030.

[121] Zhang, D.; Yu, Y.; Bekenstein, Y.; Wong, A. B.; Alivisatos, A. P.; Yang, P. Ultrathin Colloidal Cesium Lead Halide Perovskite Nanowires. *J. Am. Chem. Soc.* **2016**, *138*, 13155–13158.

[122] Dong, Y.; Qiao, T.; Kim, D.; Parobek, D.; Rossi, D.; Son, D. H. Precise Control of Quantum Confinement in Cesium Lead Halide Perovskite Quantum Dots via Thermodynamic Equilibrium. *Nano Lett.* **2018**, *18*, 3716–3722.

[123] Akkerman, Q. A.; Motti, S. G.; Srimath Kandada, A. R.; Mosconi, E.; D'Innocenzo, V.; Bertoni, G.; Marras, S.; Kamino, B. A.; Miranda, L.; De Angelis, F.; Petrozza, A.; Prato, M.; Manna, L. Solution Synthesis Approach to Colloidal Cesium Lead Halide Perovskite Nanoplatelets with Monolayer-Level Thickness Control. *J. Am. Chem. Soc.* **2016**, *138*, 1010–1016.

[124] Bohn, B. J.; Tong, Y.; Gramlich, M.; Lai, M. L.; Döblinger, M.; Wang, K.; Hoye, R. L. Z.; Müller-Buschbaum, P.; Stranks, S. D.; Urban, A. S.; Polavarapu, L.; Feldmann, J. Boosting Tunable Blue Luminescence of Halide Perovskite Nanoplatelets through Postsynthetic Surface Trap Repair. *Nano Lett.* **2018**, *18*, 5231–5238.

[125] Vale, B. R. C.; Socie, E.; Burgos-Caminal, A.; Bettini, J.; Schiavon, M. A.; Moser, J.-E. Exciton, Biexciton, and Hot Exciton Dynamics in $CsPbBr_3$ Colloidal Nanoplatelets. *J. Phys. Chem. Lett.* **2019**, *11*, 387–394.

[126] Castañeda, J. A.; Nagamine, G.; Yassitepe, E.; Bonato, L. G.; Voznyy, O.; Hoogland, S.; Nogueira, A. F.; Sargent, E. H.; Cruz, C. H. B.; Padilha, L. A. Efficient Biexciton Interaction in Perovskite Quantum Dots Under Weak and Strong Confinement. *ACS Nano* **2016**, *10*, 8603–8609.

[127] Nagamine, G.; Rocha, J. O.; Bonato, L. G.; Nogueira, A. F.; Zaharieva, Z.; Watt, A. A. R.; de Brito Cruz, C. H.; Padilha, L. A. Two-Photon Absorption and Two-Photon-Induced Gain in Perovskite Quantum Dots. *J. Phys. Chem. Lett.* **2018**, *9*, 3478–3484.

[128] Wang, S.; Wang, W.; Donmez, S.; Xin, Y.; Mattoussi, H. Engineering Highly Fluorescent and Colloidally Stable Blue-Emitting $CsPbBr_3$ Nanoplatelets Using Polysalt/$PbBr_2$ Ligands. *Chem. Mater.* **2022**, *34*, 4924–4936.

[129] Hintermayr, V. A.; Polavarapu, L.; Urban, A. S.; Feldmann, J. Accelerated Carrier Relaxation through Reduced Coulomb Screening in Two-Dimensional Halide Perovskite Nanoplatelets. *ACS Nano* **2018**, *12*, 10151–10158.

Chapter 2

Spectroscopic techniques

This chapter is centered on broadband fluorescence upconversion spectroscopy, the principal method used in this thesis. After having an overlook of the available experimental techniques used for time-resolved photoluminescence spectroscopy, the setup is described in great detail. Data acquisition and treatment processes are illustrated with an example using a standard coumarin 153 dye solution. Furthermore, this chapter introduces fs-transient absorption spectroscopy, the other ultrafast time-resolved technique used in the following chapters.

2.1 Time-resolved photoluminescence spectroscopy

2.1.1 Introduction

The term photoluminescence (PL) refers to light emission from a photoexcited compound. Taking the example of semiconductor (SC) materials and what has been discussed previously, PL arises from the radiative recombination between photogenerated charge carriers. In chemistry, PL is often divided into two distinct categories: fluorescence and phosphorescence. The former results from a spin-allowed radiative deactivation of the excited state and is usually fast (nanosecond or sub-nanosecond-scale) and intense. Conversely, phosphorescence describes a quantum-mechanically "forbidden" transition, usually from an excited triplet state to the singlet ground state, exhibiting slow rates (from 10^{-6} to 10^{0} s^{-1}) and low intensities.

Typical PL measurements are performed by illuminating the sample with a continuous light beam and by integrating the subsequent emission over a long time scale. These techniques are called steady-state PL measurements and display the total amount of photons emitted by the sample:[1]

$$\mathrm{PL}(\lambda) = \int_0^\infty \mathrm{PL}(\lambda, t) \cdot dt \tag{2.1}$$

One of the most important photophysical parameters for light-emitting applications is the photoluminescence quantum yield (PLQY or Φ_{PL}). The PLQY is defined as the ratio of the number of photons emitted, N_{em} [-], to the number of photons absorbed by the sample, N_{abs} [-]:

$$\Phi_{\mathrm{PL}} = \frac{N_{\mathrm{em}}}{N_{\mathrm{abs}}} = \frac{k_f}{\sum k} \tag{2.2}$$

where k_f is the fluorescence rate constant [s^{-1}] and $\sum k$ the sum of all relaxation processes [s^{-1}]. Ideal light-emitting diodes (LEDs) would have PLQYs close to unity, meaning that all the absorbed photons are subsequently emitted. Nonetheless, as already mentioned beforehand, photogenerated charge carriers can recombine through non-radiative pathways, which competes with the radiative recombination and lowers the PLQY. Experimentally speaking, the most common and the fastest way to measure PLQY is the comparative method.[2] Here the integrated emission of the sample is divided by the integrated emission of a standard dye with a known PLQY. To ensure reliability, the standard dye emission should be in the same region as the sample emission, and both PL spectra should be recorded under the same conditions: same instrumentation, same excitation wavelength, same absorption at the excitation wavelength...

While steady-state PL provides information on the excited state, it cannot help to understand the mechanistic and kinetic details of the photophysical processes. In time-resolved photoluminescence (TRPL)

spectroscopy, the sample emission is monitored as a function of time after excitation by a short flash of light. Coming back to SC materials, the PL intensity is proportional to the number of charge carriers populating an emissive state. Hence, the PL decay is correlated to a population decay of this particular state. To unveil the mechanistic details in SCs, the temporal resolution of TRPL techniques should be faster than the excited state dynamics. For example, charge carrier cooling, which takes place on a femtosecond time scale, and carrier trapping on a picosecond scale, require the utilization of pulsed lasers. Some processes like solvation and photoinduced carrier transfer may also induce a change in the fluorescence spectral shape. Therefore, being able to record two-dimensional (2D) spectro-temporal PL (PL = PL(λ,t)) is crucial as well.

2.1.2 Experimental techniques for time-resolved fluorescence spectroscopy

Multiple experimental techniques currently exist to measure PL dynamics, and they are divided into two classes: electronic and optical. In the first category, the emitted photons are collected to produce electrons, which are then recorded by fast electronic detectors. However, due to the photon-to-electron conversion, these techniques are limited to a temporal resolution of a few picoseconds. To probe ultrafast fluorescence dynamics, the emission of the sample can be recorded using nonlinear optics and femtosecond lasers but these methods are usually more complicated and require high light intensities. **Table 2.1** summarizes the main characteristics of the five methods described below.

Table 2.1: Summary of the most common TRPL techniques.

Spectroscopy technique	Temporal resolution	2D Data	Signal intensity/replicability
TCSPC	$>$ 10 ps (often 1 ns)[3]	No	Good/Good
Streak Camera	$>$ 1 ps[4,5]	Yes	Good/Poor
Optical Kerr shutter	$>$ 200 fs[6–8]	Yes	Very Poor/OK
FLUPS	$<$ 100 fs[9–14]	No	OK/OK
Broadband FLUPS	$<$ 100 fs[15,16]	Yes	OK/OK

TCSPC – Time-correlated single-photon counting (TCSPC) is the most used and well-known TRPL technique due to its low cost and simple operation. First, a light source (mode-locked laser, pulsed-laser diode or light-emitting diode) excites the sample at a low photon fluence with a high repetition rate. Then, the emitted photons are detected by a photomultiplier tube (PMT), and the time with respect to the excitation pulse is measured by an increasing voltage ramp. Finally, the data are stored in a histogram which displays the photon population over time. The main limitation of TCSPC is due to the electronic detection, which limits the temporal resolution to hundreds of picoseconds. Besides, the PL is only monitored at a single wavelength, and 2D spectro-temporal data have to be reconstructed.

Streak Camera – Compared to standard TCSPC, streak cameras have a huge advantage as they yield 2D spectra in a single experiment. The emitted photons from the sample are collected and sent to a diffraction grating, providing spectral discrimination. Then, the horizontally dispersed photons hit a photocathode to produce electrons. The temporal resolution is achieved through the deflection of the electrons by an increasing electric field. Finally, the deflected electrons hit a phosphor screen producing an image recorded by a charge-coupled device (CCD) camera. Nevertheless, streak camera are expensive and are also limited, in the visible range, to a temporal resolution of several picoseconds due to the repulsion of the produced electrons.

Optical Kerr shutter – The fluorescence can be directly measured making use of the optical Kerr effect to overcome the temporal resolution limitation from electronic methods. Under intense polarized light, there is a change in the index of refraction of a non-isotropic material induced by the applied electric field. In such an experiment, the fluorescence is set to a particular polarization, for example vertical, by a first polarizer and then crosses a nonlinear medium before being blocked by a second polarizer. Together, these three optics are called a Kerr shutter. Within a given time delay, an intense gate pulse, horizontally polarized in this example, overlaps with the vertically polarized fluorescence in the nonlinear medium. The gate beam induces a rotation of the fluorescence polarization due to the third-order optical Kerr effect. The fluorescence is now allowed to cross the shutter and reach the spectrograph. The temporal resolution of the setup only depends on the laser pulse duration and is faster than any electronic detection-based technique. Still, since the optical Kerr effect is a χ^3 nonlinearity, it requires high intensity gate pulses and materials with high Kerr nonlinearities (such as CS_2), which strongly limit the intensity of the signal and the range of samples that can be measured.

Fluorescence upconversion – Similarly to the optical Kerr shutter, fluorescence upconversion spectroscopy (FLUPS) relies on nonlinear optical sampling. After excitation by a first laser pulse (pump), the fluorescence is upconverted (or gated) by another ultrashort pulse in a nonlinear optical crystal (**Figure 2.1**). The overlap between the fluorescence and the gate pulse generates a third pulse with an energy corresponding to the sum of the energies of the two incoming photons (sum-frequency mixing). Since sum-frequency generation (SFG) only occurs when the two incoming pulses cross the nonlinear medium at the same time (temporal matching), the temporal resolution is comparable to the laser pulse width. The time evolution is then obtained by setting a delay, τ_{delay}, between the excitation and the gate pulse. Compared to the optical Kerr effect, SFG has a χ^2 nonlinearity, and so the signal intensity will be higher. Nonetheless, SFG also requires a high gate intensity and phase matching between the fluorescence and the gate beam. In a nonlinear medium, the phase velocity depends on the wave fre-

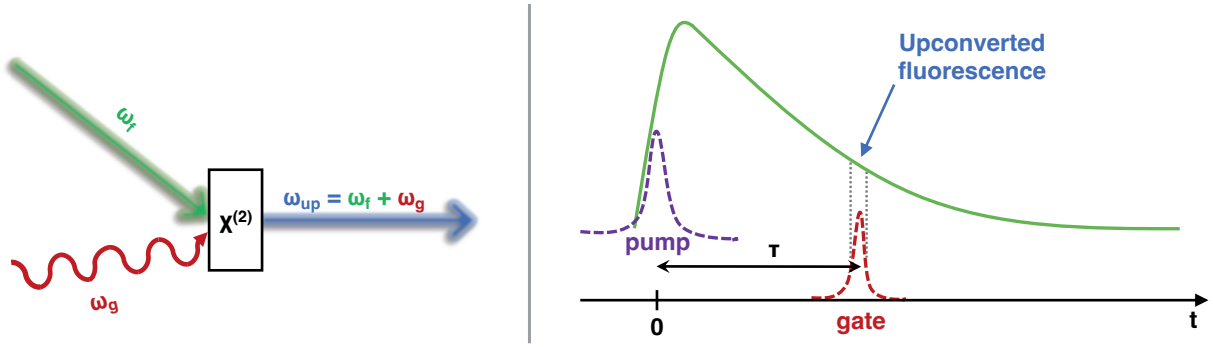

Figure 2.1: Schematic diagrams depicting the fluorescence upconversion process.

quency. Hence, phase-matching conditions should be adjusted according to the fluorescence wavelength. Traditional fluorescence upconversion setups are, therefore, limited to recording fluorescence emission at a single spectral point. In the next part, the conditions to obtain phase-matching over a wide range of wavelengths and record spectro-temporal data in a single scan will be discussed.

2.1.3 Broadband fluorescence upconversion spectroscopy

To address the question of broadband SFG, one could look at the quantum efficiency of the upconversion process, η_{NLO} [-] :[15,16]

$$\eta_{\mathrm{NLO}} = \frac{N_U(z=L_c)}{N_F(z=0)} \propto I_G(z=0) \cdot \left[\frac{\omega_U \cdot \omega_F \cdot d_{\mathrm{eff}}^2}{n_e(\omega_U) \cdot n_o(\omega_F) \cdot n_e(\omega_G)}\right] \cdot \left[\frac{\sin(\Delta k \cdot L_c/2)}{\Delta k \cdot L_c/2}\right] \cdot L_c^2 \qquad (2.3)$$

where indexes F, G and U depict the fluorescence, the gate and the upconverted fluorescence beams, respectively. N is the photon flux [photon/(s·m^2)], L_c is the crystal thickness [m], I_G is the intensity of the gate beam [W/m^2], ω is the angular frequency [s^{-1}], d_{eff} is the effective nonlinear susceptibility [-], n_e and n_o are the extraordinary and ordinary refractive indices [-] and Δk is the phase mismatch [m^{-1}].

The goal of a broadband FLUPS setup is to obtain high upconversion efficiencies over a wide range of wavelengths while keeping a sub-picosecond temporal resolution. Hereafter, we highlight and discuss three critical points for building the upconversion setup that fulfills these needs. 1) Since SFG is a nonlinear optical process, the intensity of the gate pulse at the crystal position should be as high as possible. Using the output of an ultrafast laser, a gate intensity of 70 μJ over 100 fs was obtained. 2) The efficiency depends quadratically on the thickness of the nonlinear crystal. Nevertheless, thicker crystals also induce larger group velocity dispersion and lower the temporal resolution of the setup. In addition, the acceptance bandwidth of the crystal is narrowed when the length of the crystal is increased, which

is detrimental for broadband applications. Here, a type I beta barium borate (BBO) crystal with L_c = 100 µm was chosen to have a good compromise between signal intensity, short temporal resolution and broad spectral coverage. 3) Δk, should be minimized over a wide range of wavelengths. In this way, the fluorescence and the gate have perpendicular polarization to achieve type II phase matching. Moreover, setting a large angle between the near-IR gate (λ_G = 1300 nm) and the fluorescence is crucial to get broadband upconversion. In this setup, the gate is tilted by 18° at the crystal position, which also offers a good temporal resolution over a broad range of wavelengths.

2.1.4 Experimental setup

The following setup used during this PhD thesis was purchased from LIOP-TEC and installed by Prof. Nikolaus Ernsting from Humboldt University.[15] It was later adapted during this PhD thesis with the help of Arnulf Rosspeintner. The setup displayed in **Figure 2.2** will be described part by part in the next section. The laser source was a chirp-pulsed amplification (CPA) Ti:sapphire laser (Libra-Coherent), which generated 45 fs pulses centred at 800 nm with an average power of 3.4 mJ with a 1 kHz repetition rate. The fundamental output was split into three beams for the FLUPS setup.

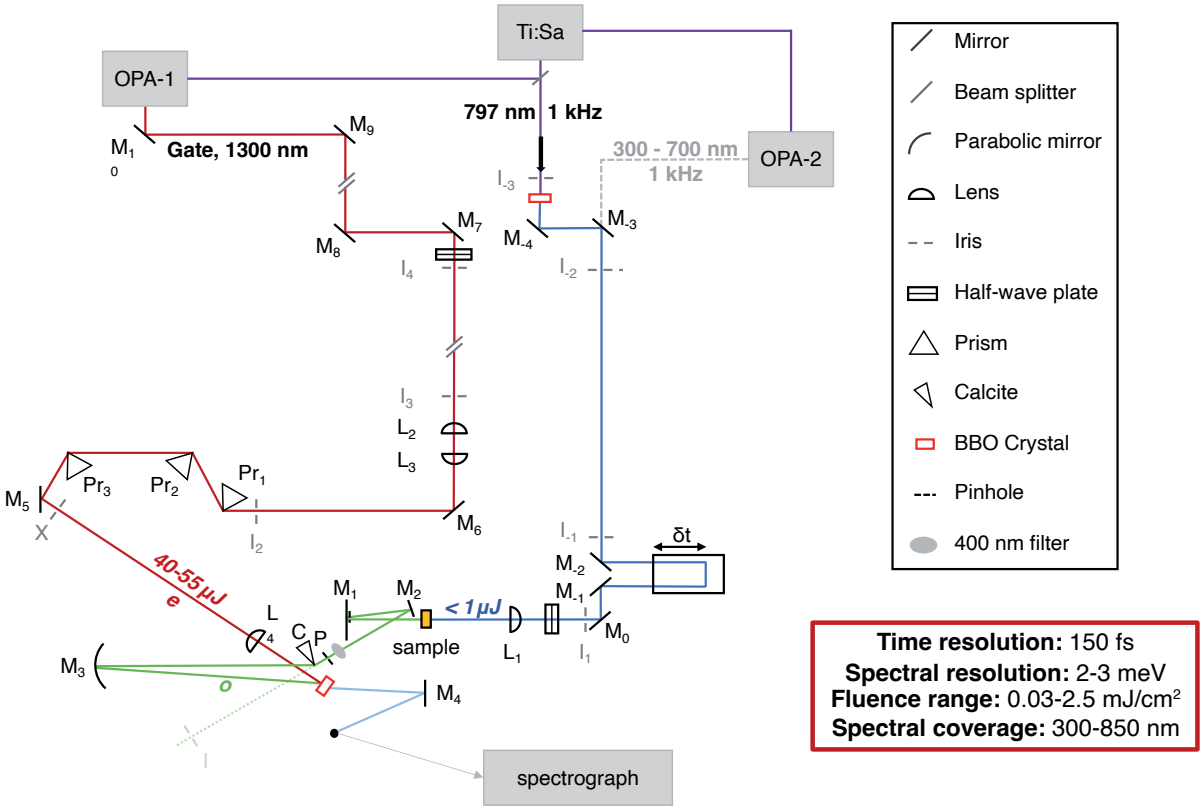

Figure 2.2: Representation of the experimental FLUPS setup.

Pump beam – The first beam was either sent to a white light-seeded optical parametric amplifier (OPerA-Solo, Coherent called OPA-2 in **Figure 2.2**) to generate a tunable output in the visible/near UV range (λ_{exc} = 300-700 nm), or was frequency doubled to 400 nm by a type I BBO crystal. The light polarization was adjusted afterwards by a $\lambda/2$ plate and set to the magic angle (54.7°) to only consider the population dynamics. The pump beam was attenuated to less than 1 μJ and focused by a lens (L_1) on the sample position with an effective diameter of 200 μm.

Fluorescence collection – While most of the transmitted pump light was blocked by a long-pass filter, the generated fluorescence was amplified sevenfold and focused at the pinhole (P) position by a Schwarzschild objective (M_1/M_2). It was then separated according to its polarization by a calcite prism (C). The vertically polarized light was imaged with an angle of 3° onto the BBO crystal, while the remaining was less deviated and stopped before M_3.

Gate beam – The second part of the laser output was used to pump another white light-seeded OPA (called OPA-1 in **Figure 2.2**) to generate close to 130 μJ gate pulses at 1300 nm. The gate beam was set to horizontal polarization and was widened and collimated by a pair of lenses (telescope L_1-L_2) to obtain an effective diameter of 3 mm. The pulse compression and tilt were achieved by a combination of three prisms (Pr_1, Pr_2 and Pr_3), while X represents the theoretical position of a fourth prism if a conventional compressor was used. The tilt angle was adjusted to 3.55° at point X. The apex region was imaged onto the BBO crystal with a demagnification of 5:1 by a lens (L_4). In this way, the tilt angle was magnified up to 18° at the BBO surface.

Sum-frequency generation and detection – As mentioned above, broadband SFG was achieved through a) type II phase matching conditions between the vertically polarized fluorescence and the horizontally polarized gate beam, and b) the large 21° angle between the fluorescence and the gate. The two beams interacted inside a 100 μm thick BBO crystal (EKSMA OPTICS), which had an optical axis in the horizontal plane. The upconverted signal was focused onto a fiber by a concave mirror M_4, while the frequency doubled gate beam and the *non-upconverted* fluorescence were blocked. Finally, the upconverted fluorescence was separated by wavelength with an unfolded Czerny-Turner spectrograph and detected by a CCD camera (Newton 920, Andor). The spectrograph and CCD camera calibration were performed with a standard Hg lamp having characteristic spectral lines in the UV/Vis range at 365 nm, 398.3 nm, 435.8 nm and 546.0 nm. The gratings were set to span the 340 - 680 nm region but can be adjusted afterwards for Vis/IR detection.

2.1.5 Data acquisition and treatment

2D PL spectra were obtained with a computer-controlled delay stage (Physik Instrumente) on the pump path controlled by a homemade LabVIEW program. Before each measurement, several dark spectra at Δt = -10 ps were recorded and averaged to minimise the background noise. In addition, multiple spectra (from 2 to 10) were averaged for 0.5 to 2 s integration time for the CCD camera to achieve a good signal-to-noise ratio. The data were stored as 2D matrices where the number of counts is given as a function of the time delay and the pixel number (P) of the CCD camera. Then they were treated with a homemade Matlab routine.

Wavelength and intensity correction – Firstly, P was converted into wavelength (λ_U) using a calibration curve recorded with a standard Hg lamp. Then, the gate energy (λ_G = 1300 nm) was subtracted from λ_U to obtain the "true" fluorescence wavelength, λ_F. Furthermore, since the pixels of the CCD camera have different energy widths (pixels in the UV have a larger energy width than pixels in the visible), the number of counts had to be multiplied by λ_U^2/λ_F^2.

Correction for group delay dispersion – For instantaneous fluorescence rise, the correction of the group delay was performed by looking at the travel time difference between the transmitted pump beam and the fluorescence signal. Otherwise, the group delay of light pulses through a given distance of fused silica was calculated and adjusted to match the experimental data. Then, the shifted time delays were interpolated to give the time corrected signal.

Time zero correction and temporal resolution – The SFG between the transmitted pump beam and the gate produces an intense signal at time zero (t_0). The temporal resolution of the experiment was calculated by fitting the cross-correlation peak with a 2D Gaussian function. Finally, each time was subtracted from t_0.

2.1.6 Standard characterization of the setup

The characterization of the setup was accomplished with a solution of coumarin 153 (C153) in ethanol since this dye has become a standard in the field.[15–18] The concentration of C153 was adjusted to get an absorption value of 0.6 at 400 nm in a 1 mm path length optical cuvette. **Figure 2.3** shows a 2D time-resolved emission spectrum acquired with a 400 nm excitation wavelength and some spectral slices at different time delays. The CCD camera was set to a full-vertical and 2-horizontal binning mode so that each pixel is 27 μm wide, corresponding to a sub-nanometer resolution in the visible range. The pump

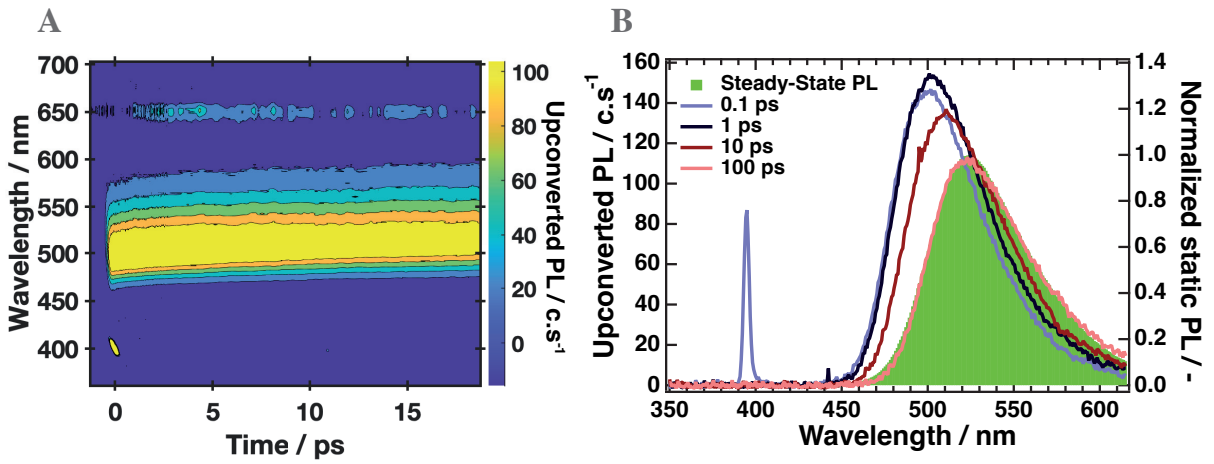

Figure 2.3: A) 2D time-resolved emission spectra of C153 in EtOH and B) comparison between the emission spectral slices and the normalized steady-state PL for λ_{exc} = 400 nm.

beam was set to the magic-angle, and attenuated to 0.3 mJ/cm^2, the CCD camera integration time was fixed to 0.5 ps, and 8 spectral slices were averaged. The filled 2D contour plot (**Figure 2.3.A**) shows the dynamic solvation and the vibrational relaxation of the photogenerated carriers within the first 20 ps (λ_{max} = 490-520 nm), which is visible on the spectral slices (**Figure 2.3.B**) as well. After 100 ps, the signal recorded with the FLUPS overlaps well with the steady-state emission obtained with the UV/Vis spectrophotometer. Furthermore, the cross-correlation between the transmitted pump and the gate is visible around 400 nm at time-zero. As mentioned previously, this peak was fitted with a 2D Gaussian function to obtain the temporal resolution of the experiment (190 fs) and for time correction. Finally, the noisy part around 650 nm arises from the frequency-doubled gate beam and prevents any quantitative analysis in this region. However, λ_G can be tuned from 1240 nm to 1360 nm only with a slight decrease of the upconversion efficiency to shift this noise from 620 to 680 nm.

2.2 Ultrafast transient absorption spectroscopy

In this thesis, FLUPS was combined with ultrafast transient absorption spectroscopy (TA) for each work presented in Chapters 3, 4 and 5.

TA is a time-resolved optical method used to probe the photogenerated excited states of a given material with a sub-picosecond temporal resolution. In such experiments, a fraction of the charge carriers are promoted from the electronic ground state to an excited state using a short laser pulse (pump). After a given time delay τ_{delay}, a weak white-light continuum (WLC) pulse is focused on the same sample area to probe absorbance modification induced by the pump. The dynamics are obtained by modifying the time delay between the pump and the probe, while the temporal resolution is given by the cross-correlation

between the two pulses. The TA signal is given by:

$$\Delta A(\lambda, \tau_{delay}) = A_{on}(\tau_{delay}) - A_{off} \tag{2.4}$$

where A_{on} is the absorbance of the excited system [-] and A_{off} is the system absorbance with the probe only [-]. In TA, the detected signal can be either positive (if the photoexcited system absorbs a part of the probe pulse) or negative (if the amount of probe light reaching the detector is increased). There are three types of contributions to ΔA: ground-state bleaching (GSB), stimulated emission (SE) and photo-induced absorption (PIA) (**Figure 2.4**). GSB arises from the depletion of the ground state and the filling of one or multiple excited states by the pump pulse, which reduces the absorption of the probe light at these particular energies. Therefore, the GSB process is expressed as a negative signal and usually mirrors the steady-state absorbance spectrum. Besides, the probe pulse can interact with the charge carriers in the excited state to cause relaxation to the ground state via SE. As this process will increase the number of photons detected by the camera, it is also seen as a negative signal overlapping with the steady-state fluorescence. Finally, PIA covers all processes related to an additional absorption from the photoexcited system (excitation to higher excited states, absorption from new species...) and appears as a positive signal in the TA spectrum.

While fluorescence spectroscopy only probes the emissive population, the TA signal is a combination of the electron and the hole population: it can be used to investigate carrier trapping into dark states, charge carrier transfer or carrier relaxation from higher electronic states. But, as seen in **Figure 2.4**, TA signal is a sum of multiple contributions that can overlap spectrally. Consequently, the interpretation is less straight-forward than for TRPL data.

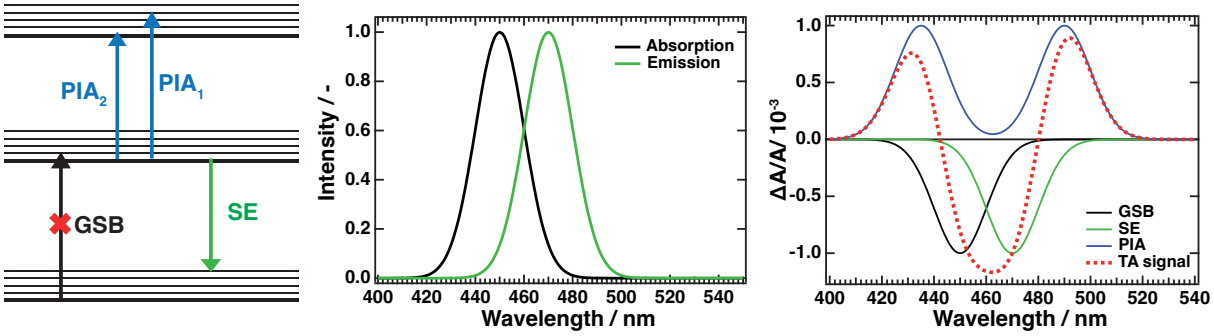

Figure 2.4: Left) Photophysical processes that can be probed using transient absorption spectroscopy: GSB, SE, PIA. Center) Example of an steady-state absorption and emission spectrum and right) the corresponding signals observed by TA.

2.2.1 Experimental setup

The setup described below was developed by S. Pelet[19] and modified by B. Wenger[20] and J. Teuscher, J. Risse, A. Marchioro and N. Banerji.[21] A schematic representation of the setup is shown in **Figure 2.5**.

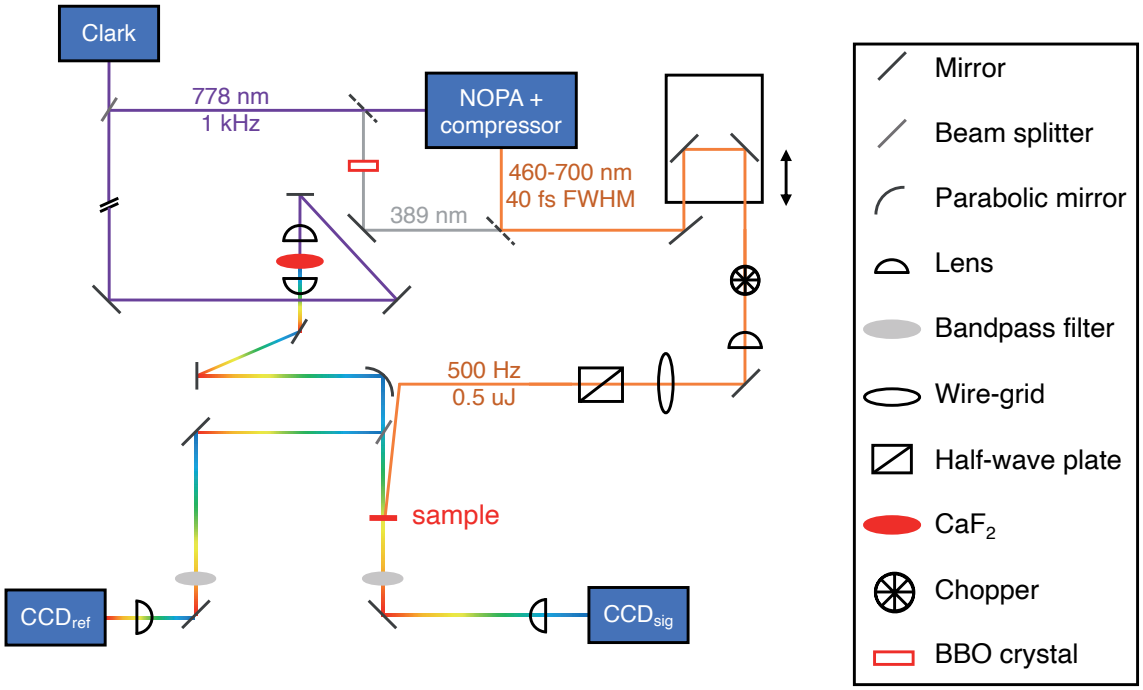

Figure 2.5: Experimental TA setup.

The laser source was a CPA Ti:Sapphire laser (CPA-2001, Clark-MXT), which generated 120 fs pulses centered at 778 nm with an average power of 1 mJ with a 1 kHz repetition rate. A part of the output was used to excite the sample, either with the double frequency of the fundamental using a type I BBO crystal or with the output of a Noncollinear Optical Parametric Amplifier (NOPA-Plus, Clark-MXT), which was later re-compressed with a pair of SF10 prisms (pump beam). The rest of the output was focused onto a CaF_2 crystal to generate the WLC (probe beam). The probe was split into a signal beam (attenuated and focused on the sample) and a reference beam (sent to the reference camera). The signal and reference beams were detected by two spectrographs (Princeton instruments, SpectraPro 2500i) coupled with two CCD cameras (Hamamatsu S7030-0906). A chopper (500 Hz) was placed on the pump path to measure the sample absorption with and without the pump beam. Similarly to the FLUPS setup, the TA dynamics were obtained with a motorized delay stage controlled by a LabVIEW software. The temporal resolution of the TA and the correction for group delay dispersion were measured after set of measurements with the cross-correlation of the pump and the probe on a blank sample (glass substrate or cuvette filled with solvent). For each measurement, the raw spectral slices were corrected by substituting a background signal from an average of 50 spectra between τ_{delay} = -2 ps and τ_{delay} = -1 ps.

2.2.2 Global analysis of the ultrafast data

Along this thesis, ultrafast processes were often investigated by applying a global analysis procedure for the TA and FLUPS dynamics.[22] Here the term "global" refers to simultaneous analysis of every spectral slice of a given data set obtained by TA or FLUPS. By considering that the photoinduced processes are first-order and evolve independently from each other, we can simplify the fitting equation to a sum of n monoexponential decay functions weighted with different amplitudes (A_n):

$$S(\lambda, t) = y_0 + \sum_{i=1}^{n} A_i(\lambda) \cdot \exp\left(\frac{t - t_0}{\tau_i}\right) \tag{2.5}$$

where τ_i are the time constants for each processes and remain the same (i.e. are linked together) for every wavelength. This sum is sometimes convoluted with a Gaussian function to account for the instrument response function for studying processes on the sub-picosecond timescale:

$$S(\lambda, t) = \frac{1}{2} \sum_{i=1}^{n} A_i(\lambda) \cdot \exp\left(\frac{t - t_0}{\tau_i}\right) \cdot \left[1 + \mathrm{ERF}\left(\frac{t - \left(\mu + \frac{\sigma^2}{t}\right)}{\sqrt{2}\sigma}\right)\right] \tag{2.6}$$

Then, the A_n are extracted and can be plotted versus the wavelength (A_n (λ)) to give the so-called decay-associated spectrum (DAS). DAS becomes powerful to unveil the spectral dependence of processes evolving on different timescales.

Bibliography

[1] Lakowicz, J. R. *Principles of Fluorescence Spectroscopy*; Springer Science & Business Media, 2013.

[2] Williams, A. T. R.; Winfield, S. A.; Miller, J. N. Relative fluorescence quantum yields using a computer-controlled luminescence spectrometer. *Analyst* **1983**, *108*, 1067.

[3] Murao, T.; Yamazaki, I.; Yoshihara, K. Applicability of a microchannel plate photomultiplier to the time-correlated photon counting technique. *Appl. Opt.,* **1982**, *21*, 2297–2298.

[4] Barbara, P. F.; Brus, L. E.; Rentzepis, P. M. A picosecond time-resolved fluorescence study of s-tetrazine vibrational relaxtion in solution. *Chem. Phys. Lett.* **1980**, *69*, 447–451.

[5] Bradley, D. J.; Liddy, B.; Sleat, W. E. Direct linear measurement of ultrashort light pulses with a picosecond streak camera. *Opt. Commun.* **1971**, *2*, 391–395.

[6] Arzhantsev, S.; Maroncelli, M. Design and Characterization of a Femtosecond Fluorescence Spectrometer Based on Optical Kerr Gating. *Appl. Spectrosc.* **2005**, *59*, 206–220.

[7] Matousek, P.; Towrie, M.; Ma, C.; Kwok, W. M.; Phillips, D.; Toner, W. T.; Parker, A. W. Fluorescence suppression in resonance Raman spectroscopy using a high-performance picosecond Kerr gate. *J. Raman Spectrosc.* **2001**, *32*, 983–988.

[8] Schmidt, B.; Laimgruber, S.; Zinth, W.; Gilch, P. A broadband Kerr shutter for femtosecond fluorescence spectroscopy. *Appl. Phys. B-Lasers O.* **2003**, *76*, 809–814.

[9] Bonati, C.; Mohamed, M. B.; Tonti, D.; Zgrablic, G.; Haacke, S.; van Mourik, F.; Chergui, M. Spectral and dynamical characterization of multiexcitons in colloidal CdSe semiconductor quantum dots. *Phys. Rev. B* **2005**, *71*.

[10] Cannizzo, A.; Bräm, O.; Zgrablic, G.; Tortschanoff, A.; Oskouei, A. A.; van Mourik, F.; Chergui, M.

Femtosecond fluorescence upconversion setup with broadband detection in the ultraviolet. *Opt. Lett.* **2007**, *32*, 3555.

[11] Mahr, H.; Hirsch, M. D. An optical up-conversion light gate with picosecond resolution. *Opt. Commun.* **1975**, *13*, 96–99.

[12] Shah, J.; Damen, T. C.; Deveaud, B.; Block, D. Subpicosecond luminescence spectroscopy using sum frequency generation. *Appl. Phys. Lett.* **1987**, *50*, 1307–1309.

[13] Damen, T. C.; Shah, J. Femtosecond luminescence spectroscopy with 60 fs compressed pulses. *Appl. Phys. Lett.* **1988**, *52*, 1291–1293.

[14] Kahlow, M. A.; Jarzeba, W.; DuBruil, T. P.; Barbara, P. F. Ultrafast emission spectroscopy in the ultraviolet by time-gated upconversion. *Rev. Sci. Instrum.* **1988**, *59*, 1098–1109.

[15] Gerecke, M.; Bierhance, G.; Gutmann, M.; Ernsting, N. P.; Rosspeintner, A. Femtosecond broadband fluorescence upconversion spectroscopy: Spectral coverage versus efficiency. *Rev. Sci. Instrum.* **2016**, *87*, 053115.

[16] Zhang, X.-X.; Würth, C.; Zhao, L.; Resch-Genger, U.; Ernsting, N. P.; Sajadi, M. Femtosecond broadband fluorescence upconversion spectroscopy: Improved setup and photometric correction. *Rev. Sci. Instrum.* **2011**, *82*, 063108.

[17] Pérez-Lustres, J. L.; Rodriguez-Prieto, F.; Mosquera, M.; Senyushkina, T. A.; Ernsting, N. P.; Kovalenko, S. A. Ultrafast Proton Transfer to Solvent: Molecularity and Intermediates from Solvation- and Diffusion-Controlled Regimes. *J. Am. Chem. Soc.* **2007**, *129*, 5408–5418.

[18] Eom, I.; Joo, T. Polar solvation dynamics of coumarin 153 by ultrafast time-resolved fluorescence. *J. Chem. Phys.* **2009**, *131*, 244507.

[19] Pelet, S. Femtosecond Dynamics of Electron Transfer in the Photosensitization of Wide Bandgap Semiconductors. Ph.D. thesis, École polytechnique fédérale de Lausanne, 2002.

[20] Wenger, B. Effect of electronic and nuclear factors on the dynamics of dye-to-semiconductor electron transfer. Ph.D. thesis, École polytechnique fédérale de Lausanne, 2006.

[21] Risse, J. Ultrafast dynamics of photoinduced charge separation in cyanine- and polymer-based organic photovoltaic systems. Ph.D. thesis, École polytechnique fédérale de Lausanne, 2015.

[22] van Stokkum, I. H. M.; Larsen, D. S.; van Grondelle, R. Global and target analysis of time-resolved spectra. *Biochimica et Biophysica Acta (BBA) - Bioenergetics* **2004**, *1657*, 82–104.

Chapter 3

Characterization of lead halide perovskite nanoplatelets

This chapter discusses the standard characterization of as-synthesized strongly confined $CsPbBr_3$ NPls and serves as an introduction to chapters 4, 5 and 6, which will review the ultrafast excited state dynamics in detail. Firstly, the synthetic procedure is described and the $CsPbBr_3$ NPls are characterized with TEM, cyclic voltammetry and UV-Vis spectroscopy. The effects of the quantum confinement on the photophysical properties are highlighted and typical TA and broadband FLUPS data are also examined. Lastly, the conventional approaches to treat the NPl surface and improve their long-term stability is introduced.

This chapter is based on the studies *"Exciton, Biexciton and Hot Exciton Dynamics in $CsPbBr_3$ Colloidal Nanoplatelets"* [1] and *"Direct Observation of Shallow Trap States in Thermal Equilibrium with Band-Edge Excitons in Strongly Confined $CsPbBr_3$ Perovskite Nanoplatelets"* [2] conducted equally by Dr. Vale and myself. Dr. Vale wrote entirely the first manuscript while I wrote the second. The contribution of Dr. Burgos-Caminal in the data analysis is also gratefully acknowledge.

3.1 Introduction

Over the last 15 years, lead halide perovskite (LHP) materials with an $APbX_3$ structure (A = Cs^+, $CH_3NH_3^+$, $CH(NH_2)_2^+$; X = Cl^-, Br^-, I^-) gathered great interest for photovoltaic devices.[3–5] Today, perovskite-based solar cells power-conversion efficiency has been pushed to 25.7%, making them one of the most efficient single-junction solar cells.[6] Likewise, nanoparticles of the same material, called perovskite nanocrystals (PNCs), have become promising for light-emitting diodes (LED) and lasing applications.[7–13] The most common all-inorganic PNCs are weakly confined three-dimensional nanocubes with dimensions slightly larger than the perovskite bulk-exciton Bohr radius.[14] The perovskite core is surrounded by long-chain organic ligands, which play a crucial role in preserving the size and the shape of the NCs. PNCs are particularly attractive for light-emitting devices because they display high absorption coefficients (up to 10^{-10} cm^2),[15] high photoluminescence quantum yields (PLQYs) (close to 100%),[16] high color purity (< 100 meV emission line widths), and a broad color gamut through halide and size-tunability. Nonetheless, because of the instability of $CsPbCl_3$ NCs and ultra-small zero-dimensional (0D) $CsPbBr_3$ compounds, cubic PNC-based devices show limited performance in the blue range.

Two-dimensional (2D) $CsPbBr_3$ nanoplatelets (NPls) or one-dimensional (1D) $CsPbBr_3$ nanowires (NWs) offer a great alternative for blue-emitting devices by shifting the material band gap to the blue through the quantum confinement of the charge carriers. A strong quantum confinement regime is achieved when at least one dimension of the NC becomes smaller than its bulk-exciton radius (3.5 nm for $CsPbBr_3$).[14] The NPl or NW optical properties can be controlled by tuning the shorter dimension (e.g. the thickness of the NPls or the radius of the NWs), while the lateral size only plays a minor role.[17–19] Due to the quantum confinement of the perovskite structure, NPls exhibit different photophysical behaviors when compared to traditional PNCs. Notably, the charge carrier interactions are enhanced, leading to thermally stable excitons and short fluorescence lifetimes. Nonetheless, because of the increased number of surface trap states, PLQYs of perovskite NPls barely reach 50%.[19,20] Therefore, there is an urge to fully understand the physical and structural limitations of these materials to optimize the NPl-based devices.

Herein, a new synthetic procedure was reported for preparing quasi-1D $CsPbBr_3$ NPls (23 x 4 x 1.8 nm) with a narrow size distribution. The NPl colloidal solutions were characterized using steady-state spectroscopy, highlighting the effect of the quantum confinement on their optical properties. These NPls display an extended band gap compared to other $CsPbBr_3$ NCs, as well as larger exciton binding energy and narrower PL line width, making them attractive for blue-emitting devices. However, we also evidenced charge carrier trapping, which is detrimental to the device efficiency. Particularly, the

importance of understanding their surface chemistry was evidenced by studying the effect of long-term storage on the NPl properties. Due to ligand desorption from the surface, the number of trap states increases, lowering the material PLQY. Finally, the ultrafast charge-carrier dynamics were investigated by discussing typical data obtained by broadband fluorescence upconversion spectroscopy (FLUPS) and fs-transient absorption (TA). This section serves as an introduction to the next chapters, in which a detailed analysis will be presented.

3.2 Results and discussion

3.2.1 NPl synthesis

Strongly confined $CsPbBr_3$ NPls were synthesized following a previously reported procedure,[21] with some adaptations (**Scheme 3.1**). For the cesium source, Cs_2CO_3 (2 mmol) was mixed with oleic acid (OA) (2.5 mL) in 1-octadecene (17.5 mL). The solution was degassed and dried under vacuum at 120 °C on a Schlenk line for one hour. Then, to complete the formation of Cs-oleate, the solution was heated to 150 °C under an inert atmosphere for 30 minutes. The Cs-oleate solution is stable for months, but it precipitates at room temperature (RT) and should be heated up to at least 100 °C before use.

At the same time, the lead bromide source was prepared by mixing $PbBr_2$ (0.20 mmol), OA (1 mL) and oleylamine (OAm) (1mL) in dodecane (5 mL). The passivation of the NPl surface was achieved by adding an excess of bromide via $ZnBr_2$ (0.13 mmol) with the starting compounds. The lead solution was degassed and dried under vacuum at 50 °C on a Schlenk line for 30 minutes. $PbBr_2$ was completely soluble in dodecane by increasing the temperature to 150 °C under an inert atmosphere. Then, the solution was slowly cooled down to RT before injection of Cs-oleate (0.2 mL) under vigorous stirring. After 5 minutes, the reaction was quenched in an ice bath. To purify the NPls, 5 mL of dry isopropanol (IPA) was added to the solution before centrifugation at 5000 rpm for 5 minutes. The precipitate containing unreacted Pb^{2+} and large NPls was discarded, and another 10 mL of dry IPA was added

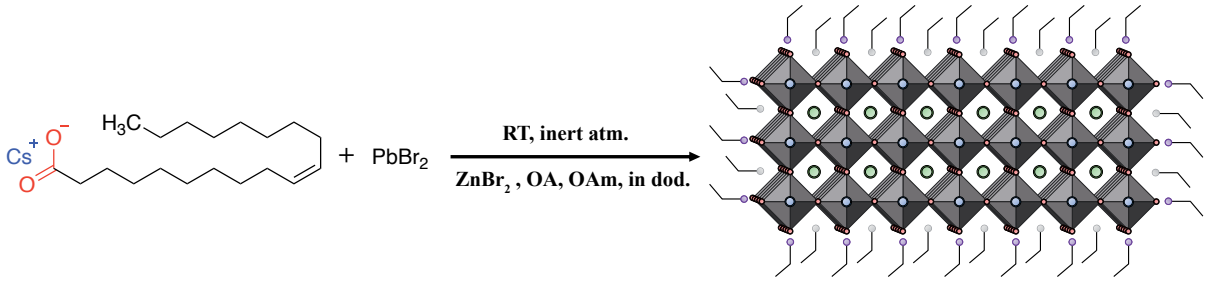

Scheme 3.1: Synthesis of the $CsPbBr_3$ NPl colloidal solution.

to the supernatant. After a second round of purification (5000 rpm, 15 minutes) to remove the excess ligands, the precipitate (purified $CsPbBr_3$ NPls) is dissolved in dodecane (2 mL) and kept at RT for days. For further spectroscopic investigations the sample was diluted in dodecane and placed in an 1 mm optical path quartz cuvette (Type 61, FireflySci) to obtain an absorbance of ≈ 0.6 at the excitonic absorption peak.

3.2.2 Effect of confinement on $CsPbBr_3$ NPl' optical properties

Transmission electron microscopy (TEM) images of the as-synthesized $CsPbBr_3$ NPls are shown in **Figure 3.1**. The particles have a rectangular shape with a length, $l_{NPl} = 23 \pm 7$ nm and a lateral size, $w_{NPl} = 4 \pm 2$ nm, close to the exciton Bohr radius (3.5 nm).[14] The NPl thickness could be estimated by looking at the steady-state absorption spectrum (**Figure 3.2, A and B**). The absorption of the colloidal solution in dodecane is dominated by a strong excitonic feature at 2.78 eV (448 nm) followed by a continuous band absorption above 3.02 eV (< 410 nm). The transition energy of the excitonic absorption corresponds to 3 monolayers (MLs) of $CsPbBr_3$ NPls, with a total thickness of 1.8 nm.[19] This excitonic peak is a direct consequence of the strong quantum confinement of the charge carriers and agrees with the 0.66 eV blue shift of the band edge absorption compared to bulk $CsPbBr_3$.[22] Compared to other square-shaped 2D LHPs,[19,23–27] the as-synthesized NPls are smaller ($V_{NPl} = 166$ nm^3) with an additional intermediate quantum confinement in the lateral direction, inducing even more confined charge carriers. The electrochemical band gap obtained by cyclic voltammetry (CV), $E_g = 2.70$ eV (**Figure 3.2.C**), matches the optical observations. Compared to larger $CsPbBr_3$ NCs, the valence band maximum energy is slightly increased to -5.48 eV but the conduction band minimum energy is even more shifted up (to -2.78 eV), which results in a larger band gap.[28–30]

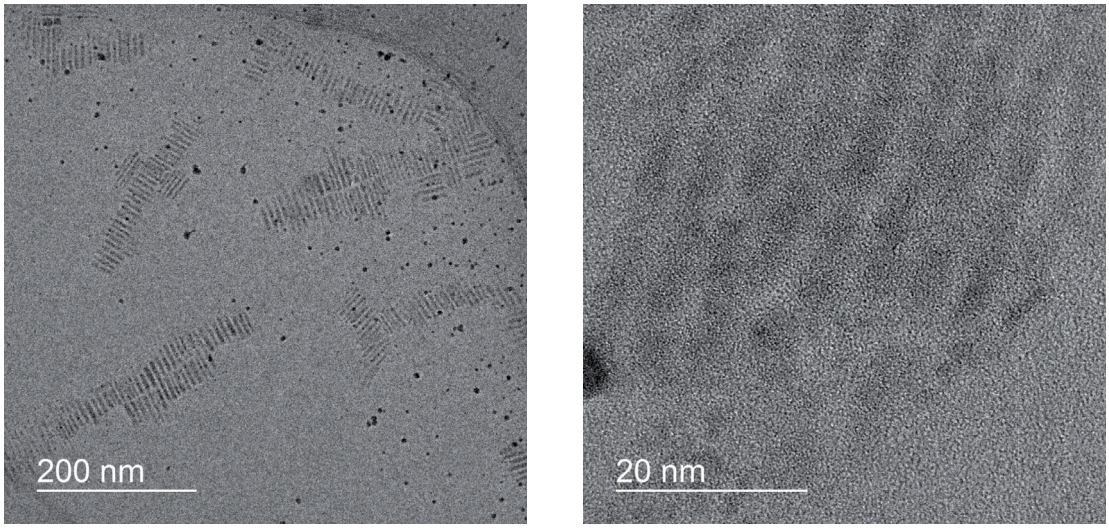

Figure 3.1: TEM images of fresh $CsPbBr_3$ NPls.

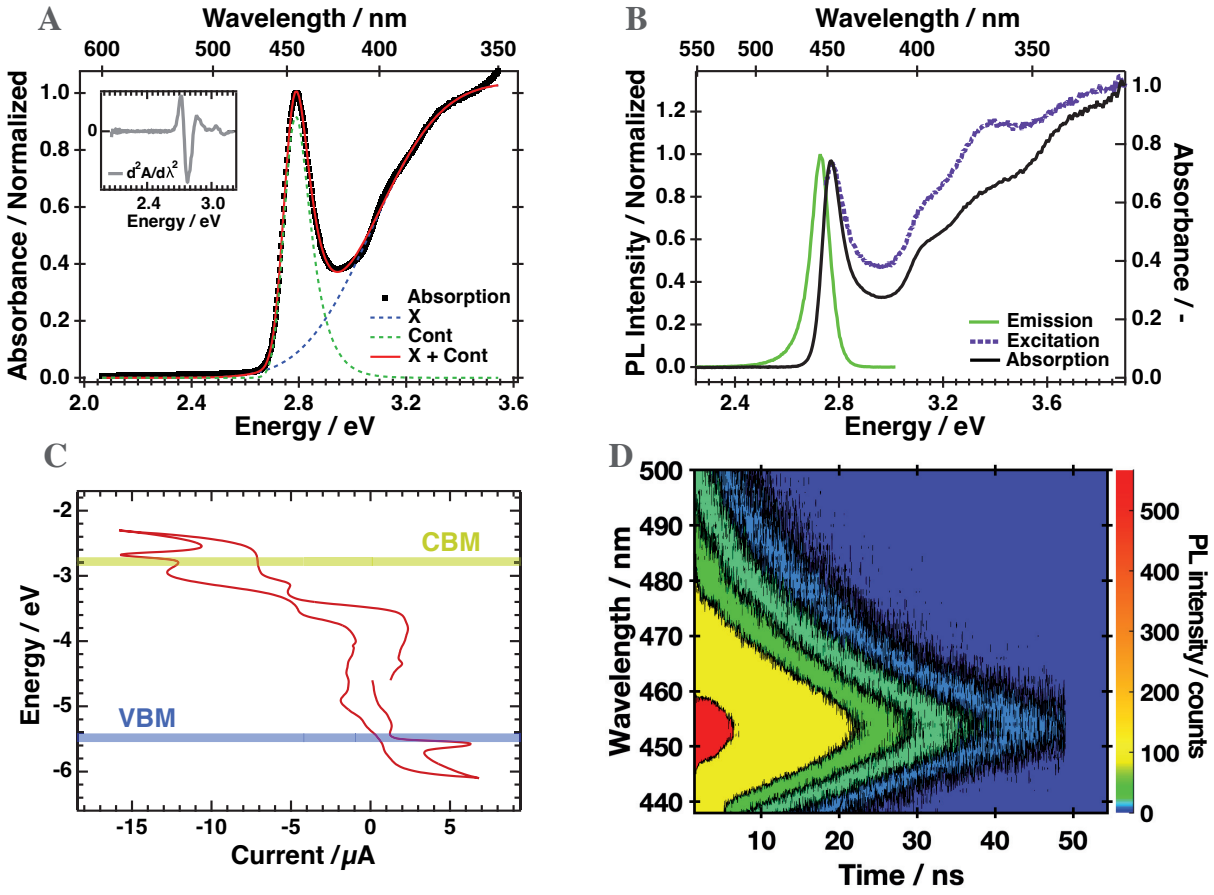

Figure 3.2: A) Absorption spectrum of $CsPbBr_3$ NPls in dodecane with the best-fitted curve (red line) using the quantum-well model described in the Appendices. Inset: second derivative of the absorption spectrum. B) Absorption, excitation and emission spectra spectrum of a fresh NPl solution. C) Voltammogram of $CsPbBr_3$ NPls and the corresponding band edge energies. D) 2D time-resolved emission spectra obtained by TCSPC.

The absorption can be fitted by a quantum-well model (Appendix, section A.1)[31,32] to get an upper estimation of the exciton binding energy, Δ_x, and the best fitting curve is visible in **Figure 3.2.A**. The fit deviates from the experimental data at higher energies due to the second and the third excitonic transitions at 3.10 eV (400 nm) and 3.35 eV (370 nm) in the continuum absorption. These higher lying transitions limits the estimation of the binding energy and a more comprehensive formalism is needed to account for the excitonic contributions. An exciton binding energy of $\Delta_x = 334 \pm 12$ meV is obtained, which is a greater value than for other NPls,[23,32] and one order of magnitude larger than for bulk CsPbBr3 (40 meV).[14] This enhancement cannot only be explained by the size confinement, but also by a contribution from dielectric confinement due to the difference of optical permittivity between the perovskite core ($\varepsilon = 6$) and the surrounding organic ligands ($\varepsilon = 2$).[33,34]

Besides, the colloidal NPls exhibit an intense, narrow and short-lived emission peak at 455 nm (**Figure**

3.2, B and D), which is highly promising for blue-emitting devices. The PL lifetime is estimated to be 8.6 ± 0.1 ns by fitting the time-correlated single photon counting (TCSPC) data with an exponential decay function (Appendix, **Figure A.2**), and is in the range of what has been reported for $CsPbBr_3$ NPls.[19,32] At late times ($\tau_{delay} > 30$ ns), the data deviate slightly from the fit, presumably due to shallow trap states causing delayed fluorescence (see next chapter).[35–37] Using the comparative method with a standard coumarin-102 solution, the PLQY is estimated to be ≈ 30% (Appendix, section A.1). This value is lower than traditional PNCs due to the increased number of surface states acting as exciton traps. The small PL full width at half maximum (84 meV) indicates weak exciton-phonon coupling, as expected for strongly confined systems due to the restriction of certain vibrational modes.[38–41] In addition, the 46 meV (7 nm) Stokes shift between the excitonic absorption and the emission is smaller than the theoretical value for 0D quantum dots (QDs) with the same radius because the NPls are not equally confined.[42] The origin of the Stokes shift is intriguing for strongly confined particles and will be discussed later on.

Finally, the shoulder on the red side of the PL is a typical signature of trap states for strongly confined NCs.[31,43,44] TCSPC data (**Figure 3.2.D** and Appendix, **Figure A.3**) confirm that this tail does not result from the presence of different particle sizes because the same time constant is applied to fit each wavelength. Besides, the second derivative of the absorption (inset **Figure 3.2.A**) has a single minimum around the exciton transition, and the absorption spectrum is flat in the 2.0-2.6 eV region, suggesting a homogeneous particle size distribution and the absence of bulk or bigger $CsPbBr_3$ NPls. Finally, the emission spectrum does not shift with time, indicating that there is no energy transfer from different particle sizes.

3.2.3 Ultrafast signatures of $CsPbBr_3$ NPls

As for every other semiconductor, the excited state dynamics in LHP NPls depend on the density of photogenerated charge carriers. In $CsPbBr_3$ NPls, the exciton binding energy greatly overcomes the thermal energy (k_B·T) at RT, so it can be safely considered that electron-hole pairs (excitons) constitute the primary photoinduced species. Consequently, instead of talking about the charge carrier density, it becomes more relevant to use the average number of excitons per NPl, $\langle N_x \rangle$ [-]. $\langle N_x \rangle$ is proportional to the density of photons per unit area, j [cm^{-2}]:

$$\langle N_x \rangle = j \cdot \sigma_\lambda \tag{3.1}$$

where σ_λ is the absorption cross-section at the excitation wavelength [cm^2]. This value is calculated using a procedure based on Poisson statistics.[45–47] The probability, $P(n)$, of having n excitons in a single NPl

is given by:

$$P(n) = \frac{\langle N_x \rangle \cdot \exp\left(\langle N_x \rangle\right)}{n!} \tag{3.2}$$

Moreover, since multi-exciton annihilation is expected to be fast (τ_{xx} = 10-15 ps, see chapter 5), a maximum of one exciton remains per NPl for $\tau_{delay} > 50$ ps. Knowing that the PL intensity is proportional to the number of NPls containing one exciton, the PL amplitude at late time delays (τ_{delay} = 100 ps) can be fitted with **Equation 3.3** to obtain σ_λ:

$$PL_{max} = A \cdot [1 - P(0)] = A \cdot \left[1 - \exp\left(-\langle N_x \rangle\right)\right] = A \cdot \left[1 - \exp\left(-j \cdot \sigma_\lambda\right)\right] \tag{3.3}$$

For λ_{exc} = 400 nm, $\sigma_{400} = 3.4 \cdot 10^{-15}$ cm^2 (**Figure 3.3, A and B**), which is one order of magnitude smaller than for traditional PNCs. This difference is explained by the smaller particles volume and the lower density of states at 400 nm.[18,48] Yet, this value is still three to four orders of magnitude greater than traditional CdSe/CdS/CdTe QDs,[49] which makes LHP NPls more suitable for light-harvesting devices.

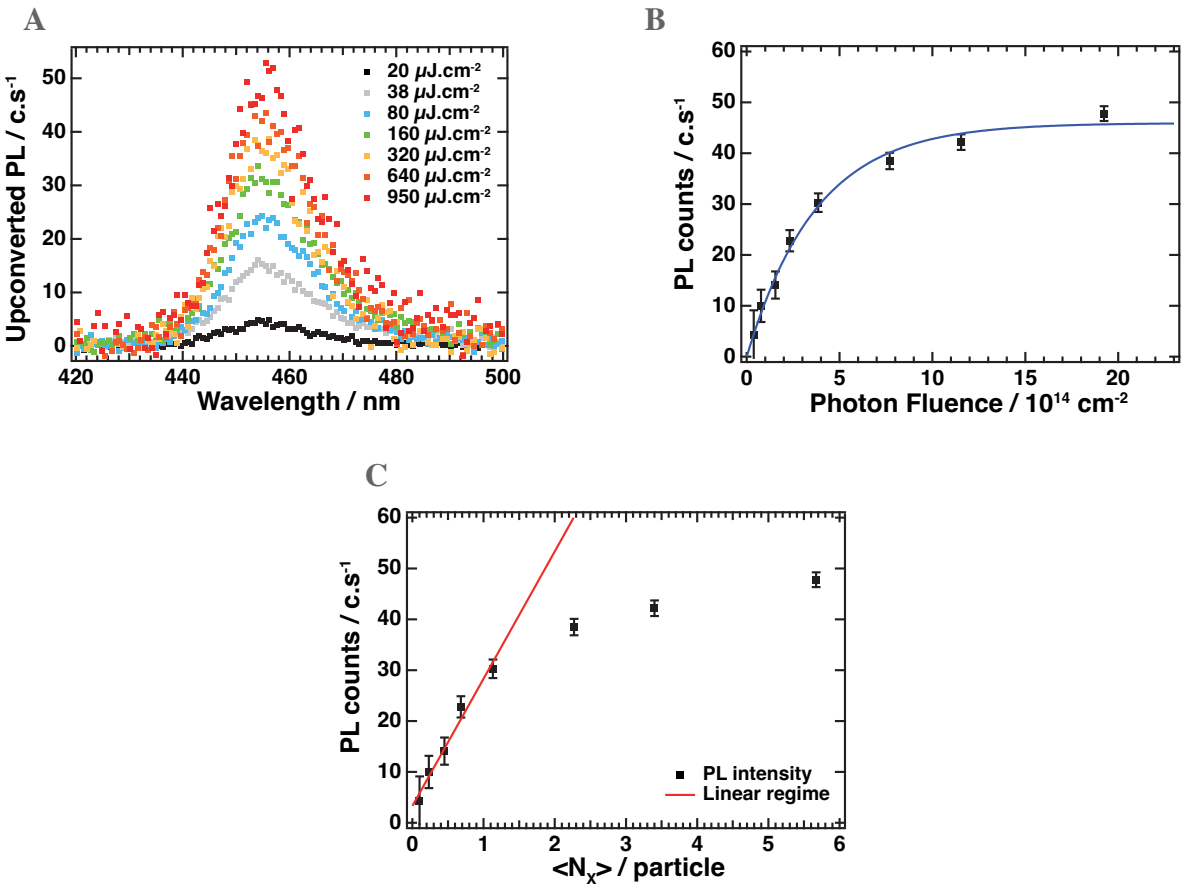

Figure 3.3: A) FLUPS spectral slices (λ_{exc} = 400 nm) at τ_{delay} = 100 ps for different excitation intensities. B) PL intensity obtained by fitting the spectral slices with a Gaussian function and the best fitted curve obtained from Equation 3.3. C) Dependence of the PL intensity on $\langle N_x \rangle$ with a line illustrating the linear regime.

Finally, $\langle N_x \rangle$ is calculated for each pump intensity using **Equation 3.1**. As expected for an ensemble of independent NPls, the PL intensity increases linearly with $\langle N_x \rangle$ for low excitation densities since more and more NPls are photoexcited. For $\langle N_x \rangle > 1$, the PL intensity deviates from the linear regime and reaches a plateau. This deviation is a typical signature of exciton-exciton annihilation, which will be discussed in more detail in chapter 5. Unless mentioned otherwise, $\langle N_x \rangle$ is kept below 0.2 to avoid multi-exciton interactions since it gives a probability of 1.7% to have more than one exciton per NPl.

This thesis mostly combines broadband FLUPS with fs-TA to study the charge carrier dynamics in $CsPbBr_3$ NPls . As mentioned previously, FLUPS data are rather straightforward since the PL intensity only depends on the emissive population. Nevertheless, since the TA signal is a combination of electron and hole populations, it can unveil more complex processes. The following paragraph overlooks the typical response of $CsPbBr_3$ NPls with FLUPS and TA spectroscopies. Some open questions are also raised and will be answered in the next chapter.

The transient PL of $CsPbBr_3$ NPls (**Figure 3.4.A**) overlaps well with the steady-state emission spec-

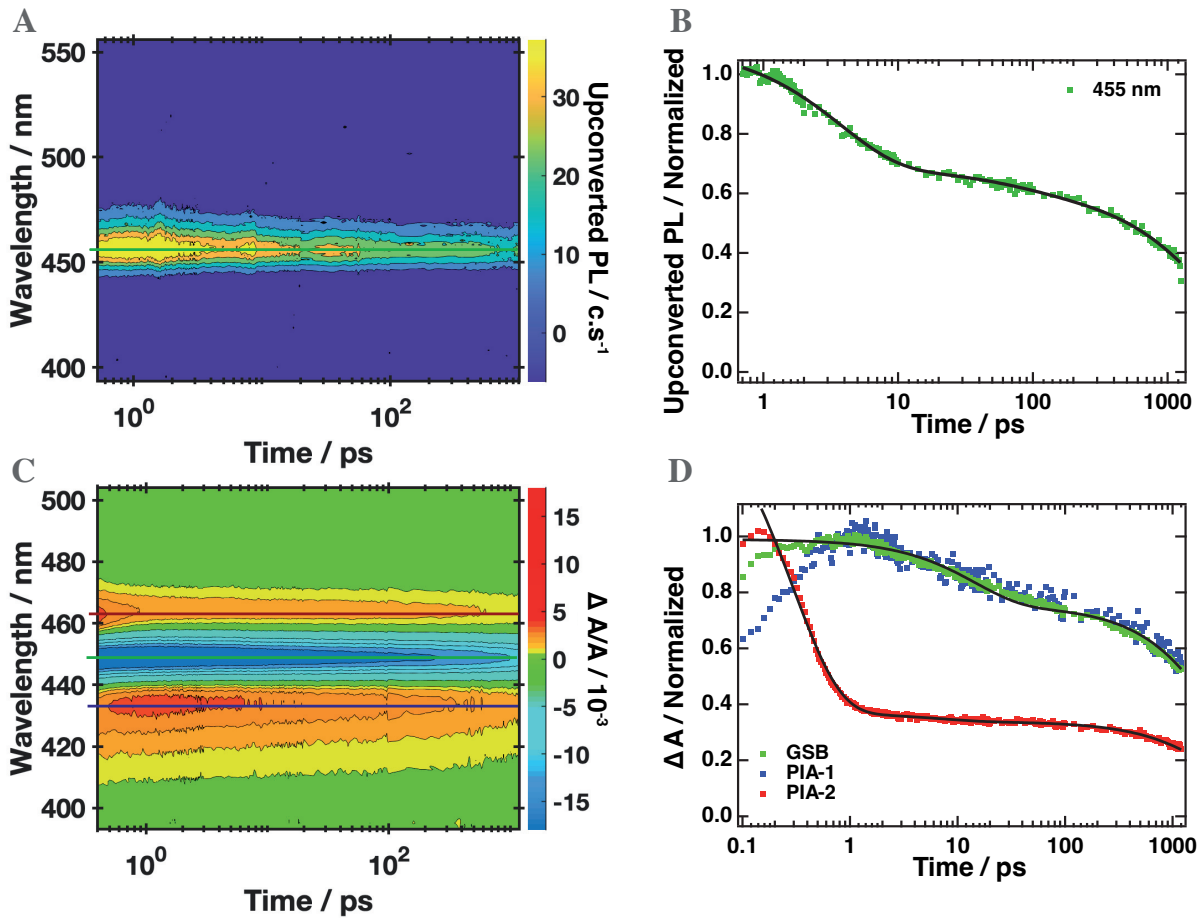

Figure 3.4: 2D A) broadband FLUPS and C) TA spectra acquired at a low excitation intensity, $\langle N_x \rangle < 0.2$. Dynamic slices of B) FLUPS and D) TA at the peaks maxima.

trum showing a maximum intensity at 455 nm. The PL shape remains identical over time, meaning that the signal comes from a unique population set. A broad size distribution of NPls would have induced an energy transfer from the smaller (with a bigger band gap) to the bigger particles (with a smaller band gap) over a few picoseconds resulting in a shift of the PL towards the red side.[50–52] The origin of the 48 meV Stokes shift between the excitonic absorption and the main emission is unexpected for a strongly confined system and will be addressed within the next chapter. The PL decay at low pump intensity could be well fitted with a three-exponential decay function (**Figure 3.4.B**) with associated time constants (and relative amplitudes) of 4.8 ± 0.2 ps (40%), 43 ± 4 ps (15%) and 3.5 ± 0.2 ns (45%). The origin of the first, fast decay, remains poorly understood and will be one of the points discussed within chapter 4. The two slower decays are usually assigned to exciton trapping into defect states and radiative recombination, respectively.[19,37,53] The exciton recombination lifetime estimated by FLUPS is two times smaller than the value obtained by TCSPC because of the short time window.

The TA spectra (**Figure 3.4.C**) show one negative feature at 448 nm alongside two positive peaks around 435 (PIA-1) and 465 nm (PIA-2). The negative signal is a typical ground state bleaching (GSB) signature since it matches with the steady-state absorption, and its amplitude is proportional to the population of excitons in the lowest excited state. The GSB signal grows within the temporal resolution of the setup (250 fs) and can be fitted with a two-exponential decay function with associated time constants (and relative amplitudes) of 25 ± 1 ps (21%) and 3.0 ± 0.1 ns (79%) (**Figure 3.4.D**). The decays corroborate with the FLUPS data and are related to exciton trapping and radiative recombination. The broad positive signal on the blue side of the GSB (PIA-1) is a consequence of the strong quantum confinement and is related to a forbidden exciton transition, which is activated by the presence of charge carriers in the lowest excited state ("free" excitons).[1,54] Since this transition depends on the exciton population, it follows the same decay dynamics as the GSB signal. Finally, PIA-2 around 465 nm is believed to arise from the Coulomb interaction between an exciton with excess energy produced by the pump pulse and a "free" exciton generated by the probe.[54–56] Since the TA spectrum at early times is analogous to the second derivative of the absorption spectrum (**Appendix, Figure A.5**), this feature is assigned to the biexcitonic Stark effect and is often used to calculate the biexciton binding energy. The fast, ≈ 0.3 ps, decay is highly debated in the literature and will be discussed in the next chapter.

3.2.4 NPl' long-term stability and surface passivation

Before moving on to a more *in-depth* study of the ultrafast photophysical processes in $CsPbBr_3$ NPls, the question of the particle long-term stability need to be addressed. Firstly, it directly affects the reproducibility and reliability of the optical measurements, and secondly, it is crucial to enhance LHP

stability for optoelectronic applications.

Looking at the colloidal solution absorption and emission spectra is the easiest and fastest way to determine whether or not the NPl optical properties are altered over ageing. **Figure 3.5.A** shows the steady-state absorption and emission of a freshly synthesized $CsPbBr_3$ colloidal solution and the same solution after 80 days of storage under ambient conditions. Both display the same shape and are red shifted by only 5 nm. Since aggregation from 3 to 4 NPl MLs would lead to a much larger redshift of the band gap (> 20 nm),[19] it indicates that the NPl' thickness is preserved. The small change is attributed to a growth of the NPls in the non-confined dimension, which does not affect the confinement of the charge carriers. Even after 80 days, the absorption spectrum remains flat for $\lambda > 475$ nm, denoting a homogeneous size distribution.

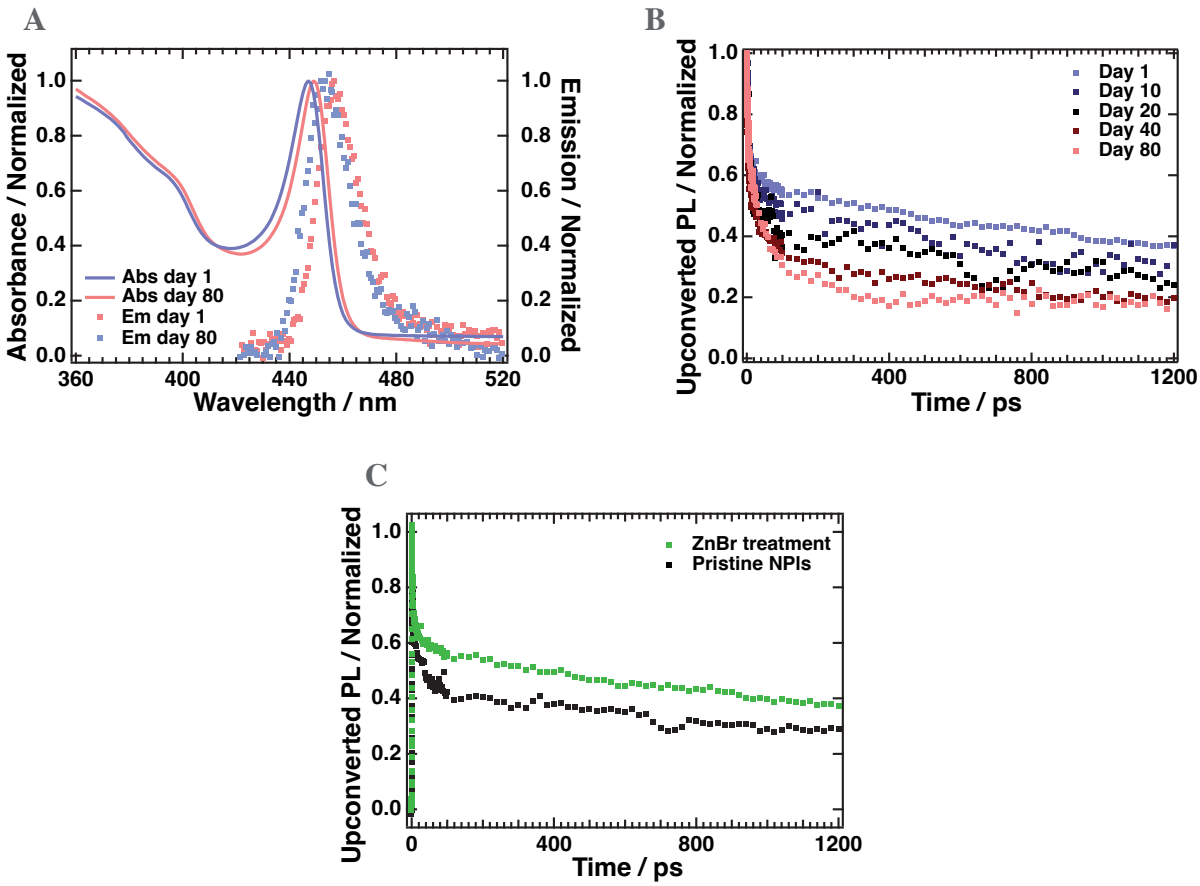

Figure 3.5: A) Normalized absorption and emission spectra of a fresh NPl colloidal solution and after 80 days. Evolution of the normalized PL decay dynamics B) upon ageing and C) for different synthetic procedures.

However, the PL dynamics are considerably affected after ageing, as can be seen in **Figure 3.5.B**. By fitting the dynamics with a three-exponential decay function, it is evidenced that the relative amplitude associated with exciton trapping ($\tau_D = 43$ ps) increases from 15% to 40% over 80 days, lowering by more

than 50% the PL intensity after 1 ns. A more accurate fitting strategy will be described in the next chapter. This drop is ascribed to the formation of new surface trap states arising from the desorption of capping ligands on the NPl surface. By looking back to **Figure 1.10**, ligand desorption results in under-coordinated Pb^{2+} or Br^{-} atoms at the surface, which then act as charge carrier traps and ultimately lower the PLQY from ≈ 40% to ≈ 5%.[57,58] It has already been shown that OA/OAm binding to the perovskite surface is highly dynamic and is one of the main concerns for further applications.[26,59–64] Since the exciton radiative recombination rate is two orders of magnitude smaller than charge carrier trapping, preventing the last process is crucial to obtain efficient optoelectronic devices.

A way to reduce the proportion of trap states is by substituting the usual capping ligands with less labile ones, such as quaternary ammonium,[65–67] or by passivating the NPl surface with post-synthetic surface treatment.[68,69] Here, the last option was investigated by adding an excess of bromide achieved through adding $ZnBr_2$ in the lead-source solution before the synthesis to passivate the excess of lead at the surface. This resulted in an increase of the PL intensity (**Figure 3.5.C**) and the reduction of the relative amplitude associated with exciton trapping (from 25 to 13%), indicating the passivation of the surface trap states. This is accompanied by an increase in the PLQY from ≈ 30% for the pristine $CsPbBr_3$ NPls solution to ≈ 40% for the NPls treated with $ZnBr_2$.

3.3 Conclusion

In conclusion, homogeneous colloidal solutions of strongly confined $CsPbBr_3$ LHP NPls with 23 x 4 x 1.8 nm dimensions have been synthesized and characterized.

The combination of quantum and dielectric confinement of the charge carriers led to: 1) a larger band gap between the valence and the conduction band (3.11 eV vs 2.45 eV for bulk $CsPbBr_3$), 2) a strong excitonic absorption (λ_{abs} = 448 nm), 3) a large exciton binding energy (334 meV vs 40 meV for their bulk counterparts), and 4) an intense, narrow (84 meV) and short-lived (8.4 ns) emission at λ_{em} = 455 nm. In addition, the NPls retained some bulk LHP properties, such as high absorption coefficients (10^{-15} cm^2 vs 10^{-18} - 10^{-20} cm^2 for traditional chalcogenide QDs) and a low intrinsic interband trap density. Because of the increased number of surface states, careful synthetic procedures should be followed to overcome the creation of new trap states. Under-coordinated Pb^{2+} atoms lying at the surface could be passivated by adding an excess of bromide during the synthesis, while new organic capping ligands could be used to prevent ligand desorption from the surface.

Altogether, these results are promising towards the use of $CsPbBr_3$ NPls for blue-emitting devices. Still, there is a lack of understanding about the underlying photophysics and the charge carrier dynamics at ultrafast time scales. To address these points, typical data obtained by broadband FLUPS and TA were introduced and led to three central questions: 1) Why is there an additional, fast, decay for the PL compared to the GSB dynamics observed by TA? 2) What is the origin of the Stokes shifted emission in strongly confined NPls? This shift indicates that different states are involved during absorption and emission, but how are they linked together? 3) What happens if the excitation intensity is increased to generate more than one exciton per NPl? 4) Is the presence of tightly bound excitons and long chain organic capping ligands hindering charge separation?

3.4 Methods

3.4.1 Sample characterization

TEM – TEM images of the NPls were taken at the Brazilian Nanotechnology National Laboratory (Sao Paulo) on a JEOL JEM 2100F microscope with an Orius camera (SC200). The samples were prepared by drop-casting a small amount of the concentrated NPl solution on a TEM grid covered with an ultrathin carbon film.

UV-Visible absorption – Linear absorption spectra were taken on a Perkin Elmer Lambda 950 UV-Vis-NIR spectrophotometer. Since the intensity and the location of the excitonic absorption is strongly dependent on the $CsPbBr_3$ NPl dimensions, this method is helpful to quickly track any change in the sample. Therefore, UV-visible spectra are taken before and after each ultrafast measurement to ensure the stability of the solution.

Cyclic voltammetry – The electrochemical measurements were performed according to the protocol reported previously for LHP nanocrystals.[70] Initially, 4 mL of CH_2Cl_2 (dried over 3 Å molecular sieves for 48 hours) was purged with N_2 for 15 minutes to remove dissolved oxygen. Then, 100 mg of tetrabutylammonium hexafluorophosphate electrolyte was dissolved by stirring under an N_2 atmosphere. A three electrode system was adopted: a platinum disk with a diameter of 1.4 mm as working electrode, Ag/AgCl wire as the quasi-reference electrode (QRE), and platinum wire as the counter electrode. The working electrode was polished with 100 µm alumina slurry, washed through cyclic voltammetry in H_2SO_4 0.5 M several times, rinsed with ultra-pure water and acetone, and dried under N_2 airflow before each experiment. The Ag/AgCl QRE was prepared by immersing an Ag wire (pre-cleaned with concentrated

HNO_3) in a solution of $FeCl_3$ 0.25 M in HCl 0.20 M for 5 minutes. The electrode potential was calibrated by CV with a ferrocene standard (Appendix, **Figure A.1**, E_0 = 0.403 ± 0.003 V vs Normal Hydrogen Electrode). 150 µl of the NPl suspension was directly added to the electrochemical cell and stirred for 5 seconds before the measurements. CV experiments were performed from -2.2 to 1.6 V vs $Fc^{0/+}$ with a scan rate of 50 $mV.s^{-1}$. All these electrochemical experiments were carried out with a potentiostat/galvanostat (Multi Autolab PGSTAT 101, Metrohm/Ecochemie).

Steady-state and ns PL – Steady-state PL and TCSPC measurements were carried out on a Horiba Jobin Yvon Fluorolog-3 instrument and are suitable to assess the reliability and calibration of the FLUPS signal. The excitation source for the TCSPC measurements was a nanoLED N-390, which had a repetition rate of 1 MHz, a pulse duration of 1.3 ns and an excitation wavelength of 390 nm. The transient PL was detected with a PMT set at 90° relative to the excitation source.

Ultrafast characterization – Broadband FLUPS and TA measurements were acquired with the setups described in sections 2.1.4 and 2.2.1. Here, the excitation wavelength was generated by frequency-doubling the Ti:sapphire laser output (λ_{exc} = 400 nm and 389 nm for FLUPS and TA, respectively). To only consider the population dynamics, the pump beams were set to the magic angle (54.7°). The beams were attenuated to 22 $\mu J/cm^2$ at the sample position. The dynamics were taken from -1 ps to 1.2 ns with time steps increasing from 0.02 ps to 20 ps. Generally, in these experimental conditions, the temporal resolution of the instruments are 200 fs and 250 fs for FLUPS and TA, respectively.

Bibliography

[1] Vale, B. R. C.; Socie, E.; Burgos-Caminal, A.; Bettini, J.; Schiavon, M. A.; Moser, J.-E. Exciton, Biexciton, and Hot Exciton Dynamics in $CsPbBr_3$ Colloidal Nanoplatelets. *J. Phys. Chem. Lett.* **2019**, *11*, 387–394.

[2] Socie, E.; Vale, B. R. C.; Burgos-Caminal, A.; Moser, J. Direct Observation of Shallow Trap States in Thermal Equilibrium with Band-Edge Excitons in Strongly Confined $CsPbBr_3$ Perovskite Nanoplatelets. *Adv. Opt. Mater.* **2020**, 2001308.

[3] Grätzel, M. The light and shade of perovskite solar cells. *Nat. Mater.* **2014**, *13*, 838–842.

[4] Grätzel, M. The Rise of Highly Efficient and Stable Perovskite Solar Cells. *Acc. Chem. Res.* **2017**, *50*, 487–491.

[5] Saliba, M.; Correa-Baena, J.-P.; Grätzel, M.; Hagfeldt, A.; Abate, A. Perovskite Solar Cells: From the Atomic Level to Film Quality and Device Performance. *Angew. Chem. Int. Ed.* **2018**, *57*, 2554–2569.

[6] NREL, Best Research-Cell Efficiency Chart | Photovoltaic Research. 2022; https://www.nrel.gov/pv/cell-efficiency.html (accessed on 03/03/2022).

[7] Xu, J.; Li, X.; Xiong, J.; Yuan, C.; Semin, S.; Rasing, T.; Bu, X. Halide Perovskites for Nonlinear Optics. *Adv. Mater.* **2020**, *32*, 1806736.

[8] Lin, Y.-H. et al. Deciphering photocarrier dynamics for tuneable high-performance perovskite-organic semiconductor heterojunction phototransistors. *Nat. Commun.* **2019**, *10*.

[9] Kang, C. H.; Dursun, I.; Liu, G.; Sinatra, L.; Sun, X.; Kong, M.; Pan, J.; Maity, P.; Ooi, E.-N.; Ng, T. K.; Mohammed, O. F.; Bakr, O. M.; Ooi, B. S. High-speed colour-converting photodetector with all-inorganic $CsPbBr_3$ perovskite nanocrystals for ultraviolet light communication. *Light Sci. Appl.* **2019**, *8*.

[10] Gong, M.; Sakidja, R.; Goul, R.; Ewing, D.; Casper, M.; Stramel, A.; Elliot, A.; Wu, J. Z. High-Performance All-Inorganic $CsPbCl_3$ Perovskite Nanocrystal Photodetectors with Superior Stability. *ACS Nano* **2019**, *13*, 1772–1783.

[11] Lin, K. et al. Perovskite light-emitting diodes with external quantum efficiency exceeding 20 per cent. *Nature* **2018**, *562*, 245–248.

[12] Chiba, T.; Hayashi, Y.; Ebe, H.; Hoshi, K.; Sato, J.; Sato, S.; Pu, Y.-J.; Ohisa, S.; Kido, J. Anion-exchange red perovskite quantum dots with ammonium iodine salts for highly efficient light-emitting devices. *Nat. Photonics* **2018**, *12*, 681–687.

[13] Cao, Y. et al. Perovskite light-emitting diodes based on spontaneously formed submicrometre-scale structures. *Nature* **2018**, *562*, 249–253.

[14] Protesescu, L.; Yakunin, S.; Bodnarchuk, M. I.; Krieg, F.; Caputo, R.; Hendon, C. H.; Yang, R. X.; Walsh, A.; Kovalenko, M. V. Nanocrystals of Cesium Lead Halide Perovskites ($CsPbX_3$, X = Cl, Br, and I): Novel Optoelectronic Materials Showing Bright Emission with Wide Color Gamut. *Nano Lett.* **2015**, *15*, 3692–3696.

[15] Maes, J.; Balcaen, L.; Drijvers, E.; Zhao, Q.; De Roo, J.; Vantomme, A.; Vanhaecke, F.; Geiregat, P.; Hens, Z. Light Absorption Coefficient of $CsPbBr_3$ Perovskite Nanocrystals. *J. Phys. Chem. Lett.* **2018**, *9*, 3093–3097.

[16] Di Stasio, F.; Christodoulou, S.; Huo, N.; Konstantatos, G. Near-Unity Photoluminescence Quantum Yield in $CsPbBr_3$ Nanocrystal Solid-State Films via Postsynthesis Treatment with Lead Bromide. *Chem. Mater.* **2017**, *29*, 7663–7667.

[17] Shamsi, J.; Dang, Z.; Bianchini, P.; Canale, C.; Di Stasio, F.; Brescia, R.; Prato, M.; Manna, L. Colloidal Synthesis of Quantum Confined Single Crystal $CsPbBr_3$ Nanosheets with Lateral Size Control up to the Micrometer Range. *J. Am. Chem. Soc.* **2016**, *138*, 7240–7243.

[18] Gramlich, M.; Bohn, B. J.; Tong, Y.; Polavarapu, L.; Feldmann, J.; Urban, A. S. Thickness-Dependence of Exciton–Exciton Annihilation in Halide Perovskite Nanoplatelets. *J. Phys. Chem. Lett.* **2020**, *11*, 5361–5366.

[19] Bohn, B. J.; Tong, Y.; Gramlich, M.; Lai, M. L.; Döblinger, M.; Wang, K.; Hoye, R. L. Z.; Müller-Buschbaum, P.; Stranks, S. D.; Urban, A. S.; Polavarapu, L.; Feldmann, J. Boosting Tunable Blue Luminescence of Halide Perovskite Nanoplatelets through Postsynthetic Surface Trap Repair. *Nano Lett.* **2018**, *18*, 5231–5238.

[20] Ravi, V. K.; Swarnkar, A.; Chakraborty, R.; Nag, A. Excellent green but less impressive blue luminescence from $CsPbBr_3$ perovskite nanocubes and nanoplatelets. *Nanotechnology* **2016**, *27*, 325708.

[21] Peng, L.; Geng, J.; Ai, L.; Zhang, Y.; Xie, R.; Yang, W. Room temperature synthesis of ultra-small, near-unity single-sized lead halide perovskite quantum dots with wide color emission tunability, high color purity and high brightness. *Nanotechnology* **2016**, *27*, 335604.

[22] Butkus, J.; Vashishtha, P.; Chen, K.; Gallaher, J. K.; Prasad, S. K. K.; Metin, D. Z.; Laufersky, G.; Gaston, N.; Halpert, J. E.; Hodgkiss, J. M. The Evolution of Quantum Confinement in $CsPbBr_3$ Perovskite Nanocrystals. *Chem. Mater.* **2017**, *29*, 3644–3652.

[23] Li, Q.; Lian, T. Ultrafast Charge Separation in Two-Dimensional $CsPbBr_3$ Perovskite Nanoplatelets. *J. Phys. Chem. Lett.* **2019**, *10*, 566–573.

[24] Li, Q.; Yang, Y.; Que, W.; Lian, T. Size- and Morphology-Dependent Auger Recombination in $CsPbBr_3$ Perovskite Two-Dimensional Nanoplatelets and One-Dimensional Nanorods. *Nano Lett.* **2019**, *19*, 5620–5627.

[25] Marjit, K.; Ghosh, G.; Ghosh, S.; Sain, S.; Ghosh, A.; Patra, A. Structural Analysis and Carrier Relaxation Dynamics of 2D $CsPbBr_3$ Nanoplatelets. *J. Phys. Chem. C* **2021**, *125*, 12214–12223.

[26] Yang, D.; Zou, Y.; Li, P.; Liu, Q.; Wu, L.; Hu, H.; Xu, Y.; Sun, B.; Zhang, Q.; Lee, S.-T. Large-scale synthesis of ultrathin cesium lead bromide perovskite nanoplates with precisely tunable dimensions and their application in blue light-emitting diodes. *Nano Energy* **2018**, *47*, 235–242.

[27] Weidman, M. C.; Seitz, M.; Stranks, S. D.; Tisdale, W. A. Highly Tunable Colloidal Perovskite Nanoplatelets through Variable Cation, Metal, and Halide Composition. *ACS Nano* **2016**, *10*, 7830–7839.

[28] Maity, P.; Dana, J.; Ghosh, H. N. Multiple Charge Transfer Dynamics in Colloidal $CsPbBr_3$ Perovskite Quantum Dots Sensitized Molecular Adsorbate. *J. Phys. Chem. C* **2016**, *120*, 18348–18354.

[29] De, A.; Mondal, N.; Samanta, A. Hole Transfer Dynamics from Photoexcited Cesium Lead Halide Perovskite Nanocrystals: 1-Aminopyrene as Hole Acceptor. *J. Phys. Chem. C* **2018**, *122*, 13617–13623.

[30] Begum, R.; Parida, M. R.; Abdelhady, A. L.; Murali, B.; Alyami, N. M.; Ahmed, G. H.; Hedhili, M. N.; Bakr, O. M.; Mohammed, O. F. Engineering Interfacial Charge Transfer in $CsPbBr_3$ Perovskite Nanocrystals by Heterovalent Doping. *J. Am. Chem. Soc.* **2017**, *139*, 731–737.

[31] Wu, Y.; Wei, C.; Li, X.; Li, Y.; Qiu, S.; Shen, W.; Cai, B.; Sun, Z.; Yang, D.; Deng, Z.; Zeng, H. In Situ Passivation of $PbBr_6^{4-}$ Octahedra toward Blue Luminescent $CsPbBr_3$ Nanoplatelets with Near 100% Absolute Quantum Yield. *ACS Energy Lett.* **2018**, *3*, 2030–2037.

[32] Li, J.; Luo, L.; Huang, H.; Ma, C.; Ye, Z.; Zeng, J.; He, H. 2D Behaviors of Excitons in Cesium Lead Halide Perovskite Nanoplatelets. *J. Phys. Chem. Lett.* **2017**, *8*, 1161–1168.

[33] Ha, S. K.; Mauck, C. M.; Tisdale, W. A. Toward Stable Deep-Blue Luminescent Colloidal Lead Halide Perovskite Nanoplatelets: Systematic Photostability Investigation. *Chem. Mater.* **2019**, *31*, 2486–2496.

[34] Shukla, A.; Kaur, G.; Babu, K. J.; Ghorai, N.; Goswami, T.; Kaur, A.; Ghosh, H. N. Effect of Confinement on the Exciton and Biexciton Dynamics in Perovskite 2D-Nanosheets and 3D-Nanocrystals. *J. Phys. Chem. Lett.* **2020**, *11*, 6344–6352.

[35] Vonk, S. J. W.; Fridriksson, M. B.; Hinterding, S. O. M.; Mangnus, M. J. J.; van Swieten, T. P.; Grozema, F. C.; Rabouw, F. T.; van der Stam, W. Trapping and Detrapping in Colloidal Perovskite Nanoplatelets: Elucidation and Prevention of Nonradiative Processes through Chemical Treatment. *J. Phys. Chem. C* **2020**, *124*, 8047–8054.

[36] Chirvony, V. S.; González-Carrero, S.; Suárez, I.; Galian, R. E.; Sessolo, M.; Bolink, H. J.; Martínez-Pastor, J. P.; Pérez-Prieto, J. Delayed Luminescence in Lead Halide Perovskite Nanocrystals. *J. Phys. Chem. C* **2017**, *121*, 13381–13390.

[37] Chirvony, V. S.; Sekerbayev, K. S.; Pashaei Adl, H.; Suárez, I.; Taurbayev, Y. T.; Gualdrón-Reyes, A. F.; Mora-Seró, I.; Martínez-Pastor, J. P. Interpretation of the photoluminescence decay kinetics in metal halide perovskite nanocrystals and thin polycrystalline films. *J. Lumin.* **2020**, *221*, 117092.

[38] Liu, A.; Bonato, L. G.; Sessa, F.; Almeida, D. B.; Isele, E.; Nagamine, G.; Zagonel, L. F.; Nogueira, A. F.; Padilha, L. A.; Cundiff, S. T. Effect of dimensionality on the optical absorption properties of $CsPbI_3$ perovskite nanocrystals. *J. Chem. Phys.* **2019**, *151*, 191103.

[39] Scott, R.; Prudnikau, A. V.; Antanovich, A.; Christodoulou, S.; Riedl, T.; Bertrand, G. H. V.; Owschimikow, N.; Lindner, J. K. N.; Hens, Z.; Moreels, I.; Artemyev, M.; Woggon, U.; Achtstein, A. W. A comparative study demonstrates strong size tunability of carrier–phonon coupling in CdSe-based 2D and 0D nanocrystals. *Nanoscale* **2019**, *11*, 3958–3967.

[40] Kelley, A. M. Electron-Phonon Coupling in CdSe Nanocrystals. *J. Phys. Chem. Lett.* **2010**, *1*, 1296–1300.

[41] Achtstein, A. W.; Schliwa, A.; Prudnikau, A.; Hardzei, M.; Artemyev, M. V.; Thomsen, C.; Woggon, U. Electronic Structure and Exciton–Phonon Interaction in Two-Dimensional Colloidal CdSe Nanosheets. *Nano Lett.* **2012**, *12*, 3151–3157.

[42] Brennan, M. C.; Herr, J. E.; Nguyen-Beck, T. S.; Zinna, J.; Draguta, S.; Rouvimov, S.; Parkhill, J.; Kuno, M. Origin of the Size-Dependent Stokes Shift in $CsPbBr_3$ Perovskite Nanocrystals. *J. Am. Chem. Soc.* **2017**, *139*, 12201–12208.

[43] Wright, A. D.; Milot, R. L.; Eperon, G. E.; Snaith, H. J.; Johnston, M. B.; Herz, L. M. Band-Tail Recombination in Hybrid Lead Iodide Perovskite. *Adv. Funct. Mater.* **2017**, *27*, 1700860.

[44] Li, J.; Gan, L.; Fang, Z.; He, H.; Ye, Z. Bright Tail States in Blue-Emitting Ultrasmall Perovskite Quantum Dots. *J. Phys. Chem. Lett.* **2017**, *8*, 6002–6008.

[45] Mondal, A.; Aneesh, J.; Kumar Ravi, V.; Sharma, R.; Mir, W. J.; Beard, M. C.; Nag, A.; Adarsh, K. V. Ultrafast exciton many-body interactions and hot-phonon bottleneck in colloidal cesium lead halide perovskite nanocrystals. *Phys. Rev. B* **2018**, *98*, 115418.

[46] Makarov, N. S.; Guo, S.; Isaienko, O.; Liu, W.; Robel, I.; Klimov, V. I. Spectral and Dynamical Properties of Single Excitons, Biexcitons, and Trions in Cesium–Lead-Halide Perovskite Quantum Dots. *Nano Lett.* **2016**, *16*, 2349–2362.

[47] Castañeda, J. A.; Nagamine, G.; Yassitepe, E.; Bonato, L. G.; Voznyy, O.; Hoogland, S.; Nogueira, A. F.; Sargent, E. H.; Cruz, C. H. B.; Padilha, L. A. Efficient Biexciton Interaction in Perovskite Quantum Dots Under Weak and Strong Confinement. *ACS Nano* **2016**, *10*, 8603–8609.

[48] Xu, Y.; Chen, Q.; Zhang, C.; Wang, R.; Wu, H.; Zhang, X.; Xing, G.; Yu, W. W.; Wang, X.; Zhang, Y.; Xiao, M. Two-Photon-Pumped Perovskite Semiconductor Nanocrystal Lasers. *J. Am. Chem. Soc.* **2016**, *138*, 3761–3768.

[49] Yu, W. W.; Qu, L.; Guo, W.; Peng, X. Experimental Determination of the Extinction Coefficient of CdTe, CdSe, and CdS Nanocrystals. *Chem. Mater.* **2003**, *15*, 2854–2860.

[50] Bouduban, M. E. F.; Burgos-Caminal, A.; Ossola, R.; Teuscher, J.; Moser, J.-E. Energy and charge transfer cascade in methylammonium lead bromide perovskite nanoparticle aggregates. *Chem. Sci.* **2017**, *8*, 4371–4380.

[51] Yuan, M.; Quan, L. N.; Comin, R.; Walters, G.; Sabatini, R.; Voznyy, O.; Hoogland, S.; Zhao, Y.; Beauregard, E. M.; Kanjanaboos, P.; Lu, Z.; Kim, D. H.; Sargent, E. H. Perovskite energy funnels for efficient light-emitting diodes. *Nat. Nanotechnol.* **2016**, *11*, 872–877.

[52] Williams, O. F.; Guo, Z.; Hu, J.; Yan, L.; You, W.; Moran, A. M. Energy transfer mechanisms in layered 2D perovskites. *J. Chem. Phys.* **2018**, *148*, 134706.

[53] Sarkar, S.; Banerjee, S.; Swarnkar, A.; Mandal, P. Effect of Capping Ligand Engineering on Transport Properties and Carrier Dynamics in Cubic $CsPbI_3$ Nanocrystal Film. *J. Phys. Chem. C* **2021**, *125*, 10539–10548.

[54] Rossi, D.; Wang, H.; Dong, Y.; Qiao, T.; Qian, X.; Son, D. H. Light-Induced Activation of Forbidden Exciton Transition in Strongly Confined Perovskite Quantum Dots. *ACS Nano* **2018**, *12*, 12436–12443.

[55] Li, Y.; Lai, R.; Luo, X.; Liu, X.; Ding, T.; Lu, X.; Wu, K. On the absence of a phonon bottleneck in strongly confined $CsPbBr_3$ perovskite nanocrystals. *Chem. Sci.* **2019**, *10*, 5983–5989.

[56] Mondal, N.; De, A.; Das, S.; Paul, S.; Samanta, A. Ultrafast carrier dynamics of metal halide perovskite nanocrystals and perovskite-composites. *Nanoscale* **2019**, *11*, 9796–9818.

[57] Grisorio, R.; Di Clemente, M. E.; Fanizza, E.; Allegretta, I.; Altamura, D.; Striccoli, M.; Terzano, R.; Giannini, C.; Irimia-Vladu, M.; Suranna, G. P. Exploring the surface chemistry of cesium lead halide perovskite nanocrystals. *Nanoscale* **2019**, *11*, 986–999.

[58] Kidokoro, K.; Iso, Y.; Isobe, T. Complete self-recovery of photoluminescence of photodegraded cesium lead bromide quantum dots. *J. Mater. Chem. C.* **2019**, *7*, 8546–8550.

[59] Pan, A.; He, B.; Fan, X.; Liu, Z.; Urban, J. J.; Alivisatos, A. P.; He, L.; Liu, Y. Insight into the Ligand-Mediated Synthesis of Colloidal $CsPbBr_3$ Perovskite Nanocrystals: The Role of Organic Acid, Base, and Cesium Precursors. *ACS Nano* **2016**, *10*, 7943–7954.

[60] Ravi, V. K.; Santra, P. K.; Joshi, N.; Chugh, J.; Singh, S. K.; Rensmo, H.; Ghosh, P.; Nag, A. Origin of the Substitution Mechanism for the Binding of Organic Ligands on the Surface of $CsPbBr_3$ Perovskite Nanocubes. *J. Phys. Chem. Lett.* **2017**, *8*, 4988–4994.

[61] Smock, S. R.; Williams, T. J.; Brutchey, R. L. Quantifying the Thermodynamics of Ligand Binding to $CsPbBr_3$ Quantum Dots. *Angew. Chem. Int. Ed.* **2018**, *57*, 11711–11715.

[62] Nenon, D. P.; Pressler, K.; Kang, J.; Koscher, B. A.; Olshansky, J. H.; Osowiecki, W. T.; Koc, M. A.; Wang, L.-W.; Alivisatos, A. P. Design Principles for Trap-Free $CsPbX_3$ Nanocrystals: Enumerating and Eliminating Surface Halide Vacancies with Softer Lewis Bases. *J. Am. Chem. Soc.* **2018**, *140*, 17760–17772.

[63] De Roo, J.; Ibáñez, M.; Geiregat, P.; Nedelcu, G.; Walravens, W.; Maes, J.; Martins, J. C.; Van Driessche, I.; Kovalenko, M. V.; Hens, Z. Highly Dynamic Ligand Binding and Light Absorption Coefficient of Cesium Lead Bromide Perovskite Nanocrystals. *ACS Nano* **2016**, *10*, 2071–2081.

[64] Wang, S.; Wang, W.; Donmez, S.; Xin, Y.; Mattoussi, H. Engineering Highly Fluorescent and Colloidally Stable Blue-Emitting $CsPbBr_3$ Nanoplatelets Using Polysalt/$PbBr_2$ Ligands. *Chem. Mater.* **2022**, *34*, 4924–4936.

[65] Zhang, X.; Chun Sun,; Zhang, Y.; Wu, H.; Ji, C.; Chuai, Y.; Wang, P.; Wen, S.; Zhang, C.; Yu, W. W. Bright Perovskite Nanocrystal Films for Efficient Light-Emitting Devices. *J. Phys. Chem. Lett.* **2016**, *7*, 4602–4610.

[66] Shynkarenko, Y.; Bodnarchuk, M. I.; Bernasconi, C.; Berezovska, Y.; Verteletskyi, V.; Ochsenbein, S. T.; Kovalenko, M. V. Direct Synthesis of Quaternary Alkylammonium-Capped Perovskite Nanocrystals for Efficient Blue and Green Light-Emitting Diodes. *ACS Energy Lett.* **2019**, *4*, 2703–2711.

[67] Zhang, L.; Liang, W.; Xu, L.; Zhu, M.; Wang, X.; Su, J.; Li, L.; Liu, N.; Zhang, Z.; Gao, Y. Room-temperature quaternary alkylammonium passivation toward morphology-controllable $CsPbBr_3$ nanocrystals with excellent luminescence and stability for white LEDs. *Chem. Eng. J.* **2021**, *417*, 129349.

[68] Koscher, B. A.; Swabeck, J. K.; Bronstein, N. D.; Alivisatos, A. P. Essentially Trap-Free $CsPbBr_3$ Colloidal Nanocrystals by Postsynthetic Thiocyanate Surface Treatment. *J. Am. Chem. Soc.* **2017**, *139*, 6566–6569.

[69] Nakahara, S.; Tahara, H.; Yumoto, G.; Kawawaki, T.; Saruyama, M.; Sato, R.; Teranishi, T.; Kanemitsu, Y. Suppression of Trion Formation in $CsPbBr_3$ Perovskite Nanocrystals by Postsynthetic Surface Modification. *J. Phys. Chem. C* **2018**, *122*, 22188–22193.

[70] Fonseca, A. F. V. d.; Vale, B. R. C.; Carvalho, T. A. d. S.; Bettini, J.; Pereira, A. C.; Schiavon, M. A. Charge Transfer Improvement after Solvent-Induced Phase Change in Type-I Cs_4PbBr_6@$CsPbBr_3$ Core–Shell Perovskites. *J. Phys. Chem. C* **2021**, *125*, 27363–27371.

Chapter 4

Early excited state dynamics in lead halide perovskite nanoplatelets

This chapter focuses on the charge carrier dynamics in strongly confined $CsPbBr_3$ NPls within the first few picoseconds. Firstly, a simplified model to fit the FLUPS and TA data is drawn and used to unveil the presence of shallow trap states, altering the PL dynamics. Secondly, the Stokes shifted emission is attributed to an ultrafast hole localization into confined hole states. Lastly, we show that photon recycling cannot be ignored for highly concentrated NPl solutions.

This chapter is based on the studies *"Direct Observation of Shallow Trap States in Thermal Equilibrium with Band-Edge Excitons in Strongly Confined $CsPbBr_3$ Perovskite Nanoplatelets"* [1] and *"Resonant Band-Edge Emissive States in Strongly Confined $CsPbBr_3$ Perovskite Nanoplatelets"* [2] with the participation of Dr. Vale in the experimental planning as well as Dr. Burgos-Caminal and Aaron Terpstra in the data analysis.

4.1 Introduction

Inorganic lead halide perovskite nanocrystals (PNCs) have gained interest in the scientific community over the last years. Here, the inorganic core is surrounded by long-chain organic capping ligands to control the NC size and shape, and passivate the surface states. With large band gap tunability, narrow photoluminescence (PL) linewidths and near 100% PLQY,[3–6] PNCs have become ideal candidates for light-emitting diodes (LED) and lasing applications.[7–11] In addition to their potential for optoelectronic applications, PNCs show complex photophysical behaviors making them fascinating for fundamental studies.[12–15] Compared to more traditional and widely studied three-dimensional nanocubes, the size of strongly confined PNCs, such as nanoplatelets (NPls), is reduced in one dimension, increasing the Coulomb interaction between the photogenerated charge carriers. Their exciton binding energies, of a few hundreds of meV,[16,17] overcome the thermal energy, resulting in stable and tightly bound electron-hole pairs. Furthermore, strongly confined PNCs have an increased surface-to-volume ratio, and their surface states become fundamental for the global charge carrier dynamics. So far, the PLQY of lead halide perovskite (LHP) NPls barely exceeds 50% because of the increased number of under-coordinated atoms at the surface acting as deep trap states.[18,19] The increased proportion of capping ligands at the surface also provides an additional pathway to dissipate the excess energy after photoexcitation: due to the rapid phonon transfer into the organic ligands, ultrafast charge carrier cooling rates have been reported for strongly confined PNCs, even under strong photoexcitation.[20]

During the last chapter, the synthesis of strongly confined $CsPbBr_3$ NPls has been detailed and their optical properties highlighted. Yet, some questions remain open: why are the dynamics assigned to excitons in the lowest excited state different when observed by transient absorption (TA) and fluorescence upconversion spectroscopy (FLUPS)? Besides, a 49 meV Stokes shift has been pointed out, indicating that different states are involved in the absorption and the emission processes. While, for bulk semiconductors, the Stokes shift is usually attributed to the vibrational relaxation to the lowest excited state, there is not such a continuum of states in NPls experiencing strong quantum confinement (at least around the exciton transition). What could explain this shift? Is it only due to the homogeneous particle size distribution?

Throughout this chapter, the aforementioned questions were addressed by connecting our ultrafast spectroscopic data with what has been reported in the literature. Firstly, we set up a model for fitting the TA and FLUPS signals at early time scales and unveiled the presence of shallow trap states close to the lowest excited state, giving rise to reversible exciton trapping. The location of the shallow states appears

to be directly affected by the nature of the capping ligands. Secondly, the discussion focused on the short-lived PL observed by FLUPS, which overlaps with the exciton absorption. It was attributed to the emission from excitons in the lowest excited state, while the main PL feature was assigned to the radiative recombination between electrons in the conduction band (CB) and holes in a confined state. A procedure to isolate the hole localization process was implemented, giving a time constant of 300 fs. It helps gaining insights for understanding the TA data, which are complicated by an overlap of multiple contributions. Finally, for highly concentrated NPl solutions, larger particles can re-absorb photons emitted by smaller ones, leading to an extended Stokes shift and a redshift of the PL. In $CsPbBr_3$ NPl colloidal solutions, photon recycling is an almost instantaneous process.

4.2 Results and discussion

4.2.1 Exciton trapping in shallow trap states

The characterization of fresh $CsPbBr_3$ NPls has been discussed in the last chapter. Standard TA and FLUPS two-dimensional (2D) spectra acquired at low fluence are shown in **Figure 3.4** and are similar for every batch prepared for these investigations. As mentioned earlier on, the PL dynamics exhibit a fast decay on a few picosecond time scale that is not visible by TA (**Figure 4.1.A**). To explain this difference, the physical processes underlying FLUPS and TA signals need to be understood. While the PL intensity observed by FLUPS is proportional to the population of a given emissive state, the ground state bleaching (GSB) probes the transition between the ground and the lowest excited states, whether they are emissive states or not. Accordingly, the fast decay in the PL may arise from a rapid transfer from excitons in the lowest excited states to localized shallow trap states. These shallow traps are, by nature, lying close to the lowest excited state (< 15 meV) and cannot be distinguished spectrally using TA spectroscopy. In this case, the thermal energy ($k_B\mathrm{T} = 25$ meV) is sufficient to allow de-trapping of excitons from the shallow traps back to the lowest excited state. The presence of trap states close to the band edge has already been introduced to explain the delayed luminescence observed in lead halide PNCs.[21,22] In addition, even if shallow trap states should not be as detrimental as mid-gap (deep) trap states for the NC-based device performances, they can induce PL intermittency or PL blinking.[23–26]

Here, a simplified model (**Figure 4.1.B**) is proposed to fit the experimental data and verify this assumption. The model applies to an ensemble of NPls excited with a low excitation intensity, $\langle N_\mathrm{x} \rangle < 0.2$, to avoid multi-excitonic events. Four states are considered: *0* the ground state, X_1 the lowest excited state, S the shallow trap state and D the deep trap state. After photoexcitation, the exciton population in

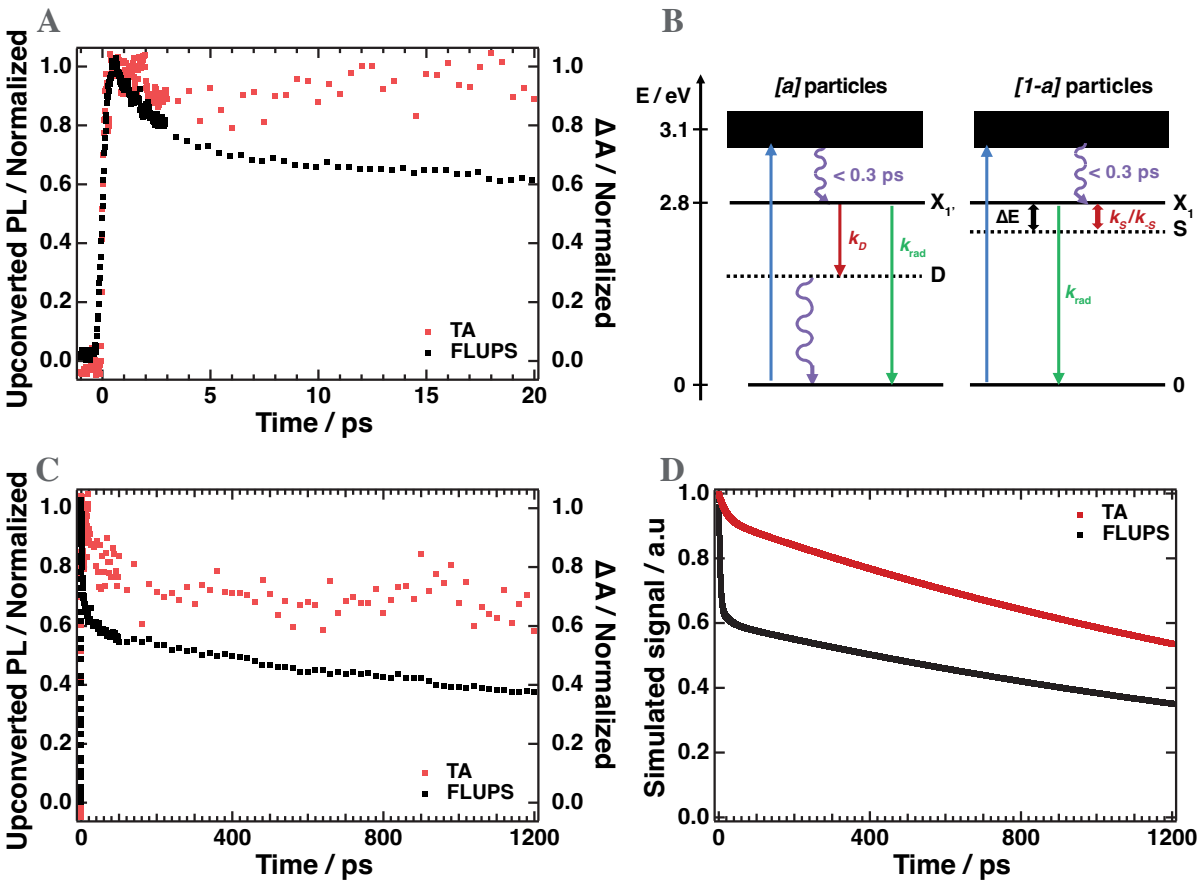

Figure 4.1: Normalized GSB and PL decays obtained by TA (λ_{GSB} = 448 nm) and FLUPS (λ_{PL} = 455 nm) at the A) picosecond and C) nanosecond time scale. B) Energy diagrams illustrating the model proposed in the text. D) Simulated TA and FLUPS signals obtained by analytically solving the model.

X_1 can 1) be trapped into S with a rate constant k_S [s^{-1}] (and de-trapped with a rate constant k_{-S}) [s^{-1}], 2) be trapped into D with a rate k_D [s^{-1}] (irreversible and leading to non-radiative recombination) or 3) recombine radiatively with a rate constant k_{rad} [s^{-1}]. Since $\tau_S = 1/k_S$ (a few picoseconds) and $\tau_D = 1/k_D$ (tens of picoseconds) are expected to be at least one order of magnitude different, the four states model could be simplified into two unrelated three-state ensembles to get analytical solutions. Hence, a proportion $N_{X_{1'}} = a$ of NPls without shallow trap states and $N_{X_1} = 1 - a$ of NPls without deep trap states are considered. Three energy levels are available for the first population set (labelled $X_{1'} - D{-}0$), and $X_1 - S{-}0$ are set for the NPls free of deep traps. As already expressed by Bohn et al.,[27] a gives the proportion of NPls having defects detrimental to the PL, most likely NPls with under-coordinated atoms at the surface. Finally, it is assumed that X_1 and S are in thermal equilibrium since the energy difference between the two states, ΔE [eV], is lower than the thermal energy $k_B \cdot T$ at room temperature (RT). Hence, the population distribution between X_1 and S follows a Maxwell-Boltzmann distribution, and the back transfer rate constant k_{-S} is related to k_S via **Equation 4.1**.

$$k_S = k_{-S} \cdot \exp\left(-\Delta E / k_B \cdot T\right) \tag{4.1}$$

Right after hot carrier relaxation, all photoexcited carriers should be in the lowest excited states. Consequently, the initial conditions are assumed to be $N_{X_1} + N_{X_{1'}} = 1$ and $N_S = N_D = 0$. Then, the evolution of the population of each state is given by:

$$\frac{dN_{X_1}}{dt} = -k_{\text{rad}} \cdot N_{X_1} - k_S \cdot N_{X_1} + k_{-S} \cdot N_S \tag{4.2}$$

$$\frac{dN_{X_{1'}}}{dt} = -k_{\text{rad}} \cdot N_{X_{1'}} - k_D \cdot N_{X_{1'}} \tag{4.3}$$

$$\frac{dN_S}{dt} = k_S \cdot N_{X_1} - k_{-S} \cdot N_S \tag{4.4}$$

$$\frac{dN_D}{dt} = k_D \cdot N_{X_{1'}} \tag{4.5}$$

In **Equation 4.5**, the non-radiative relaxation from D to 0 has been neglected because trapped excitons do not contribute to the TA or FLUPS signals. Finally, the PL intensity is only proportional to the sum of N_{X_1} and $N_{X_{1'}}$ while the TA signal is a combination of N_{X_1}, $N_{X_{1'}}$ and N_S since these states cannot be resolved spectrally (**Equations 4.6** and **4.7**).

$$\text{Sig}_{\text{FLUPS}} = N_{X_1} + N_{X_{1'}} \tag{4.6}$$

$$\text{Sig}_{\text{TA}} = N_{X_1} + N_{X_{1'}} + N_{X_S} \tag{4.7}$$

The simulated TA and FLUPS signals obtained by solving **Equations 4.1-4.5** follow the trend of the experimental data (**Figure 4.1, D**). Therefore, experimental data were fitted using the previous model for a) different surface passivation strategies and b) various NPl ages. The fitting procedure is described in the Appendices (section B.1).

To study the impact of the NPl surface on the charge carrier dynamics, $CsPbBr_3$ NPls with different surface passivation strategies were synthesized: 1) conventional (or "pristine") NPls with oleic acid (OA) and oleylamine (OAm) as capping ligands, 2) NPls treated with $ZnBr_2$ and 3) NPls with trioctylphosphine oxide (TOPO) substituting OAm. It has previously been shown that adding $ZnBr_2$ to the precursor solution brings an excess of Br^- ions, reducing the number of surface trap states and boosting the solution PLQY.[27,28] Besides, TOPO is believed to bind more strongly to the perovskite surface than OAm, therefore improving the NPl's long term stability.[4,29,30] **Figure 4.2** shows normalized PL decays and the best obtained fits, and **Table 4.1** summarizes the fitting parameters. Each sample displays similar rate

constants, with associated time constants of τ_S = 3-8 ps, τ_D = 21-35 ps and τ_{rad} = 1.2-1.4 ns for exciton trapping into shallow states, exciton trapping into mid-gap states and exciton radiative recombination, respectively. The trapping and recombination rates corroborate with previous reports,[3,21,22,27,31] and are close to the results obtained by fitting the data with a three-exponential decay function (chapter 3). It should be mentioned that τ_{rad} may be underestimated due to the short time window of the FLUPS instrumentation, which makes it impossible to record PL dynamics after 1.2 ns.

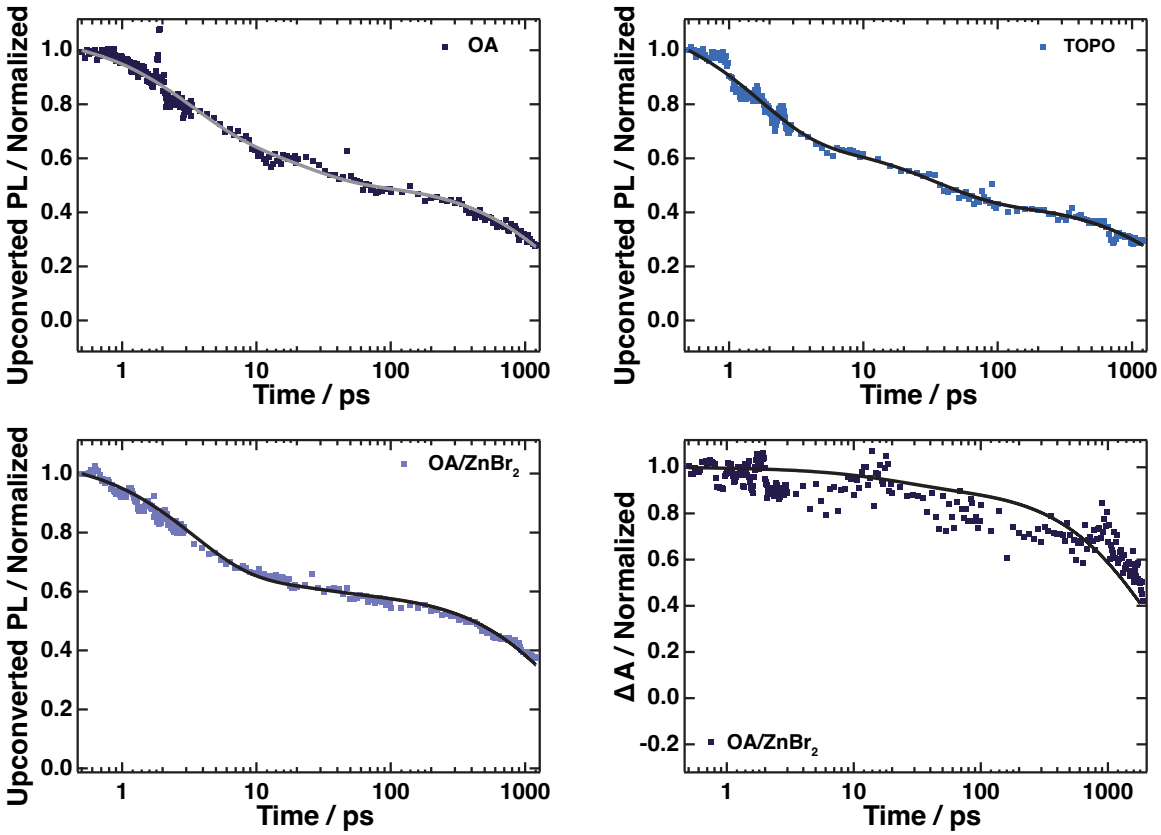

Figure 4.2: Normalized PL and GSB (bottom right) decays and best fits obtained with the proposed model for different surface passivation strategies.

Table 4.1: Parameters from the fits displayed in Figure 4.2.

Passivation strategy	k_S [s^{-1}]	k_D [s^{-1}]	k_{rad} [s^{-1}]	ΔE [meV]	a
Pristine	1.4×10^{11}	4.9×10^{10}	8.3×10^{8}	10	0.19
TOPO	3.2×10^{11}	2.9×10^{10}	7.7×10^{8}	-2	0.20
$ZnBr_2$	1.2×10^{11}	4.5×10^{10}	7.5×10^{8}	10	0.05

Besides, ΔE remains smaller than the thermal energy at RT for each sample and is close to the TA spectral resolution: around 445 nm, a difference of 10 meV induces a shift of 1.6 nm, which is less than 2 pixels of the CCD camera. Interestingly, substituting OAm by TOPO induces a change of ΔE and

imply that the nature of the ligands may shift the trap state location. More importantly, it means that shallow traps are formed, at least partially, by surface states. The simulations show that the traps could be slightly below (intraband) or above (interband) the lowest excited states. Still, further investigations should be conducted to evaluate these preliminary observations. For example, obtaining temperature-dependent early time PL dynamics may give crucial information on the trapping and de-trapping process. Finally, as discussed beforehand, treatment with an excess of Br^- ions reduces the percentage of NPls having deep trap states from 19 to 5%. As already argued, bromide ions can fill the halide vacancies at the surface, which is one of the primary sources of defects for strongly confined PNCs.[27,28]

The long-term stability of NPl colloidal solutions has been discussed in the previous chapter: the dynamic nature of ligand binding on the perovskite surface results in mid-gap trap states. Here, the simplified model is applied to monitor the effect of sample aging on the PL dynamics. The NPl colloidal solutions with a excess of bromide at the surface were stored for 80 days under ambient conditions, and ultrafast PL measurements were performed after 10, 20, 40, and 80 days (**Figure 4.3**). A global fitting procedure was applied on the FLUPS data to evaluate the five samples. The rate constants k_1, k_2, k_3 and the energy difference between S and X_1, ΔE, were fixed to the initial values found previously, while the percentage of NPls having deep trap states, a, was fitted. The results of the global fitting procedure are displayed in **Table 4.2**. According to the model, a increases from 0.05 for fresh solutions to 0.49 after 80 days. This result goes along with a decrease of the PL signal intensity at 1 ns and corroborates the last chapter's argumentation. Besides, experimental data deviate from the simulation for the two older solutions, where a becomes large. This is presumably due to an increased number of NPls having both shallow and deep trap states, giving rise to a competition between exciton de-trapping from S to X_1 with exciton trapping from X_1 (or S) to D, which is not taken into account in this simplified model.

Table 4.2: Parameters from the fits displayed in Figure 4.3.

Sample age	k_S [s^{-1}]	k_D [s^{-1}]	k_{rad} [s^{-1}]	ΔE [meV]	a
Fresh	1.2×10^{11}	4.5×10^{10}	7.5×10^{8}	10	0.05
10 days	1.2×10^{11}	4.5×10^{10}	7.5×10^{8}	10	0.22
20 days	1.2×10^{11}	4.5×10^{10}	7.5×10^{8}	10	0.28
40 days	1.2×10^{11}	4.5×10^{10}	7.5×10^{8}	10	0.38
80 days	1.2×10^{11}	4.5×10^{10}	7.5×10^{8}	10	0.49
Fresh (TA)	1.2×10^{11}	4.5×10^{10}	7.5×10^{8}	10	0.07

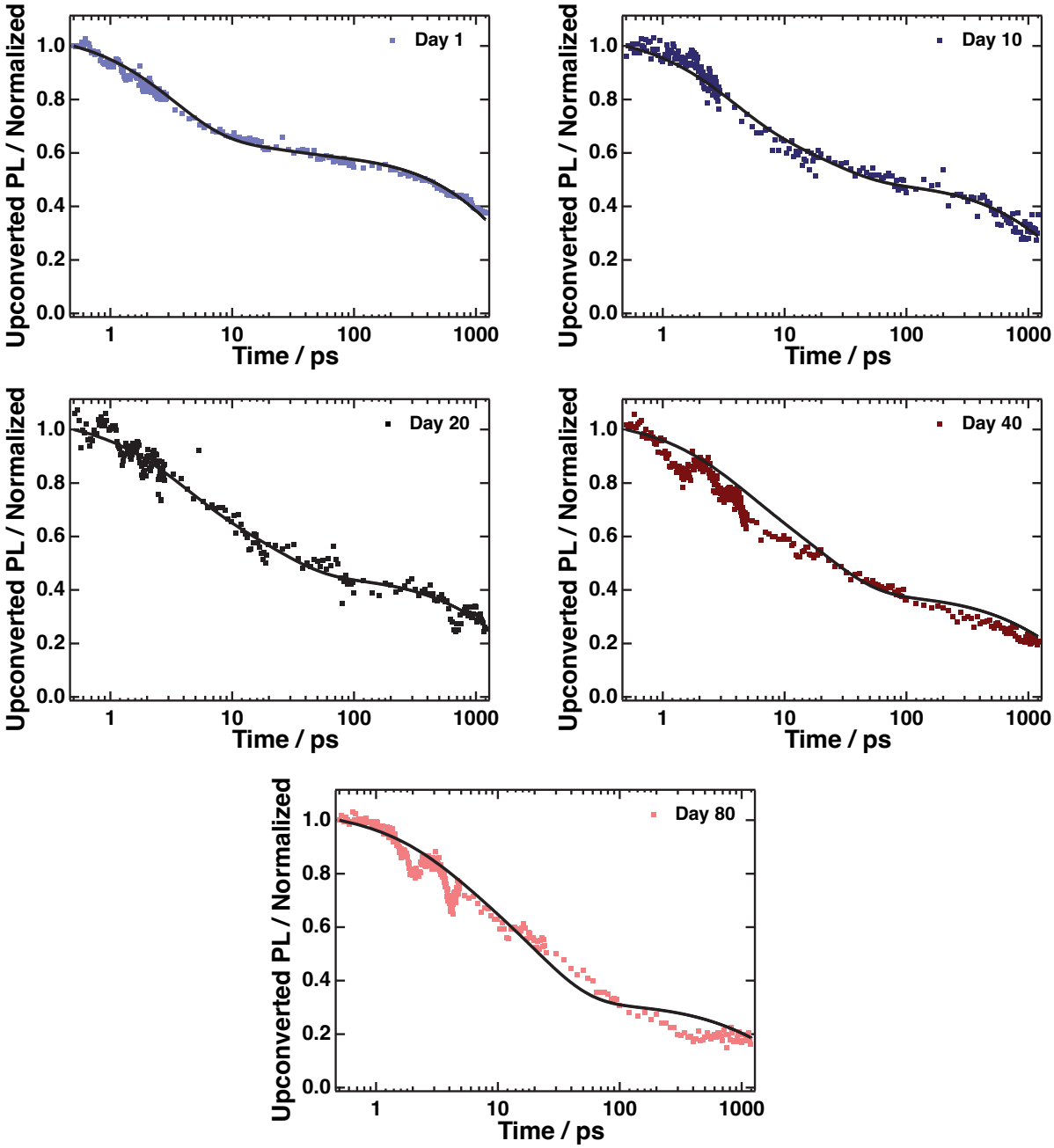

Figure 4.3: Normalized PL decays and best fits obtained with the proposed model for different NPl solution ages.

We have highlighted the effect of shallow trap states on the exciton dynamics but the nature of those states remains uncertain. In 2D perovskites it has been suggested that the exciton fine structure exhibit two peaks for so-called "bright" and "dark" excitons.[32,33] The dark states lie 8-10 meV below the bright ones and might also be responsible for the fast radiative decay observed by FLUPS. More recently, Gramlich et al.[34] have reported a thickness-dependent dark-bright exciton splitting in $CsPbBr_3$ NPls using magneto-optical spectroscopy and revealed a 18 meV shift for 3 ML, which is greater than the

values estimated here. At this point, it becomes crucial to investigate the temperature-dependent PL dynamics of the NPls to distinguish between extrinsic (presence of shallow trap) and intrinsic (exciton splitting) processes. Additional intensity dependence analysis might also be carried out to probe a state-filling effect which would reveal the presence of shallow traps.

4.2.2 Origin of the Stokes shifted emission

Last chapter raised a question about the 46 meV Stokes shift (ΔE_S) between the steady-state excitonic absorption and emission spectra of $CsPbBr_3$ NPls. The ΔE_S indicates that there are two different states involved in the absorption and the emission processes, which is puzzling since there is not a continuous band at 448 nm but localized exciton states. Several explanations have been raised in the literature to explain ΔE_S in weakly confined PNCs, such as photon recycling due to the broad size distribution,[35] formation of polarons inducing lattice relaxation,[36] and the presence of a confined hole state (CHS).[37] In the following paragraphs, these hypotheses will be investigated by combining FLUPS and TA data.

An elbow on the blue side of the emission peak is observed by FLUPS in the sub-picosecond time scale (**Figure 4.4a**) and vanishes within the first picosecond. By isolating this signal (the procedure is described in section 4.4.2), its shape is found to be close to the excitonic absorption with a maximum at λ = 445 nm. In addition, the decay of this peak matches the rise of the main emission with a time constant of τ_{CHS} = 0.3 ps (**Figure 4.4.B**). As shown in the Appendices (**Figure B.1**), the isolated signal is homogeneously broadened, indicating that only a unique population state is involved. The NPls were excited closer to the band edge to ascertain that the short-lived signal does not come from carrier relaxation, even though the charge carrier cooling is expected to be ultrafast for such experimental conditions (low excess energy and low exciton density).[20] The PL dynamics and spectral slices for λ_{exc} = 435 nm are shown in **Figure 4.4, C** and **D**. The dynamics at λ_{probe} = 455 nm remain unchanged by pumping close to the band edge, but the dynamics of the short-lived signal are impossible to track because of the overlap with the cross-correlation peak between the pump and the gate beam around t_0. Nevertheless, by increasing the pump intensity a lengthening of the blue-shifted PL is observed, alike for λ_{exc} = 400 nm (and will be discussed in chapter 5). Thus, the blue-shifted elbow is attributed to the radiative recombination of excitons in the lowest excited states, while the main emission comes from a relaxation from states located 50 meV below. These states have been previously assigned to CHSs,[37,38] which are dark in absorption due to a low density of states but bright in emission, explaining the size dependence of ΔE_S for PNCs. Brennan et al.[37] have shown that ΔE_S increases when the NC dimension decreases, which is explained by a continuous expansion of the band gap due to quantum confinement while the CHS energy levels remain constant. By fitting the lowest excited state and CHS dynamics

(Appendix, section B.1), a mono-exponential decay (or rise) time constant of 290 ± 20 fs is found, corresponding to the hole localization into the CHSs. So far, emission spectra do not present a spectral redshift which would be the signature of lattice-induced relaxation (or polaron formation). However, since the polaron formation in weakly confined PNCs is close to the FLUPS temporal resolution, it cannot be excluded yet.[39]

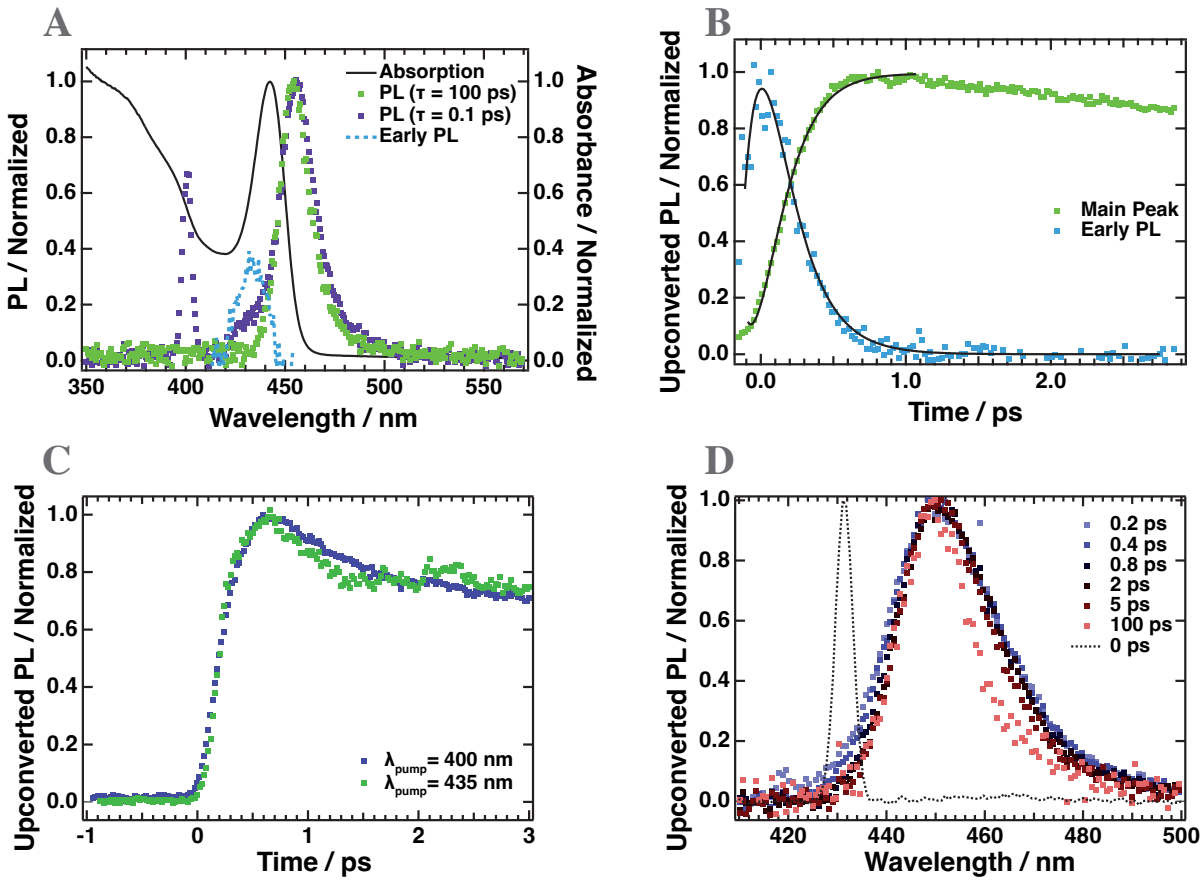

Figure 4.4: A) Absorption spectrum (black line), FLUPS spectral slices at $\tau_{\text{delay}} = 100$ ps (green dots) and $\tau_{\text{delay}} = 0.1$ ps (purple dots), and isolated band edge emission (blue dots). B) Normalized main emission ($\lambda_{\text{probe}} = 455$ nm) and isolated band edge emission ($\lambda_{\text{probe}} = 440$ nm) dynamics. C) Normalized main emission dynamics for NPl solutions excited at different wavelengths. D) FLUPS spectral slices for $\lambda_{\text{exc}} = 435$ nm and $\langle N_{\text{x}} \rangle = 3.3$.

We then tried to support the assumptions drawn in the previous paragraph by analyzing the more complex TA data, keeping in mind the time scale of the hole localization. **Figure 4.5, A** and **B** displays the evolution over the first few picoseconds of the three main contributions observed by TA under weak photoexcitation: GSB (450 nm), PIA-1 (440 nm) and PIA-2 (460 nm). There are three main points to be borne in mind: 1) a growth of GSB and PIA-1, 2) a decay of PIA-2, which is formed instantaneously upon photoexcitation and 3) a slight 2 nm (14 meV) redshift of the whole spectrum over less than a picosecond. After one picosecond, all features have reached a plateau before decaying with the time constants reported

in the last chapter. Interestingly, by fitting PIA-1 (PIA-2) with a convolution of a Gaussian function and a mono-exponential decay (rise) function, a time constant of $\tau = 0.29$ ps is obtained, similar than for the hole localization observed by FLUPS. To date, PIA-1 has been assigned to the forbidden exciton transition activated by the presence of an exciton at the lowest excited state, while the red-shifted PIA-2 signal has been linked to the biexcitonic Stark effect induced by Coulomb interaction between the exciton and all biexcitonic states.[40–42] For that reason, the decay of PIA-2 is often tracked to get information on the cooling process.[43,44] However, as already mentioned, charge carrier cooling in $CsPbBr_3$ NPls is expected to be faster than the temporal resolution of the TA setup ($\approx$ 200 fs), especially with a 400 meV excess of energy and at low carrier density.

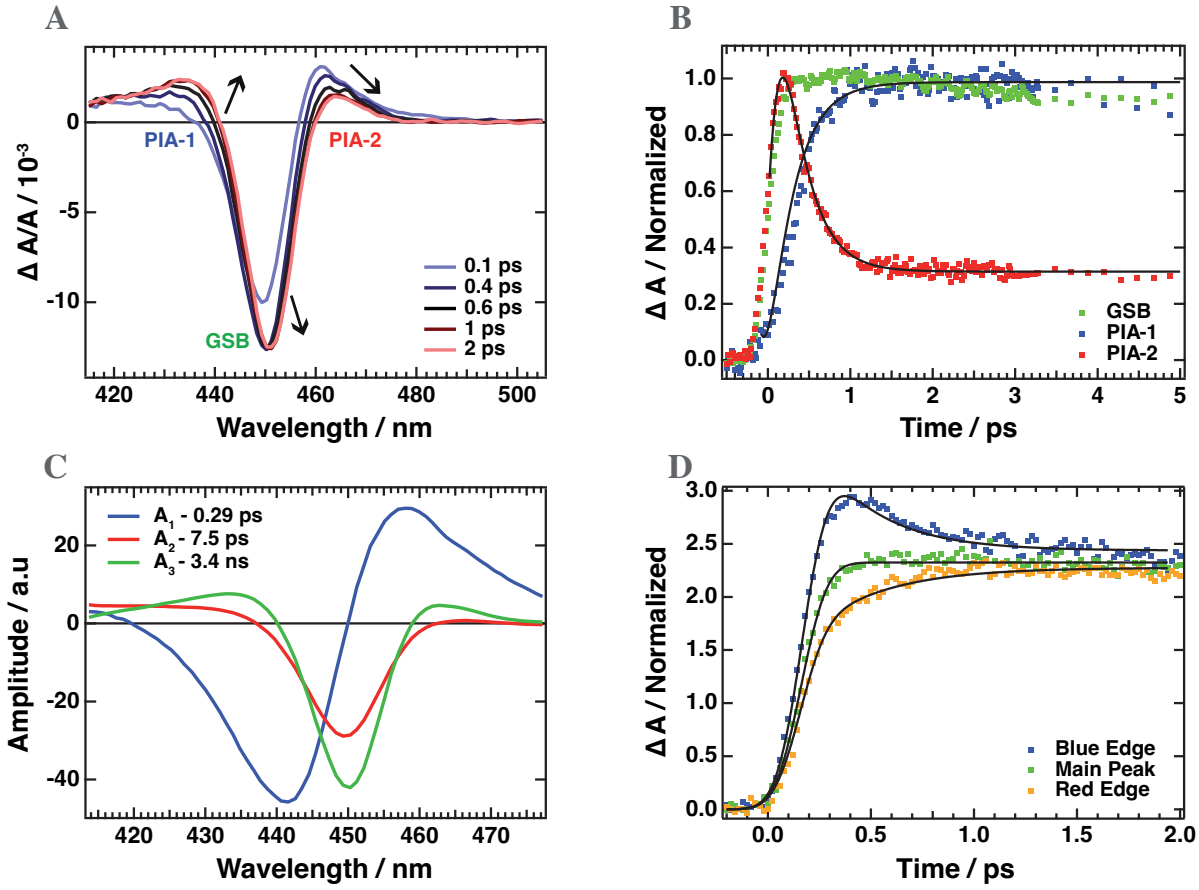

Figure 4.5: A) Early time scales TA spectral slices for $\lambda_{exc} = 389$ nm. B) GSB ($\lambda_{probe} = 450$ nm), PIA-1 ($\lambda_{probe} = 438$ nm) and PIA-2 ($\lambda_{probe} = 462$ nm) normalized dynamics. C) Decay associated spectra obtained by applying a global fitting procedure with a three-exponential decay function on the TA dynamics. D) Normalized, at $\tau_{delay} = 2.0$ ps, TA dynamics around the GSB maximum.

Another way to estimate the proportion of hot carriers in the system is to fit the blue tail of the TA spectrum and extract the carrier temperature (T_c).[45] The electron and hole temperatures are roughly the same since the effective masses of the charge carriers are similar in LHPs.[46,47] Considering an excess

energy of 400 meV, electrons and holes should have an initial $T_c = E/k_B = 2320$ K, where E and k_B are the excess energy per carrier [J] and the Boltzmann constant [J/K], respectively. By fitting the TA data at $\tau_{delay} = 200$ fs, the carrier temperature 350 K, which indicates the complete cooling of the charge carriers by this time delay (Appendix, **Figure B.2**). Hence, the decay of PIA-2 with a time constant of $\tau = 290$ fs cannot be assigned to charge carrier relaxation to the lowest excited state.

Besides, a global fitting procedure with a three-exponential decay function was performed on the TA data for λ = 415-480 nm to investigate the spectral dependence of the different processes. The decay associated spectra (**Figure 4.5.C**) associated to the fit show that A_1, linked to the fast component (τ_{CHS} = 0.29 ps), is positive around PIA-2 (λ_{max} = 455 nm) and negative around PIA-1 (λ_{min} = 444 nm), confirming what has been observed by fitting individual traces. Our interpretation is that PIA-2 has a predominant contribution from the Stark effect between "free" excitons produced by the pump and all biexcitonic states. Then, once photoexcited holes are localized into CHSs, the interaction between the two excitons is reduced, ultimately decreasing the PIA-2 signal intensity. Consequently, the decay lifetime of the PIA-2 peak is related to the hole localization time constant. Note that hole localization in CHSs should also induce a decay of the initial GSB signal with the same time constant, since the CB-VB transition is no longer blocked. However, as shown in **Figure 4.5.C**, the positive and negative components for A_1 overlap and cancel out around 448 nm, most probably because of the large bandwidths of the VB-CB and CHS-CB transitions. By shifting the probed wavelength to the blue (or red) side of the GSB, the VB-CB (or CHS-CB) transition is maximized, as shown in **Figure 4.5.D**. As expected, the decay of the signal at the blue edge matches the rise of the one on the red side, supporting the conclusion of a sub-picosecond hole localization from the lowest excited state. After one picosecond, all traces display the same dynamics (Appendix, **Figure B.3**), indicating that they are all correlated to the same state.

Some evidence for the localization of holes within the first picosecond have been shown, yet it cannot explain the final observation related to the small, 14 meV, spectral redshift (Appendix, **Figure B.4**). This value does not match the calculated ΔE_s, but is similar to the reported exciton-polaron interaction in confined LHP systems.[48] Similarly to what has been done for 2D $MAPbI_3$,[12] more focused investigations should be conducted to clarify the nature of the interaction between the perovskite lattice and the charge carriers in weakly confined $CsPbBr_3$ systems. The localization of holes at Br atoms has already been unveiled for weakly confined PNCs using time-resolved X-ray absorption spectroscopy.[49] This localization is ascribed to the formation of a small polaron, while electrons are delocalized in the CB. The structural distortion of the $PbBr_6$ octahedra is believed to arise from the 18 meV LO phonon mode in $CsPbBr_3$.[50] It remains unclear if and how polarons affect the charge carrier dynamics in such small systems. Rossi et al.

have argued that since the exciton wave function and the lattice distortion from polaron exist in the same volume, the influence of polaron is even greater than in weakly confined PNCs.[41] In opposition, Weidman et al.[16] have claimed that the polaron formation is incomplete in NPls due to their reduced dimensions. Therefore, additional investigations should be conducted to relate the hole localization process presented here with the polaron formation.

4.2.3 Efficient photon recycling for concentrated solutions

Some studies in the field have argued that photon recycling and energy transfer are the main reasons for the apparent Stokes shift observed in PNC aggregates or films.[35,51,52] However, colloidal solutions are likely to inhibit the energy transfer due to the inter-particle separation caused by the capping ligand shell.[53] Since the NPl size distribution is homogeneous, bigger particles, which have a narrower band gap, can re-absorb the photons emitted from smaller ones, enlarging the external ΔE_s. To ascertain that the previous observations are not a consequence of photon recycling, several NPl solutions with different concentrations were prepared. Because of the spatial overlap between particles for highly concentrated NPl solutions, these conditions should favor photon recycling and predict what could happen for NPl thin films. Here, four samples, NPl-0.3, NPl-0.5, NPl-1.2 and NPl-1.6, were prepared and labelled according to their absorbance at 400 nm (Appendix, **Figure B.5**). As expected, static absorption spectra do not show any noticeable shift after normalization (**Figure 4.6.A**). Even for the highest NPl concentration, the size distribution remains homogeneous, and there is no sign of aggregation. Nevertheless, the PL maximum is shifted by 8 nm between NPl-0.3 and NPl-1.6, extending the apparent ΔE_s from 46 meV to 93 meV. In addition, the relative intensity of the blue-shifted emission vanishes progressively from NPl-0.3 to NPl-1.6 (**Figure 4.6, C-F**). It is worth noting that the time constant for the hole confinement remains unaffected for NPl-0.3, NPl-0.5 and NPl-1.2 (**Figure 4.6.B**). It becomes clear that when the NPl concentration is high enough, the NPls experience photon recycling, akin to what has already been observed for films where the particle stacking is even more prominent.[35,54,55] In addition, the absence of PL spectral dynamics for NPl-1.6 indicates that the re-absorption process is faster than the temporal resolution of the FLUPS instrumentation ($<$ 150 fs). Since the time constant for photon recycling does not match the reported decay lifetime for the band edge emission, this further excludes the photon re-absorption process for being the cause of the Stokes shifted emission. To summarize, photon recycling may increase the external Stokes shift in highly concentrated NPl solutions but has only a minor or no impact at all in diluted solutions. Therefore, it becomes crucial to differentiate the external (observed) Stokes shift, which depends on the NC size distribution and concentration, with the intrinsic value, presumably arising from hole localization.

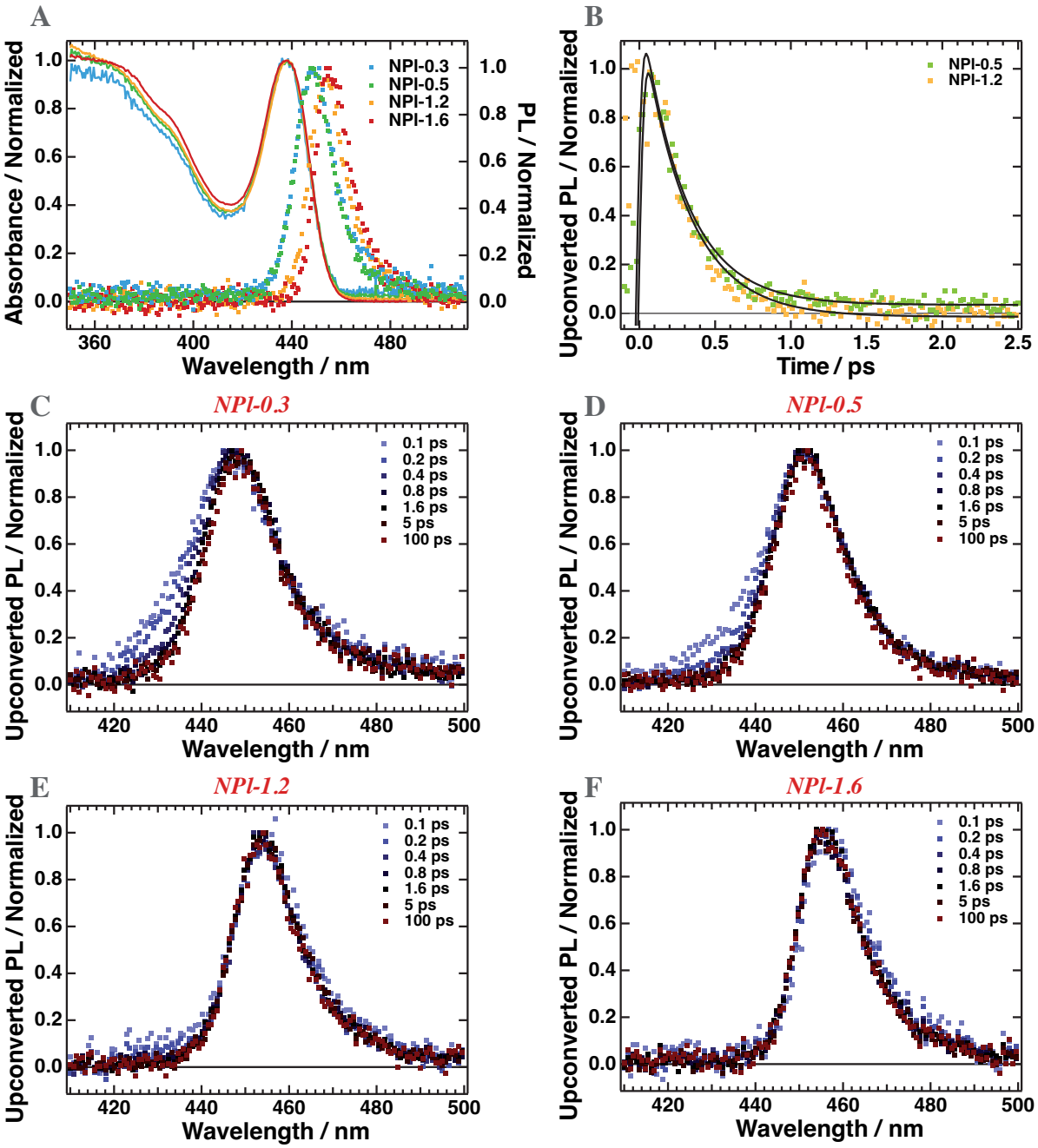

Figure 4.6: A) Normalized absorption (lines) and emission (dots) spectra for different NPl concentrations. B) Normalized band edge PL decays (λ_{probe} = 440 nm for NPl-0.5 and NPl-1.2 solutions. C-F) FLUPS spectral slices for different NPl concentrations.

4.3 Conclusion

The previous sections discussed the physical processes occurring in the first few picoseconds in freshly synthesized $CsPbBr_3$ NPls, combining multiple ultrafast spectroscopic techniques.

Firstly, it has been unveiled that the charge carrier dynamics are affected by the presence of traps states lying close to the lowest excited state. The exciton trapping to the dark states is fast, 3-8 ps, and reversible at RT, causing the lengthening of the overall PL decay.[21,56,57] The data were fitted by drawing a simplified model for an ensemble of uncorrelated NPls and highlighted the importance of the organic capping ligands on the trap state density and on the location of the shallow states. These results not only pointed out the importance of having control of the NPl surface chemistry to passivate trap states, but that a complete understanding of the trapping mechanism is crucial as well for improving device performances.

Secondly, the origin of the 49 meV Stokes shift between the excitonic absorption and the PL maximum was investigated. On the sub-picosecond time scales, the PL is a convolution of two emission peaks centered at 445 nm and 455 nm. The former was assigned to the recombination of excitons in the lowest excited state and decays quickly (τ_{CHS} = 300 fs) with the same time constant as the rise of the second, and more intense, feature. This transition was assigned to the rapid localization of band edge holes into CHSs, which are dark in absorption but bright in emission. The existence of CHSs has already been brought up by Brennan et al. to explain the Stokes shift dependence on the size of the PNCs.[37] Furthermore, even if the interpretation of TA data is challenging due to the overlap of multiple contributions with large bandwidths, a global fitting procedure was performed to demonstrate that the decay of the PIA-2 band, previously assigned to charge carrier cooling, is more likely due to the confinement of the holes into the CHSs. The predominant contribution of PIA-2 is the biexciton Stark effect between "free" excitons and excitons produced by the probe. Further investigations should be conducted to relate the hole localization process presented here with the polaron formation.

Finally, it has been showed that the external Stokes shift was increased by 50 meV for highly concentrated NPl solutions due to photon recycling. When the NPls are stacked together, the bigger particles, with narrower band gaps, can re-absorb the emitted photons from smaller ones, shifting the PL to the red. This effect has already been reported for PNC films[36,54] and is faster than the temporal resolution of the instrumentation ($<$ 150 fs).

In summary, these findings show the utility of combining ultrafast spectroscopic techniques for understanding the complex photophysical processes occurring in LHP NPls. However, this broad picture is only valid under weak photoexcitation for an ensemble of un-correlated excitons. For some applications, such as lasing, the exciton density increases and it is crucial to understand and predict carrier-carrier interactions. This will be the focus of the next chapter.

4.4 Methods

4.4.1 Sample preparation

For each set of measurements, the NPl solution was prepared according to the detailed procedure described during chapter 3. An excess of bromide on the surface was achieved by adding $ZnBr_2$ salt to the lead precursor solution. It has been previously showed that it helps reduce the number of surface trap states and increase the long term stability of the NPls. The samples were diluted in dodecane to obtain an absorbance of 0.5 at 400 nm in a 1 mm optical path quartz cuvette right before the spectroscopic measurement to avoid, as much as possible, ligand desorption from the NPl surface.

4.4.2 Experimental measurements and data treatment

Ultrafast characterization – Broadband FLUPS and TA measurements were performed with the setups described previously. For most of the experiments, the excitation wavelength (λ_{exc} = 400 nm and 389 nm for FLUPS and TA, respectively) was obtained by frequency-doubling the laser output, which gives the most stable beams. Additional FLUPS measurements were conducted using λ_{exc} = 435 nm to ascertain that the sub-picosecond time scales dynamics are not linked to the cooling of hot carriers. However, setting the excitation wavelength close to the probed region prevents quantitative analysis in the 425-445 nm region due to the cross-correlation between the transmitted pump beam and the gate at t_0.

Band edge emission isolation – A homemade procedure has been written to isolate the short-lived and blue shifted emission. Firstly, for each time delay, the spectral slices (PL_{norm}) were normalized at λ = 455 nm. Then, PL_{norm} (τ_{delay} = 0-20 ps) was subtracted from PL_{norm} at late times (τ_{delay} > 100 ps) to suppress the signal coming from the radiative recombination of single excitons in the lowest excited state. An average of 5 slices around τ_{delay} = 100 ps was used for the subtraction to increase the signal-to-noise ratio.

Bibliography

[1] Socie, E.; Vale, B. R. C.; Burgos-Caminal, A.; Moser, J. Direct Observation of Shallow Trap States in Thermal Equilibrium with Band-Edge Excitons in Strongly Confined $CsPbBr_3$ Perovskite Nanoplatelets. *Adv. Opt. Mater.* **2020**, 2001308.

[2] Socie, E.; Vale, B. R. C.; Terpstra, A. T.; Schiavon, M. A.; Moser, J.-E. Resonant Band-Edge Emissive States in Strongly Confined $CsPbBr_3$ Perovskite Nanoplatelets. *J. Phys. Chem. C* **2021**, *125*, 14317–14325.

[3] Li, Y.; Wang, X.; Xue, W.; Wang, W.; Zhu, W.; Zhao, L. Highly luminescent and stable $CsPbBr_3$ perovskite quantum dots modified by phosphine ligands. *Nano Res.* **2019**, *12*, 785–789.

[4] Ambroz, F.; Xu, W.; Gadipelli, S.; Brett, D. J. L.; Lin, C.-T.; Contini, C.; McLachlan, M. A.; Durrant, J. R.; Parkin, I. P.; Macdonald, T. J. Room Temperature Synthesis of Phosphine-Capped Lead Bromide Perovskite Nanocrystals without Coordinating Solvents. *Part. Part. Syst. Char.* **2020**, *37*, 1900391.

[5] Di Stasio, F.; Christodoulou, S.; Huo, N.; Konstantatos, G. Near-Unity Photoluminescence Quantum Yield in $CsPbBr_3$ Nanocrystal Solid-State Films via Postsynthesis Treatment with Lead Bromide. *Chem. Mater.* **2017**, *29*, 7663–7667.

[6] Koscher, B. A.; Swabeck, J. K.; Bronstein, N. D.; Alivisatos, A. P. Essentially Trap-Free $CsPbBr_3$ Colloidal Nanocrystals by Postsynthetic Thiocyanate Surface Treatment. *J. Am. Chem. Soc.* **2017**, *139*, 6566–6569.

[7] Xu, J.; Li, X.; Xiong, J.; Yuan, C.; Semin, S.; Rasing, T.; Bu, X. Halide Perovskites for Nonlinear Optics. *Adv. Mater.* **2020**, *32*, 1806736.

[8] Lin, Y.-H. et al. Deciphering photocarrier dynamics for tuneable high-performance perovskite-organic semiconductor heterojunction phototransistors. *Nat. Commun.* **2019**, *10*.

[9] Gong, M.; Sakidja, R.; Goul, R.; Ewing, D.; Casper, M.; Stramel, A.; Elliot, A.; Wu, J. Z. High-Performance All-Inorganic $CsPbCl_3$ Perovskite Nanocrystal Photodetectors with Superior Stability. *ACS Nano* **2019**, *13*, 1772–1783.

[10] Lin, K. et al. Perovskite light-emitting diodes with external quantum efficiency exceeding 20 per cent. *Nature* **2018**, *562*, 245–248.

[11] Chiba, T.; Hayashi, Y.; Ebe, H.; Hoshi, K.; Sato, J.; Sato, S.; Pu, Y.-J.; Ohisa, S.; Kido, J. Anion-exchange red perovskite quantum dots with ammonium iodine salts for highly efficient light-emitting devices. *Nat. Photonics* **2018**, *12*, 681–687.

[12] Srimath Kandada, A. R.; Silva, C. Exciton Polarons in Two-Dimensional Hybrid Metal-Halide Perovskites. *J. Phys. Chem. Lett.* **2020**, *11*, 3173–3184.

[13] Saran, R.; Heuer-Jungemann, A.; Kanaras, A. G.; Curry, R. J. Giant Bandgap Renormalization and Exciton–Phonon Scattering in Perovskite Nanocrystals. *Adv. Opt. Mater.* **2017**, *5*, 1700231.

[14] Chen, Y.; Liu, Y.; Hong, M. Cation-doping matters in caesium lead halide perovskite nanocrystals: from physicochemical fundamentals to optoelectronic applications. *Nanoscale* **2020**, *12*, 12228–12248.

[15] Li, J.; Luo, L.; Huang, H.; Ma, C.; Ye, Z.; Zeng, J.; He, H. 2D Behaviors of Excitons in Cesium Lead Halide Perovskite Nanoplatelets. *J. Phys. Chem. Lett.* **2017**, *8*, 1161–1168.

[16] Weidman, M. C.; Goodman, A. J.; Tisdale, W. A. Colloidal Halide Perovskite Nanoplatelets: An Exciting New Class of Semiconductor Nanomaterials. *Chem. Mater.* **2017**, *29*, 5019–5030.

[17] Shamsi, J.; Dang, Z.; Bianchini, P.; Canale, C.; Di Stasio, F.; Brescia, R.; Prato, M.; Manna, L. Colloidal Synthesis of Quantum Confined Single Crystal $CsPbBr_3$ Nanosheets with Lateral Size Control up to the Micrometer Range. *J. Am. Chem. Soc.* **2016**, *138*, 7240–7243.

[18] Ravi, V. K.; Swarnkar, A.; Chakraborty, R.; Nag, A. Excellent green but less impressive blue luminescence from $CsPbBr_3$ perovskite nanocubes and nanoplatelets. *Nanotechnology* **2016**, *27*, 325708.

[19] Wang, S.; Wang, W.; Donmez, S.; Xin, Y.; Mattoussi, H. Engineering Highly Fluorescent and Colloidally Stable Blue-Emitting $CsPbBr_3$ Nanoplatelets Using Polysalt/$PbBr_2$ Ligands. *Chem. Mater.* **2022**, *34*, 4924–4936.

[20] Gramlich, M.; Bohn, B. J.; Tong, Y.; Polavarapu, L.; Feldmann, J.; Urban, A. S. Thickness-Dependence of Exciton–Exciton Annihilation in Halide Perovskite Nanoplatelets. *J. Phys. Chem. Lett.* **2020**, *11*, 5361–5366.

[21] Chirvony, V. S.; González-Carrero, S.; Suárez, I.; Galian, R. E.; Sessolo, M.; Bolink, H. J.; Martínez-Pastor, J. P.; Pérez-Prieto, J. Delayed Luminescence in Lead Halide Perovskite Nanocrystals. *J. Phys. Chem. C* **2017**, *121*, 13381–13390.

[22] Chirvony, V. S.; Sekerbayev, K. S.; Pashaei Adl, H.; Suárez, I.; Taurbayev, Y. T.; Gualdrón-Reyes, A. F.; Mora-Seró, I.; Martínez-Pastor, J. P. Interpretation of the photoluminescence decay kinetics in metal halide perovskite nanocrystals and thin polycrystalline films. *J. Lumin.* **2020**, *221*, 117092.

[23] Cordones, A. A.; Leone, S. R. Mechanisms for charge trapping in single semiconductor nanocrystals probed by fluorescence blinking. *Chem. Soc. Rev.* **2013**, *42*, 3209.

[24] Gibson, N. A.; Koscher, B. A.; Alivisatos, A. P.; Leone, S. R. Excitation Intensity Dependence of Photoluminescence Blinking in $CsPbBr_3$ Perovskite Nanocrystals. *J. Phys. Chem. C* **2018**, *122*, 12106–12113.

[25] Yuan, G.; Gómez, D. E.; Kirkwood, N.; Boldt, K.; Mulvaney, P. Two Mechanisms Determine Quantum Dot Blinking. *ACS Nano* **2018**, *12*, 3397–3405.

[26] Ahmed, T.; Seth, S.; Samanta, A. Mechanistic Investigation of the Defect Activity Contributing to the Photoluminescence Blinking of $CsPbBr_3$ Perovskite Nanocrystals. *ACS Nano* **2019**, *13*, 13537–13544.

[27] Bohn, B. J.; Tong, Y.; Gramlich, M.; Lai, M. L.; Döblinger, M.; Wang, K.; Hoye, R. L. Z.; Müller-Buschbaum, P.; Stranks, S. D.; Urban, A. S.; Polavarapu, L.; Feldmann, J. Boosting Tunable Blue Luminescence of Halide Perovskite Nanoplatelets through Postsynthetic Surface Trap Repair. *Nano Lett.* **2018**, *18*, 5231–5238.

[28] Park, J.; Kim, Y.; Ham, S.; Woo, J. Y.; Kim, T.; Jeong, S.; Kim, D. A relationship between the surface composition and spectroscopic properties of cesium lead bromide ($CsPbBr_3$) perovskite nanocrystals: focusing on photoluminescence efficiency. *Nanoscale* **2020**, *12*, 1563–1570.

[29] Almeida, G.; Ashton, O. J.; Goldoni, L.; Maggioni, D.; Petralanda, U.; Mishra, N.; Akkerman, Q. A.; Infante, I.; Snaith, H. J.; Manna, L. The Phosphine Oxide Route toward Lead Halide Perovskite Nanocrystals. *J. Am. Chem. Soc.* **2018**, *140*, 14878–14886.

[30] Wu, L.; Zhong, Q.; Yang, D.; Chen, M.; Hu, H.; Pan, Q.; Liu, H.; Cao, M.; Xu, Y.; Sun, B.; Zhang, Q. Improving the Stability and Size Tunability of Cesium Lead Halide Perovskite Nanocrystals Using Trioctylphosphine Oxide as the Capping Ligand. *Langmuir* **2017**, *33*, 12689–12696.

[31] Wu, Y.; Wei, C.; Li, X.; Li, Y.; Qiu, S.; Shen, W.; Cai, B.; Sun, Z.; Yang, D.; Deng, Z.; Zeng, H. In Situ Passivation of $PbBr_6^{4-}$ Octahedra toward Blue Luminescent $CsPbBr_3$ Nanoplatelets with Near 100% Absolute Quantum Yield. *ACS Energy Lett.* **2018**, *3*, 2030–2037.

[32] Chen, L.; Li, B.; Zhang, C.; Huang, X.; Wang, X.; Xiao, M. Composition-Dependent Energy Splitting between Bright and Dark Excitons in Lead Halide Perovskite Nanocrystals. *Nano Lett.* **2018**, *18*, 2074–2080.

[33] Folpini, G.; Cortecchia, D.; Petrozza, A.; Kandada, A. R. S. The role of a dark exciton reservoir in the luminescence efficiency of two-dimensional tin iodide perovskites. *J. Mater. Chem. C* **2020**, *8*, 10889–10896.

[34] Gramlich, M.; Swift, M. W.; Lampe, C.; Lyons, J. L.; Döblinger, M.; Efros, A. L.; Sercel, P. C.; Urban, A. S. Dark and Bright Excitons in Halide Perovskite Nanoplatelets. *Advanced Science* **2022**, *9*, 2103013, _eprint: https://onlinelibrary.wiley.com/doi/pdf/10.1002/advs.202103013.

[35] Gan, Z.; Chen, W.; Yuan, L.; Cao, G.; Zhou, C.; Huang, S.; Wen, X.; Jia, B. External stokes shift of perovskite nanocrystals enlarged by photon recycling. *Appl. Phys. Lett.* **2019**, *114*, 011906.

[36] Guo, Y.; Yaffe, O.; Hull, T. D.; Owen, J. S.; Reichman, D. R.; Brus, L. E. Dynamic emission Stokes shift and liquid-like dielectric solvation of band edge carriers in lead-halide perovskites. *Nat. Commun.* **2019**, *10*.

[37] Brennan, M. C.; Herr, J. E.; Nguyen-Beck, T. S.; Zinna, J.; Draguta, S.; Rouvimov, S.; Parkhill, J.; Kuno, M. Origin of the Size-Dependent Stokes Shift in $CsPbBr_3$ Perovskite Nanocrystals. *J. Am. Chem. Soc.* **2017**, *139*, 12201–12208.

[38] Brennan, M. C.; Forde, A.; Zhukovskyi, M.; Baublis, A. J.; Morozov, Y. V.; Zhang, S.; Zhang, Z.; Kilin, D. S.; Kuno, M. Universal Size-Dependent Stokes Shifts in Lead Halide Perovskite Nanocrystals. *J. Phys. Chem. Lett.* **2020**, *11*, 4937–4944.

[39] Kaur, G.; Babu, K. J.; Ghosh, H. N. Temperature-Dependent Interplay of Polaron Formation and Hot Carrier Cooling Dynamics in $CsPbBr_3$ Nanocrystals: Role of Carrier–Phonon Coupling Strength. *J. Phys. Chem. Lett.* **2020**, *11*, 6206–6213.

[40] Combescot, M.; Combescot, R. Optical Stark effect of the exciton: Biexcitonic origin of the shift. *Phys. Rev. B* **1989**, *40*, 3788–3801.

[41] Rossi, D.; Wang, H.; Dong, Y.; Qiao, T.; Qian, X.; Son, D. H. Light-Induced Activation of Forbidden Exciton Transition in Strongly Confined Perovskite Quantum Dots. *ACS Nano* **2018**, *12*, 12436–12443.

[42] Li, Y.; Lai, R.; Luo, X.; Liu, X.; Ding, T.; Lu, X.; Wu, K. On the absence of a phonon bottleneck in strongly confined $CsPbBr_3$ perovskite nanocrystals. *Chem. Sci.* **2019**, *10*, 5983–5989.

[43] Klimov, V. I. Spectral and Dynamical Properties of Multiexcitons in Semiconductor Nanocrystals. *Annu. Rev. Phys. Chem.* **2007**, *58*, 635–673.

[44] Yumoto, G.; Tahara, H.; Kawawaki, T.; Saruyama, M.; Sato, R.; Teranishi, T.; Kanemitsu, Y. Hot Biexciton Effect on Optical Gain in $CsPbI_3$ Perovskite Nanocrystals. *J. Phys. Chem. Lett.* **2018**, *9*, 2222–2228.

[45] Mondal, A.; Aneesh, J.; Kumar Ravi, V.; Sharma, R.; Mir, W. J.; Beard, M. C.; Nag, A.; Adarsh, K. V. Ultrafast exciton many-body interactions and hot-phonon bottleneck in colloidal cesium lead halide perovskite nanocrystals. *Phys. Rev. B* **2018**, *98*, 115418.

[46] Shamsi, J.; Urban, A. S.; Imran, M.; De Trizio, L.; Manna, L. Metal Halide Perovskite Nanocrystals: Synthesis, Post-Synthesis Modifications, and Their Optical Properties. *Chem. Rev.* **2019**, *119*, 3296–3348.

[47] Makarov, N. S.; Guo, S.; Isaienko, O.; Liu, W.; Robel, I.; Klimov, V. I. Spectral and Dynamical Properties of Single Excitons, Biexcitons, and Trions in Cesium–Lead-Halide Perovskite Quantum Dots. *Nano Lett.* **2016**, *16*, 2349–2362.

[48] Straus, D. B.; Hurtado Parra, S.; Iotov, N.; Gebhardt, J.; Rappe, A. M.; Subotnik, J. E.; Kikkawa, J. M.; Kagan, C. R. Direct Observation of Electron–Phonon Coupling and Slow Vibrational Relaxation in Organic–Inorganic Hybrid Perovskites. *J. Am. Chem. Soc.* **2016**, *138*, 13798–13801.

[49] Santomauro, F. G. et al. Localized holes and delocalized electrons in photoexcited inorganic perovskites: Watching each atomic actor by picosecond X-ray absorption spectroscopy. *Structural Dynamics* **2017**, *4*, 044002.

[50] Cannelli, O. et al. Quantifying Photoinduced Polaronic Distortions in Inorganic Lead Halide Perovskite Nanocrystals. *J. Am. Chem. Soc.* **2021**, *143*, 9048–9059.

[51] Sharma, D. K.; Hirata, S.; Vacha, M. Energy localization vs. charge funneling in aggregates of $CsPbBr_3$ perovskite nanocrystals. *J. Lumin.* **2020**, *222*, 117119.

[52] Giovanni, D.; Righetto, M.; Zhang, Q.; Lim, J. W. M.; Ramesh, S.; Sum, T. C. Origins of the long-range exciton diffusion in perovskite nanocrystal films: photon recycling vs exciton hopping. *Light Sci. Appl.* **2021**, *10*, 2.

[53] van der Laan, M.; de Weerd, C.; Poirier, L.; van de Water, O.; Poonia, D.; Gomez, L.; Kinge, S.; Siebbeles, L. D. A.; Koenderink, A. F.; Gregorkiewicz, T.; Schall, P. Photon Recycling in $CsPbBr_3$ All-Inorganic Perovskite Nanocrystals. *ACS Photonics* **2021**, *8*, 3201–3208.

[54] Davis, N. J. L. K.; de la Peña, F. J.; Tabachnyk, M.; Richter, J. M.; Lamboll, R. D.; Booker, E. P.; Wisnivesky Rocca Rivarola, F.; Griffiths, J. T.; Ducati, C.; Menke, S. M.; Deschler, F.; Greenham, N. C. Photon Reabsorption in Mixed $CsPbCl_3$:$CsPbI_3$ Perovskite Nanocrystal Films for Light-Emitting Diodes. *J. Phys. Chem. C* **2017**, *121*, 3790–3796.

[55] Navarro-Arenas, J.; Suárez, I.; Chirvony, V. S.; Gualdrón-Reyes, A. F.; Mora-Seró, I.; Martínez-Pastor, J. Single-Exciton Amplified Spontaneous Emission in Thin Films of $CsPbX_3$ (X = Br, I) Perovskite Nanocrystals. *J. Phys. Chem. Lett.* **2019**, *10*, 6389–6398.

[56] Shi, H.; Zhang, X.; Sun, X.; Chen, R.; Zhang, X. Direct and Indirect Recombination and Thermal Kinetics of Excitons in Colloidal All-Inorganic Lead Halide Perovskite Nanocrystals. *J. Phys. Chem. C* **2019**, *123*, 19844–19850.

[57] Vonk, S. J. W.; Fridriksson, M. B.; Hinterding, S. O. M.; Mangnus, M. J. J.; van Swieten, T. P.; Grozema, F. C.; Rabouw, F. T.; van der Stam, W. Trapping and Detrapping in Colloidal Perovskite Nanoplatelets: Elucidation and Prevention of Nonradiative Processes through Chemical Treatment. *J. Phys. Chem. C* **2020**, *124*, 8047–8054.

Chapter 5

Multiexciton processes in lead halide perovskite nanoplatelets

This chapter reviews the response of strongly confined $CsPbBr_3$ NPls under strong photoexcitation regimes combining broadband FLUPS and TA. The presence of thermally stable biexcitons is firstly unveiled and their main properties discussed. Then, the influence of the exciton density on the hole localization into confined hole states is investigated.

This chapter is based on the studies *"Exciton, Biexciton and Hot Exciton Dynamics in $CsPbBr_3$ Colloidal Nanoplatelets"* [1] and *"Resonant Band-Edge Emissive States in Strongly Confined $CsPbBr_3$ Perovskite Nanoplatelets"* [2] conducted equally by Dr. Vale and myself. Dr. Vale wrote entirely the first manuscript while I wrote the second.

5.1 Introduction

Perovskite nanocrystal (PNC)-based devices are one of the most promising materials for lighting technologies.[3–6] PNCs exhibit high photoluminescence quantum yields (PLQYs), narrow and tunable emission bandwidths along with high absorption coefficients.[7–9] Strongly confined PNCs, such as two-dimensional nanoplatelets (2D NPls), have also gained interest over the past years for non-linear applications.[10–12] In such semiconductors (SCs), the charge carriers experience quantum confinement because of the reduced dimension(s) of the perovskite structure. Since the bulk-exciton radius for $CsPbBr_3$ is $r_0 = 3.5$ nm, strongly confined $CsPbBr_3$ NCs have, at least, one dimension smaller than r_0. Confinement of the charge carrier is further enhanced by the organic ligands binding the perovskite surface. These capping ligands have a lower optical permittivity ($\varepsilon_0 \approx 2$) than the inorganic core ($\varepsilon_0 \approx 6$), giving rise to a dielectric confinement. Strongly confined PNCs offer unique photophysical properties because of the enhanced carrier-carrier interactions leading to stable single and multi-excitons.

For example, some studies have already reported biexciton binding energies up to several tens of meV for small PNCs, overcoming the thermal energy at room temperature (RT).[13,14] The term biexciton refers to a quasi-particle formed by the attraction between two excitons inside the same molecule. There are two primary ways to generate biexcitons: 1) under a strong photoexcitation regime which can produce multiple excitons per nanoparticle, or 2) by absorbing a high-energy photon (greater than twice the band gap), which can generate two free excitons via carrier multiplication.[15–17] Biexciton states are linked to optical gain through population inversion and amplified spontaneous emission (ASE) in SC NCs; the biexciton lifetime can vary from a few picoseconds to hundreds of picoseconds, depending on the shape, size and composition of the PNCs.[18–20] Usually, biexciton lifetimes are limited by the rate of exciton-exciton annihilation, a process comparable to Auger recombination for bulk SCs.[21,22] This non-radiative process, where the first electron-hole pair recombines by transferring its energy to a second electron-hole pair which is excited to a higher energy level, becomes the main efficiency loss pathway for devices under large exciton densities.

Therefore, understanding the response of the lead halide perovskite (LHP) NPls under high carrier density is crucial for specific optoelectronic applications, such as lasing. Here, broadband fluorescence upconversion spectroscopy (FLUPS) was combined with femtosecond transient absorption (TA) spectroscopy at high excitation intensities to investigate as-synthesized $CsPbBr_3$ NPl colloidal solutions. Firstly, we highlighted the signatures of stable and emissive biexciton species on FLUPS and TA spectra. The methods used to isolate the biexciton signal were then discussed, yielding a calculated biexciton binding energy of

≈ 70 meV, which is close to the theoretical prediction for 2D biexcitons in quantum well structures. By fitting the biexciton signal decay, the lifetime was estimated to be 11 ps, and was assigned to the time constant for exciton-exciton annihilation. Secondly, we investigated the influence of the pump intensity on the hole localization process, which was discussed in the last chapter. By increasing the exciton density, the hole localization from band edge states to confined hole states (CHSs) becomes slower, presumably due to the filling of CHSs. Finally, we showed that hot carrier cooling and photon re-absorption remain faster than the temporal resolution of the setups, even under strong photoexcitation conditions.

5.2 Results and discussion

5.2.1 Biexciton properties

The standard characterization of $CsPbBr_3$ NPls, as well as the FLUPS and TA dynamics under low excitation intensity, were discussed in the previous chapters. Here, the focus is set on the optical response of the NPls when the excitation intensity is increased to generate more than one exciton per particle.

The number of exciton per NPl, $\langle N_x \rangle$, is estimated using Poisson statistics (**Equations 3.2-3.3**) and taking into consideration the fact that the absorption cross section, $\sigma_{400} = 3.4 \cdot 10^{-15}$ cm^2, does not change between the two broad excitation wavelengths $\lambda_{FLUPS} = 400$ nm and $\lambda_{TA} = 389$ nm. The 2D FLUPS and TA spectra for different excitation intensities are shown in the Appendices (**Figure C.1** and **2**). As seen in **Figure 5.1**, increasing the pump intensity greatly affects the PL spectral shape within the first tens of picoseconds. On the blue side of the peak, the emission previously assigned to band edge recombination ($\lambda_{max} = 445$ nm) is more pronounced and decays within the first five picoseconds. The dependence of the hole localization process on the carrier density will be discussed in detail later on. In

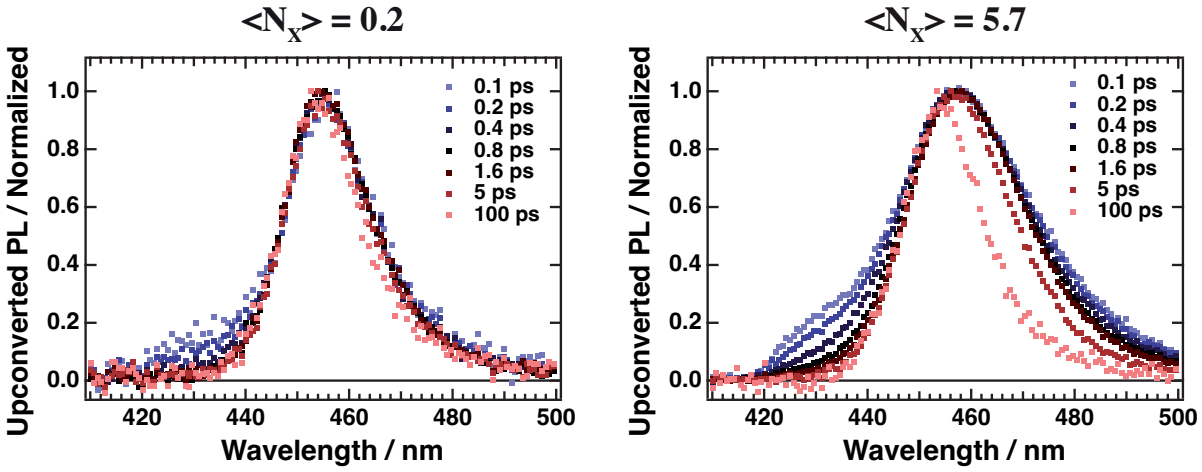

Figure 5.1: Normalized FLUPS spectral slices for left) $\langle N_x \rangle = 0.2$ and right) $\langle N_x \rangle = 5.7$.

addition, the PL becomes broader for a few tens of picoseconds on the red side. For $\tau_{\text{delay}} > 50$ ps, the PL overlaps with the spectra obtained under weak photoexcitation regimes. The emission broadening arises from a second Gaussian component related to the presence of emissive biexcitons. A biexciton is a quasi-particle formed by the attractive interaction between two single excitons and is likely to be induced by the vicinity of the photogenerated charge carriers in such small PNCs. Biexcitons can recombine radiatively to single exciton states by emitting photons with an energy slightly smaller than those arising from single exciton recombination (**Figure 5.2.A**). This energy difference is seen as the biexciton binding energy, Δ_{xx}. Hence, Δ_{xx} can be easily estimated using time-resolved PL techniques if the PL coming from single excitons is deconvoluted from biexciton emission. The method used to isolate the biexciton emission is described in section 5.4.2 and allows us to get a spectrum corresponding to the biexciton alone (**Figure 5.2.C**). The shape of the biexciton emission matches the one for single excitons and has a maximum at $\lambda = 467$ nm, which gives a biexciton binding energy $\Delta_{xx} = 74$ meV.

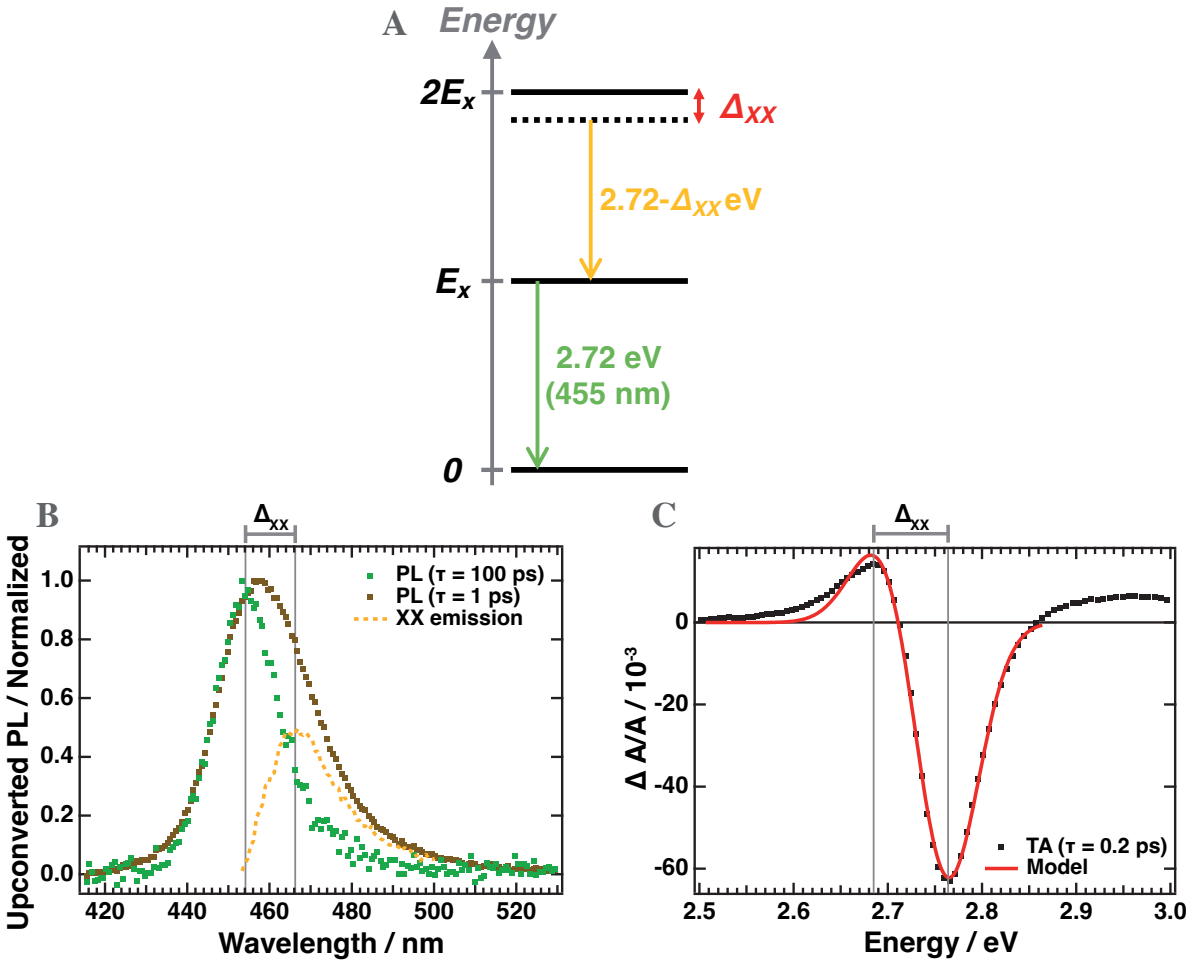

Figure 5.2: A) Energetic representation of biexciton (yellow) and single exciton (green) radiative recombinations. B) FLUPS spectral slices at $\tau_{\text{delay}} = 100$ ps and $\tau_{\text{delay}} = 1$ ps with the isolated biexciton emission for $\langle N_{\text{x}} \rangle = 5.7$. C) TA spectral slice at $\tau_{\text{delay}} = 0.2$ ps for $\langle N_{\text{x}} \rangle = 4.0$ and the best fitted curve from the model presented in the text.

Alternatively, Δ_{xx} can be estimated by fitting the TA spectrum at early time scales (**Figure 5.2.C**). As already discussed before, the positive feature (PIA-2) at 460 nm (2.69 eV) is ascribed to the biexciton-induced Stark effect caused by Coulomb interaction between the exciton and all biexcitonic states. The Coulomb interaction between the two single excitons produces a photoinduced absorption at lower energy ($E_x \rightarrow 2 \cdot E_x - \Delta_{xx}$). Consequently, by fitting the TA spectrum with a combination of two Gaussian functions, one accounting for the bleaching of the first excitonic band and one for the Stark effect photoinduced absorption,[23] one can obtain Δ_{xx} with:

$$\Delta A(E, \tau_{delay} = 0.2 \text{ ps}) = -A_1 \cdot \exp\left[-\left(\frac{E - E_x}{w}\right)^2\right] + A_2 \cdot \exp\left[-\left(\frac{E - E_x - \Delta_{xx}}{w}\right)^2\right] \quad (5.1)$$

where A_1 and A_2 are the amplitudes of the ground state bleaching (GSB) and PIA-2 peaks [-], E_x is the exciton transition energy determined by the static absorption spectrum [eV], and w is the line width of the transition [eV]. Here, $\Delta_{xx} = 65 \pm 7$ meV, which is close to what was found by examining the FLUPS data. It is worth mentioning that fitting the TA spectrum is an indirect method and may lead to larger errors than those found using the method which isolates the biexciton emission.

The values calculated here greatly exceed thermal energy at RT and not differ much from from the saturation value of 100 meV determined experimentally for $CsPbBr_3$ NCs by Castaneda et al.[14] As expected, Δ_{xx} firstly increases when the size of the NC is reduced due to the enhanced interaction between the photogenerated charge carriers.[24,25] Then the binding energy starts to decrease again for very small PNCs because repulsive electron-electron and hole-hole interactions compete with the attractive nature of the biexciton. For biexcitons in 2D quantum well structures, theoretical models predict a ratio $\Delta_x/\Delta_{xx} = 0.228$.[26,27] From the NPl static absorption spectrum $\Delta_x = 334 \pm 12$ meV, resulting in Δ_{xx} (theoretical) $= 76 \pm 3$ meV. This value matches the biexciton binding energy calculated by FLUPS, indicating that in $CsPbBr_3$ NPls, the charge carrier interactions are similar to other quantum well materials. The presence of stable biexcitons should be accompanied by a lower energy threshold for ASE, which is crucial for optoelectronic applications, such as lasing.[25,28] However, we did not detect any ASE at RT for these $CsPbBr_3$ NPl colloidal solutions, even under the strongest photoexcitation (> 1.9 mJ/cm^2) and for the highest NPl concentration (absorption > 4 at 400 nm). Indeed, most studies reporting ASE for LHP-based systems are conducted on thin films and not colloidal solutions to overcome losses due to nonradiative exciton-exciton recombination (see below). Thin films offer a higher particle density which considerably decreases the threshold value.[29] Here, we were unable to obtain stable NPl films by spin coating the concentrated colloidal solution on a glass substrate because the NPls tend to aggregate and form bigger particles. Finally, it is worth mentioning that the Δ_{xx} values reported in the literature are still under

debate due to the lack of direct evidence for biexcitons.[30,31] As already expressed before, TA spectra are often complicated to interpret due to their complexity, especially under strong photoexcitation, and most of the temporal resolved PL setups are limited to the few tens or hundreds of picoseconds temporal resolution hindering the direct emission from biexcitons. The presented method combining FLUPS and TA techniques, should be more straightforward. More recently, polarization-dependent 2D electronic spectroscopy have also been used to accurately estimate the biexciton binding energy.[32,33]

As mentioned before, one of the main limiting factors for ASE is the fast biexciton recombination through exciton-exciton annihilation. In this process, the first exciton recombines non radiatively by transferring its energy to the second exciton, which is subsequently excited to higher energy levels. The isolated biexciton signal observed by FLUPS is displayed in **Figure 5.3.A** in order to study the biexciton recombination. The PL is well fitted by an exponential decay function with a time constant of 11.0 ± 0.1 ps, indicating that biexciton recombination can be described using first order kinetics. In theory, the radiative lifetime of n-excitons is related to that of a single exciton by $\tau_{\text{n-x,rad}} = \tau_{\text{x,rad}}/n^2$. Therefore, the biexciton radiative lifetime is predicted to be one-fourth of the radiative lifetime under low pump fluence. Since a value of $\tau_{\text{x,rad}} = 8.6$ ns was previously found, the theoretical biexciton lifetime would be $\tau_{\text{xx,rad}} = 2.15$ ns. Here, the experimental decay is at least two orders of magnitude faster and it is safe to assume that exciton-exciton annihilation is the main deactivation channel for biexciton species.

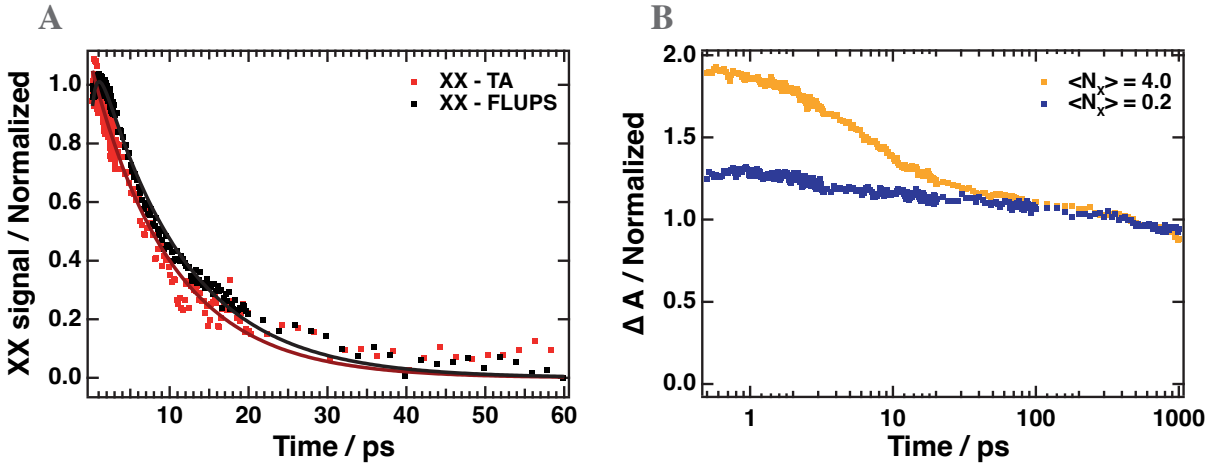

Figure 5.3: A) Isolated biexciton decays obtained by TA and FLUPS. B) Normalized, at $\tau_{\text{delay}} = 500$ ps, GSB decays ($\lambda_{\text{probe}} = 445$ nm) at the lowest and the highest pump intensity.

The exciton-exciton annihilation process is also visible by TA when comparing the normalized GSB decays for different excitation intensities (**Figure 5.3.B**). The effect of exciton-exciton annihilation is isolated by subtracting the normalized GSB signal acquired under weak photoexcitation from the one under strong

photoexcitation, and a lifetime of 10.2 ± 0.2 ps is obtained, which is close to the one obtained by FLUPS. The exciton-exciton annihilation lifetime, $\tau_{xx,A)}$, matches what has already been reported in the literature for small PNCs.[34] $\tau_{xx,A}$ only depends on the NPl thickness (or NC lateral size), not on the NC shape, and decreases for smaller particles.[14,19,20] This trend is explained by enhanced Coulomb interactions between the charge carriers as well as the breaking of the energy and momentum conservation law for Auger-type recombination under strong quantum confinement conditions.[20] Interestingly, the recombination rate observed in PNCs is much higher than for their metal chalcogenide counterparts because of the similar effective masses between electrons and holes.[19,35] In PbSe or CdSe NCs, heavy holes cannot be easily re-excited, which reduces the exciton-exciton annihilation rate. It is also worth noting that the biexciton dynamics do not depend on the excitation intensity (Appendix, **Figure C.3**), but the proportion of biexcitons compared to single excitons increases under high photoexcitation regimes.

5.2.2 Influence of the exciton density on the hole localization

The previous chapter highlighted the presence of a short-lived emission peak, overlapping with the static absorption ($\lambda = 445$ nm) and blue-shifted compared to the principal one ($\lambda = 455$ nm). This was assigned to the recombination of excitons in the lowest excited state, while the Stokes shifted emission arises from the localization of holes in CHSs. By isolating the blue-shifted PL, the hole localization time constant was determined to be 0.30 ps, which corroborates with the decay of the PIA-2 feature in TA.

Nevertheless, as displayed in **Figure 5.1**, the PL signal around 440 nm is more pronounced and longer-lived under high pump intensities. Thus, the influence of the carrier density on the hole localization process was investigated by increasing the average number of excitons per NPl from $\langle N_x \rangle = 0.1$ to $\langle N_x \rangle$

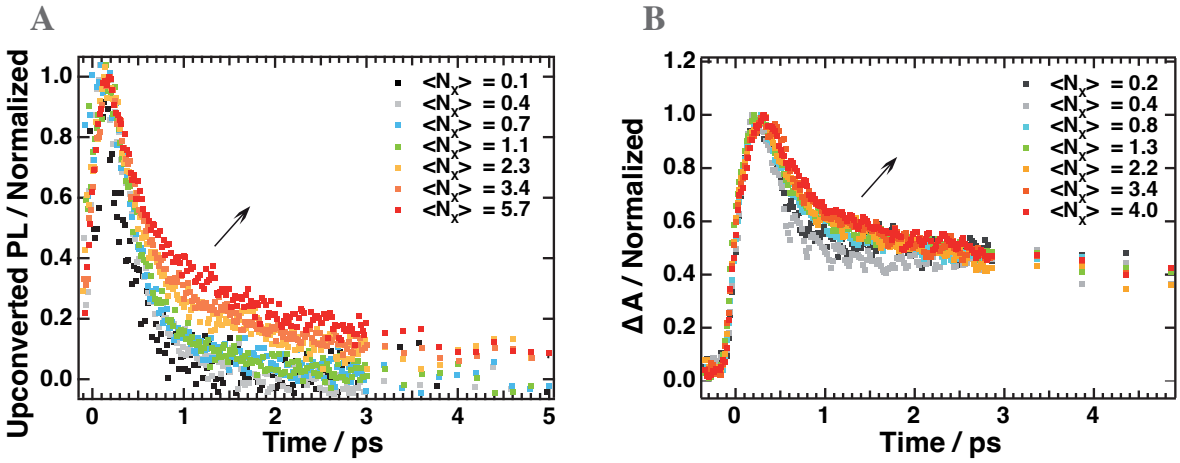

Figure 5.4: Normalized dynamics of A) the isolated band edge emission ($\lambda_{probe} = 455$ nm) and B) PIA-2 ($\lambda_{probe} = 460$ nm) for different excitation intensities. The best fitting parameters are summarized in the Appendices.

= 5.7. **Figure 5.4** displays the normalized dynamics of the isolated band edge emission as well as the normalized PIA-2 slices for each intensity. Firstly, it has to be mentioned that both signals rise "instantaneously", within the temporal resolution of the setups, indicating ultrafast carrier cooling, even under high pump intensities. This result is not surprising since Hintermayr *et al.* reported a hot carrier lifetime of < 300 fs for strongly confined $CsPbI_3$ NPls excited with 1.0 eV excess energy.[36] They explained the fast carrier relaxation to the band edge by suggesting that the energy transfer from the perovskite core to the capping ligands is promoted by the high surface-to-volume ratio in confined NCs. Since the NPl dimensions in the study are even more reduced, and the excess energy is smaller (400 meV), the relaxation rate should be further increased. All traces were fitted with a bi-exponential decay function convoluted with a Gaussian function. The detailed procedure and the extracted parameters are reported in the Appendices (section C.1). At low excitation intensity, the band edge emission (and PIA-2) decay exponentially with a time constant of 0.35 ± 0.05 ps (and 0.30 ± 0.02 ps). These lifetimes match those for hole localization discussed in the previous chapter. An additional component, $\tau_2 = 2.0 \pm 0.2$ ps (2.5 ± 0.1 ps for PIA-2) appears when $\langle N_x \rangle > 1$ with a relative amplitude up to 42% (23%) at the highest excitation intensity.

Many possibilities could explain the lengthening of the hole localization: a hot phonon bottleneck as for bulk LHPs,[36,37] Auger heating due to exciton-exciton interactions,,[36,38] polaron formation,[39] or a state filling effect.[40,41] The last effect may arise by saturation of the localized states with the large exciton population created upon high photoexcitation intensities. Brennan *et al.*[40] have shown that the density of states (DOS) of the CHS in $CsPbBr_3$ NCs is 50 times lower than the one of the CB edge, which would lead us toward a state filling effect. Moreover, a hot phonon bottleneck is expected to only have a minor (or no) influence due to the rapid energy transfer from the perovskite to the organic capping ligands. Besides, a lifetime of 11 ps has been estimated for exciton-exciton annihilation, which is one order of magnitude longer than the time constant for hole localization, also ruling out Auger heating for being the main reason for the slower hole localization. Yet, the large density of excitons might also overcome the lattice relaxation process, reducing the polaron formation rate discussed in the last chapter. Pieces of evidence should be brought by ultrafast X-ray spectroscopy on the bromide atom.[42] By looking more carefully at **Figure C.3**, it has also been observed that the biexciton formation may be slightly delayed at the highest pump fluence, following the trend for hole localization. This might indicate that biexcitons are formed upon localization of holes, even if more evidences are required.

Finally, the impact of the carrier density on the photon recycling process is investigated. It has been previously shown that photon re-absorption by bigger particles was faster than the temporal resolution

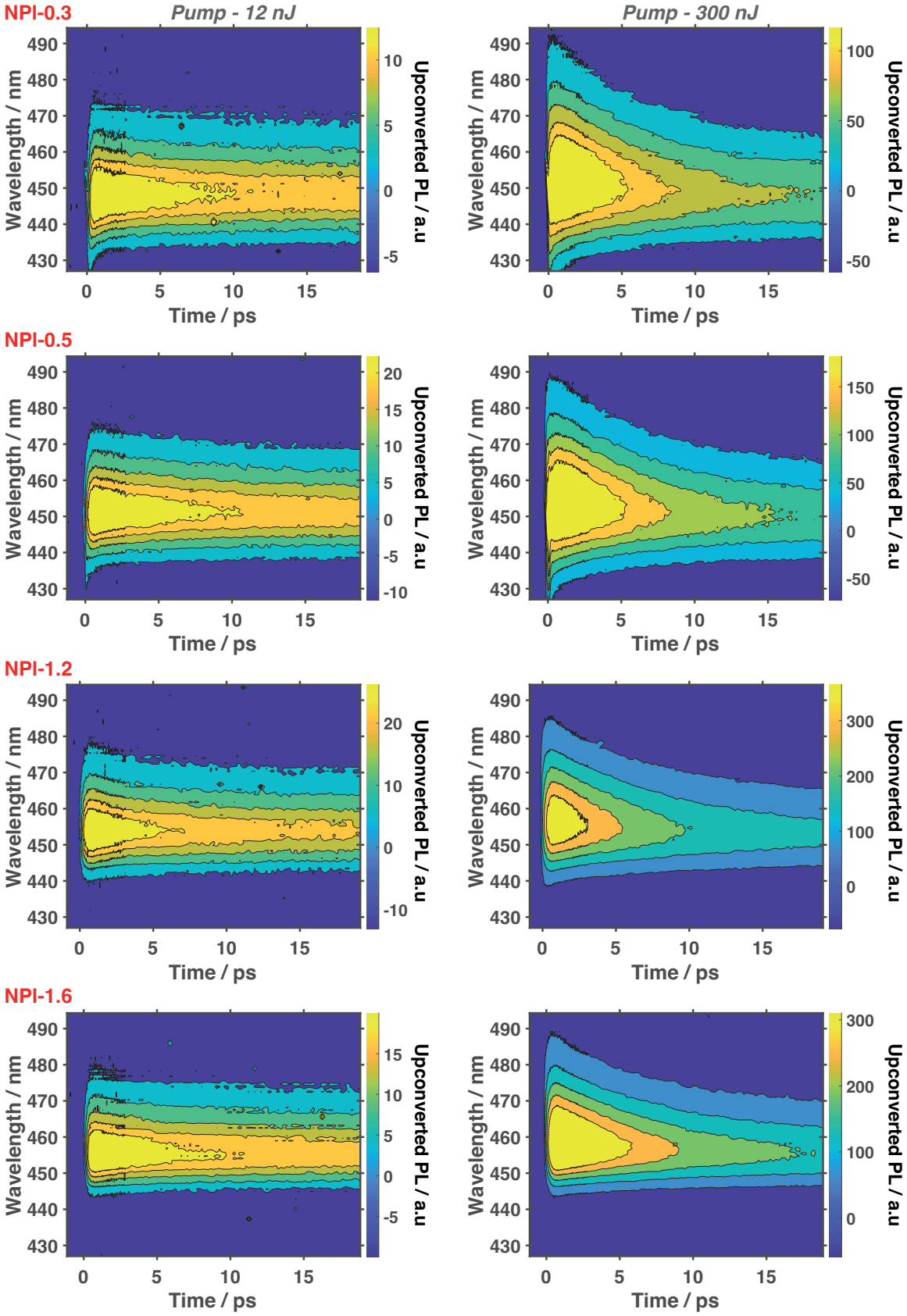

Figure 5.5: 2D FLUPS spectra of different NPl concentrations at (left) low and (right) high excitation intensities.

of the instrumentation for low excitation intensity and led to an extension of the external Stokes shift. The same four samples, labelled NPl-0.3, NPl-0.5, NPl-1.2 and NPl-1.6, according to their absorption at λ = 400 nm, were studied. The pump fluence was set to the maximum (950 $\mu J/cm^2$) to generate multiple excitons per NPl (**Figure 5.5**). Even for the highest excitation intensity, the re-absorption of photons by larger NPls remains faster than the temporal resolution of the setup as the spectral slices for NPl-1.6 do not display the typical features corresponding to band edge emission. Yet, by probing the isolated blue-shifted emission for NPl-0.3, NPl-0.5 and NPl-1.2 (**Figure 5.6.A**), it is clear that for a similar excitation intensity, the hole localization becomes faster for concentrated solutions. **Table C.3** summarizes the parameters obtained by fitting the decays according to the procedure described in the Appendices (section C.1). As has already been reported previously, each sample exhibits a bi-exponential decay behavior with $\tau_1 \approx 0.3$ ps and $\tau_2 \approx$ 1.5-2 ps, but the amplitude A_2 decreases when the NPl concentration is increased. This difference is explained by looking at **Figure 5.6.B**, which displays the dependence of the PL intensities after 100 ps on the excitation intensity. The absorption cross-section of the solution, σ_{400}, is obtained by fitting the data with Poisson statistics (the description of the fitting procedure is detailed in chapter 3). **Table 5.1** highlights that σ_{400} decreases by increasing the NPl concentration. It has to be noted that σ_{400} might be overestimated for NPl-1.2 and NPl-1.6 since a plateau is not reached, even at the highest excitation intensity. Consequently, for similar pump intensities, the average number of excitons per NPl, $\langle N_x \rangle$, is inversely proportional to the concentration. It ultimately leads to faster hole localization, as it has already been discussed.

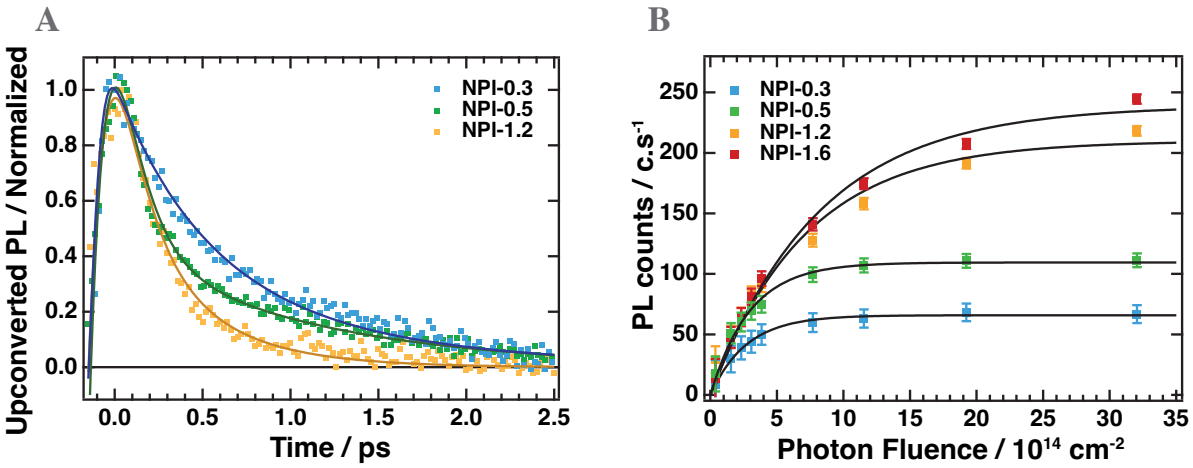

Figure 5.6: A) Normalized isolated band edge decays (λ_{probe} = 445 nm obtained at high excitation intensity for different NPl concentrations. The lines show the best fits obtained from the procedure described in the Appendices. B) PL intensity at τ_{delay} = 100 ps with the fitted Poisson model (lines) for different NPl concentrations.

To understand the reason for the dependence of σ_λ on the NPl concentration, one could estimate the

average distance between two neighbouring NPls, $\langle d \rangle$ [nm] by:[43]

$$\langle d \rangle = \frac{\Gamma \cdot 4/3}{\left(4\pi N/3\right)^{\frac{1}{3}}} = 0.554 \cdot N^{-1/3} \tag{5.2}$$

where N is the particle density [NPl/cm^3]. Furthermore, N is proportional to the NPl concentration, c_{NPl} [mol/L]:

$$N = c_{\mathrm{NPl}} \cdot \frac{N_A}{10^3} \tag{5.3}$$

where N_A is the Avogadro constant [mol^{-1}]. Finally, the NPl concentration is given by the Beer-Lambert law:

$$c_{\mathrm{NPl}} = \frac{A_\lambda}{\epsilon \cdot l} = \frac{10^3 \cdot \ln(10) \cdot A_\lambda}{N_A \cdot \sigma_\lambda \cdot l} \tag{5.4}$$

where A_λ is the absorbance [-], ϵ is the molar attenuation coefficient [cm^2/mol], l is the optical path length [cm], and σ_λ is the cross-section [cm^2]. Thus, by substituting **Equation 5.4** and **Equation 5.3** into **Equation 5.2**:

$$\langle d \rangle = 0.554 \cdot \left(\frac{\ln(10) \cdot A_\lambda}{\sigma_\lambda \cdot l} \right)^{-1/3} \tag{5.5}$$

As reported in **Table 5.1**, for NPl-1.2 and NPl-1.6 $\langle d \rangle$ becomes smaller than the average NPl length, l_{NPl} = 23 nm. In these samples, there is an overlap between the NPls, which breaks the required conditions for obeying the Beer-Lambert law. The NPls cast shadows onto each other, reducing the amount of light absorbed by the solution and ultimately decreasing the value of the *global* cross-section. Here, the term *global* is introduced since the cross-section is a physical quantity for a given particle or molecule and must be constant. To summarize, the hole localization becomes faster in highly concentrated NPl solutions because of the reduced number of excitons per particle caused by the spatial overlap between individual NPls. Even under high pump intensity, photon recycling remains faster than the FLUPS time-resolution.

Table 5.1: Absorption cross-section at the pump wavelength, σ_{400}, average distance between NPls, $\langle d \rangle$, and average number of excitons per particle for a pump intensity set at 300 nJ, $\langle N_{\mathrm{x}} \rangle_{300nJ}$, for different NPl concentrations.

Sample	$\mathbf{A_{400\ nm}}$	$\boldsymbol{\sigma_{400}}$ **/** $\mathbf{10^{-15}\ cm^2}$	$\langle \boldsymbol{d} \rangle$ **/ nm**	$\langle \boldsymbol{N_{\mathrm{x}}} \rangle_{\mathbf{300\ nJ}}$
NPl-0.3	0.3	3.7 ± 0.2	45	7.1 ± 0.4
NPl-0.5	0.5	3.4 ± 0.2	37	6.5 ± 0.4
NPl-1.2	1.2	1.4 ± 0.2	21	2.7 ± 0.3
NPl-1.6	1.6	1.2 ± 0.1	17	2.2 ± 0.2

5.3 Conclusion

Throughout this chapter, the response of strongly confined $CsPbBr_3$ NPls under strong photoexcitation regimes was scrutinized combining broadband FLUPS and TA. The average number of photogenerated excitons per NPl was monitored with Poisson statistics and varied from $\langle N_x \rangle = 0.1$ to $\langle N_x \rangle = 5.7$.

For $\langle N_x \rangle > 1$, the presence of stable biexcitons was unveiled, which show a red-shifted emission compared to the main peak. A biexciton binding energy of $\Delta_{xx} = 74$ meV was found by isolating the biexciton contribution of the FLUPS spectrum, which matches the estimation made by fitting TA data at early time scale ($\Delta_{xx} = 65 \pm 7$ meV). The values are close to the theoretical limit calculated for $CsPbBr_3$ NCs,[14] and agree well with the theoretical model for 2D biexcitons in quantum well structures, which predicts $\Delta_{xx} = 76 \pm 3$ meV based on the exciton binding energy.[26] These findings are promising for lasing applications since high biexciton binding energies should be accompanied by low ASE thresholds. However, we did not manage to synthesize stable NPl thin films or obtain NPl solutions with sufficient particle density for observing ASE.

Then, to determine the biexciton recombination processes, the FLUPS and TA dynamics associated with the biexciton population were fitted and resulted in first-order kinetic behavior with time constants of 11.0 ± 0.1 ps and 10.2 ± 0.2 ps, respectively. The biexciton recombination lifetime is solely due to exciton-exciton annihilation since the biexciton radiative lifetime is expected to be much longer (> 2 ns).

Finally, even under high excitation intensities, hot carrier cooling and photon recycling remained faster than the time-resolution of the setups (< 150 fs). Nevertheless, increasing the exciton density delayed the hole localization process up to a few picosecond, most probably because of the low DOS of the CHSs giving rise to a state filling effect.

Altogether, these results complement the investigations conducted under weak photoexcitation regimes, highlighting the differences between $CsPbBr_3$ NPls and weakly confined PNCs. Still, some applications, such as photovoltaic devices, also require efficient charge carrier separation which is controlled by the interfacial dynamics between the photoactive layer, here the perovskite, and the electron or hole acceptor. The fundamental characterization of LHP NPls in a donor/acceptor configuration will be investigated within the next chapter.

5.4 Methods

5.4.1 Sample preparation

For each set of measurements, a fresh $CsPbBr_3$ NPl solution was prepared following the procedure detailed in chapter 3. Besides, 0.13 mmol of $ZnBr_2$ was added to the lead precursor solution to bring an excess of bromide ions and passivate the NPl surface. It resulted in a decrease of the number of defects as well as an increase in long term stability of the solution. The samples were diluted in dodecane to obtain an absorbance of 0.5 at 400 nm in a 1 mm optical path quartz cuvette right before the spectroscopic measurement to avoid as much as possible desorption of ligands from the NPl surface.

5.4.2 Experimental measurements and data treatment

Ultrafast characterization – Broadband FLUPS and TA measurements were acquired with the setups described previously. The excitation wavelength (λ_{exc} = 400 nm and 389 nm for FLUPS and TA, respectively) was obtained by frequency-doubling the laser output, which gives the most stable beams. The pump photon fluence was adjusted from 22 $\mu J/cm^2$ to 950 $\mu J/cm^2$ with a variable neutral density filter to study multi-exciton dynamics. UV-visible absorption spectra were taken before and after each measurement to ensure that the NPls were not deteriorated by high pump intensities.

Biexciton emission isolation – A homemade MATLAB procedure has been written to isolate the short-lived emission observed on the red-edge of the main peak by FLUPS. Firstly, for each time delay, the spectral slices (PL_{norm}) were normalized at λ = 455 nm. Then, PL_{norm} at early time scales (τ_{delay} = 0-50 ps) was subtracted from PL_{norm} at $\tau_{delay} > 100$ ps for the same photon fluence. In this way, the emission of band edge single excitons was suppressed.

Bibliography

[1] Vale, B. R. C.; Socie, E.; Burgos-Caminal, A.; Bettini, J.; Schiavon, M. A.; Moser, J.-E. Exciton, Biexciton, and Hot Exciton Dynamics in $CsPbBr_3$ Colloidal Nanoplatelets. *J. Phys. Chem. Lett.* **2019**, *11*, 387–394.

[2] Socie, E.; Vale, B. R. C.; Terpstra, A. T.; Schiavon, M. A.; Moser, J.-E. Resonant Band-Edge Emissive States in Strongly Confined $CsPbBr_3$ Perovskite Nanoplatelets. *J. Phys. Chem. C* **2021**, *125*, 14317–14325.

[3] Lin, K. et al. Perovskite light-emitting diodes with external quantum efficiency exceeding 20 per cent. *Nature* **2018**, *562*, 245–248.

[4] Chiba, T.; Hayashi, Y.; Ebe, H.; Hoshi, K.; Sato, J.; Sato, S.; Pu, Y.-J.; Ohisa, S.; Kido, J. Anion-exchange red perovskite quantum dots with ammonium iodine salts for highly efficient light-emitting devices. *Nat. Photonics* **2018**, *12*, 681–687.

[5] Lin, Y.-H. et al. Deciphering photocarrier dynamics for tuneable high-performance perovskite-organic semiconductor heterojunction phototransistors. *Nat. Commun.* **2019**, *10*.

[6] Gong, M.; Sakidja, R.; Goul, R.; Ewing, D.; Casper, M.; Stramel, A.; Elliot, A.; Wu, J. Z. High-Performance All-Inorganic $CsPbCl_3$ Perovskite Nanocrystal Photodetectors with Superior Stability. *ACS Nano* **2019**, *13*, 1772–1783.

[7] Protesescu, L.; Yakunin, S.; Bodnarchuk, M. I.; Krieg, F.; Caputo, R.; Hendon, C. H.; Yang, R. X.; Walsh, A.; Kovalenko, M. V. Nanocrystals of Cesium Lead Halide Perovskites ($CsPbX_3$, X = Cl, Br, and I): Novel Optoelectronic Materials Showing Bright Emission with Wide Color Gamut. *Nano Lett.* **2015**, *15*, 3692–3696.

[8] Di Stasio, F.; Christodoulou, S.; Huo, N.; Konstantatos, G. Near-Unity Photoluminescence Quantum

Yield in $CsPbBr_3$ Nanocrystal Solid-State Films via Postsynthesis Treatment with Lead Bromide. *Chem. Mater.* **2017**, *29*, 7663–7667.

[9] Maes, J.; Balcaen, L.; Drijvers, E.; Zhao, Q.; De Roo, J.; Vantomme, A.; Vanhaecke, F.; Geiregat, P.; Hens, Z. Light Absorption Coefficient of $CsPbBr_3$ Perovskite Nanocrystals. *J. Phys. Chem. Lett.* **2018**, *9*, 3093–3097.

[10] Zhu, H.; Fu, Y.; Meng, F.; Wu, X.; Gong, Z.; Ding, Q.; Gustafsson, M. V.; Trinh, M. T.; Jin, S.; Zhu, X.-Y. Lead halide perovskite nanowire lasers with low lasing thresholds and high quality factors. *Nat. Mater.* **2015**, *14*, 636–642.

[11] Booker, E. P.; Price, M. B.; Budden, P. J.; Abolins, H.; Redondo, Y. d. V.-I.; Eyre, L.; Nasrallah, I.; Phillips, R. T.; Friend, R. H.; Deschler, F.; Greenham, N. C. Vertical Cavity Biexciton Lasing in 2D Dodecylammonium Lead Iodide Perovskites. *Adv. Opt. Mater.* **2018**, *6*, 1800616.

[12] Xu, J.; Li, X.; Xiong, J.; Yuan, C.; Semin, S.; Rasing, T.; Bu, X. Halide Perovskites for Nonlinear Optics. *Adv. Mater.* **2020**, *32*, 1806736.

[13] Li, J.; Jing, Q.; Xiao, S.; Gao, Y.; Wang, Y.; Zhang, W.; Sun, X. W.; Wang, K.; He, T. Spectral Dynamics and Multiphoton Absorption Properties of All-Inorganic Perovskite Nanorods. *J. Phys. Chem. Lett.* **2020**, *11*, 4817–4825.

[14] Castañeda, J. A.; Nagamine, G.; Yassitepe, E.; Bonato, L. G.; Voznyy, O.; Hoogland, S.; Nogueira, A. F.; Sargent, E. H.; Cruz, C. H. B.; Padilha, L. A. Efficient Biexciton Interaction in Perovskite Quantum Dots Under Weak and Strong Confinement. *ACS Nano* **2016**, *10*, 8603–8609.

[15] Li, M.; Begum, R.; Fu, J.; Xu, Q.; Koh, T. M.; Veldhuis, S. A.; Grätzel, M.; Mathews, N.; Mhaisalkar, S.; Sum, T. C. Low threshold and efficient multiple exciton generation in halide perovskite nanocrystals. *Nat. Commun.* **2018**, *9*, 4197.

[16] Villamil Franco, C.; Mahler, B.; Cornaggia, C.; Gustavsson, T.; Cassette, E. Auger Recombination and Multiple Exciton Generation in Colloidal Two-Dimensional Perovskite Nanoplatelets: Implications for Light-Emitting Devices. *ACS Appl. Nano Mater.* **2021**, *4*, 558–567.

[17] Cong, M.; Yang, B.; Chen, J.; Hong, F.; Yang, S.; Deng, W.; Han, K. Carrier Multiplication and Hot-Carrier Cooling Dynamics in Quantum-Confined $CsPbI_3$ Perovskite Nanocrystals. *J. Phys. Chem. Lett.* **2020**, *11*, 1921–1926.

[18] Eperon, G. E.; Jedlicka, E.; Ginger, D. S. Biexciton Auger Recombination Differs in Hybrid and Inorganic Halide Perovskite Quantum Dots. *J. Phys. Chem. Lett.* **2018**, *9*, 104–109.

[19] Li, Y.; Ding, T.; Luo, X.; Chen, Z.; Liu, X.; Lu, X.; Wu, K. Biexciton Auger recombination in mono-dispersed, quantum-confined $CsPbBr_3$ perovskite nanocrystals obeys universal volume-scaling. *Nano Res.* **2019**, *12*, 619–623.

[20] Li, Q.; Yang, Y.; Que, W.; Lian, T. Size- and Morphology-Dependent Auger Recombination in $CsPbBr_3$ Perovskite Two-Dimensional Nanoplatelets and One-Dimensional Nanorods. *Nano Lett.* **2019**, *19*, 5620–5627.

[21] García-Santamaría, F.; Chen, Y.; Vela, J.; Schaller, R. D.; Hollingsworth, J. A.; Klimov, V. I. Suppressed Auger Recombination in "Giant" Nanocrystals Boosts Optical Gain Performance. *Nano Lett.* **2009**, *9*, 3482–3488.

[22] Nagamine, G.; Jeong, B. G.; Ferreira, T. A. C.; Chang, J. H.; Park, K.; Lee, D. C.; Bae, W. K.; Padilha, L. A. Efficient Optical Gain in Spherical Quantum Wells Enabled by Engineering Biexciton Interactions. *ACS Photonics* **2020**, *7*, 2252–2264.

[23] Aneesh, J.; Swarnkar, A.; Kumar Ravi, V.; Sharma, R.; Nag, A.; Adarsh, K. V. Ultrafast Exciton Dynamics in Colloidal $CsPbBr_3$ Perovskite Nanocrystals: Biexciton Effect and Auger Recombination. *J. Phys. Chem. C* **2017**, *121*, 4734–4739.

[24] Huang, H.; Zhao, W.; Yang, H.; Zhang, X.; Su, J.; Hu, K.; Nie, Z.; Li, Y.; Zhong, J. *In situ* synthesis of blue-emitting bromide-based perovskite nanoplatelets towards unity quantum efficiency and ultrahigh stability. *J. Mater. Chem. C* **2021**, *9*, 5535–5543.

[25] Nagamine, G.; Rocha, J. O.; Bonato, L. G.; Nogueira, A. F.; Zaharieva, Z.; Watt, A. A. R.; de Brito Cruz, C. H.; Padilha, L. A. Two-Photon Absorption and Two-Photon-Induced Gain in Perovskite Quantum Dots. *J. Phys. Chem. Lett.* **2018**, *9*, 3478–3484.

[26] Birkedal, D.; Singh, J.; Lyssenko, V. G.; Erland, J.; Hvam, J. M. Binding of Quasi-Two-Dimensional Biexcitons. *Phys. Rev. Lett.* **1996**, *76*, 672–675.

[27] Li, J.; Luo, L.; Huang, H.; Ma, C.; Ye, Z.; Zeng, J.; He, H. 2D Behaviors of Excitons in Cesium Lead Halide Perovskite Nanoplatelets. *J. Phys. Chem. Lett.* **2017**, *8*, 1161–1168.

[28] Yakunin, S.; Protesescu, L.; Krieg, F.; Bodnarchuk, M. I.; Nedelcu, G.; Humer, M.; De Luca, G.; Fiebig, M.; Heiss, W.; Kovalenko, M. V. Low-threshold amplified spontaneous emission and lasing from colloidal nanocrystals of caesium lead halide perovskites. *Nat. Commun.* **2015**, *6*, 8056.

[29] Tan, M. J. H.; Wang, Y.; Chan, Y. Solution-based green amplified spontaneous emission from colloidal perovskite nanocrystals exhibiting high stability. *Appl. Phys. Lett.* **2019**, *114*, 183101.

[30] Ashner, M. N.; Shulenberger, K. E.; Krieg, F.; Powers, E. R.; Kovalenko, M. V.; Bawendi, M. G.; Tisdale, W. A. Size-Dependent Biexciton Spectrum in $CsPbBr_3$ Perovskite Nanocrystals. *ACS Energy Lett.* **2019**, *4*, 2639–2645.

[31] Shulenberger, K. E.; Ashner, M. N.; Ha, S. K.; Krieg, F.; Kovalenko, M. V.; Tisdale, W. A.; Bawendi, M. G. Setting an Upper Bound to the Biexciton Binding Energy in $CsPbBr_3$ Perovskite Nanocrystals. *J. Phys. Chem. Lett.* **2019**, *10*, 5680–5686.

[32] Huang, X.; Chen, L.; Zhang, C.; Qin, Z.; Yu, B.; Wang, X.; Xiao, M. Inhomogeneous Biexciton Binding in Perovskite Semiconductor Nanocrystals Measured with Two-Dimensional Spectroscopy. *J. Phys. Chem. Lett.* **2020**, *11*, 10173–10181.

[33] Liu, A.; Almeida, D. B.; Padilha, L. A.; Cundiff, S. T. Perspective: multi-dimensional coherent spectroscopy of perovskite nanocrystals. *J. Phys. Mater.* **2022**, *5*, 021002.

[34] Gramlich, M.; Bohn, B. J.; Tong, Y.; Polavarapu, L.; Feldmann, J.; Urban, A. S. Thickness-Dependence of Exciton–Exciton Annihilation in Halide Perovskite Nanoplatelets. *J. Phys. Chem. Lett.* **2020**, *11*, 5361–5366.

[35] Makarov, N. S.; Guo, S.; Isaienko, O.; Liu, W.; Robel, I.; Klimov, V. I. Spectral and Dynamical Properties of Single Excitons, Biexcitons, and Trions in Cesium–Lead-Halide Perovskite Quantum Dots. *Nano Lett.* **2016**, *16*, 2349–2362.

[36] Hintermayr, V. A.; Polavarapu, L.; Urban, A. S.; Feldmann, J. Accelerated Carrier Relaxation through Reduced Coulomb Screening in Two-Dimensional Halide Perovskite Nanoplatelets. *ACS Nano* **2018**, *12*, 10151–10158.

[37] Li, M.; Bhaumik, S.; Goh, T. W.; Kumar, M. S.; Yantara, N.; Grätzel, M.; Mhaisalkar, S.; Mathews, N.; Sum, T. C. Slow cooling and highly efficient extraction of hot carriers in colloidal perovskite nanocrystals. *Nat. Commun.* **2017**, *8*.

[38] Davis, N. J. L. K.; de la Peña, F. J.; Tabachnyk, M.; Richter, J. M.; Lamboll, R. D.; Booker, E. P.; Wisnivesky Rocca Rivarola, F.; Griffiths, J. T.; Ducati, C.; Menke, S. M.; Deschler, F.; Greenham, N. C. Photon Reabsorption in Mixed $CsPbCl_3$:$CsPbI_3$ Perovskite Nanocrystal Films for Light-Emitting Diodes. *J. Phys. Chem. C* **2017**, *121*, 3790–3796.

[39] Cannelli, O. et al. Quantifying Photoinduced Polaronic Distortions in Inorganic Lead Halide Perovskite Nanocrystals. *J. Am. Chem. Soc.* **2021**, *143*, 9048–9059.

[40] Brennan, M. C.; Herr, J. E.; Nguyen-Beck, T. S.; Zinna, J.; Draguta, S.; Rouvimov, S.; Parkhill, J.; Kuno, M. Origin of the Size-Dependent Stokes Shift in $CsPbBr_3$ Perovskite Nanocrystals. *J. Am. Chem. Soc.* **2017**, *139*, 12201–12208.

[41] Brennan, M. C.; Forde, A.; Zhukovskyi, M.; Baublis, A. J.; Morozov, Y. V.; Zhang, S.; Zhang, Z.; Kilin, D. S.; Kuno, M. Universal Size-Dependent Stokes Shifts in Lead Halide Perovskite Nanocrystals. *J. Phys. Chem. Lett.* **2020**, *11*, 4937–4944.

[42] Santomauro, F. G. et al. Localized holes and delocalized electrons in photoexcited inorganic perovskites: Watching each atomic actor by picosecond X-ray absorption spectroscopy. *Structural Dynamics* **2017**, *4*, 044002.

[43] Chandrasekhar, S. Stochastic Problems in Physics and Astronomy. *Rev. Mod. Phys.* **1943**, *15*, 1–89.

Chapter 6

Charge carrier separation in lead halide perovskite nanoplatelets

This chapter is devoted to investigating the charge separation mechanism between $CsPbBr_3$ NPls and commonly used organic acceptors. Firstly, fast interfacial hole and electron transfer from the perovskite band edge were unveiled, while charge recombination appears to be four orders of magnitude slower. Moreover, hot carrier transfer from higher energy states is even enhanced, overcoming the charge carrier cooling.

This chapter is based on the manuscript *"Charge-separation Mechanism in Strongly Confined Quasi-one-dimensional $CsPbBr_3$ Perovskite Nanocrystals"* which has just been submitted. The contribution of all co-authors is acknowledge. Dr. Vale participated in the experimental planning and data discussion. Mr. Fonseca and Dr. Bettini obtained the cyclic voltammetry data and TEM images.

6.1 Introduction

All inorganic cesium lead halide perovskite nanocrystals (PNCs), $CsPbX_3$ (X = Cl, Br, I), have emerged as promising materials for optoelectronic applications.[1–6] PNCs display large absorption coefficients and high photoluminescence quantum yields (PLQYs),[7–9] along with enhanced charge carrier lifetimes and diffusion lengths,[10] making them suitable for photovoltaics or to drive photocatalytic reactions.[11–13] Besides these intrinsic properties, layered PNC-based devices also require fast charge separation (CS) and slow charge recombination (CR) to efficiently extract the photogenerated carriers. Therefore, ultrafast intermolecular charge transfer becomes crucial for obtaining efficient photovoltaic systems. Several studies have already shown rapid, a few picoseconds to 200 ps, interfacial electron or hole transfer from the perovskite to organic molecules.[14–19] The interfacial charge transfer (ICT) is favored by the lability of the usual capping ligands,[20,21] which are substituted by the acceptor units on the PNC surface and give rise to donor-acceptor complexes. Additionally, efficient extraction of hot carriers has been reported due to 1) a strong electronic coupling between the perovskite hot states and the organic moiety, 2) long charge carrier cooling rates in weakly confined PNCs.[22,23] The collection of energetic carriers, overcoming the band gap energy, can push the solar cell efficiency beyond the Shockley-Queisser limit and is of considerable importance.

Two-dimensional (2D) $CsPbBr_3$ nanoplatelets (NPls) offer a great alternative to the unstable $CsPbCl_3$ NCs for blue-emitting devices as their optical band gaps are widened due to quantum and dielectric confinement. Besides, the 2D morphology gives rise to narrow and intense absorption and emission peaks,[24–26] making them suitable for photocatalysis as well. While the disparities of the carrier dynamics and carrier-carrier interactions between strongly and weakly confined PNCs have already been discussed, the impact of the reduced dimensionality on the CS process remains unexplored. For example, lead halide perovskite (LHP) NPls exhibit tightly bound excitons, due to enhanced Coulomb interaction, which might hamper CS.[27] On the other hand, their larger surface area should promote the formation of perovskite-acceptor complexes,[28] as well as slowing CR due to carrier delocalization.[29] Last but not least, the ultrafast charge carrier cooling rates observed in strongly confined PNCs may be detrimental for simultaneous hot charge carrier extraction.[30]

Here, basic NPl-acceptor complexes were synthesized, using phenothiazine (PTZ) and p-benzoquinone (BQ) as hole and electron acceptors, respectively. Ultrafast spectroscopic methods were applied to understand the fundamentals of the CS process. Firstly, we unveiled that adding PTZ or BQ does not change the NPl size, shape and light absorption properties but induces a strong quenching of the

PL. The quenching results from ICT and depends on the acceptor concentration. Then, broadband fluorescence upconversion spectroscopy (FLUPS) was used to investigate the transfer of cold charge carriers, i.e., carriers that have relaxed to the lowest excited state. Hole transfer (HT) and electron transfer (ET) display sub-nanosecond time constants and compete with exciton trapping. Since the NPl-acceptor complexes also exhibit long-lived, on the µs time scale, charge transfer (CT) states, $CsPbBr_3$ NPls become of great promises for light-harvesting devices. Finally, despite the ultrafast charge carrier relaxation rates in LHP NPls, we demonstrated efficient hot electron and hole transfers.

6.2 Results and discussion

6.2.1 Standard characterization of charge carrier transfer

To investigate the ICT dynamics from strongly confined $CsPbBr_3$ NPls to organic acceptor molecules, NPl-acceptor complexes were synthesized by adding PTZ (or BQ) to the pristine NPl colloidal solution.

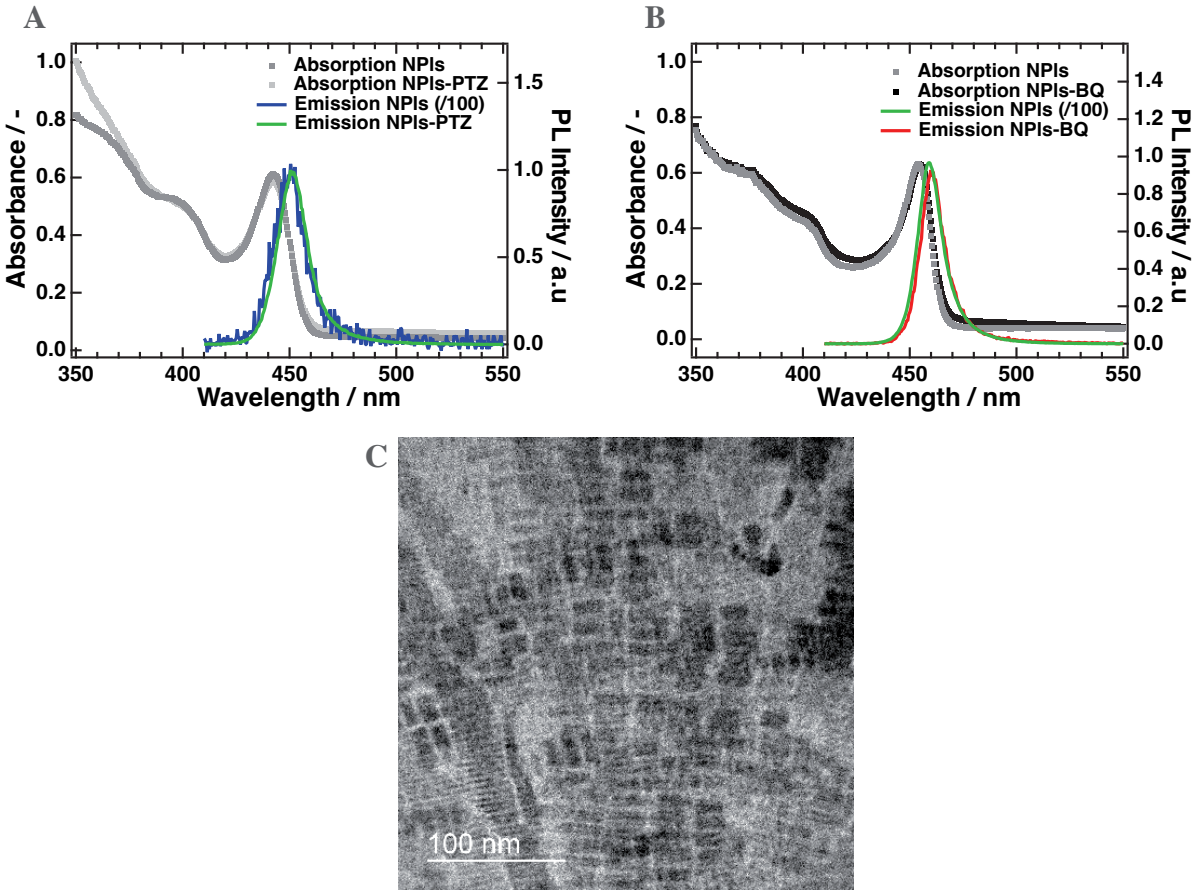

Figure 6.1: Absorption and emission spectra of pristine $CsPbBr_3$ NPls alongside A) NPl-PTZ and B) NPl-BQ complexes. For comparison reasons, the emission of the pristine solution has been reduced hundredfold. C) TEM images of NPl-PTZ complexes: the complexes retain the neat NPl shape and size distribution (Figure 3.1).

Upon sonification, organic acceptors are likely to substitute the capping ligands and bind to the perovskite surface.[17,23,31] It is worth noting that, the size, shape and light absorption properties of the NPls do not change upon the addition of the organic compound (**Figure 6.1**). Furthermore, NPl-BQ complexes are more prone to aggregation and deterioration after days of storage under ambient conditions (Appendix, **Figure D.1**), while the NPl-PTZ counterpart remain intact. Future works shall focus on finding molecular acceptors that do not affect the long-term stability of the NPls, while keeping efficient CS. Yet, PTZ and BQ are standard, cheap and well-referenced organic acceptors and are convenient to study the fundamental aspects of the CS mechanism. The emission of NPl-acceptor complexes, when compared to pristine NPl solutions, is reduced by two orders of magnitude (**Figure 6.1, A and B**). This PL quenching is assigned to a fast electron transfer from $CsPbBr_3$ to BQ (or from PTZ to $CsPbBr_3$), arising before excitonic radiative recombination. To match the literature, we will, from now on, rather employ the terms electron transfer (ET) from the NPls to BQ and hole transfer (HT) from the NPls to PTZ. Therefore, even tightly bound excitons are easily broken by the presence of organic acceptors conjugated on the NPl surface. To ensure that the ICT is thermodynamically favored, the highest occupied and lowest unoccupied molecular orbitals (HOMO and LUMO) levels of the molecular acceptors were calculated using cyclic voltammetry (Appendix, **Figure D.2**). As displayed in **Figure 6.2**, the PTZ HOMO and BQ LUMO levels lie within the semiconductor (SC) band gap, and induce large, and similar, thermodynamic driving forces for HT (0.87 eV) and ET (0.85 eV).

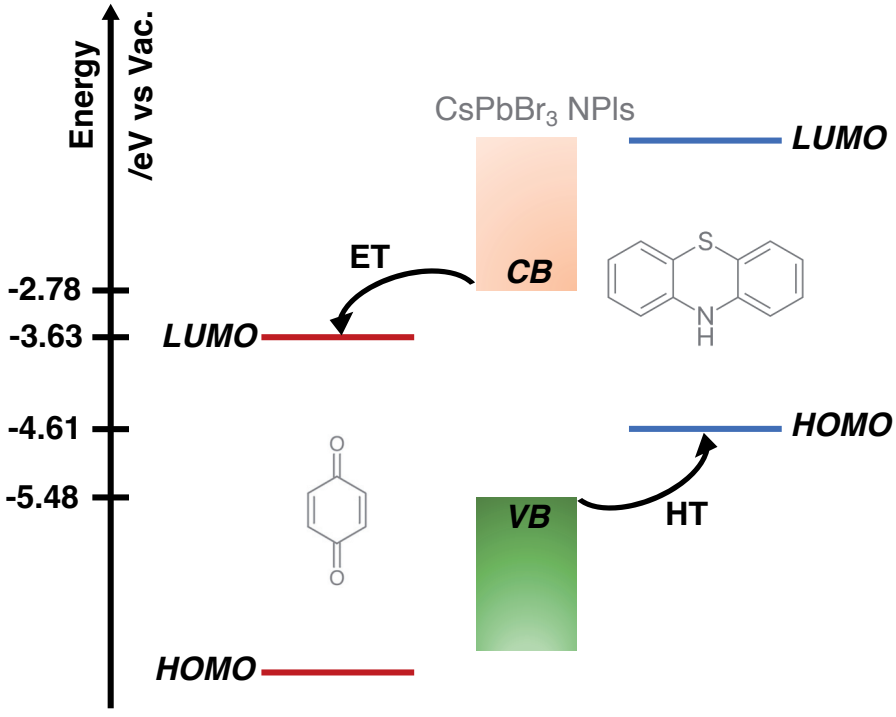

Figure 6.2: Schematic illustration of the estimated energy levels for $CsPbBr_3$ NPls, BQ (red) and PTZ (blue) via cyclic voltammetry.

In addition, by looking at **Figure 6.3, A** to **C**, it is clear that the PL quenching gets faster when the acceptor concentration is increased. Indeed, increasing the acceptor concentration in solution reduces the number of "free" $CsPbBr_3$ NPls (particles without any acceptor on the surface). Since the signal intensity is the global response of an ensemble of distinct NPl colloids, the more NPl-acceptor complexes are formed, the faster the overall PL decay is. Therefore, it is crucial to quantify, m, the average number of molecular acceptors bound to a NPl [-]. m is calculated by considering that the adsorption of acceptor on the NPl surface follows the Langmuir adsorption isotherm (**Equation 6.1**):[23,32]

$$\theta = \frac{m}{N_B} = \theta_{\max} \cdot \frac{K_{\text{acc}}[A]}{1 + K_{\text{acc}}[A]} \tag{6.1}$$

where θ is the mean fractional coverage of acceptors on a single NPl [-], N_B is the number of available binding sites per NPl [-], $\theta_{\max}$ is the maximum fractional coverage of acceptors on a single NPl [-], K_{acc}

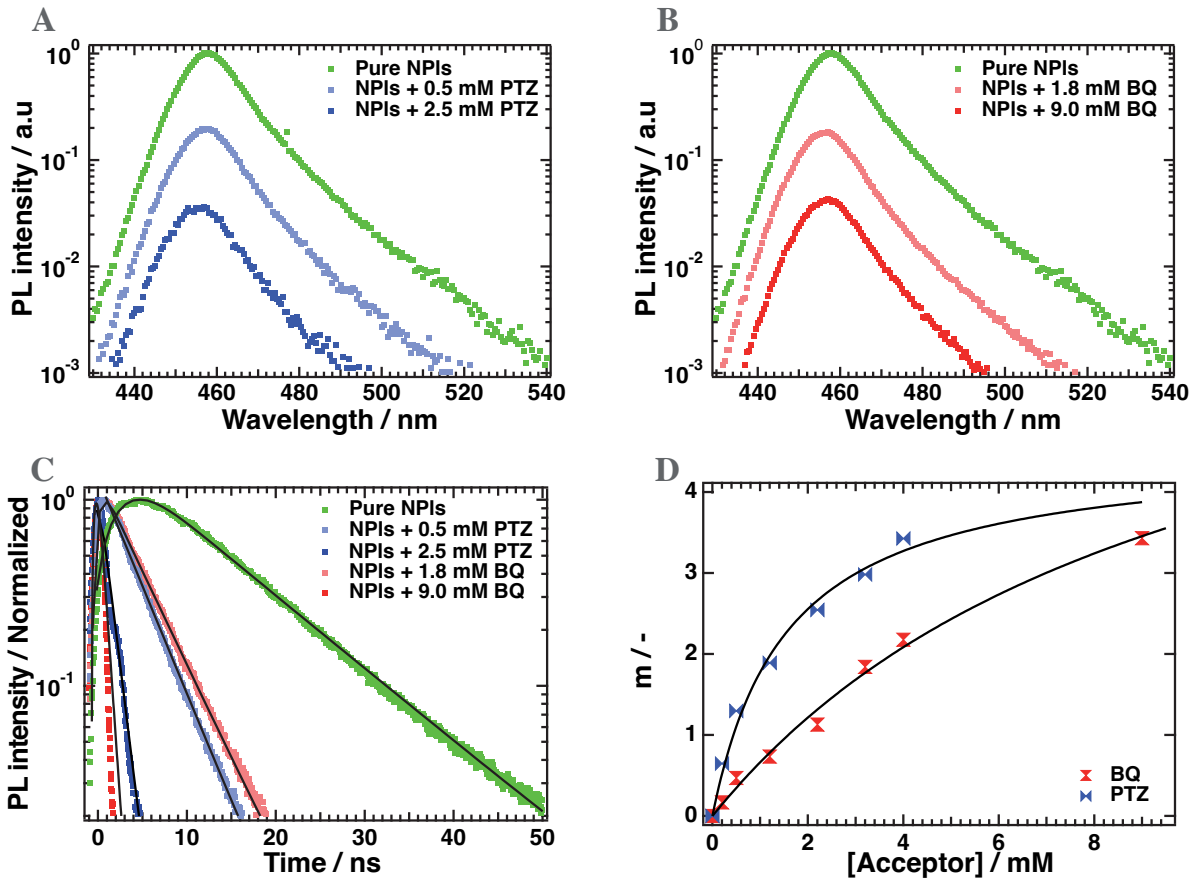

Figure 6.3: Static emission spectra of NPl-acceptor complexes with different concentrations of A) PTZ and B) BQ. Each trace has been corrected with the same constant. C) ns-PL decays of NPl-acceptor complexes with different concentrations of acceptor molecules. D) Average number of PTZ (blue) and BQ (red) attached per NPl as a function of the acceptor concentration.

the acceptor binding constant [-], and $[A]$ is the acceptor concentration [mol/L]. Assuming that PTZ and BQ can only bind to Pb^{2+} on the NPl surface, the number of available sites is equal to:

$$N_B = \frac{\pi}{4} \cdot \frac{6 \cdot l_{\mathrm{NPl}} \cdot w_{\mathrm{NPl}}}{\pi \cdot r^2_{\mathrm{Pb}^{2+}}} \tag{6.2}$$

where l_{NPl} and w_{NPl} are the length and the lateral size of the NPl [nm], while r^{2+}_{Pb} is the lead ionic radius and is equal to 0.119 nm. Applied to these NPls, $N_B = 9750$. Besides, the probability to have m acceptors attached per NPl is given by the binomial distribution:[33]

$$P(m|N,\theta) = \binom{N}{m} \cdot \theta^m \cdot (1-\theta)^{N_B - m} \tag{6.3}$$

The probability of finding a "free" NPl, $P(0|N,\theta)$, is also equal to the ratio between the integrated PL intensity of the NPl-acceptor complex solution ($\mathrm{PL_{acc}}$) and the integrated PL intensity of the pure NPls solution ($\mathrm{PL_0}$), which gives:

$$P(0|N,\theta) = \frac{\mathrm{PL_{acc}}}{\mathrm{PL_0}} = (1-\theta)^{N_B} \tag{6.4}$$

Therefore, m is computed via:

$$m = N_B \cdot \left(1 - \sqrt[N_B]{\frac{\mathrm{PL_{acc}}([A])}{\mathrm{PL_0}}}\right) \tag{6.5}$$

Figure 6.3.D displays the average number of acceptor molecules bound to the NPl surface as a function of the acceptor concentration. The PTZ (BQ) concentration should be equal to 0.45 mM (1.7 mM) to obtain an average of one acceptor per NPl, and get values that can be compared to the literature. For the highest acceptor concentrations, the proportion of particles without any acceptor on the surface is less than 4%, explaining why the PL decay is faster than the time-correlated single-photon counting (TCSPC) temporal resolution.

6.2.2 Cold charge transfer

Hence, ultrafast spectroscopic techniques are needed to investigate the CS mechanism in strongly confined LHP NPls. For example, FLUPS could be a powerful tool because the charge transfer can be directly monitored by tracking the PL decay. Here, NPl-acceptor complexes were excited at $\lambda = 400$ nm with a low excitation intensity, $\langle N_{\mathrm{x}} \rangle < 0.2$, to avoid multi-excitonic contributions. **Figure 6.4.A** and **B** displays the dynamics at $\lambda = 455$ nm (emission maximum) for five samples: pristine NPls and NPl-complexes with two different electron and hole acceptor concentrations to induce $m < 1$ and $m \approx 3$ acceptors per NPl. As already mentioned, the PL decay becomes faster upon the addition of PTZ (or BQ) because of the HT (or ET) from the perovskite to the molecular acceptor. The emission intensity even vanishes before one

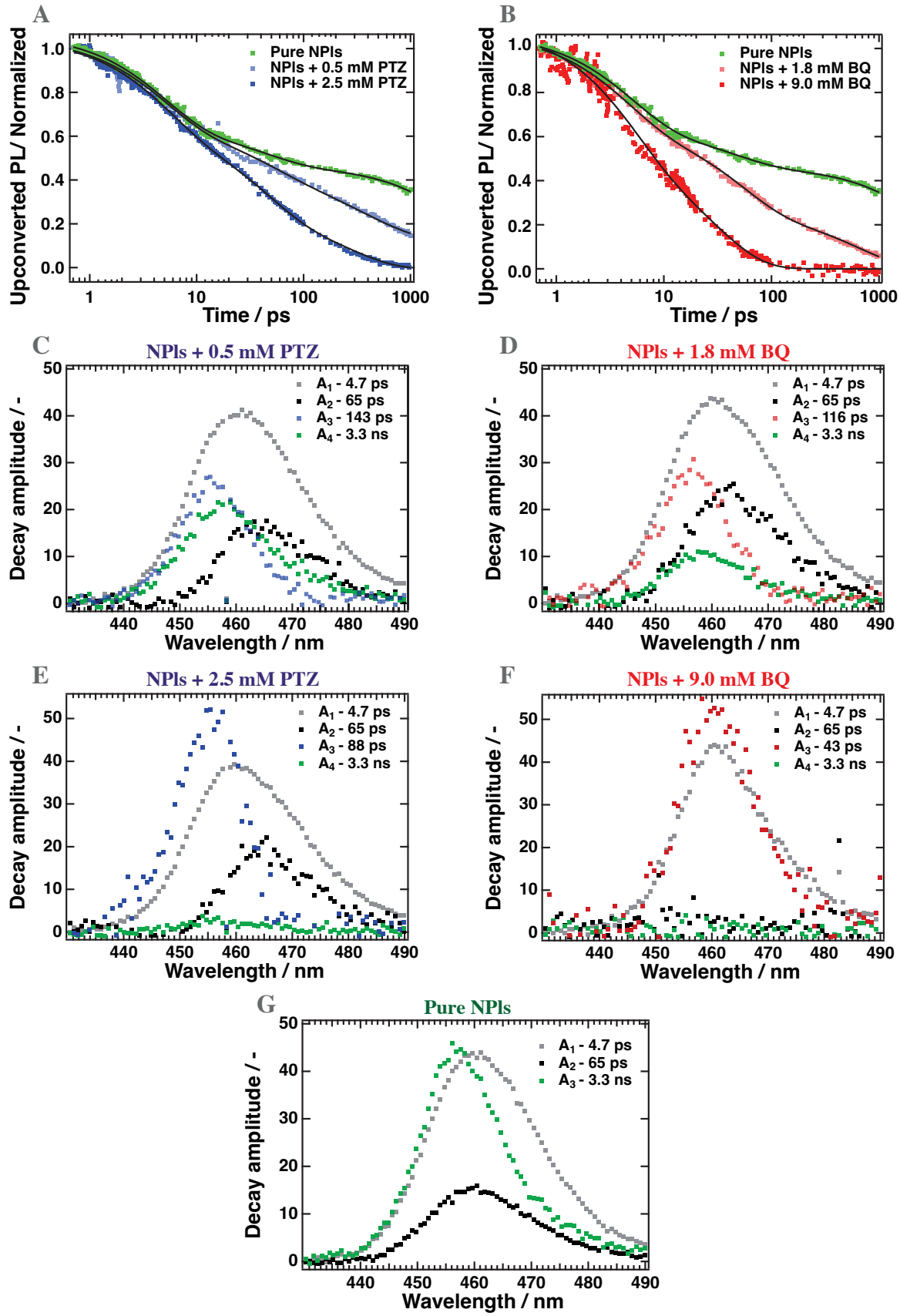

Figure 6.4: Normalized PL dynamics (λ_{probe} = 455 nm) for pristine NPls and NPls with various concentrations of A) PTZ and B) BQ and the best curves from the global fitting procedure described in the text. C-G) Decay associated spectra arising from the global fitting procedure for each sample.

nanosecond for the highest acceptor concentration, corroborating the TCSPC measurements. The ICT time constant is estimated by applying a global fitting procedure for the five samples. The procedure is discussed in section 6.4.3, the best fits and the resulting decay associated spectra (DAS) are displayed in **Figure 6.4**. The PL dynamics follow a tri-exponential decay behavior for pristine NPls, with time constants (and relative amplitudes) of 4 ps (A_1, grey dots, 42%), 65 ps (A_2, black dots, 14%) and 2.3 ns (A_3, green dots, 44%). The values obtained here match what has already been discussed in chapters 3 and 4 and are assigned to charge carrier trapping into shallow and deep trap states and radiative recombination, respectively. In addition, another component of 40 ps to 150 ps, attributed to ICT, is needed to fit the NPl-acceptor complexes dynamics. As previously pointed out, the CS rate increases with increasing acceptor concentration but remains always more than two orders of magnitude higher than exciton radiative recombination. In addition, the relative amplitude of the ICT feature, shown in blue for PTZ and red for BQ, grows from $\approx 25\%$ to $\approx 50\%$ by increasing the acceptor concentration, while the relative amplitude of the radiative recombination drops from 44% (pristine NPls) to 0% (NPls + 2.5 mM PTZ and NPls + 9.0 mM BQ). Nonetheless, since the time constant for ICT and exciton trapping are similar, it becomes tougher to deconvolute the two processes, and the global fitting procedure might not be accurate. For example, for NPls + 9.0 mM BQ, the amplitude associated with ET seems to be the sum between the black and the red components.

Another approach is required to isolate the CS process and determine the percentage of charges transferred to the molecular acceptor. In this way, it is assumed that the addition of PTZ or BQ on the NPl surface does not create new trap states, which is supported by noticing that A_1 is independent of the acceptor concentration. Therefore, the normalized PL decay of the pristine NPl solution (called PL_0) was substituted from the normalized PL decays of the NPl-acceptor complexes (PL_{acc}) to isolate the ICT contribution. Fourteen NPl-acceptor solutions were investigated varying the acceptor concentration from 0.2 mM to 4.0 mM. Three key features should be highlighted from the resulting signals in **Figure 6.5.A** and **B**. Firstly, $PL_{acc} - PL_0$ decays over the first hundreds of picoseconds because, for NPl-acceptor complexes, excitons are split; by fitting the signal with a exponential decay function, the HT and ET time constants are calculated. Secondly, $PL_{acc} - PL_0$ reaches a minimum value near 150 ps, depending on the acceptor concentration: this minimum value gives the percentage of photogenerated charges transferred to the molecular acceptors. For example, if $PL_{acc} - PL_0$ reaches -1, it would mean that 100% of the charges are transferred to the acceptor. Thirdly, $PL_{acc} - PL_0$ increases after a few hundreds of picoseconds for acceptor concentrations higher than 2 mM because at this point all the excitons are trapped or have split and the signal has reached 0, while PL_0 keeps decreasing due to the radiative recombination of excitons. To sum up these points, the ICT time constants and the percentage of charge carrier transferred for

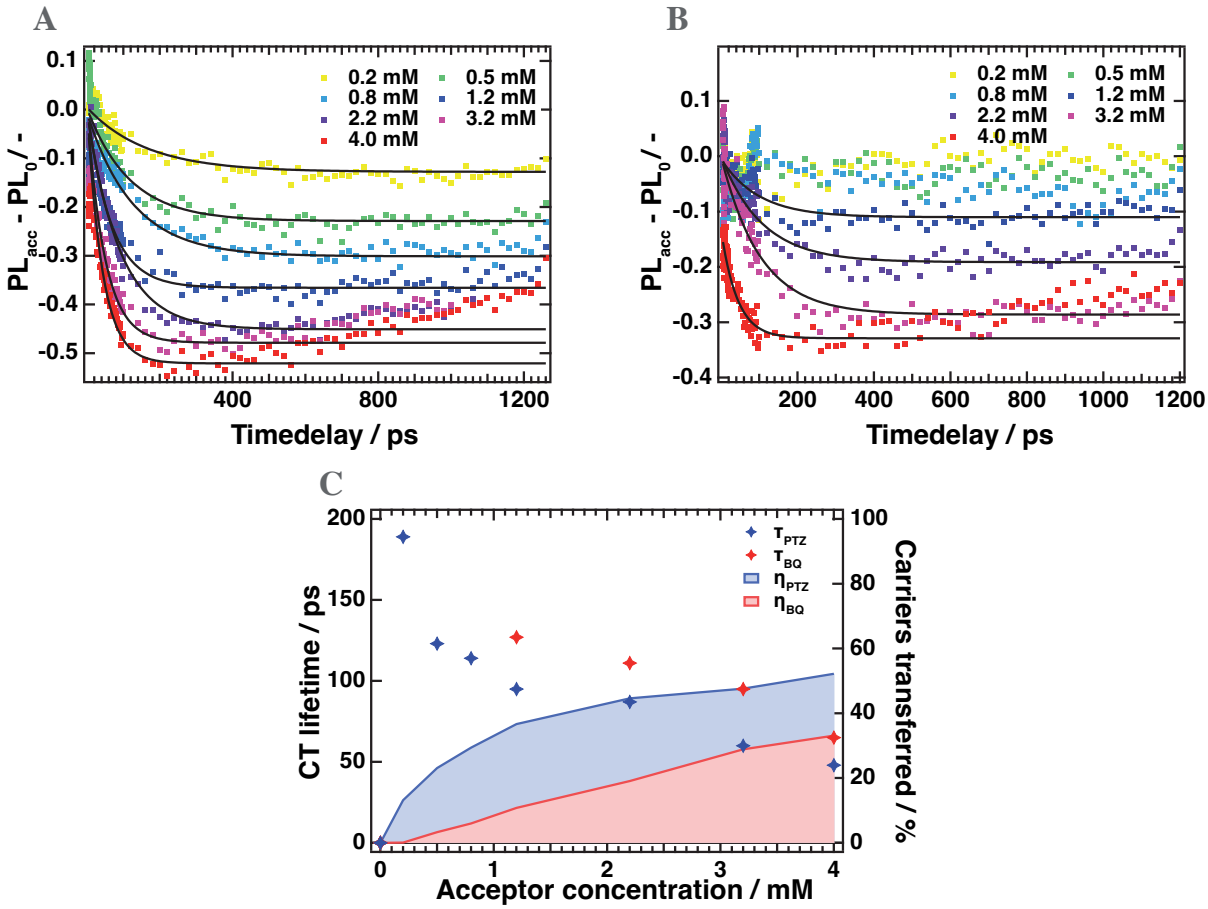

Figure 6.5: Isolated A) HT and B) ET dynamics for different acceptor concentrations. C) "Cold" ICT time constants and the percentage of charge carriers transferred depending on the acceptor concentration.

every acceptor concentration are displayed in **Figure 6.5.C**. For BQ concentrations smaller than 0.8 mM, the average number of acceptors attached to the NPl surface is too low to produce a noticeable PL quenching. The HT (ET) time constant decreases from 200 ps to 50 ps (from 130 ps to 60 ps) by increasing the PTZ (BQ) concentration and falls in the same range as what has been observed by TA for weakly confined PNCs with less tightly bound excitons.[14,23,29] The large exciton binding energy might be balanced by substantial thermodynamic driving forces for CS and the strong electronic coupling between charge carriers in NPls and molecular acceptors,[29] providing an easy pathway to break the exciton. In addition, up to 50% (32%) of the photogenerated holes (electrons) are transferred to PTZ (BQ) for an acceptor concentration of 4 mM, which is promising for light-harvesting devices. To further enhance the transfer yield, the next step would be to reduce the number of trap states in LHP NPls, as it competes with the CS process. It has already been pointed out that the dynamic binding between the perovskite surface and the organic capping ligands may be the principal reason for the presence of deep trap states. However, it should be highlighted that substituting the usual OA and OAm with less labile capping ligands might hinder the binding between the perovskite surface and the molecular acceptors.

6.2.3 Charge recombination

The efficiency of donor-acceptor systems not only relies on their ability to separate the photogenerated charges, but also to provide long-lived CT states for subsequent charge extraction. TA spectroscopy appears more appropriate for probing the CT states since both holes and electrons contribute to the observed signal. For instance, the negative ground state bleaching (GSB) feature arises from a combination

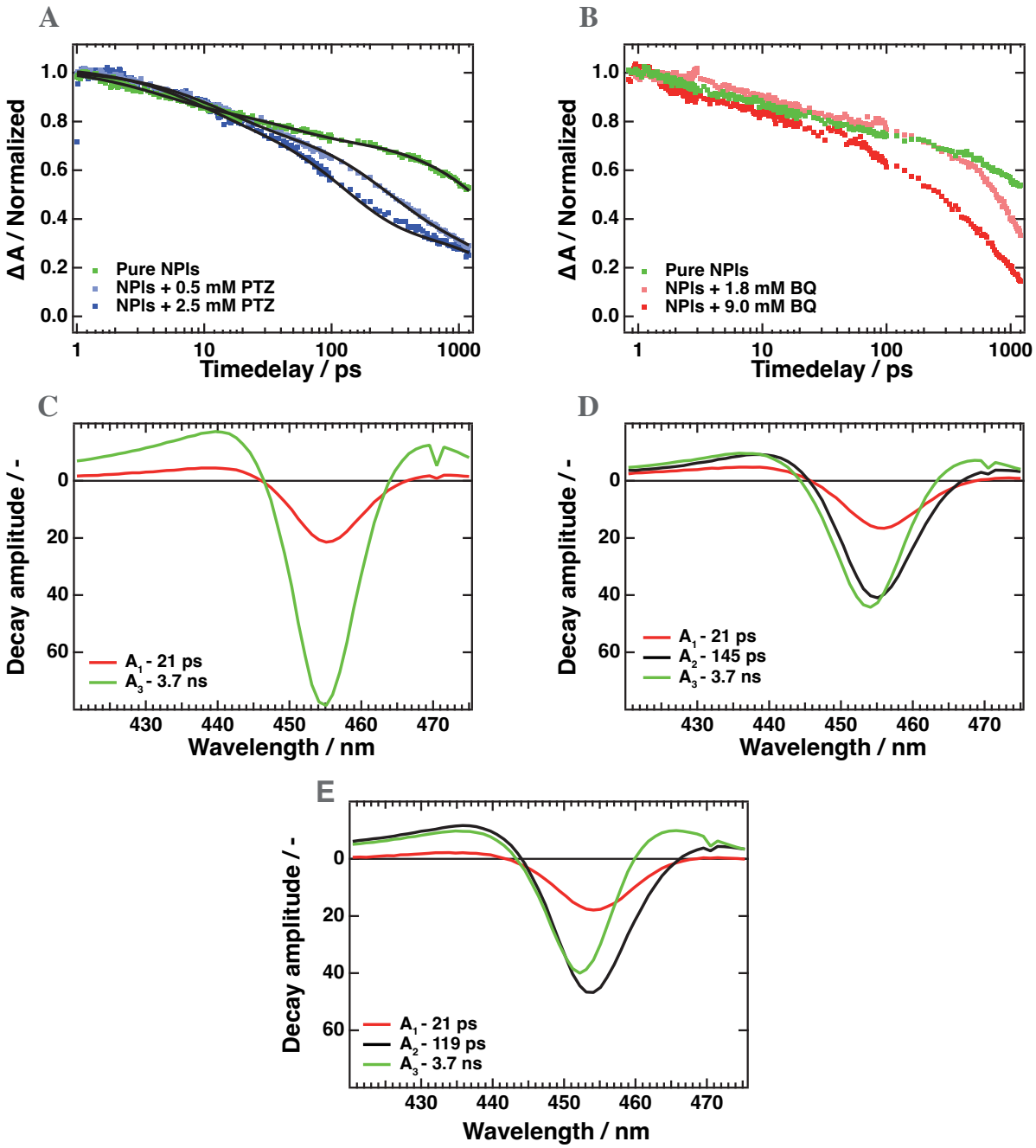

Figure 6.6: Normalized GSB dynamics (λ_{probe} = 445 nm) of pristine NPls and A) NPl-PTZ and B) NPl-BQ complexes. Decay associated spectra obtained by fitting the TA spectra of C) pristine NPls, D) NPls + 0.5 mM PTZ and E) NPls + 2.5 mM PTZ.

of holes and electrons at the band edge and may give information on the remaining carriers after ICT. **Figure 6.6** displays the normalized GSB dynamics (λ_{probe} = 448 nm) obtained by ultrafast TA with the best fits from the global fitting procedure performed on the NPl-PTZ complexes and their DAS. As already discussed in chapter 3, the TA dynamics for pristine NPls are fitted with a bi-exponential decay function with time constants of 21 ps for exciton trapping and 3.7 ns for radiative recombination. An additional component associated to HT, with a time constant of 100-150 ps, is required to fit NPl-PTZ complexes, corroborating the FLUPS measurements. Interestingly, for the highest PTZ or BQ concentration, after 1 ns the GSB intensity keeps 20% of its initial value, indicating that there are some leftover carriers at the band edge, even if the PL is quenched (**Figure 6.4.A** and **B**). Therefore, the CR rate between holes in PTZ (or electrons in BQ) and remaining electrons (or holes) in $CsPbBr_3$ NPls is slower than the time window of the instrumentation. It should also be pointed out that the GSB decay on such a late time scale might be due to a combination of CR and trapping of the leftover carriers.

Another way to probe the CR process is by tracking oxidized PTZ cations (or reduced BQ anions). While reduced BQ anions do not seem to absorb in the visible or near IR (Appendix, **Figure D.3**), it has already been reported that oxidized PTZ cations exhibit a slight absorption feature at 525 nm.[29,34] However, the absorption feature is too weak, even under strong illumination, to allow any quantitative analysis of the ultrafast TA data (Appendix, **Figure D.4**). Hence, the oxidized PTZ state was followed by nanosecond flash photolysis (**Figure 6.7**). The NPl-PTZ complexes were excited near the band edge (λ_{exc} = 430 nm), and the signal was probed from 480 nm to 550 nm. The negative feature at 527 nm is assigned to the oxidized PTZ photoinduced absorption and has a lifetime of 1 µs, assigned to back charge transfer,

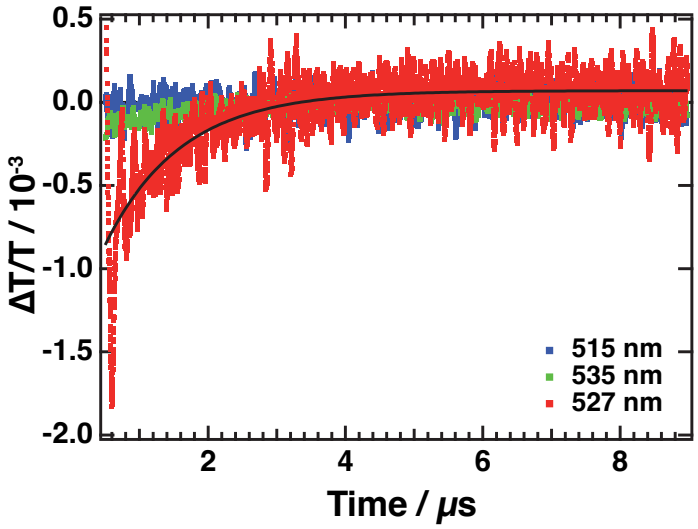

Figure 6.7: ns-TA dynamics of a NPl-PTZ complex solution around 525 nm for probing oxidized PTZ.

or CR. Long-lived CT states have already been observed in nanorods and NPl systems,[29,35,36] most probably due to the delocalization of the leftover carriers, which enables long-distance charge separation. Therefore, CR is four orders of magnitude slower than CS, demonstrating that $CsPbBr_3$ NPls are valuable candidates for light-harvesting applications. **Table 6.1** summarizes the main results obtain by combining FLUPS, fs-TA and flash photolysis for an average of one PTZ or BQ per NPl.

Table 6.1: Summary of the CT time constants, percentage of photogenerated charges carrier transferred to the acceptor, charge separated state lifetimes, acceptor concentrations and acceptor binding constants for an average of one acceptor per NPl.

m=1	$\tau_{CT,cold}$ [ns]	Charge sep. [%]	τ_{CR} [ns]	[A] [mM]	K_{acc} [M^{-1}]
NPl-PTZ	0.130	21	1000	0.45	690
NPl-BQ	0.120	15	-	1.7	130

6.2.4 Hot charge transfer

In photoactive materials, hot charge carriers are generated through absorption of high-energy photons, in other words photons with energies overcoming the SC optical band gap. Hot electrons and holes are, by definition, more energetic than band edge carriers. The relaxation of hot carriers to the lowest excited state usually induces heat, which is in most cases perceived as a loss of energy. Therefore, being able to use the excess energy before hot carrier relaxation is crucial for light-harvesting devices. It has been shown that the efficiency of solar cell devices can greatly overcome the Shockley-Queisser limit and reach 66% if hot charge carriers could be extracted.[37] Some studies have already reported efficient, sub-picosecond, hot carrier transfer from PNCs to organic acceptors.[22,23] But, while, under strong excitation regimes, weakly confined PNCs experience a phonon bottleneck effect leading to long-lived hot charge carriers, their NPl counterparts display ultrafast charge carrier cooling,[30] which is detrimental for extraction of hot charges.

To investigate hot carrier transfer in $CsPbBr_3$ NPl-acceptor complexes, the PL rise dynamics are scrutinized by exciting NPl-PTZ complexes with 0.86 eV excess energy (λ_{exc} = 340 nm, **Figure 6.8**). The initial PL intensity (PL at τ_{delay} = 0.4 ps) drops by up to 50%, and the quenching intensity depends on the PTZ concentration. Since FLUPS only probes emissive carriers, this drop accounts for an ultrafast PL quenching, at least faster than the temporal resolution of the setup, and may point out hot HT. Hence, the excess energy was further varied by pumping pristine NPls, NPl-PTZ and NPl-BQ complexes from 305 to 435 nm under a weak excitation regime. The acceptor concentration was set to 2.5 mM for the NPl-acceptor complexes. To quantitatively analyze hot carrier transfer, a careful correction procedure

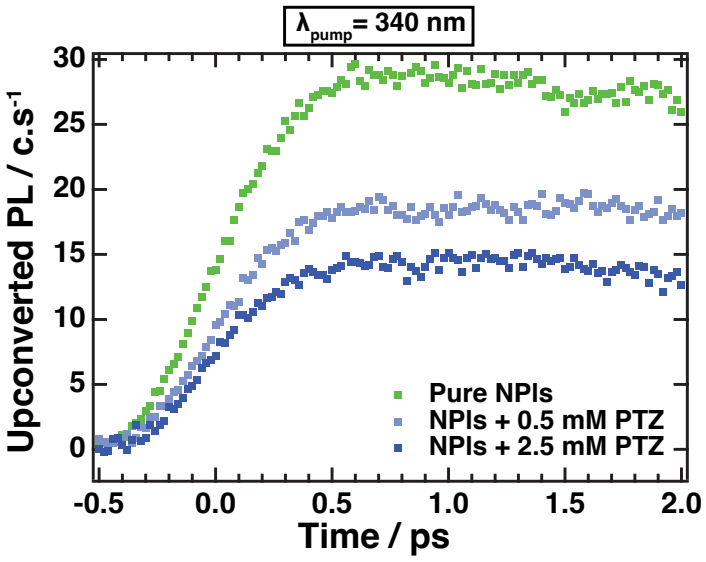

Figure 6.8: PL dynamics of NPl-PTZ complexes excited at λ_{exc} = 340 nm.

accounting for the dependence of the absorption cross-section on the pump wavelength must be set up. Indeed, for low excitation intensities the raw PL intensity scales linearly with the number of photogenerated excitons and depends on both the pump intensity and the absorption cross-section. It becomes impossible to control exactly the number of excitons per NPl when changing the excitation wavelength. To overcome this issue the PL dynamics were treated with a procedure detailed in the Appendices (section D.1). Basically, the PL intensity of pristine NPls was normalized after 0.5 ps and the same normalization factor was used for the NPl-acceptor complexes to obtain the "corrected" PL dynamics (**Figure 6.9, A and B**). In this way, if all the carriers relax to the band edge without being transferred to PTZ or BQ, the corrected PL dynamics would reach the unity. Therefore, the percentage of hot carrier transferred could be estimated by:

$$\%(\text{Hot carrier transferred}) = 1 - \frac{\text{PL}_{\text{acc}}}{\text{PL}_0} \tag{6.6}$$

where PL_0 and PL_{acc} are the normalized PL of pristine NPls and NPl-acceptor complexes [-], respectively.

The corrected PL intensity of both NPl-acceptor complexes drops with increasing excitation energy, indicating that more and more charge carriers are transferred before relaxing to the band edge. The percentage of hot carrier transferred is shown in **Figure 6.9.C**. For close-to-resonant excitation, λ_{exc} = 435 nm, the ratio between PL_{acc} and PL_0 reaches the unity, as expected. Conversely, up to 65% of hot holes (40% of hot electrons) are successfully transferred to PTZ (BQ) by exciting the NPl-acceptor complexes with 1.3 eV excess energy. As it has already been argued, hot charge transfer competes with

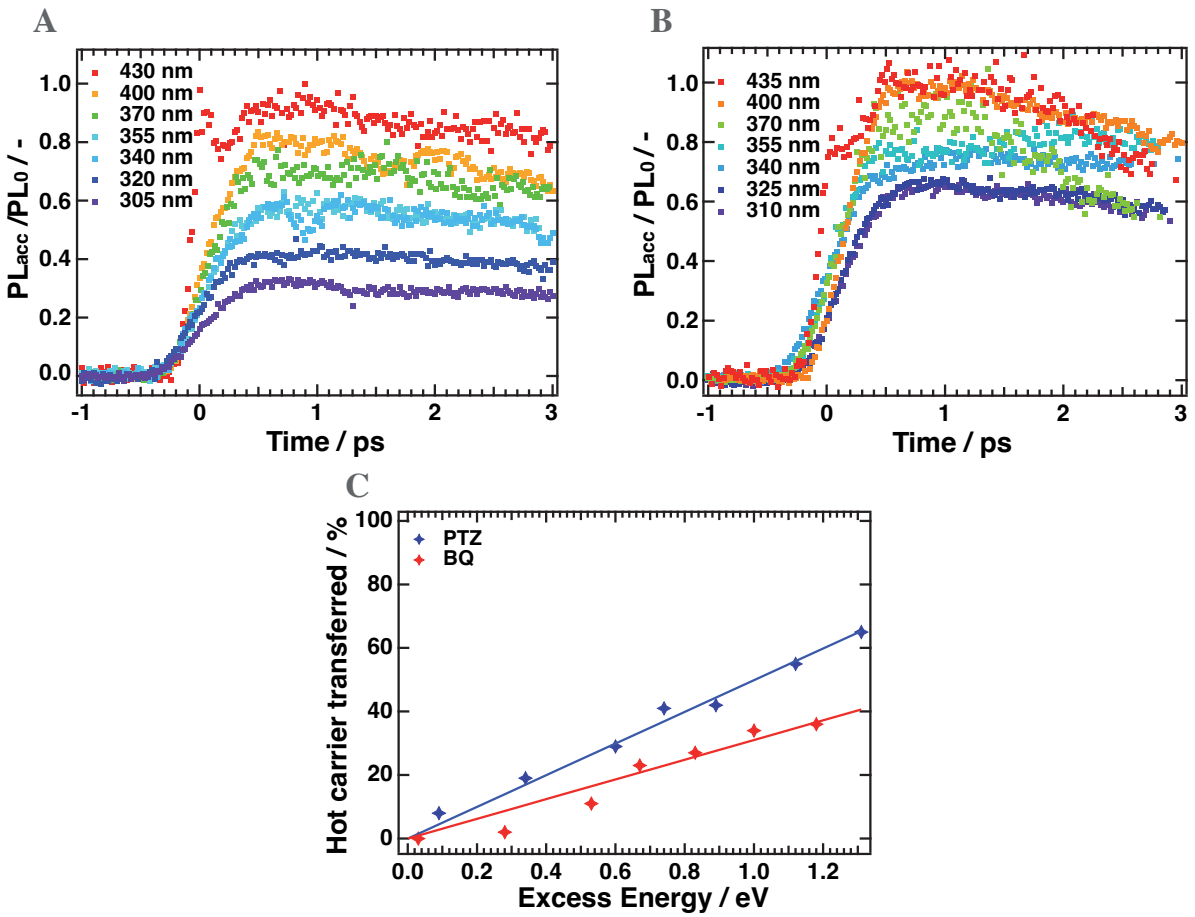

Figure 6.9: Corrected PL dynamics (λ_{probe} = 455 nm) of A) NPl-PTZ and B) NPl-BQ complexes excited at different wavelengths. C) Hot charge carrier extraction efficiency dependence on the excitation excess energy for an acceptor concentration of 2.5 mM.

charge carrier cooling, but the two processes cannot be distinguished by the FLUPS instrumentation. However, **Figure 6.10.A** shows that, even for 1.3 eV excess energy, hot carrier cooling in pristine NPls remains faster than the FLUPS temporal resolution (250 fs). Besides, **Figure 6.10.B** shows that the addition of molecular acceptors does not slow down the cooling rate of the remaining charge carriers. Therefore, by considering that hot charge carriers have a sub 250 fs lifetime, the hot HT time constant should be faster than 150 fs to achieve 60% efficiency, which is three orders of magnitude faster than cold charge transfer. This difference has been ascribed to a strong electronic coupling between the perovskite hot states and the molecular acceptors combined with larger thermodynamic driving forces,[22,38,39] making strongly confined LHP NPls promising for light-harvesting applications.

Yet, because of the ultrafast PL quenching, some fundamental questions remain open: is the hot carrier transfer becoming faster at high excitation energies, or is the enhanced transfer yield explained by the lengthening of the charge carrier relaxation? Is it possible to substitute conventional PTZ (BQ) with molecular acceptors having lower HOMO (higher LUMO) levels to harvest the excess energy?

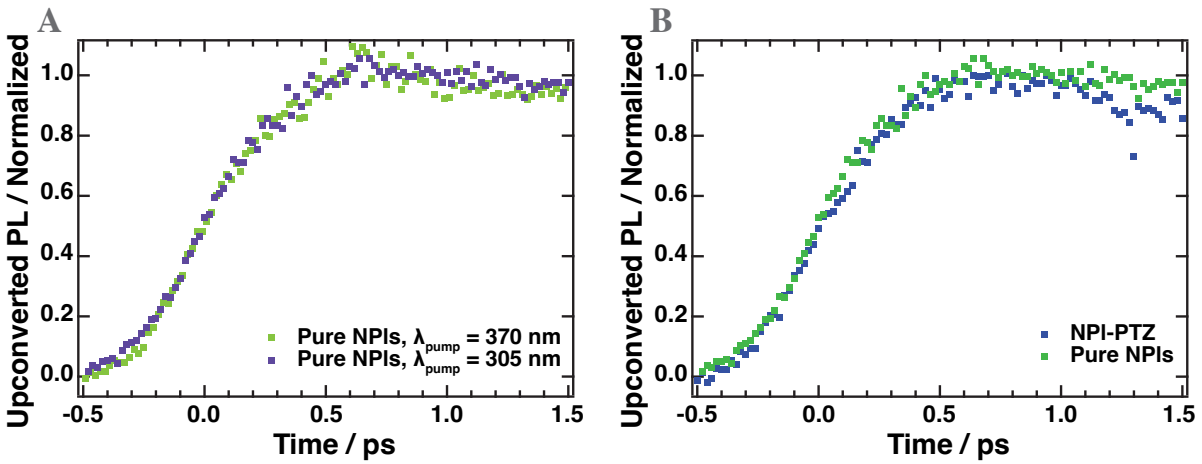

Figure 6.10: PL rise dynamics (λ_{probe} = 455 nm) for A) pristine NPls with different excitation energies and B) pristine NPls and NPl-PTZ complexes excited at λ = 305 nm.

6.3 Conclusion

To summarize, NPl-acceptor complexes were synthesized using standard organic molecules, BQ and PTZ, and we investigated the CS mechanism at the NPl surface. While the NC structure was retained upon addition of PTZ (BQ), a fast PL quenching was observed due to the HT (ET) from the perovskite band edge states to the PTZ HOMO (BQ LUMO). Tightly bound excitons in $CsPbBr_3$ NPls are easily broken, which is favored by large thermodynamic driving forces, 0.87 and 0.85 eV for the HT and ET, respectively.

ICT was then scrutinized using ultrafast spectroscopic methods. By isolating the PL decay arising from carrier transfer, HT (ET) constants were found to be 130 ps (120 ps) for an average of one acceptor molecule per NPl. The charge transfer process competes with exciton trapping into surface states, but up to 50% (32%) of the photogenerated holes (electrons) were transferred to PTZ (BQ) for an acceptor concentration of 4 mM. After the charge separation, NPl-acceptor complexes showed long-lived CT states, $\approx$ 1 µs, which is promising for further charge collection.

Finally, with 1.3 eV excess energy, up to 65% of hot holes (40% of hot electrons) were transferred to the PTZ HOMO (BQ LUMO) before reaching the band edge. Even with ultrafast charge carrier cooling rates in LHP NPls, hot carrier transfer is promoted, most likely due to enhanced electronic coupling between NPl hot states and the acceptor. Ultrafast hot charge carrier extraction opens the door for harvesting photons of higher energies.

Altogether, these results show great promise for light-harvesting applications. Additional engineering

should be conducted to tune and optimize the NPl/acceptor interface through a careful selection of molecular acceptors. The main focus should be to enhance the electronic coupling between the NPl and the acceptor (cold and hot) while retaining their stability NPl-acceptor complexes. The CS yield could also be improved by reducing the number of surface trap states in NPls with less labile capping ligands. However, this might also prevent strong binding between molecular acceptors and the perovskite surface.

6.4 Methods

6.4.1 Sample preparation

$CsPbBr_3$ NPls were synthesized according to the procedure detailed in chapter 3. The NPl solution was first diluted in dodecane to obtain an absorption of 0.5 at 400 nm in a 1 cm path length quartz cuvette (FireflySci). 1 mL of the solution was kept apart to serve as the reference sample (also called pristine NPl solution in the text). Then, a progressive amount of PTZ (from 0.2 mM to 4.0 mM) or BQ (from 0.5 mM to 9.0 mM) was added in the vial, and the mixture was sonicated for 10 minutes at room temperature.

6.4.2 Sample characterization

Cyclic voltammetry – The electrochemical measurements to estimate the HOMO/LUMO level of PTZ and BQ were performed with the same instrumentation as described in chapter 3. The acceptor solution was set to a 2.3 mM concentration with a scan rate of 50 $mV.s^{-1}$.

TEM – TEM images of the NPl-acceptor complexes were taken at the Brazilian Nanotechnology National Laboratory (Sao Paulo) on a JEOL JEM 2100F microscope with an Orius camera (SC200). The samples were prepared by drop-casting a small amount of the concentrated NPl-PTZ solution on a TEM grid covered with an ultrathin carbon film.

Steady-state PL & absorption – Steady-state PL and TCSPC measurements were carried out on a Horiba Jobin Yvon Fluorolog-3 instrument. The excitation source for TCSPC measurements was a nanoLED N-390, which emits 1.3 ns long pulses centered at 390 nm with a 1 MHz repetition rate. The sample emission was detected with a photomultiplier tube set at 90° relative to the excitation source. Linear absorption spectra were taken on a Perkin Elmer Lambda 950 UV-Vis-NIR spectrophotometer.

Flash photolysis – Flash photolysis is analogous to femtosecond transient absorption (TA) spectroscopy except with a time delay (and time window) in the nanosecond-microsecond range. Here, a frequency-

tripled Q-switched Nd:YAG laser (Surelite, Continuum, 20 Hz repetition rate) was used to pump a tunable optical parametric oscillator (OPO-355, GWU) for producing 10 ns long pulses centered at $\lambda = 430$ nm. The pump intensity was reduced to 0.3 mJ/cm^2 using neutral density filters. The photoinduced signal was probed each 10 nm between 480 and 550 nm by a continuous wave light beam (Xenon arc lamp) filtered by a monochromator. After hitting the sample with an angle of 45°, the probe beam was collected by a second grating monochromator (CS260, Newport) and sent to a Silicon Amplified Photodetector (PDA 100A-EC, Thorlabs), converting photons into electrons. The induced transient voltage was recorded by a digital signal analyser (DPO 7104C, Tektronix), and the data acquisition was averaged over 5000 laser shots to obtain a suitable signal-to-noise ratio. The data acquired with the probe only were subtracted from the ones acquired with the pump and the probe to give the ΔT.

Ultrafast characterization – Broadband FLUPS and TA measurements were acquired on the instruments previously described. The variable excitation wavelength on the FLUPS (λ_{exc} = 305-435 nm) was obtained with the output of a second optical parametric amplifier, which was focused on a 200 μm spot and attenuated to 10 nJ at the sample position with a variable neutral density filter.

6.4.3 Data treatment

A global fitting procedure was applied to treat FLUPS and TA data for pristine NPls and NPl-acceptor complexes with different acceptor concentrations. The kinetic traces were cut before one picosecond to exclude the contribution of hole localization (chapter 4) and focus on the ICT from relaxed carriers. Firstly, the pristine NPl sample was fitted with a tri-exponential decay function (bi-exponential for TA), leaving the time constants free. The fast decay was assigned to reversible charge carrier trapping, the second to trapping into deep trap states and the third radiative recombination. Then, the NPl-acceptor samples were fitted with an additional component accounting for charge carrier transfer but keeping the time constant for trapping and radiative recombination fixed to the initial values.

Bibliography

[1] Xu, J.; Li, X.; Xiong, J.; Yuan, C.; Semin, S.; Rasing, T.; Bu, X. Halide Perovskites for Nonlinear Optics. *Adv. Mater.* **2020**, *32*, 1806736.

[2] Lin, Y.-H. et al. Deciphering photocarrier dynamics for tuneable high-performance perovskite-organic semiconductor heterojunction phototransistors. *Nat. Commun.* **2019**, *10*.

[3] Kang, C. H.; Dursun, I.; Liu, G.; Sinatra, L.; Sun, X.; Kong, M.; Pan, J.; Maity, P.; Ooi, E.-N.; Ng, T. K.; Mohammed, O. F.; Bakr, O. M.; Ooi, B. S. High-speed colour-converting photodetector with all-inorganic $CsPbBr_3$ perovskite nanocrystals for ultraviolet light communication. *Light Sci. Appl.* **2019**, *8*.

[4] Gong, M.; Sakidja, R.; Goul, R.; Ewing, D.; Casper, M.; Stramel, A.; Elliot, A.; Wu, J. Z. High-Performance All-Inorganic $CsPbCl_3$ Perovskite Nanocrystal Photodetectors with Superior Stability. *ACS Nano* **2019**, *13*, 1772–1783.

[5] Lin, K. et al. Perovskite light-emitting diodes with external quantum efficiency exceeding 20 per cent. *Nature* **2018**, *562*, 245–248.

[6] Chiba, T.; Hayashi, Y.; Ebe, H.; Hoshi, K.; Sato, J.; Sato, S.; Pu, Y.-J.; Ohisa, S.; Kido, J. Anion-exchange red perovskite quantum dots with ammonium iodine salts for highly efficient light-emitting devices. *Nat. Photonics* **2018**, *12*, 681–687.

[7] Protesescu, L.; Yakunin, S.; Bodnarchuk, M. I.; Krieg, F.; Caputo, R.; Hendon, C. H.; Yang, R. X.; Walsh, A.; Kovalenko, M. V. Nanocrystals of Cesium Lead Halide Perovskites ($CsPbX_3$, X = Cl, Br, and I): Novel Optoelectronic Materials Showing Bright Emission with Wide Color Gamut. *Nano Lett.* **2015**, *15*, 3692–3696.

[8] Di Stasio, F.; Christodoulou, S.; Huo, N.; Konstantatos, G. Near-Unity Photoluminescence Quantum

Yield in $CsPbBr_3$ Nanocrystal Solid-State Films via Postsynthesis Treatment with Lead Bromide. *Chem. Mater.* **2017**, *29*, 7663–7667.

[9] Ambroz, F.; Xu, W.; Gadipelli, S.; Brett, D. J. L.; Lin, C.-T.; Contini, C.; McLachlan, M. A.; Durrant, J. R.; Parkin, I. P.; Macdonald, T. J. Room Temperature Synthesis of Phosphine-Capped Lead Bromide Perovskite Nanocrystals without Coordinating Solvents. *Part. Part. Syst. Char.* **2020**, *37*, 1900391.

[10] Xu, Y.; Cao, M.; Huang, S. Recent advances and perspective on the synthesis and photocatalytic application of metal halide perovskite nanocrystals. *Nano Res.* **2021**,

[11] DuBose, J. T.; Kamat, P. V. Probing Perovskite Photocatalysis. Interfacial Electron Transfer between $CsPbBr_3$ and Ferrocene Redox Couple. *J. Phys. Chem. Lett.* **2019**, *10*, 6074–6080.

[12] Kobosko, S. M.; DuBose, J. T.; Kamat, P. V. Perovskite Photocatalysis. Methyl Viologen Induces Unusually Long-Lived Charge Carrier Separation in $CsPbBr_3$ Nanocrystals. *ACS Energy Lett.* **2020**, *5*, 221–223.

[13] DuBose, J. T.; Kamat, P. V. Efficacy of Perovskite Photocatalysis: Challenges to Overcome. *ACS Energy Lett.* **2022**, *7*, 1994–2011.

[14] Wu, K.; Liang, G.; Shang, Q.; Ren, Y.; Kong, D.; Lian, T. Ultrafast Interfacial Electron and Hole Transfer from $CsPbBr_3$ Perovskite Quantum Dots. *J. Am. Chem. Soc.* **2015**, *137*, 12792–12795.

[15] Zhang, Y.-X.; Wang, H.-Y.; Zhang, Z.-Y.; Zhang, Y.; Sun, C.; Yue, Y.-Y.; Wang, L.; Chen, Q.-D.; Sun, H.-B. Photoluminescence quenching of inorganic cesium lead halides perovskite quantum dots ($CsPbX_3$) by electron/hole acceptor. *Phys. Chem. Chem. Phys.* **2017**, *19*, 1920–1926.

[16] Luo, X.; Liang, G.; Wang, J.; Liu, X.; Wu, K. Picosecond multi-hole transfer and microsecond charge-separated states at the perovskite nanocrystal/tetracene interface. *Chem. Sci.* **2019**, *10*, 2459–2464.

[17] De, A.; Mondal, N.; Samanta, A. Hole Transfer Dynamics from Photoexcited Cesium Lead Halide Perovskite Nanocrystals: 1-Aminopyrene as Hole Acceptor. *J. Phys. Chem. C* **2018**, *122*, 13617–13623.

[18] Maity, P.; Dana, J.; Ghosh, H. N. Multiple Charge Transfer Dynamics in Colloidal $CsPbBr_3$ Perovskite Quantum Dots Sensitized Molecular Adsorbate. *J. Phys. Chem. C* **2016**, *120*, 18348–18354.

[19] Begum, R.; Parida, M. R.; Abdelhady, A. L.; Murali, B.; Alyami, N. M.; Ahmed, G. H.; Hedhili, M. N.; Bakr, O. M.; Mohammed, O. F. Engineering Interfacial Charge Transfer in $CsPbBr_3$ Perovskite Nanocrystals by Heterovalent Doping. *J. Am. Chem. Soc.* **2017**, *139*, 731–737.

[20] Ijaz, P.; Imran, M.; Soares, M. M.; Tolentino, H. C. N.; Martín-García, B.; Giannini, C.; Moreels, I.; Manna, L.; Krahne, R. Composition, Size, and Surface Functionalization Dependent Optical Properties of Lead Bromide Perovskite Nanocrystals. *J. Phys. Chem. Lett.* **2020**,

[21] De Roo, J.; Ibáñez, M.; Geiregat, P.; Nedelcu, G.; Walravens, W.; Maes, J.; Martins, J. C.; Van Driessche, I.; Kovalenko, M. V.; Hens, Z. Highly Dynamic Ligand Binding and Light Absorption Coefficient of Cesium Lead Bromide Perovskite Nanocrystals. *ACS Nano* **2016**, *10*, 2071–2081.

[22] De, A.; Das, S.; Samanta, A. Hot Hole Transfer Dynamics from $CsPbBr_3$ Perovskite Nanocrystals. *ACS Energy Lett.* **2020**, *5*, 2246–2252.

[23] Sarkar, S.; Ravi, V. K.; Banerjee, S.; Yettapu, G. R.; Markad, G. B.; Nag, A.; Mandal, P. Terahertz Spectroscopic Probe of Hot Electron and Hole Transfer from Colloidal $CsPbBr_3$ Perovskite Nanocrystals. *Nano Lett.* **2017**, *17*, 5402–5407.

[24] Weidman, M. C.; Goodman, A. J.; Tisdale, W. A. Colloidal Halide Perovskite Nanoplatelets: An Exciting New Class of Semiconductor Nanomaterials. *Chem. Mater.* **2017**, *29*, 5019–5030.

[25] Akkerman, Q. A.; Motti, S. G.; Srimath Kandada, A. R.; Mosconi, E.; D'Innocenzo, V.; Bertoni, G.; Marras, S.; Kamino, B. A.; Miranda, L.; De Angelis, F.; Petrozza, A.; Prato, M.; Manna, L. Solution Synthesis Approach to Colloidal Cesium Lead Halide Perovskite Nanoplatelets with Monolayer-Level Thickness Control. *J. Am. Chem. Soc.* **2016**, *138*, 1010–1016.

[26] Shamsi, J.; Dang, Z.; Bianchini, P.; Canale, C.; Di Stasio, F.; Brescia, R.; Prato, M.; Manna, L. Colloidal Synthesis of Quantum Confined Single Crystal $CsPbBr_3$ Nanosheets with Lateral Size Control up to the Micrometer Range. *J. Am. Chem. Soc.* **2016**, *138*, 7240–7243.

[27] Marjit, K.; Ghosh, G.; Ghosh, S.; Sain, S.; Ghosh, A.; Patra, A. Structural Analysis and Carrier Relaxation Dynamics of 2D $CsPbBr_3$ Nanoplatelets. *J. Phys. Chem. C* **2021**, *125*, 12214–12223.

[28] Ahmed, G. H.; Liu, J.; Parida, M. R.; Murali, B.; Bose, R.; AlYami, N. M.; Hedhili, M. N.; Peng, W.; Pan, J.; Besong, T. M. D.; Bakr, O. M.; Mohammed, O. F. Shape-Tunable Charge Carrier Dynamics at the Interfaces between Perovskite Nanocrystals and Molecular Acceptors. *J. Phys. Chem. Lett.* **2016**, *7*, 3913–3919.

[29] Li, Q.; Lian, T. Ultrafast Charge Separation in Two-Dimensional $CsPbBr_3$ Perovskite Nanoplatelets. *J. Phys. Chem. Lett.* **2019**, *10*, 566–573.

[30] Hintermayr, V. A.; Polavarapu, L.; Urban, A. S.; Feldmann, J. Accelerated Carrier Relaxation through Reduced Coulomb Screening in Two-Dimensional Halide Perovskite Nanoplatelets. *ACS Nano* **2018**, *12*, 10151–10158.

[31] Wu, X.; Trinh, M. T.; Zhu, X.-Y. Excitonic Many-Body Interactions in Two-Dimensional Lead Iodide Perovskite Quantum Wells. *J. Phys. Chem. C* **2015**, *119*, 14714–14721.

[32] Morris-Cohen, A. J.; Frederick, M. T.; Cass, L. C.; Weiss, E. A. Simultaneous Determination of the Adsorption Constant and the Photoinduced Electron Transfer Rate for a Cds Quantum Dot–Viologen Complex. *J. Am. Chem. Soc.* **2011**, *133*, 10146–10154.

[33] Morris-Cohen, A. J.; Vasilenko, V.; Amin, V. A.; Reuter, M. G.; Weiss, E. A. Model for Adsorption of Ligands to Colloidal Quantum Dots with Concentration-Dependent Surface Structure. *ACS Nano* **2012**, *6*, 557–565.

[34] Karpinska, J.; Starczewska, B.; Puzanowska-Tarasiewicz, H. Analytical Properties of 2- and 10-Disubstituted Phenothiazine Derivatives. *Anal. Sci.* **1996**, *12*, 161–170.

[35] Wu, K.; Zhu, H.; Liu, Z.; Rodríguez-Córdoba, W.; Lian, T. Ultrafast Charge Separation and Long-Lived Charge Separated State in Photocatalytic CdS–Pt Nanorod Heterostructures. *J. Am. Chem. Soc.* **2012**, *134*, 10337–10340.

[36] Wu, K.; Chen, Z.; Lv, H.; Zhu, H.; Hill, C. L.; Lian, T. Hole Removal Rate Limits Photodriven H_2 Generation Efficiency in CdS-Pt and CdSe/CdS-Pt Semiconductor Nanorod–Metal Tip Heterostructures. *J. Am. Chem. Soc.* **2014**, *136*, 7708–7716.

[37] Ross, R. T.; Nozik, A. J. Efficiency of hot-carrier solar energy converters. *J. Appl. Phys.* **1982**, *53*, 3813–3818.

[38] Jiang, Y.; Wang, X.; Pan, A. Properties of Excitons and Photogenerated Charge Carriers in Metal Halide Perovskites. *Adv. Mater.* **2019**, *31*, 1806671.

[39] Grimaldi, G.; Crisp, R. W.; ten Brinck, S.; Zapata, F.; van Ouwendorp, M.; Renaud, N.; Kirkwood, N.; Evers, W. H.; Kinge, S.; Infante, I.; Siebbeles, L. D. A.; Houtepen, A. J. Hot-electron transfer in quantum-dot heterojunction films. *Nat. Commun.* **2018**, *9*, 2310.

Conclusions and outlooks

The work presented here has been initiated by the installation of a broadband fluorescence upconversion spectroscopy (FLUPS) setup along with Prof. Ernsting. Some additional adaptations were realized to push the FLUPS potential to a broader range of applications. Then, the main goal was to combine it to other spectroscopic techniques, principally fs-transient absorption (TA), to investigate ultrafast excited state dynamics in semiconductors. Since the FLUPS and TA signals provide similar but complementary results, combining their data becomes crucial to obtain pieces of evidence for understanding photophysical processes. Besides, perovskite nanocrystals (PNCs) appeared to be a central piece for optoelectronic applications since they have a band gap energy in the visible range, exhibit high absorption coefficients with an intense and short photoluminescence (PL), but their photophysics remain poorly understood. **Figure 7** summarizes the charge carrier dynamics unveiled for colloidal $CsPbBr_3$ nanoplatelets (NPls).

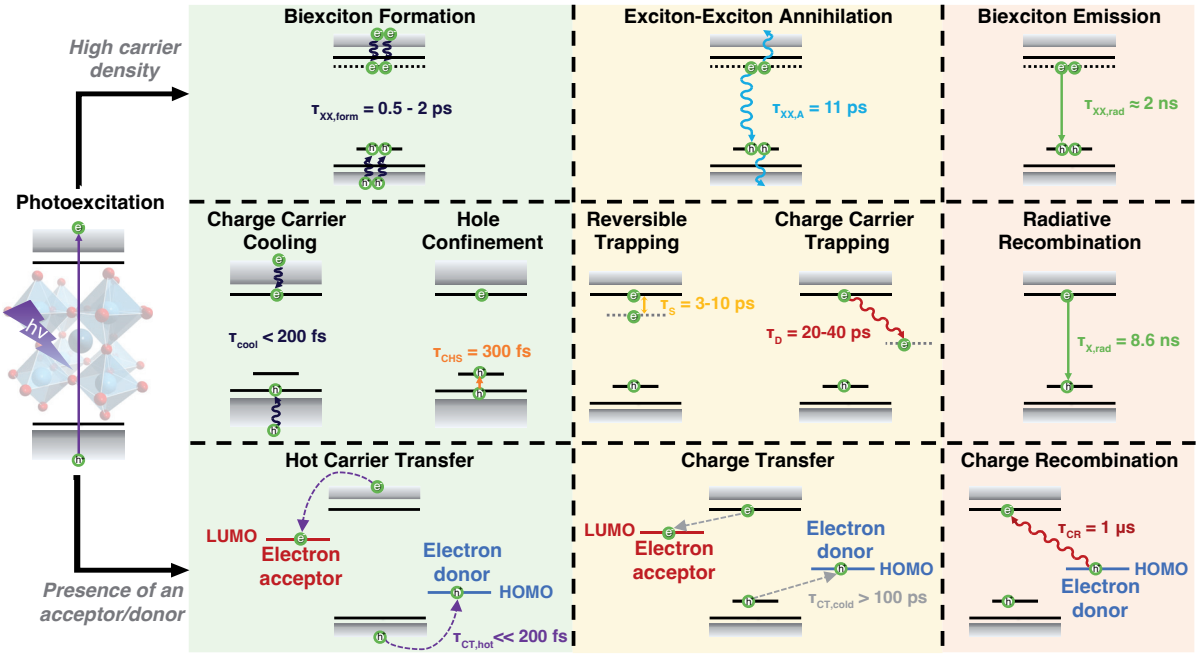

Figure 7: Summary on the photophysical processes observed for colloidal $CsPbBr_3$ NPls.

In chapter 3, the synthesis of colloidal $CsPbBr_3$ NPls capped with long-chain organic ligands was described. These NPls were characterized with standard methods such as transmission electron microscopy, cyclic voltammetry and UV-visible spectroscopy. The photogenerated charge carriers endured strong quantum and dielectric confinements leading to an intense excitonic absorption at 448 nm, an enhanced exciton binding energy (Δ_x = 334 meV) and a sharp and short-lived emission ($\tau_{x,rad}$ = 8.6 ns). Additionally, the light was shined on the role of the surface states: desorption of the capping ligands from the NPl surface led to under-coordinated Pb^{2+} atoms, which acted as trap states (τ_D = 20-40 ps) and reduced the photoluminescence quantum yield (PLQY). Overall, chapter 3 showed that $CsPbBr_3$ NPls are excellent candidates for blue-emitting devices, but they require particular attention to passivate the surface through post-synthetic treatment or capping ligand selection to further enhance the PLQY and stabilize the particles.

Chapter 4 focused on the charge carrier dynamics in $CsPbBr_3$ NPls at early, femtosecond/picosecond, time scales and under weak photoexcitation, $\langle N_x \rangle << 1$. Because of the large surface-to-volume ratio, strongly confined NPls displayed ultrafast, $\tau_{cool} < 200$ fs, charge carrier relaxation by dissipating the excess energy via vibrations of the organic capping ligands. Besides, the 49 meV Stokes shift arose from the localization of photogenerated holes in confined hole states (CHSs), while the band edge emission was short-lived, τ_{CHS} = 300 fs. The PL was also influenced by shallow trap states lying close to the main emissive state, which caused a fast, τ_S = 3-10 ps, and reversible exciton trapping. The nature of the capping ligands may influence the energy location and density of the shallow states. Finally, for highly concentrated solutions, efficient photon reabsorption by bigger NPls were observed, enlarging the external Stokes shift within the temporal resolution of the setups.

Conversely, the charge carrier dynamics under strong photoexcitation regimes, $\langle N_x \rangle > 1$, were reviewed in chapter 5. $CsPbBr_3$ NPls displayed stable and emissive biexcitons with a biexciton binding energy close to 70 meV. The biexciton recombination was dominated by exciton-exciton annihilation, $\tau_{xx,A}$ = 11 ps. Moreover, the hole localization process was slowed down to a few picoseconds at high excitation intensities, presumably because of the low density of states of the CHSs. This chapter shows that $CsPbBr_3$ NPls have an outstanding potential for lasing applications but are still limited by the challenging synthesis of stable NPl thin-films.

In chapter 6, the charge separation mechanism in $CsPbBr_3$ NPls was investigated by adding phenothiazine (PTZ) and p-benzoquinone (BQ) in solution, acting as hole and electron acceptors, respectively. It resulted in the formation of NPl-acceptor complexes which showed a PL quenching due to charge

transfer from the perovskite core to the organic molecules. The transfer of cold charge carriers exhibited a time constant of $\tau_{CT,cold} = 100$ ps, and the back recombination was four orders of magnitude slower, $\tau_{CR} = 1$ µs, due to the carrier delocalization over the NPl length. Furthermore, hot charge transfer rates, $\tau_{CT,hot} << 200$ fs, overcame the ultrafast charge carrier relaxation. The fast charge separation was promoted by a strong electronic coupling between the perovskite and the molecular acceptors, providing an efficient pathway to light harvesting. These results are of great importance for photocatalytic applications, and further work should focus on engineering the NPl/acceptor interface and tuning the capping ligands/acceptor chemistry. To enhance the separation yield, the binding of the acceptor on the NPl surface must be promoted while keeping low trap densities.

While this work emphasizes that $CsPbBr_3$ NPls are promising for optoelectronic applications, further engineering should be performed to address the aforementioned limitations: surface passivation, film formation, charge separation enhancement... The trapping dynamics must be fully characterized and understood to achieve these goals. For example, being able to settle the mechanisms of the hole localization through fs x-ray spectroscopy would be of great use. Indeed, x-ray absorption or emission spectroscopy could track the lead oxidation state, which contributes to the valence band orbital. To achieve this, a collaboration with the group of Pr. Gawelda (Autonoma University of Madrid) has been started, and proposals with the aim of obtaining beam time are ongoing.

Along this thesis, numerous disparities between PNCs of various shapes and sizes were also highlighted. By slightly varying the synthesis protocol, one can easily obtain three-dimensional to zero-dimensional PNC structures and assemble new devices with mixed perovskite dimensions. For example, controlled carrier localization (or separation) can be achieved by energy cascades (or cascade transfer), which may boost light-emitting device and solar-cell efficiencies. Besides, one may introduce functional electroactive organic moieties as capping ligands. This approach follows recent studies on the role of the organic spacer in 2D perovskites. It not only improves the material conductivity and provides a pathway for charge separation but also induces colossal changes in the charge carrier dynamics, such as fast PL quenching or formation of CT excitons.

Finally, some developments of the spectroscopic setups could be carried out to broaden the range of opportunities. Two main ideas came to mind over the last years. Firstly, one could add an optical cryostat setup to the FLUPS and measure temperature dependence PL dynamics with a sub-picosecond temporal resolution, which would be unique. For example, temperature dependence measurements would help the fundamental understanding of exciton trapping or exciton-lattice coupling. However, the FLUPS setup

would need to be considerably adjusted because of the numerous optics around the sample holder, notably the Schwarzschild objective used to amplify and focus the sample fluorescence. Secondly, on the TA setup, pump-push-probe experiments with a visible-pump and near-IR-push would have given supplementary information on the carrier relaxation, exciton trapping (or de-trapping) and charge separation processes. Yet, due to a lack of time and stability of our beloved 23 year old Clark laser, this setup has never been materialized.

Acknowledgments - Remerciements

Je souhaiterais tout d'abord remercier mon superviseur Pr. Jacques Moser pour m'avoir permis d'effectuer 4 belles années au sein de son groupe. J'ai été chanceux d'avoir été mis dans des conditions de travail presque idéales malgré la période un peu plus difficile. Nos discussions, scientifiques ou non, m'ont toujours permis d'avancer et j'en suis très reconnaissant. Je te souhaite une excellente fin de carrière et je ne doute pas que la suite sera belle !

I would also like to thank Prof. Natalie Banerji, Prof. Majed Chergui and Prof. Ajay Kandada for reading and bringing suggestions and corrections to the thesis. I express my gratitude to Prof. Sivula, who accepted to be the president of the jury.

Being part of a small group does not mean that you should have less interaction with other PhD students: they are, in fact, stronger. I truly loved spending these four year with you, Georgie, and I can't imagine a better colleague. We shared a lot, not only in the lab, but outside as well (from spinning to Marbula races via Rome and darts tournaments). You were always so smiling and cheerful (even if your jokes are not funny, ouaf ouaf), which helped me in the bad days! I truly hope we'll see each other around Lausanne or in the UK, Long live to the Queen and to Terry Boot. Yes.

I would like to acknowledge Brener, aka B-dawg, for all his work and support in the thesis. Having you by my side physically (or through Zoom) was particularly helpful. You came with your ideas and pushed me in these directions: thank you so much! In addition to being a great scientist, you are also a great friend. I loved your Brazilian stories, and I should admit that your jokes are a bit better than George's... Yes.

To the other labmates who shared wonderful year(s) with me. Firstly the old generation, Marine and

Andrès, for welcoming me into the group in 2018. Marine, tu as été une des raisons pour laquelle j'ai opté pour un doctorat dans ce groupe, ton dynamisme, ta bienveillance et tes conseils ont guidé une partie de ma vie et je te remercie du fond du coeur pour ça. Andrès, thank you for all the conversations we had, you were always asking the right questions to move forward. I wish you all the best for the future, and I hope we will see each other again. Yes. Vincent, even if you shared your time between Belgium and Lausanne, it is great to see you around and your presence will always be appreciated. Finally our two students-then-colleagues Juanma and Aaron. You brought freshness to the group and it was a pleasure to share the same offices! Aaron je suis certain que tes talents (scientifiques ou "dartsiques") te permettront d'aller où tu veux dans la vie.

Special thanks go to all the people I had the chance to collaborate with: Marko Stojanovic, Yameng Ren, Claudia Avalos, Simon Nussbaum and Anna Maron. Our interdisciplinary projects pushed me to expand my knowledge, and your help was precious. I would like to express my gratitude to all the EPFL entities (mechanical and electrical workshops, Anne-Lene and Fara in the administration) and Pr. Niko Ernsting and Dr. Arnulf Rosspeintner for helping me set up the FLUPS - without whom nothing would have been possible.

Je veux maintenant remercier mes amis qui m'ont permis de passer quatre années plus qu'agréables. Tout d'abord merci à la "Team Arcadie": Aline, Aurélien, Thomas, Gontran, Elliott et Danick. Cette thèse, vécue ensemble, nous a rapprochés et je suis sûr que nous regretterons bientôt ces moments passés à se plaindre de tout et n'importe quoi ! Je n'espère que pouvoir continuer à vous voir dans ce "monde d'après".

Merci également à mes amis de promo: Jean, Fanny, Guillaume, Manon, Joel, Manon, Manu, Alice, Roger et Robin. C'est une fierté que d'avoir pu rester proches et soudés. Nos séjours skis/randos sont merveilleux et continueront à travers les années, j'en suis certain.

Merci aux ex-Montréalais Robin, Charles, Ben, Thomas. Loin des yeux mais pas loin du coeur. Je garderai toujours cette tendresse envers cette année 2017-2018 passée avec vous...

Merci au gang d'Annemasse (+ guest): Hugo, Alex, Julien, Adrien, Vesin, Valentin, JF, Arnould, Alexis, Romain. Nos multiples soirées dans la coloc laisseront des souvenirs impérissables.

Merci aux amis de la course, ceux avec qui j'ai passé les moments les plus douloureux mais peut-être aussi les plus épanouissants. L'équipe du Marathon de Paris (et de la prépa qui va avec): Marco, Do-

rian, Charlotte, P-L, Clarisse, Alex. Les nuls du Footing, Vélo, Hypo, Apéro: Guillaume, Arthur, Joel, Maxime, Grégoire. Et également tous les habitués du centre sportif ou de CTT: Enrico, Lucas, Thomas, Gael, Julien, Enzo, Elvira, Jade, Phoebe... Merci aussi à Pascal et Fabien de m'avoir remis en place ou fait souffrir aux moments opportuns !

Je tiens également à remercier l'équipe des Jean-Mich: Maxence, Anthony, Baptiste et Jens pour ces deux séjours d'une semaine à parcourir la France à vélo. J'ai déjà hâte d'en faire plus avec vous.

Pour finir, je tiens à remercier du fond de mon coeur mon incroyable famille... Je suis ému rien qu'au fait d'écrire ces lignes... Je vais faire court mais je pourrais passer des heures à vous remercier. Merci à Papa et Maman de m'avoir toujours soutenu. J'ai vraiment une chance folle de vous avoir et ne me lasserai jamais de passer du temps avec vous. Malgré la distance (plus ou moins importante) je vous aime de tout mon coeur. Cela tient pour toi aussi ma Louloutte. Je suis vraiment fier de toi et de ce que tu es devenue et j'espère que l'on ne se séparera jamais. Pour finir, Papi, Mamie: vous êtes vraiment les grands-parents rêvés, je suis si heureux de vous rendre fier et j'espère vous garder à côté de moi le maximum de temps possible. Je vous souhaite toute la santé du monde et suis si content de vous avoir dans ma vie.

Et je n'oublierai jamais non plus cette année 2020, Louise. Je t'ai rencontré au milieu de mon doctorat et tu auras changé ma vie à jamais. Je suis si heureux de partager ma vie avec toi désormais. La fin de cette thèse signe le début d'une nouvelle page de ma vie, mais ce sera toujours à tes côtés, c'est l'essentiel. Je t'aime éperdument... Merci aussi à ta famille, Sabine et Bertrand qui m'ont accueilli les bras ouverts (et remplis de chocolat!!). Nos voyages en Alsace sont toujours très agréables grâce à vous.

Pour conclure, j'adresse ma gratitude à quelqu'un qui ne comprendra pas (et ne lira pas ces lignes) mais qui m'a permis de me changer les idées tout au long de l'écriture de la thèse: Madame Maya le chat.

Appendices

Appendix A - Characterization of $CsPbBr_3$ NPls

A - Additional derivation

Quantum-well model

The quantum well model (**Equation A.1**) was used to fit the absorption spectra of strongly confined systems,[1–3] and, particularly, $CsPbBr_3$ NPls as displayed in **Figure 3.2.A**. Here, the absorbance from the sample, Abs(E), is given by the sum of the excitonic absorption, X(E), and the continuous band absorption, Cont(E), multiplied by a constant factor:

$$\mathrm{Abs}(E) = \mathrm{cst} \cdot [\mathrm{X}(E) + \mathrm{Cont}(E)] \qquad \text{(Eq. A.1)}$$

And X(E) and Cont(E) are expressed by:

$$X(E) = \frac{1}{2\eta}\left[\mathrm{ERF}\left(\frac{E - E_\mathrm{x}}{w_\mathrm{x}} - \frac{w_\mathrm{x}}{2\eta}\right) + 1\right] \exp\left(\frac{w_\mathrm{x}^2}{4\eta^2} - \frac{E - E_\mathrm{x}}{\eta}\right) \qquad \text{(Eq. A.2)}$$

$$\mathrm{Cont}(E) = \frac{H}{2\eta}\left[\mathrm{ERF}\left(\frac{E - E_\mathrm{x} - \Delta_\mathrm{x}}{w_c} - \frac{w_\mathrm{x}}{2\eta}\right) + 1\right] \qquad \text{(Eq. A.3)}$$

where E_x is the exciton transition energy [eV], Δ_x is the exciton binding energy [eV], w_x is the exciton peak width [eV], w_c, is the continuum edge width [eV], H is the continuum step height [-], and η is the asymmetric broadening [eV]. The results of the fit are summarized in the **Table A.1**.

Table A.1 - Extracted parameters from the fitted equations displayed in Figure 3.2.A

Parameters / unit	**Values**
$\mathbf{E_x}$ / eV	$2.78 \pm 3{\cdot}10^{-4}$
$\boldsymbol{\Delta_x}$ / meV	334 ± 12
$\boldsymbol{w_x}$ / meV	49 ± 0.3
$\boldsymbol{w_c}$ / meV	286 ± 3
$\boldsymbol{H}$ / -	8.45 ± 0.08
$\boldsymbol{\eta}$ / meV	56 ± 0.8
cst / -	$0.123 \pm 9{\cdot}10^{-4}$

Cyclic voltammetry correction

To estimate the energy levels for the $CsPbBr_3$ NPls, it is more suitable to compute the values against vacuum level:

$$E \text{ (vs. vac.)} = -(E_{ox/red} + 4.5)eV \qquad \text{(Eq. A.4)}$$

The value of -4.5 eV refers to the $Fc^{0/+}$ correction to the vacuum level potential of the normal hydrogen electrode (NHE).[4]

PLQY estimation

To estimate the PLQY of the $CsPbBr_3$ NPl solution, the comparative method was applied by connecting the PL of the NPls to the one of a known standard, Coumarin 102 (C102).[5] Both samples should emit in the same energy range and be measured under the same experimental conditions (same setup, same day, same temperature, same optical path length for the cuvette) to minimize the risk of errors. In addition, each sample should absorb the same number of photons: the absorption values should be equivalent at the excitation wavelength. Thus, C102 dye in ethanol was selected, which has a PL maximum at 460 nm and a PLQY of 0.58 (**Figure A.4**).[6]

Then, a simple ratio between the integrated PL of the NPl solution with the integrated PL of the dye solution was done and the obtained value was multiplied it by the PLQY of C102.

To reduce the margin of error, one would be tempted to repeat this measurement for different dye and NPl concentrations. However, due to the dynamic binding between the capping ligand and the perovskite surface, NPls deteriorate at a low concentration (absorption < 0.2), which greatly reduces the measurement range. Since PLQY measurements are not crucial to this work but are here to give a general trend, it has been decided to measure the emission spectra at only one concentration.

A - Additional figures

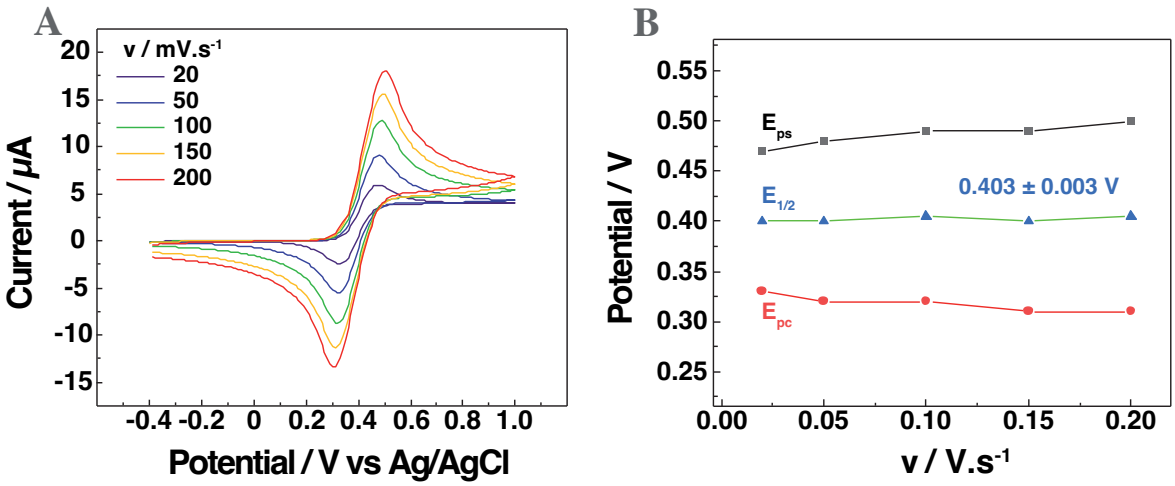

Figure A.1: Cyclic voltammogram of ferrocene (vs. QRE) A) for different scan rates and B) QRE potential calibration procedure.

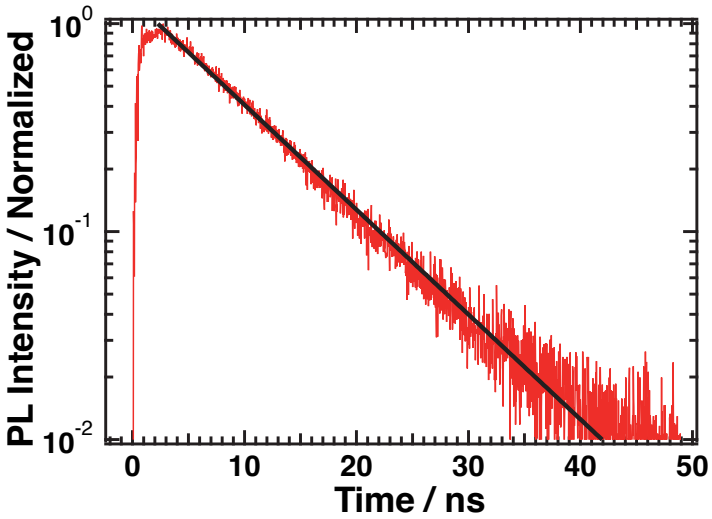

Figure A.2: PL decay ($\lambda_{\text{probe}} = 455$ nm) obtained by TCSPC (red line) with the best fitted exponential decay function (black line).

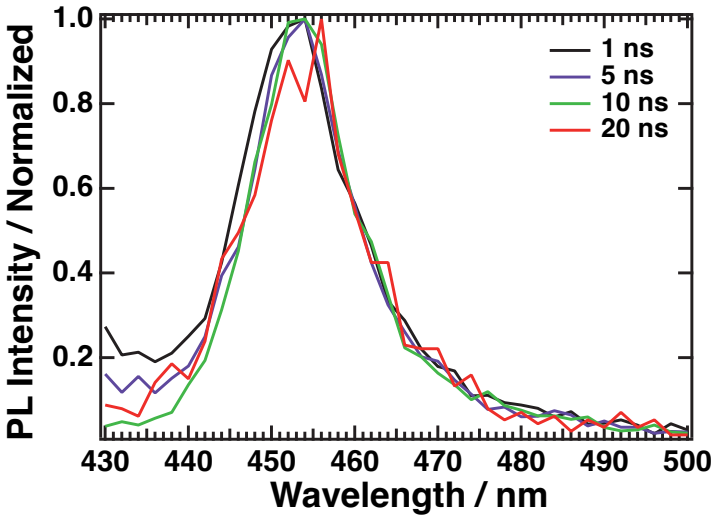

Figure A.3: Normalized TRPL spectral slices at different time delays obtained by TCSPC.

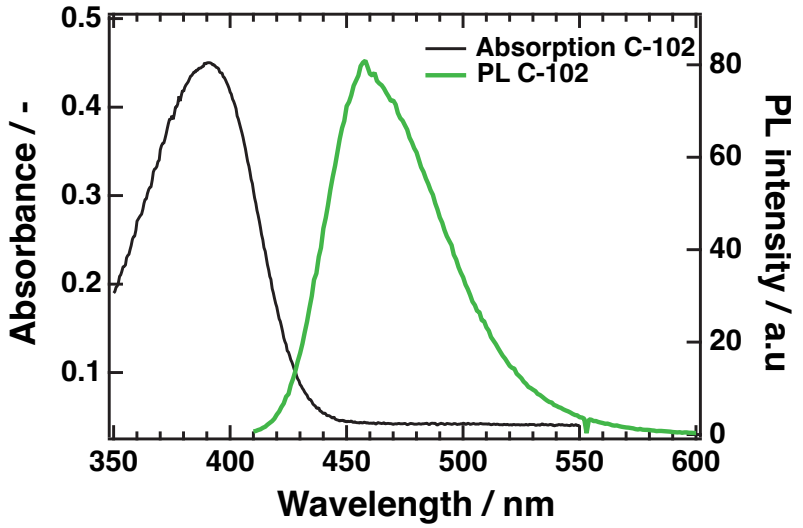

Figure A.4: Absorption and emission spectra of C102 used to estimate the NPl's PLQY.

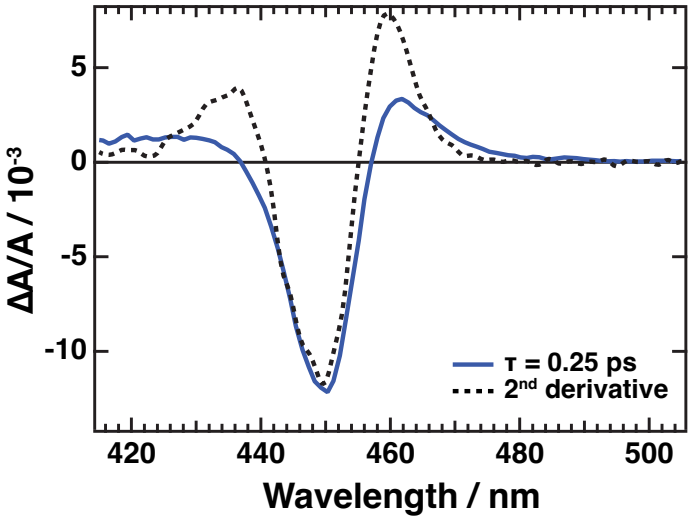

Figure A.5: TA spectral slices at $\tau_{\text{delay}} = 0.25$ ps with the second derivative of the absorption spectrum.

Appendix B - Early excited state dynamics in lead halide perovskite nanoplatelets

B - Additional derivations

Fitting of the simplified model accounting for shallow trap states

A homemade *Wolfram Mathematica* procedure was written to fit the experimental data with the model proposed in **Figure 4.1.B**. Firstly, the data before 500 fs were cut to ensure that all the photoexcited carriers are in the lowest excited state. Then, the kinetic traces from 452 to 458 nm (444-450 nm) were averaged and normalized at $\tau = 500$ fs. For each sample, the PL (TA) dynamics were fitted with **Equations 4.6-4.7**. N_{X_1}, $N_{X_{1'}}$ and N_{X_S} were determined by solving the differential **Equations 4.2-4.5** for a 0.5-1200 ps interval with the following initial conditions:

$$N_{X_1}(\tau = 0.5 \text{ ps}) = 1 - a \; ; \; N_{X_{1'}}(\tau = 0.5 \text{ ps}) = a \; ; \; N_{X_S}(\tau = 0.5 \text{ ps}) = 0 \qquad \text{(Eq. B.1)}$$

Fitting of the early time dynamics

To fit the FLUPS and TA dynamics at the sub-picosecond time scale, a convolution of a Gaussian and an exponential decay, d, (or rise, r) function was used (**Equations B.2-5**). The width of the Gaussian dynamics, w, was fixed to the value obtained by fitting the cross-correlation signal between the pump and the gate pulses (or the chirp in dodecane for TA experiments). The results are shown in **Tables B.1-B.3**.

$$d = y_0 + A_1 \cdot \exp(-t/\tau_1) \qquad \text{(Eq. B.2)}$$

$$r = y_0 + A_1\big[1 - \exp(-t/\tau_1)\big] \qquad \text{(Eq. B.3)}$$

$$g = \left(\frac{1}{w \cdot \sqrt{\pi/2}}\right) \cdot \exp\big[-2(t - t_0)^2/w^2\big] \qquad \text{(Eq. B.4)}$$

Table B.1 - Extracted parameters from the fitted equations displayed in Figure 4.4.B

Parameters / unit	**Band edge (FLUPS)**	**Main Peak (FLUPS)**
$\mathbf{A_1}$ / -	1.82 ± 0.04	1.33 ± 0.03
$\boldsymbol{w}$ / fs	190	190
$\boldsymbol{\tau_1}$ / fs	290 ± 20	290 ± 20
$\boldsymbol{t_0}$ /fs	-104 ± 6	-104 ± 6
y_0 / -	-0.02 ± 0.01	-0.35 ± 0.03

Table B.2 - Extracted parameters from the fitted equations displayed in Figure 4.5.B

Parameters / unit	**PIA red (TA)**	**PIA blue (TA)**
$\mathbf{A_1}$ / -	3.04 ± 0.10	3.96 ± 0.12
$\boldsymbol{w}$ / fs	221	221
$\boldsymbol{\tau_1}$ / fs	289 ± 11	295 ± 11
$\boldsymbol{t_0}$ /fs	-199 ±36	-204 ± 7
$\mathbf{y_0}$ / -	0.31 ± 0.02	0.99 ± 0.01

Table B.3 - Extracted parameters from the fitted equations displayed in Figure 4.6.B

Parameters / unit	**NPl-0.5**	**NPl-1.2**
$\mathbf{A_1}$ / -	2.84 ± 0.16	3.12 ± 0.14
$\boldsymbol{w}$ / fs	221	221
$\boldsymbol{\tau_1}$ / fs	320 ± 30	260 ± 20
$\boldsymbol{t_0}$ /fs	-210 ±26	-214 ± 19
$\mathbf{y_0}$ / -	0.01 ± 0.01	-0.01 ± 0.01

Carrier temperature calculation

To extract the carrier temperature the high energy tail of the TA spectrum at early-time (τ = 0.2 ps) was fitted by a Maxwell-Boltzmann distribution (**Equation B.2**).[7] This distribution is often used to approximate the Fermi-Dirac distribution function for hot carriers with energies higher than the Fermi Energy level:

$$\Delta A = A_1 \cdot \exp\left(\frac{-E}{\mathrm{T}_c \cdot k_B}\right) \qquad \text{(Eq. B.2)}$$

where E is the energy [eV], T_c is carrier temperature [K], and k_B is the Boltzmann constant [eV/K].

B - Additional figures

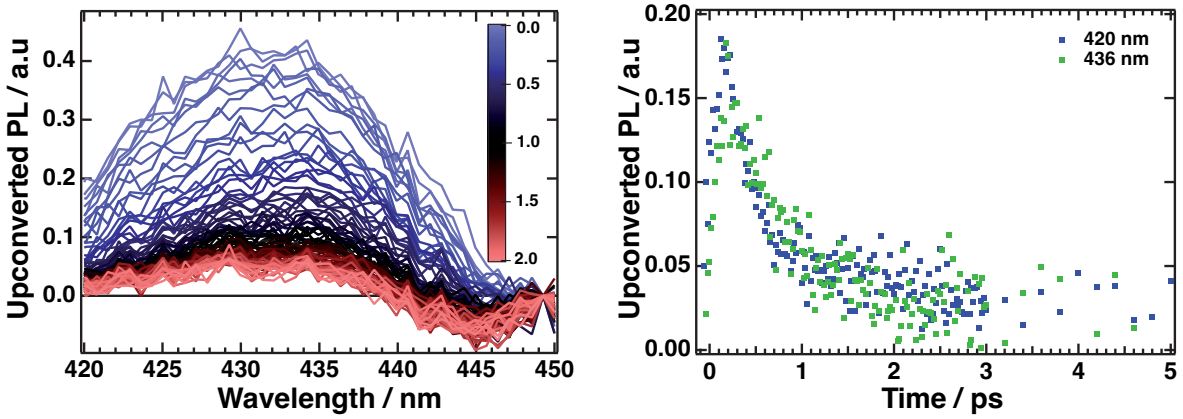

Figure B.1: Left) Isolated band edge emission spectral slices and right) dynamics.

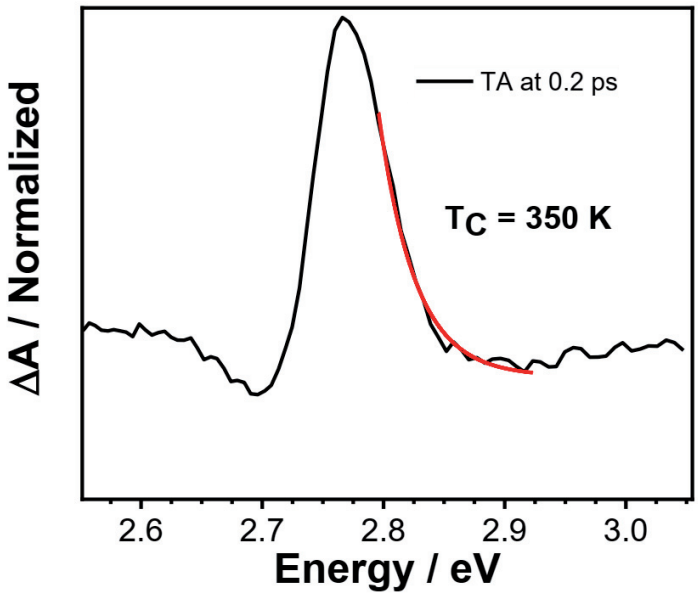

Figure B.2: TA spectral slice at $\tau = 200$ fs and the calculated carrier temperature from the procedure described in equation B.2.

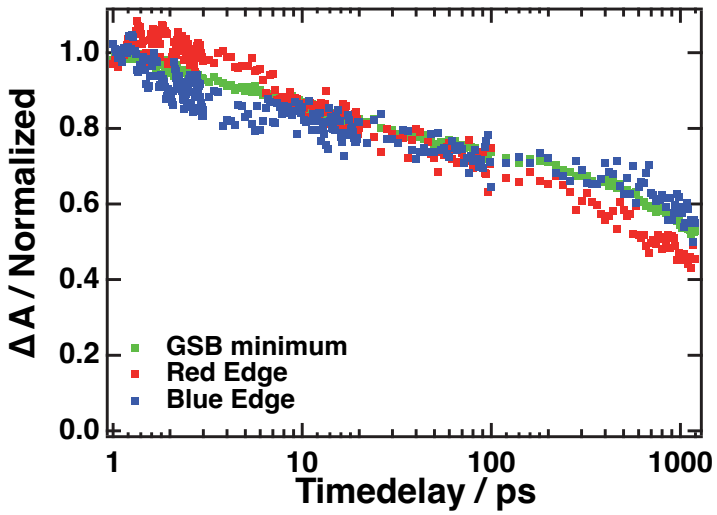

Figure B.3: Normalized, at $\tau = 1$ ps, TA dynamics at three different positions around the GSB minimum.

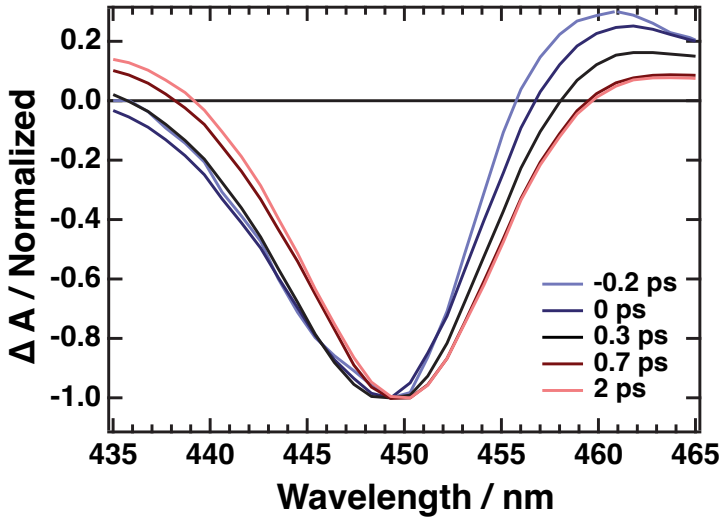

Figure B.4: Normalized TA spectral slices at early time scales showing a slight red shift.

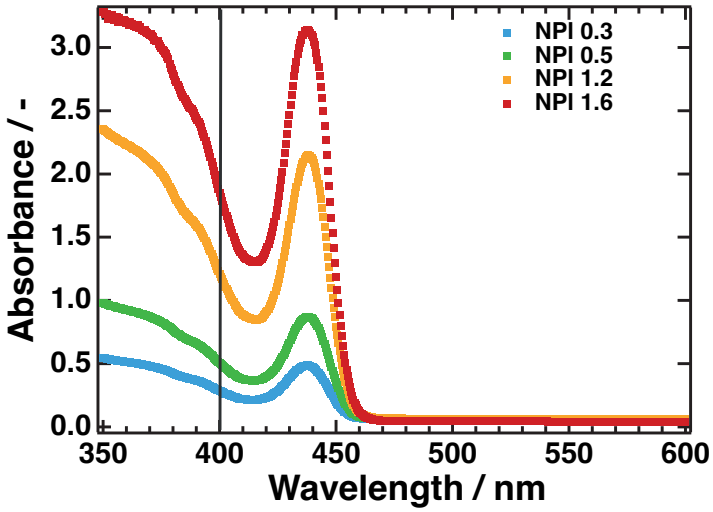

Figure B.5: Absorption spectra of $CsPbBr_3$ NPl solutions for different concentrations. The black line indicates the samples absorbance at 400 nm.

Appendix C - Multiexciton processes in lead halide perovskite nanoplatelets

C - Additional derivations

Fitting of the lowest excited state dynamics

To fit the traces in **Figure 5.4**, the PL and PIA-2 dynamics were normalized at $\tau = 0.2$ ps and fitted with a bi-exponential decay function convoluted with a Gaussian function. The amplitudes and lifetimes were fitted, while the Gaussian width and t_0 were fixed by fitting the cross-correlation signal between the pump and the gate for FLUPS experiment (or the chirp in dodecane for TA experiments). To increase the signal-to-noise ratio of the isolated band edge signal in the FLUPS an average of five dynamic slices around 442 nm was calculated before normalization.

Table C.1 - Extracted parameters from the fitted equations displayed in Figure 5.4.A.

FLUPS / $\langle N_x \rangle$	**A_1**	**τ_1 / ps**	**A_2**	**τ_2 / ps**
0.1	1.0	0.35 ± 0.05	-	-
0.4	0.97	0.36 ± 0.06	0.03	1.5 ± 2.7
0.6	0.96	0.33 ± 0.03	0.04	3.1 ± 2.5
1.1	0.92	0.35 ± 0.04	0.08	1.5 ± 0.7
2.2	0.81	0.32 ± 0.04	0.19	1.4 ± 0.3
3.2	0.77	0.32 ± 0.03	0.23	1.5 ± 0.2
5.4	0.58	0.32 ± 0.03	0.42	2.0 ± 0.2

Table C.2 - Extracted parameters from the fitted equations displayed in Figure 5.4.B.

TA / $\langle N_x \rangle$	**A_1**	**τ_1 / ps**	**A_2**	**τ_2 / ps**	**y_0**
0.2	1.0	0.30 ± 0.02	0.001	2.5 ± 0.1	0.19
0.4	0.99	0.30 ± 0.02	0.01	2.5 ± 0.1	0.17
0.8	0.97	0.30 ± 0.02	0.03	2.5 ± 0.1	0.17
1.3	0.96	0.30 ± 0.02	0.04	2.5 ± 0.1	0.19
1.7	0.87	0.30 ± 0.02	0.13	2.5 ± 0.1	0.17
2.0	0.85	0.30 ± 0.02	0.15	2.5 ± 0.1	0.19
2.5	0.80	0.30 ± 0.02	0.20	2.5 ± 0.1	0.15
3.5	0.80	0.30 ± 0.02	0.20	2.5 ± 0.1	0.15
4.0	0.77	0.30 ± 0.02	0.23	2.5 ± 0.1	0.15

Table C.3 - Extracted parameters from the fitted equations displayed in Figure 5.6.

Sample	$\mathbf{A_1}$	$\boldsymbol{\tau_1}$ **/ ps**	$\mathbf{A_2}$	$\boldsymbol{\tau_2}$ **/ ps**
NPl-0.3	0.43 ± 0.04	0.28 ± 0.04	0.57 ± 0.04	1.53 ± 0.12
NPl-0.5	0.60 ± 0.02	0.28 ± 0.02	0.40 ± 0.02	1.67 ± 0.16
NPl-1.2	0.95 ± 0.05	0.29 ± 0.02	0.05 ± 0.05	1.13 ± 0.89

C - Additional figures

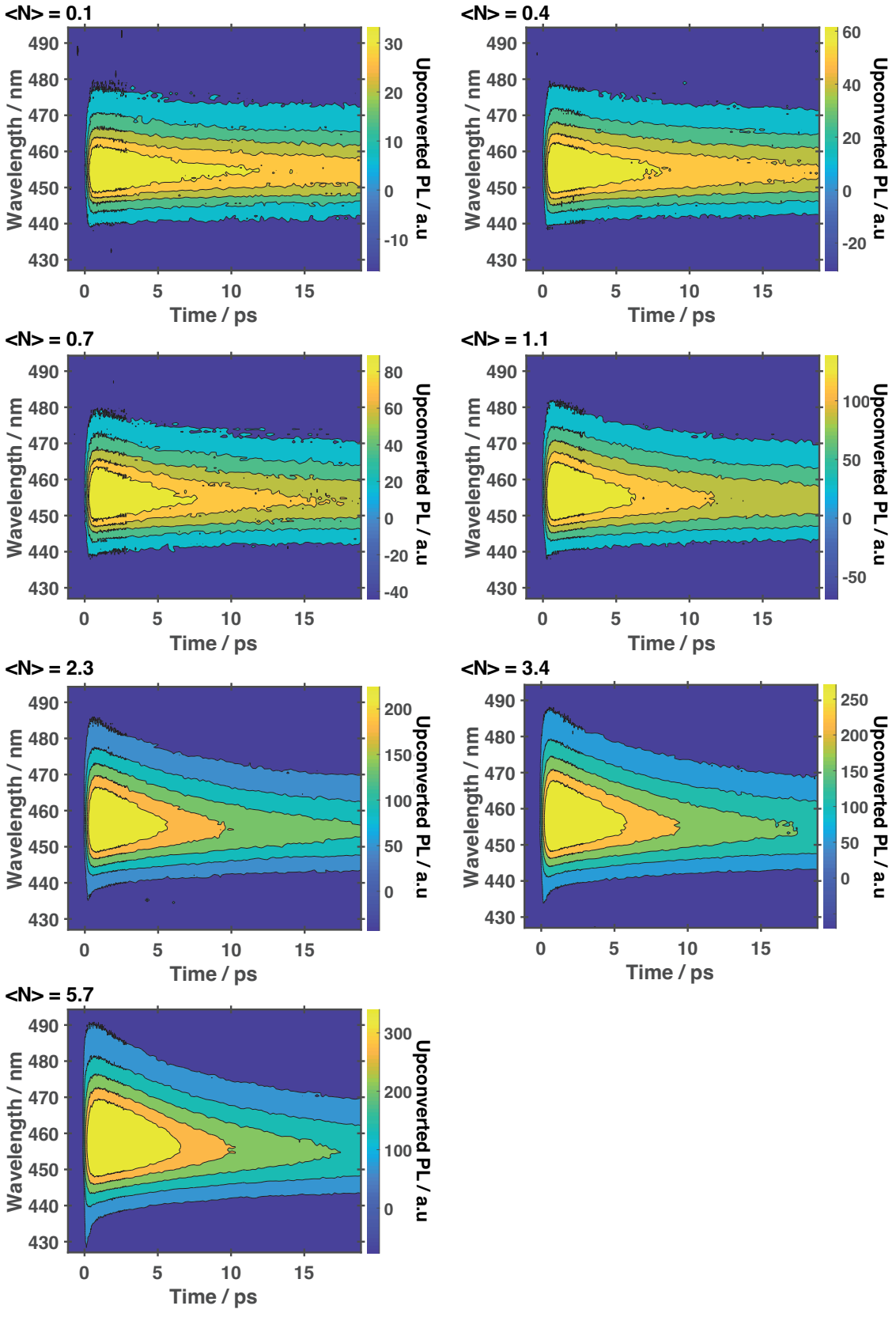

Figure C.1: 2D FLUPS spectra at early time scales for $\langle N_x \rangle$ = 0.1-5.7.

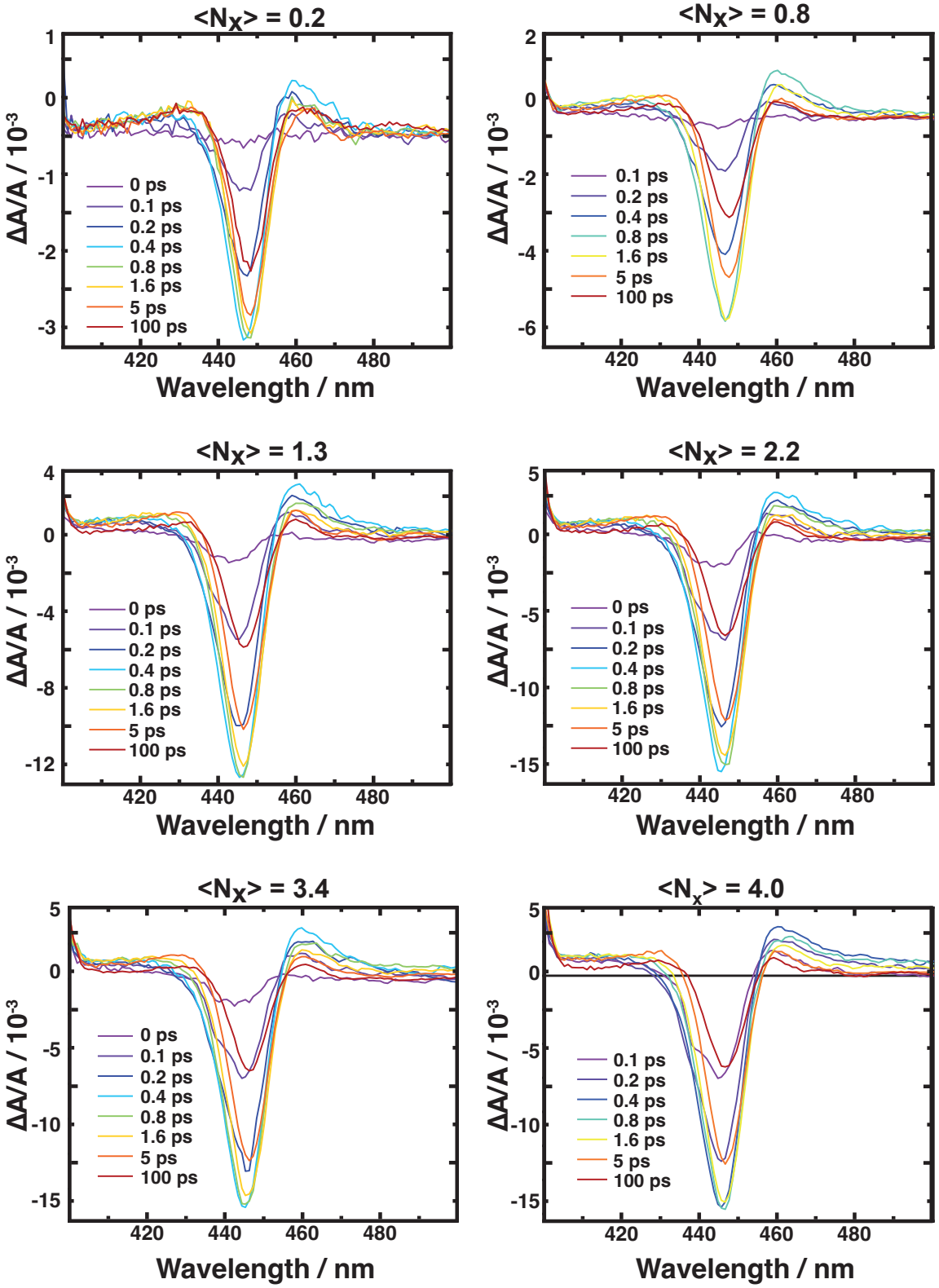

Figure C.2: TA spectral slices for $\langle N_x \rangle$ = 0.2-4.0.

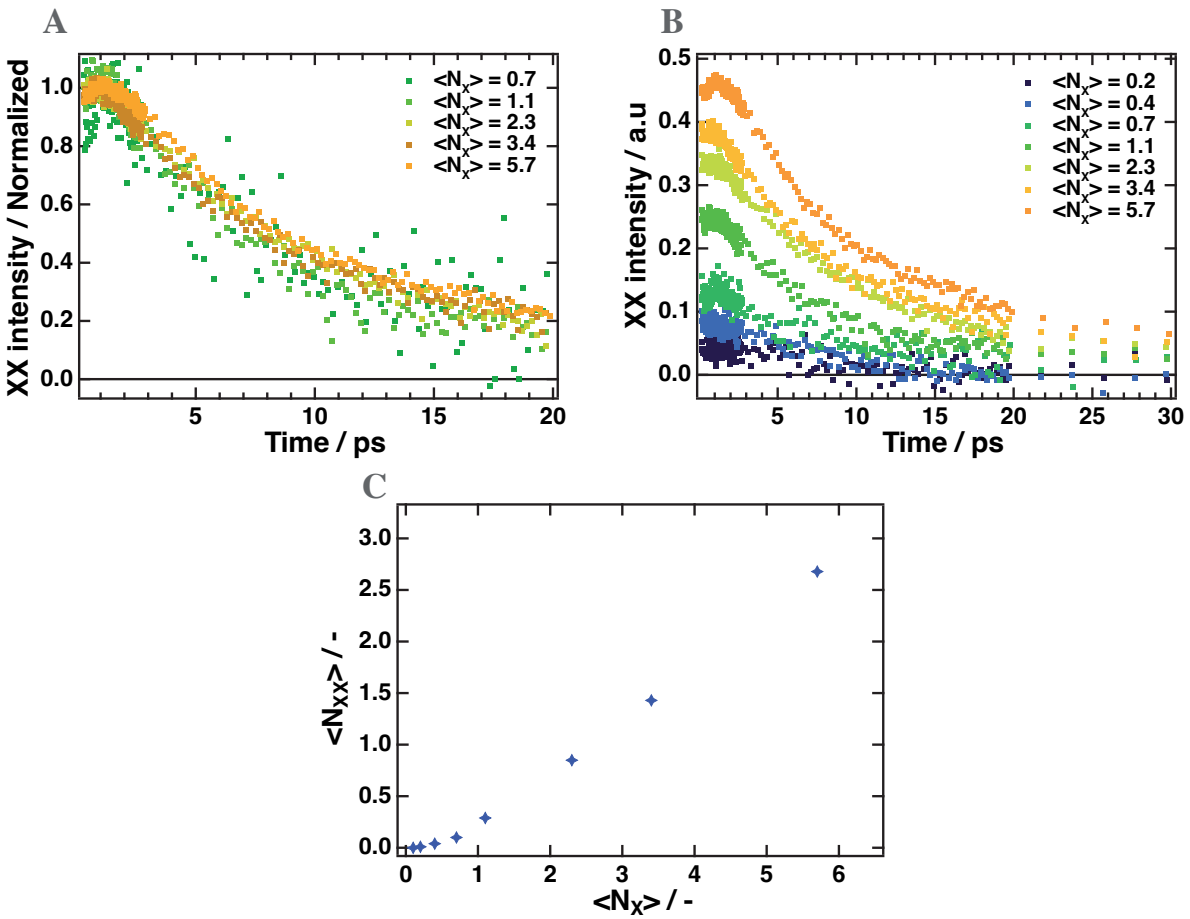

Figure C.3: A) Normalized and B) raw isolated biexciton PL dynamics ($\lambda_{\text{probe}} = 465$ nm) for $\langle N_{\text{x}} \rangle = 0.2$-5.7. C) Average number of biexcitons per NPl as a function of the average number of excitons.

Appendix D - Charge separation in $CsPbBr_3$ NPls

D - Additional derivations

Isolation of the hot charge carrier transfer

A homemade procedure was set up to evaluate the dependence of the initial PL intensity of NPl-acceptor complexes on the pump energy. As shown in **Table D.1**, the absorption cross-section slightly depends on the excitation wavelength. Hence, it becomes challenging to generate the same number of excitons by varying the excitation energy. To overcome this issue, PL dynamics of pristine NPl solutions were collected for each excitation wavelength and serve as a reference. Then, by considering that the pristine NPl signal intensity was independent of the excitation wavelength and the raw PL dynamics were normalized at $\tau = 1$ ps (**Figure D.6**). Then, the same normalization factor was applied to correct the raw PL for NPl-acceptor complexes (**Figure D.7**). Finally, the percentage of hot carriers transferred was estimated by taking the maximum of each "corrected" PL dynamics.

Side notes: a) This procedure is only valid if the pump intensity is low enough to avoid the generation of multiple excitons. Thus, the excitation beam was set at 9 nJ for each wavelength. b) The beam deflection from the organic acceptor in the 305-430 nm range was neglected . Since the absorption cross-section of the organic molecules is four orders of magnitude smaller (**Table D.1**), this assumption should be valid for low acceptor concentration. c) It has also been considered that the addition of PTZ or BQ does not create new above band edge trap states, which could lower the PL intensity when pumping at high excitation energy.

Table D.1 - Comparison of the $CsPbBr_3$ NPls absorption cross-section obtained by Poisson statistics and molecular acceptor cross-section reported in the Chemistry Webbook,[8] at different excitation wavelengths.

Excitation wavelength [nm]	$\sigma_{\mathbf{NPls}}$ **[10^{-14} cm^2]**	$\sigma_{\mathbf{PTZ}}$ **[10^{-14} cm^2]**	$\sigma_{\mathbf{BQ}}$ **[10^{-14} cm^2]**
305	0.92 ± 0.10	0.0014	< 0.0001
320	0.91 ± 0.08	0.0017	< 0.0001
340	0.85 ± 0.09	0.0009	< 0.0001
355	0.75 ± 0.06	0.0003	< 0.0001
370	0.90 ± 0.08	< 0.0001	< 0.0001
400	0.73 ± 0.06	< 0.0001	< 0.0001
435	0.58 ± 0.03	< 0.0001	< 0.0001

D - Additional figures

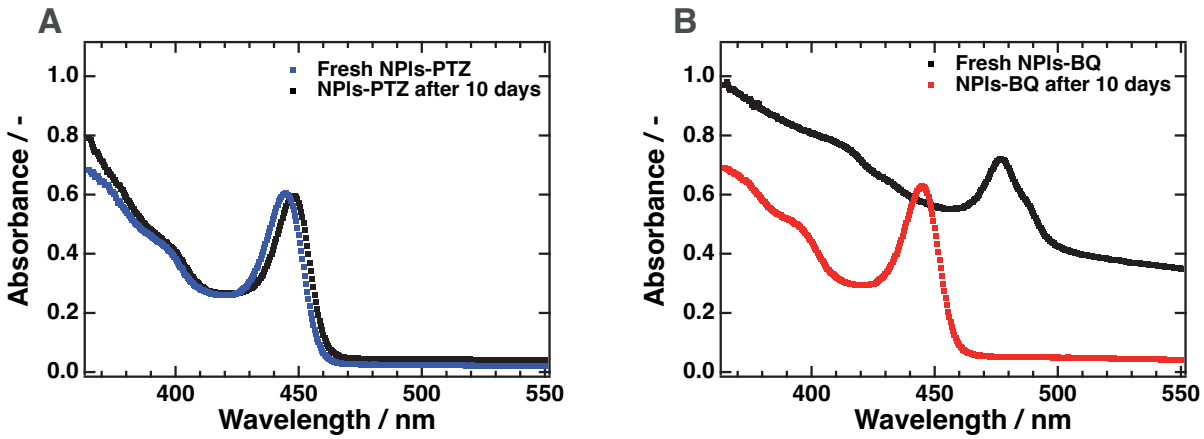

Figure D.1: Absorption spectra of fresh and aged A) NPl-PTZ and B) NPl-BQ complexes.

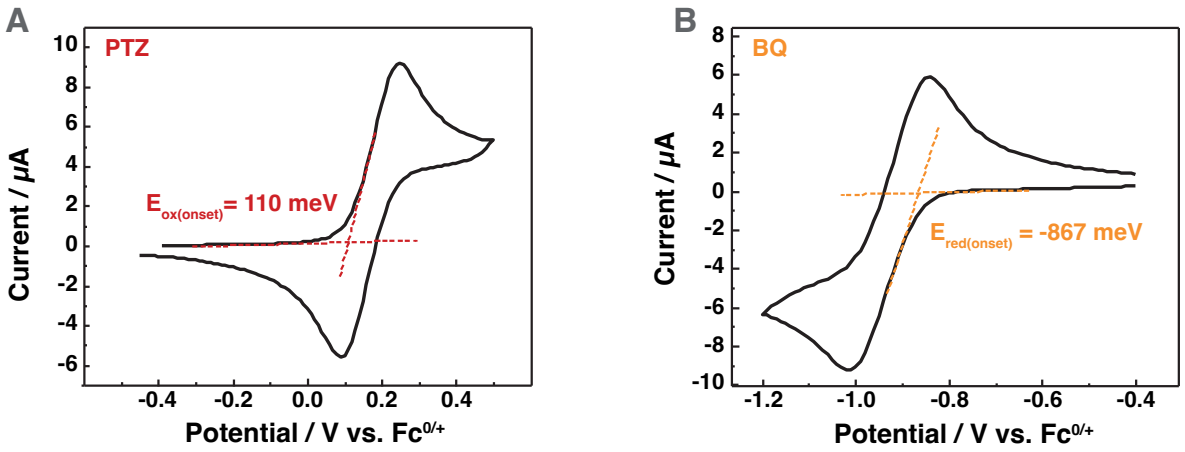

Figure D.2: Cyclic voltammogram to estimate the A) HOMO level in PTZ and B) LUMO level in BQ.

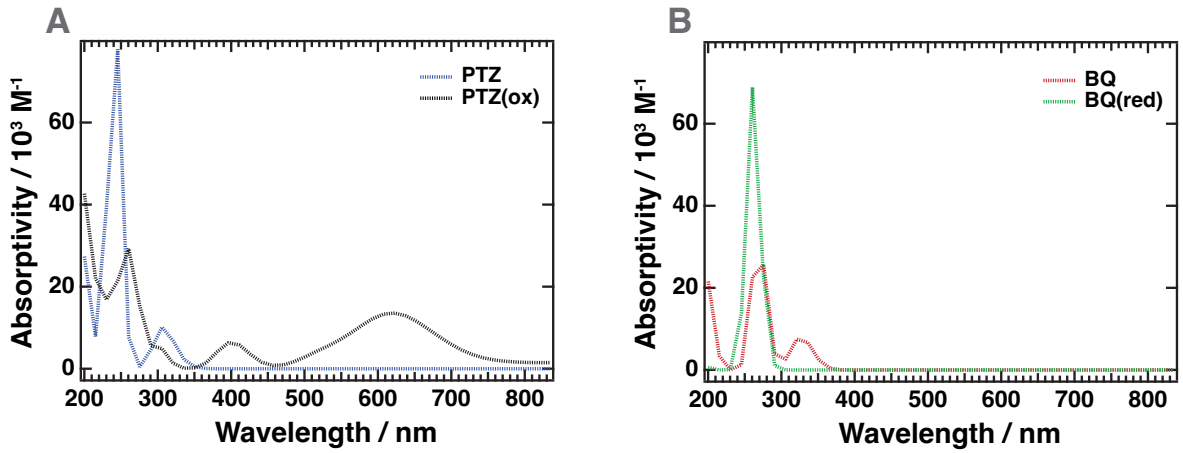

Figure D.3: Theoretical UV-Vis absorption spectra obtained by modeling BQ, reduced BQ, PTZ and oxidized PTZ in Scigress. This model is only a first approach since it does not take the effect of the solvent nor ligand-perovskite interactions.

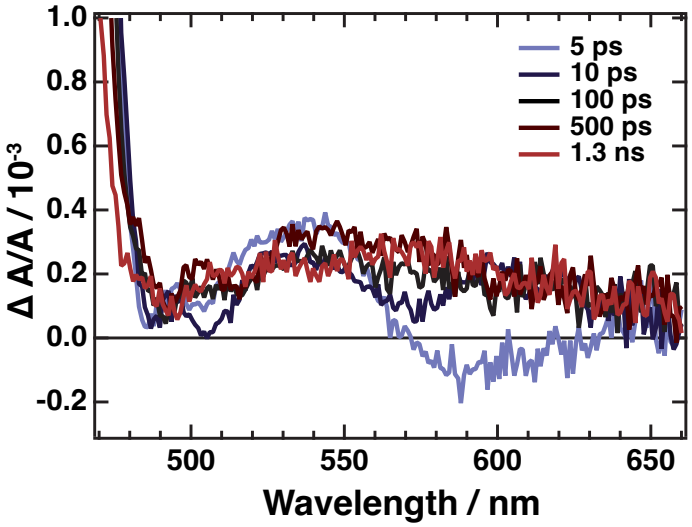

Figure D.4: TA spectral slices zoomed on the oxidized PTZ region for NPl-PTZ complexes under a strong photoexcitation intensity.

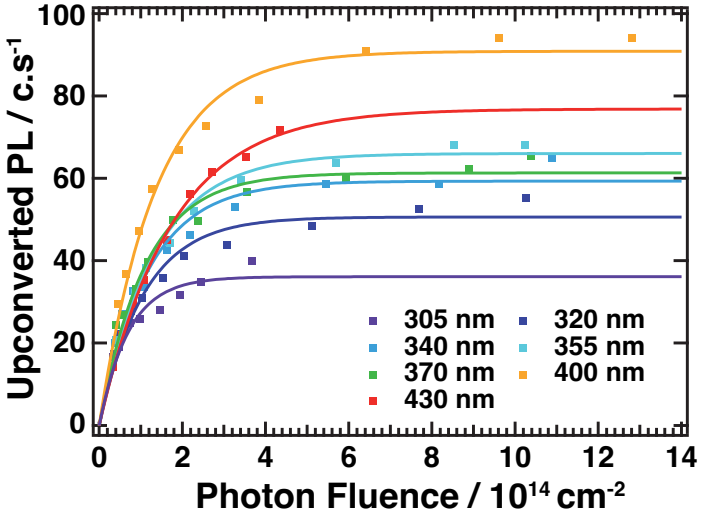

Figure D.5: PL intensity (λ_{probe} = 455 nm) at τ = 100 ps as a function of the pump photon fluence and the best fitted curves from Poisson statistics for different excitation wavelengths.

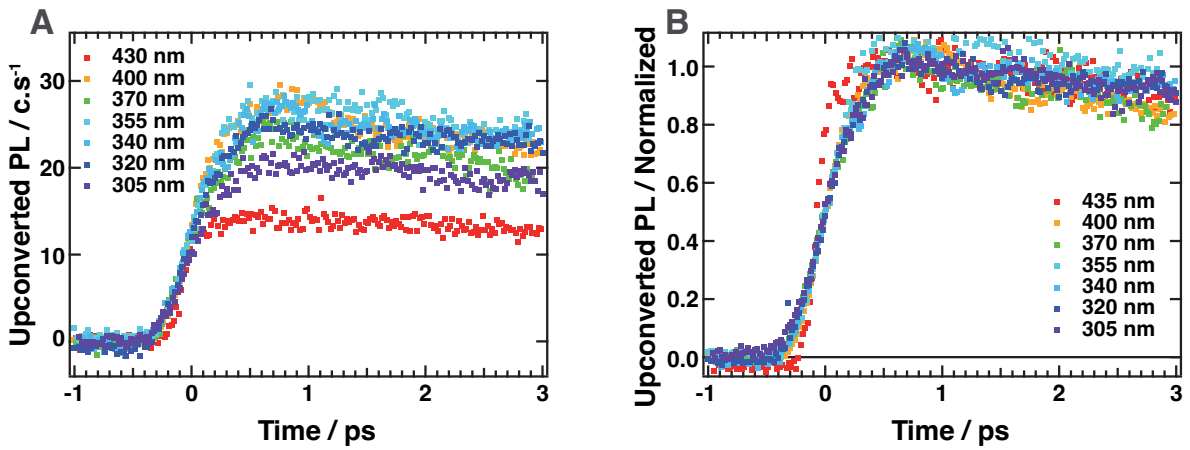

Figure D.6: A) Raw and B) normalized PL dynamics of pristine $CsPbBr_3$ NPls for different excitation wavelengths. The normalization factor is retained to correct the complexes PL.

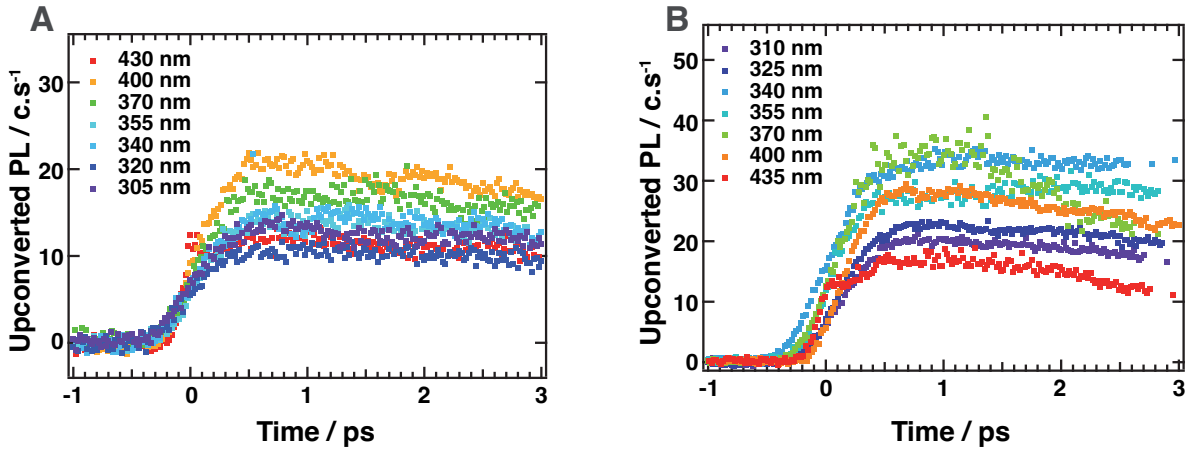

Figure D.7: Raw PL dynamics of A) NPl-PTZ and B) NPl-BQ complexes for different excitation wavelengths.

Bibliography

[1] Grim, J. Q.; Christodoulou, S.; Di Stasio, F.; Krahne, R.; Cingolani, R.; Manna, L.; Moreels, I. Continuous-wave biexciton lasing at room temperature using solution-processed quantum wells. *Nat. Nanotechnol.* **2014**, *9*, 891–895.

[2] Wu, Y.; Wei, C.; Li, X.; Li, Y.; Qiu, S.; Shen, W.; Cai, B.; Sun, Z.; Yang, D.; Deng, Z.; Zeng, H. In Situ Passivation of $PbBr_6^{4-}$ Octahedra toward Blue Luminescent $CsPbBr_3$ Nanoplatelets with Near 100% Absolute Quantum Yield. *ACS Energy Lett.* **2018**, *3*, 2030–2037.

[3] Li, J.; Luo, L.; Huang, H.; Ma, C.; Ye, Z.; Zeng, J.; He, H. 2D Behaviors of Excitons in Cesium Lead Halide Perovskite Nanoplatelets. *J. Phys. Chem. Lett.* **2017**, *8*, 1161–1168.

[4] Bard, A. J.; Faulkner, L. R. *Electrochemical Methods: Fundamentals and Applicaitons, 2e*; John Wiley & Sons, 2002.

[5] Fries, F.; Reineke, S. Statistical treatment of Photoluminescence Quantum Yield Measurements. *Sci. Rep.* **2019**, *9*, 15638.

[6] Reynolds, G.A.,; Drexhage, K. H., New Coumarin Dyes With Rigidized Structure For Flashlamp-Pumped Dye Lasers. *Opt. Commun.* **1975**, *13*, 222–225.

[7] Mondal, A.; Aneesh, J.; Kumar Ravi, V.; Sharma, R.; Mir, W. J.; Beard, M. C.; Nag, A.; Adarsh, K. V. Ultrafast exciton many-body interactions and hot-phonon bottleneck in colloidal cesium lead halide perovskite nanocrystals. *Phys. Rev. B* **2018**, *98*, 115418.

[8] NIST, Chemistry WebBook. https://webbook.nist.gov/, Accessed on May 31st, 2022.

Appendix E - Symbols and abbreviations

α	Absorption constant [cm^{-1}]
ΔA	Transient absorption signal [-]
ΔE	Energy difference between X_1 and S [eV]
ΔE_S	Stokes shift [eV]
Δk	Phase mismatch [m^{-1}]
Δ_x	Exciton binding energy [eV]
Δ_{xx}	Biexciton binding energy [eV]
ε	Permittivity [F/m]
ϵ	Molar attenuation coefficient [cm^2/mol]
η	Asymmetric broadening [eV]
θ	Mean fractional coverage of acceptors on one nanoplatelet [-]
θ_{max}	Maximum fractional coverage of acceptors on one nanoplatelet [-]
λ	Wavelength [nm]
μ	Carrier mobility [$cm^2 \cdot V^{-1} \cdot s^{-1}$]
σ_λ	Absorption cross-section at λ nm [cm^{-1}]
τ_{delay}	Time delay [ps]
$\tau_{x,rad}$	Single exciton radiative recombination lifetime [ns]
$\tau_{xx,A}$	Exciton-exciton annihilation lifetime [ps]
$\tau_{xx,r}$	Biexciton radiative recombination lifetime [ns]
$\tau_{CT,cold}$	Cold charge transfer lifetime [ns]
$\tau_{CT,hot}$	Hot charge transfer lifetime [ns]
τ_{CR}	Charge recombination lifetime [ns]
Φ_{PL}	Photoluminescence quantum yield [-]
ω	Angular frequency [s^{-1}]
$[A]$	Acceptor concentration [mol/L]
a	Proportion of nanoplatelets containing deep trap states [-]
A	Absorbance [-]
A_1 - A_4	Amplitudes [-]
c	NPl concentration [mol/L]
$\langle d \rangle$	Average distance between two nanoplatelets [nm]
d_{eff}	Effective nonlinear susceptibility [-]
e	Elementary charge [$1.60 \cdot 10^{-19}$ C]

E_F	Fermi Level [eV]
E_g	Band gap [eV]
E_{x}	Exciton transition energy [eV]
E_{xx}	Biexciton transition energy [eV]
h	Planck constant [$6.63{\cdot}10^{-34}$ J·s]
$\hbar$	Reduced Planck constant [$1.05{\cdot}10^{-34}$ J·s]
H	Continuum step height [-]
I_0	Initial light intensity [W/m^2]
$I(l)$	Light intensity at point l [W/m^2]
I_G	Intensity of the gate beam [E/m^2]
j	Density of photons per unit area [cm^{-3}]
$\mathbf{k}$	Momentum vector [-]
K_{acc}	Acceptor binding constant [-]
k_B	Boltzmann constant [$1.38{\cdot}10^{-23}$ J/K]
k_D (τ_D)	Rate constant (lifetime) for exciton trapping into deep trap states [s^{-1} (ps)]
k_S (τ_S)	Rate constant (lifetime) for exciton trapping into shallow states [s^{-1} (ps)]
k_{-S} (τ_{-S})	Rate constant (lifetime) for exciton de-trapping from shallow states [s^{-1} (ps)]
k_{rad} (τ_{rad})	Radiative recombination rate constant (lifetime) [s^{-1} (ns)]
l	Optical path length [cm]
l_{NPl}	Length of the nanoplatelet [nm]
L	Dimension of the semiconductor [m]
L_c	Crystal thickness [m]
m	Average number of acceptor molecules bound on the nanoplatelet surface [-]
m_0	Free electron mass [$9.11{\cdot}10^{-31}$ kg]
$m^*_{c/e/h}$	Carrier/electron/hole effective masses [kg]
n	Number of excitons per nanoplatelet [-]
n_e	Extraordinary refractive index [-]
n_o	Ordinary refractive index [-]
N	Particle density [particle/cm^3]
N_A	Avogadro number [$6.02{\cdot}10^{23}$ mol^{-1}]
N_{abs}	Number of photons absorbed by the sample [-]
N_b	Number of available binding sites per nanoplatelet [-]
N_c	Charge carrier density [m^{-3}]
N_{em}	Number of photons emitted [-]

$\langle N_{\mathrm{x}} \rangle$	Average number of exciton per nanoplatelet [-]
N_{X_1}	Proportion of nanoplatelets without deep trap states [-]
$N_{X_{1'}}$	Proportion of nanoplatelets without shallow trap states [-]
N_{X_D}	Proportion of excitons in deep trap states [-]
N_{X_S}	Proportion of excitons in shallow trap states [-]
p	Momentum [kg·m/s]
P	Pixel number [-]
PL_0	Normalized PL of pristine nanoplatelets [-]
$\mathrm{PL}_{\mathrm{acc}}$	Normalized PL of nanoplatelets-acceptor complexes [-]
r_0	Bulk-exciton radius [m]
R_H	Rydberg energy of the hydrogen atom [13.6 eV]
T	Temperature [K]
t_0	Time-zero [ps]
T_c	Carrier temperature [K]
V_{NPl}	Volume of the nanoplatelet [nm^3]
w	Line width of a transition [eV]
w_c	Continuum edge width [eV]
w_{NPl}	Lateral size of the nanoplatelet [nm]
w_{x}	Exciton peak width [eV]

0	Ground state
ASE	Amplified spontaneous emission
BBO	Beta barium borate
BQ	p-benzoquinone
C102	Coumarin 102
C153	Coumarin 153
CB	Conduction band
CBM	Conduction band minimum
CCD	Charge-couple device
CHS	Confined hole state
CPA	Chirped pulse amplification
CR	Charge recombination
CS	Charge separation
CT	Charge-transfer (state)

CV	Cyclic voltammetry
D	Deep trap state
DAS	Decay associated spectrum
DOS	Density of states
ETM	Electron transporting material
FA	Formamidinium $CH(NH_2)_2^+$
FLUPS	Fluorescence upconversion spectroscopy
HTM	Hole transporting material
GSB	Ground state bleaching
ICT	Interfacial charge transfer
IPA	Isopropanol
LED	Light-emitting diode
LHP	Lead halide perovskite
MA	Methylammonium, CH_3NH_3
ML	Monolayer
NC	Nanocrystal
NPl	Nanoplatelet
OA	Oleic acid
OAm	Oleylamine
OPA	Optical parametric amplifier
OPV	Organic photovoltaic
PIA	Photo-induced absorption
PL	Photoluminescence
PLQY	Photoluminescence quantum yield
PMT	Photomultiplier tube
PNC	Perovskite nanocrystal
PTZ	Phenothiazine
PV	Photovoltaic
QD	Quantum dot
QRE	Quasi-reference electrode
RT	Room temperature
S	Shallow trap state
SC	Semiconductor
SE	Stimulated emission

SFG	Sum-frequency generation
SOC	Spin-orbit coupling
SRH	Shockley-Read-Hall recombination
TA	Transient absorption spectroscopy
TCSPC	Time-correlated single photon counting
TEM	Transmission electron microscopy
TOPO	Trioctylphosphine oxide
TRPL	Time-resolved photoluminescence
VB	Valence band
VBM	Valence band maximum
X_1	Lowest excited state
WLC	White-light continuum
WM	Wannier-Mott

MR. ETIENNE SOCIE

PhD candidate at EPFL, specialized in experimental spectroscopy and photophysics of semiconducting materials. Collaborated with scientific groups all around the world. Highly motivated to work, positive attitude and strong social skills.

PERSONNAL INFORMATION

July 19th, 1995, Annemasse (France)
etienne.socie@gmail.com
(+41) 078 226 46 45
Rue de la Blancherie, 40
1022-Chavannes-près-Renens

Etienne Socie
0000-0002-7168-6180

SKILLS

Science
- **Experimental design**
- **Spectroscopy**
- **Photophysics**
- **Photochemistry**
- **Ultrafast laser handling**

Communication
- **Team Work**
- **Scientific writing**
- **Teaching**

Data analysis
- **Igor**
- **Office**
- **Matlab**

Languages
- **French**
- **English**
- **Italian**

HOBBIES

Running
Cycling
Hiking
Skiing
Cooking

OBJECTIVE

Apply my thinking and my dynamism to stimulating projects. Learn new skills and discover new working environments.

WORK HISTORY

09/2018-Present
EPFL, Lausanne
PhD Candidate
Ultrafast spectroscopy on semiconductor (nano)-materials. Specialized in fluorescence and time-resolved fluorescence experiments. Thesis director: J.-E. Moser

09/2015 - Present
EPFL, Lausanne
Teaching assistant
Help students for solving chemistry/math problems; Exam proofing/grading; Practical work supervision in analytical chemistry; Lecturer substitution; Projects supervision for master students

09/2021 - Present
Université de Lausanne
Running coach
Organize and schedule weekly running sessions for a group of $\sim$ 30-50 students. Organize a bi-annual trail week-end for $\sim$ 30 participants.

11/2013 - 06/2017
Sportal, Switzerland
Sport commentator
Cover the live action play-by-play of sporting events in many Swiss french-speaking newspapers.

EDUCATION

09/2012 - 04/2018
EPFL, Lausanne
Bachelor & Master in Chemistry
Orientation Physical, analytical and inorganic chemistry

09/2017 - 04/2018
McGill University, Montreal
Master project
Group of Pr. Kambhampati, development of a synthesis protocol to stabilize nanoparticles for ultrafast spectroscopic investigations.

ORGANIZATIONS

- Chemistry Students Association, President (2016-2017)
- Baramine: Org. to obtain funding for a study trip, President (2015-2016)

GENERAL APTITUDES

Organized | Efficient | Independent | Proactive | Cheerful

WHEEL CHART

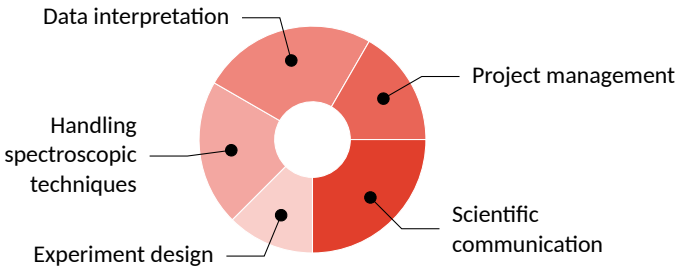

PUBLICATIONS

- E. Socie, B. R. C. Vale, A. F. V. Fonseca, J. Bettini, J.-E. Moser, Charge-separation Mechanism in Strongly Confined Quasi-one-dimensional $CsPbBr_3$ Perovskite Nanocrystals, *Submitted*.
- B. R. C. Vale, E. Socie, M. A. Schiavon, J.-E. Moser, Exciton and Multiexciton Dynamics in Lead Halide Perovskite Nanocrystals, *Submitted*.
- S. Nussbaum, E. Socie, L. Yao, J. H. Yum, J.-E. Moser, K. Sivula, Tuning Napththalenediimide Cations for Incorporation into Ruddlesden–Popper-Type Hybrid Perovskites, *Chem. Mater.*, **2022**, 34 (8), 3798-3805.
- E. Socie, B. R. C. Vale, A. T. Terpstra, M. A. Schiavon, J.-E. Moser, Resonant Band-Edge Emissive States in Strongly Confined $CsPbBr_3$ Perovskite Nanoplatelets, *J. Phys. Chem. C*, **2021**, 125 (26), 14317-14325.
- D. Zhang, M. Stojanovic, Y. Ren, Y. Cao, F. T. Eickemeyer, E. Socie, N. Vlachopoulos, J.-E. Moser, S. M. Zakeeruddin, A. Hagfeldt, M. Grätzel, A molecular photosensitizer achieves a Voc of 1.24 V enabling highly efficient and stable dye-sensitized solar cells with copper (II/I)-based electrolyte, *Nat. Commun.*, **2021**, 12 (1), 1-10.
- E. Socie, B. R. C. Vale, A. Burgos-Caminal, J.-E. Moser, Direct Observation of Shallow Trap States in Thermal Equilibrium with Band-Edge Excitons in Strongly Confined $CsPbBr_3$ Perovskite Nanoplatelets, *Adv. Opt. Mater.*, **2021**, 9 (1), 2001308.
- B. R. C. Vale, E. Socie, L. R. C. Cunha, A. F. V. Fonseca, R. Vaz, J. Bettini, J.-E. Moser, M. A. Schiavone, Revealing Exciton and Metal–Ligand Conduction Band Charge Transfer Absorption Spectra in Cu-Zn-In-S Nanocrystals, *J. Phys. Chem. C*, **2020**, 124 (50), 27858-27866.
- A. Burgos-Caminal, E. Socie, M. E. F. Bouduban, J.-E. Moser, Exciton and carrier dynamics in two-dimensional perovskites, *J. Phys. Chem. Lett.*, **2020**, 11 (18), 7692-7701.
- C. E. Avalos, S. Richert, E. Socie, G. Karthikeyan, G. Casano, G. Stevanato, D. J. Kubicki, J.-E. Moser, C. R. Timmel, M. Lelli, A. J. Rossini, O. Ouari, L. Emsley, Enhanced Intersystem Crossing and Transient Electron Spin Polarization in a Photoexcited Pentacene-Trityl Radical, *J. Phys. Chem. A.*, **2020**, 124 (29), 6068-6075.
- H. Jiang, Y. Ren, W. Zhang, Y. Wu, E. Socie, B. I. Carlsen, J.-E. Moser, H. Tian, S. M. Zakeeruddin, W.-H. Zhu, M. Grätzel, Phenanthrene-Fused-Quinoxaline as a Key Building Block for Highly Efficient and Stable Sensitizers in Copper-Electrolyte-Based Dye-Sensitized Solar Cells, *Angew. Chem. Int. Edit.*, **2020**, 132 (24), 9410-9415.
- B. R. C. Vale, E. Socie, A. Burgos-Caminal, J. Bettini, M. A. Schiavon, J. E. Moser, Exciton, Biexciton and Hot Exciton Dynamics in $CsPbBr_3$ Colloidal Nanoplatelets, *J. Phys. Chem. Lett.*, **2020**, 11 (2), 387-394.

- H. Seiler, S. Palato, C. Sonnichsen, H. Baker, E. Socie, D. P. Strandell, P. Kambhampati, Two-dimensional electronic spectroscopy reveals liquid-like lineshape dynamics in $CsPbI_3$ peovskite nanocrystals, *Nat. Commun.*, **2019**, 10 (1), 1-8.
- A. C. Pinon, J. Scchlagnitweit, P. Berruyer, A. J. Rossini, M. Lelli, E. Socie, M. Tang, T. Pham, A. Lesage, S. Schantz, L. Emsley, Measuring nano-to microstructures from relayed dynamic nuclear polarizaion, *J. Phys. Chem. C*, **2017**, 121 (29), 15993-16005.

TALKS

- Swiss chemical society fall meeting (**SCS**). 09/2021, *Online.*
- International Conference on Photochemistry (**ICP**). 07/2021, *Geneva (Online).*

POSTERS

- Swiss chemical society fall meeting (**SCS**), 09/2019, *Zurich.*
- Int. conference on perovskite solar cells and optoelectronics (**PSCO**), 09/2019, *Lausanne.*
- Int. conference on hybrid and organic photovoltaics (**HOPV**), 05/2019, *Roma.*
- Int. conference on molecular ultrafast science and technology (**MUST**), 01/2019, *Grindelwald.*

TEACHING

- Advanced chemistry (French), 1st year of bachelor in Chemistry, 2018-2022.
- Chemistry Lab (French/English), 1st year of bachelor in Chemistry, 2019.
- General and analytical chemistry II (French, ex cathedra), 1st year of bachelor in Biology and Pharmaceutical sciences, 2019.
- Linear algebra (French), 1st year of bachelor in Chemistry, 2019.
- Analytical chemistry lab (French/English), 2nd year of bachelor in Chemistry, 2021.
- Project in molecular sciences II (English), 1st year of master in Chemistry, 2018; 2020.
- Journée des Gymnasiens, introduction and demonstration for secondary school students, 2020-2021, EPFL.